UNIVERSITY OF CALIFORNIA, SAN DIEGO

Experimental studies of the head-disk interface from a tribological and controls point of view for flying heights below 2 nm

A dissertation submitted in partial satisfaction of the
requirements for the degree
Doctor of Philosophy

in

Engineering Sciences (Mechanical Engineering)

by

Liane Manuela Matthes

Committee in charge:

Frank E. Talke, Chair
Thomas R. Bewley
Raymond A. de Callafon
Vitaliy Lomakin
Vlado A. Lubarda

2016

The dissertation of Liane Manuela Matthes is approved, and it is acceptable in quality and form for publication on microfilm and electronically:

_____

_____

_____

_____

_____

Chair

University of California, San Diego

2016

DEDICATION

To my family and friends.

TABLE OF CONTENTS

LIST OF ACRONYMS

ΔTDP	Change in touch-down power
AC	Alternating current
ABS	Air bearing surface
AE	Acoustic emission
AFM	Atomic force microscopy
AMR	Anisotropic magneto resistance
BAR	Bit aspect ratio
BPI	Bits per inch
BPM	Bit patterned media
BLR	Bonded lubricant ratio
CMRR	Center for Memory and Recording Research
CNF	Composite nonlinear feedback
CPU	Central processing unit
CS	Contact sensors, also called touch-down sensor (TDS)
CVD	Chemical vapor deposition
DAQ	Data acquisition system
DC	Direct current
DLC	Diamond like carbon
DRAM	Direct random-access memory
DSA	Dual-stake actuators
EFM	Electrostatic force microscopy
FCVA	Filtered cathodic vacuum arc
GB	Gigabyte, 1GB = 10^9 bytes
GHz	Gigahertz
GMR	Giant magneto resistance

GRA	Generalized realization algorithm
GW	Greenwood-Williamson (model)
HAMR	Heat-assisted magnetic recording
HD	High-definition
HDD	Hard disk drive
HDI	Head-disk interface
HGA	Head gimbal assembly
HMS	Head-medium spacing
IBM	International Business Machines Corporation
kB	Kilobyte, 1kB = 10^3 bytes
LDV	Laser Doppler vibrometer
LMR	Longitudinal magnetic recording
MAMR	Microwave assisted magnetic recording
MB	Megabyte, 1 MB = 10^6 bytes
NIST	National Institute of Standards and Technologies
NRRO	Non-repeatable run-out
PB	Petabyte, 1PB = 10^{15} bytes
PES	Position error signal
PFPE	Perfluoropolyether, lubricant type
PID	Proportional-integral-derivative (controller)
PMR	Perpendicular magnetic recording
PTOS	Proximate time-optimal servo (control)
PZT	Piezoelectric transducer
R	Read (element)
RAMAC	Random access method of accounting and control
RH	Relative humidity

rpm	Revolutions per minute
RRO	Repeatable run-out
R/W	Read/write
SSD	Solid state drive
SEM	Scanning electron microscopy
SFM	Scanning force microscopy, also called atomic force microscopy (AFM)
SMR	Shingled magnetic recording
SNR	Signal-to-noise ratio
STOS	Shaped time-optimal servo
SVD	Singular value decomposition
SVGA	Servo-variable gain amplifier
TB	Terabyte, 1TB = 10^{12} bytes
TD	Touch-down, contact between recording head and disk
TDMR	Two-dimensional magnetic recording
TDS	Touch-down sensor
TDP	Touch-down power, heater power of TFC slider at the onset of head-disk contact
TFC	Thermal flying height control
TMR	Track mis-registration
TMR	Tunnel magnetoresistance
TOF-SIMS	Time of flight secondary ion mass spectrometry
TPI	Tracks per inch
VCM	Voice coil motor
W	Write shield
w.r.t	With respect to

ZB	Zettabyte, 1 ZB = 10^{21} bytes
ZBR	Zone bit recording

LIST OF FIGURES

LIST OF TABLES

ACKNOWLEDGEMENTS

This dissertation would not have been possible without the help and support of the many teachers, collaborators, and administrators whom I have learned and benefited from over the past years.

First, I would like to express my gratitude towards my Ph.D. advisor Professor Frank E. Talke for his continuous guidance and support. Professor Talke was always available and accessible, including weekends and evenings, and spent immense time and effort providing feedback. Professor Talke's connections to industry were of great value to me, and he always went above and beyond to ensure that I received recognition for my work. I first joined Professor Talke's lab at the Center for Memory and Recording Research (CMRR) in 2010 as a visiting graduate student, and it was thanks to his encouragement that I decided to pursue my Ph.D. in 2011. At this point I must also thank Professor Bewley, Professor de Oliveira and Professor Lienig for their support getting me into the Ph.D. program at the University of California, San Diego (UCSD).

Second, I wish to acknowledge my Professor Raymond A. de Callafon for his valuable input and suggestions to my research. Professor de Callafon's advice was always spot on, and I am thankful and humbled for having had the opportunity to work with and learn from him. I am also deeply grateful for many other great and dedicated Professors at UCSD who have taught me, and especially the ones who served as members on my Ph.D. committee: Professor Thomas R. Bewley, Professor Vitaly Lomakin and Professor Vlado A. Lubarda. Your advice, time, and encouragement have been very much appreciated.

Also of tremendous help was Dr. Frederick E. Spada: I learned a lot from him about pretty much everything. His dedication, exactness, acute level of detail, and his approach to experimental research are truly inspiring - I feel fortunate to have had him as one of my collaborators. Our CMRR technician Ray Descoteaux has also been of

great help with his extensive electronics knowledge and bountiful, endless-seeming lab supplies. I also want to thank Christopher A. Lacey for his generous help with our spin-stand tester.

Western Digital was also of immense value for my Ph.D studies, and I am grateful for collaboration, help and support during our industry projects and my two internships. I would like to acknowledge Dr. Bernhard Knigge, Dr. Andrey Ovcharenko, Dr. Ralf Brunner, Dr. J.P. Peng, Daniel K. Bilich and Susan Lee. Susan shared all her tribology testing secrets with me which proved to be extremely valuable for the remainder of my Ph.D studies. Dr. Bernhard Knigge deserves recognition as my manager during my two internships, and the main contact during our collaborative industry projects. He provided me with great input and suggestions, valuable discussions and tremendously contributed to new research ideas (for which, of course, he already had patents). Special thanks also to Andrey Ovcharenko for his interest in our work, prompt replies and always providing us with samples.

I wish to acknowledge the generous financial support for six months of my Ph.D. studies from Cymer for which I must thank Dr. Wayne Dunstan, Michelle Vavra, Professor Miroslav Krstic, and Professor Talke who played a critical role in making this happen. It all started at the UC San Diego research expo in 2014, when Dr. Daniel Riggs and Dr. Wayne Dunstan spotted my poster - thank you very much! I am truly grateful that UCSD provides such excellent networking opportunities. Cymer also became my employer as of October 2015, and I feel fortunate to work with such smart and dedicated people who truly understand how to balance work with an excellent sense of humor. I am also thankful for emotional support from my co-workers during the last stages of my Ph.D.

The MAE women's group, which was founded by Professor Allison Marsden was a place for motivating discussions. Similarly, the Gordon scholar program run by

Dr. Ebonee Williams provided a stimulating environment outside of the technical Ph.D. work, for which I am grateful for.

Many thanks also to the staff at CMRR for help with administrative matters and beyond, and for reminding us of upcoming holidays: Betty Manoulian, Kevin Wong, Lauren Coleman, Julie Matsuda, Kelly Huang, Agapi 'Gabby' Tshamjyan, Jonathan Chae, and especially Iris Villanueva. Similarly, I would like to thank the administrators at the International Center, Graduate Division and the Mechanical and Aerospace Engineering (MAE) department: Lydia Ramirez, Patrick Mallon, Charlotte Lauve, Linda McKamey, Sandra de Souza, and Brandy Carrasco. Also many thanks to the former and current CMRR directors Professor Paul Siegel and Professor Eric Fullerton, respectively, for always having an open door and fostering a positive environment for the students at CMRR.

I wish to express my gratitude to former Talke lab member Dr. Uwe Boettcher, who taught me a lot about the lab during my visiting year and introduced me to the topic of hard disk drives, giving me a head start for my Ph.D. studies. Many thanks also to former and current Talke lab students, post-docs, classmates and fellow students for many great conversations and discussions inside and outside the lab, including but not limited to: Dr. Pablo Salas, Dr. Hao Zheng, Youyi Fu, Karcher Morris, Young Woo Seo, Tan Trinh, Andreas Hegetschweiler, Joerg Schroeter, Ben Suen, Alex Phan, Dr. Phi Nguyen, Dr. Nasim Eibagi, Sohini Manna, and Dr. Mark Hoefer. It was a pleasure being around all of you!

Special mention shall be given to my dissertation proof-reading heroes Jane Howell and Karcher Morris, thank you very much.

From the bottom of my heart, I thank my family, extended family and friends for their love and emotional support during my Ph.D., and for always being there for me, even if far away. Mein besonderer Dank gilt hierbei meinen Eltern, Manuela und Frank†

Matthes, und meinen Großeltern mütterlicherseits, Gisela und Karl-Heinz Güntner: Ihr habt uns zu neugierigen, selbstständigen und kritischen Denkern erzogen, und mich frei entfalten lassen. Ebenso habe ich enorm von meinem älteren Bruder profitiert: Kristian, du hast mich definitiv abgehärtet, aber ich habe auch viel von dir gelernt. Sarah, Duc Anh, und Thomas – ihr seid unbezahlbar; ich schätze mich glücklich, euch in meinem Leben zu haben. Lastly, I want to thank Zachary Gemmell for his love, support, graphical inspirations and patience with me during the final stages of my Ph.D.

Section 2.3.2 in chapter 2, in part, is a reprint of "Head wear of thermal flying height control sliders as a function of bonded-lubricant ratio, temperature and relative humidity", Liane M. Matthes, Ralf Brunner, Bernhard E. Knigge, and Frank E. Talke, *Tribology Letters*, vol. 60, no. 3, p. 39 (2015). The dissertation author was the primary investigator and author of this paper.

Chapter 4, in part, is a reprint of "Contact and temperature rise of thermal flying height control sliders in hard disk drives", Liane M. Matthes, Uwe Boettcher, Bernhard E. Knigge, Raymond A. de Callafon, Frank E. Talke, *Microsystem Technologies*, vol. 18, no. 9-10, pp. 1693-1701 (2012). The dissertation author was the primary investigator and author of this paper.

Chapter 5, in part, is a reprint of "Head wear of thermal flying height control sliders as a function of bonded-lubricant ratio, temperature and relative humidity", Liane M. Matthes, Ralf Brunner, Bernhard E. Knigge, and Frank E. Talke, *Tribology Letters*, vol. 60, no. 3, p. 39 (2015). The dissertation author was the primary investigator and author of this paper.

Chapter 6, in part, is a reprint of "Effect of head-disk interface biasing and relative humidity on wear of thermal flying height control sliders", Liane M. Matthes, Frederick E. Spada, Andrey Ovcharenko, Bernhard E. Knigge, and Frank E. Talke (currently being prepared for submission for publication). The dissertation author was the

primary investigator and author of this paper.

Chapter 7, in part, is a reprint of "Head-disk proximity sensing using contact sensors in hard disk drives", Liane M. Matthes, Bernhard E. Knigge, and Frank E. Talke, *IEEE Transactions on Magnetics*, vol. 50, no. 11 (2014). The dissertation author was the primary investigator and author of this paper.

Chapter 8, in part, is a reprint of "Near contact thermal flying height control in hard disk drives", Liane M. Matthes, Raymond A. de Callafon, Bernhard E. Knigge, and Frank E. Talke, *IEEE Transactions on Control Systems Technology*, vol. PP, no. 99, pp. 1-8 (2016). The dissertation author was the primary investigator and author of this paper.

VITA

08/2010	Bachelor of Science in Industrial Engineering and Management, Technical University of Dresden, Germany.
09/2010 - 09/2011	Visiting scholar at the Center for Memory and Recording Research (CMRR), University of California, San Diego, CA, USA.
09/2011 - 07/2015	Graduate Research Assistant and Teaching Assistant at the Center for Memory and Recording Research (CMRR) and the Department for Mechanical and Aerospace Engineering (MAE), University of California, San Diego, CA, USA.
06/2012 - 09/2012	Summer intern at Western Digital, San Jose, CA, USA.
05/2013	Master of Science in Engineering Sciences (Mechanical Engineering), University of California, San Diego, USA.
06/2013 - 09/2013	Full-time summer intern at Western Digital, San Jose, CA, USA.
10/2015-present	Sr. Systems Performance Engineer at Cymer, an ASML company, San Diego, CA, USA.
2016	Doctor of Philosophy in Engineering Sciences (Mechanical Engineering), University of California, San Diego, CA, USA.

PUBLICATIONS

Journal Papers

Liane M. Matthes, Uwe Boettcher, Bernhard E. Knigge, Raymond A. de Callafon, Frank E. Talke, "Contact and temperature rise of thermal flying height control sliders in hard disk drives", *Microsystem Technologies*, vol. 18, no. 9-10, pp. 1693-1701, 2012.

Uwe Boettcher, Liane M. Matthes, Bernhard E. Knigge, Raymond A. de Callafon, and Frank E. Talke, "Suppression of slider off-track vibrations using a Self-sensing Microactuator in Hard Disk Drives", *Microsystem Technologies*, vol. 18, no. 9-10, pp. 1309-1317, June, 2012.

Wenping Song, Liane M. Matthes, Andrey Ovcharenko, Bernhard E. Knigge, Frank E. Talke, "Experimental Study of Slider Dynamics Induced by Contacts with Disk Asperities", *Microsystem Technologies*, vol. 19, no. 9-10, pp. 1369-1375, June, 2013.

Liane M. Matthes, Bernhard E. Knigge, and Frank E. Talke, "Head-disk proximity sensing using contact sensors in hard disk drives", *IEEE Transactions on Magnetics*, vol. 50, no. 11, 2014.

Liane M. Matthes, Ralf Brunner, Bernhard E. Knigge, and Frank E. Talke, "Head wear of thermal flying height control sliders as a function of bonded-lubricant ratio, temperature and relative humidity", *Tribology Letters*, vol. 60, no. 3, p. 39, 2015.

Liane M. Matthes, Raymond A. de Callafon, Bernhard E. Knigge, and Frank E. Talke, "Near contact thermal flying height control in hard disk drives", *IEEE Transactions on Control Systems Technology*, vol. PP, no. 99, pp. 1-8 (2016).

Liane M. Matthes, Frederick E. Spada, Andrey Ovcharenko, Bernhard E. Knigge, and Frank E. Talke, "Effect of head-disk interface biasing and relative humidity on wear of thermal flying height control sliders", (currently being prepared for submission for publication)

Conference papers

Liane M. Matthes, Ralf Brunner, Bernhard E. Knigge, and Frank E. Talke, "Investigation of Head Burnishing of Thermal Flying Height Control Sliders", ASME 2013 Conference on Information Storage and Processing Systems, Santa Clara, USA, June 24-25, 2013.

Andreas Hegetschweiler, Liane M. Matthes, and Frank E. Talke, "Nano Wear of Thermal Flying Height Control Sliders", ASME 2014 Conference on Information Storage and Processing Systems, Santa Clara, USA, June 23-24, 2014.

ABSTRACT OF THE DISSERTATION

Experimental studies of the head-disk interface from a tribological and controls point of view for flying heights below 2 nm

by

Liane Manuela Matthes

Doctor of Philosophy in Engineering Sciences (Mechanical Engineering)

University of California, San Diego, 2016

Frank E. Talke, Chair

Since the introduction of the IBM 305 RAMAC system in 1956, performance and storage capacities of hard disk drives have improved tremendously. To reliably read and write data, the slider must follow the data stored on the magnetic disk closely enough while maintaining a near constant spacing. Currently, the spacing between the recording and the magnetic disk – the flying height – is on the order of 1-2 nm during reading and writing. At such low spacings, intermittent contacts are inevitable, giving rise to wear and degradation of the head-disk interface. Flying heights of 1-2 nm are achieved using thermal flying height control (TFC) technology. TFC recording heads,

or TFC sliders (the terms (recording) head and slider are used interchangeably in this dissertation), feature thin-film resistive heater elements near the read and write elemesnt. Actuating the heater element heats up the nearby material. The material expands due to the heat which causes the slider to (thermally) protrude towards the disk at the location of the read and write element. An increase in heater power increases this protrusion, thus locally reducing the slider flying height. In this dissertation, we focus on experimental investigations of the interface between a TFC slider and a magnetic disk from both a tribological and controls point of view.

First, contact and temperature rise between thermal flying height control (TFC) sliders and magnetic disks were studied. Head-disk contact was established by gradually increasing the power input to the resistive heater element of a TFC slider. Laser Doppler vibrometry was employed for studying the dynamics of the vertical gimbal velocity. The gimbal is part of the suspension which the slider is attached to. The temperature rise upon head-disk contact was estimated from the resistance change at the read element via auxiliary calibration measurements.

Next, wear of TFC sliders was studied. Head wear was determined by measuring the change in the heater touch-down power before and after wear testing. The touch-down power denotes the power input to the heater of a TFC slider at which the onset of slider-disk contact occurs. After wear testing, selected heads were examined using scanning electron microscopy to identify regions of wear on the write shields. Furthermore, atomic force microscopy images of worn and unworn recording heads were acquired to determine changes in surface roughness. The effect of bonded fraction of the lubricant, relative humidity, and temperature on head wear was investigated.

In addition, we studied head wear as a function of relative humidity and DC bias voltage applied across the head-disk interface. Wear tests were performed at < 8 %, 30 %, and 52 % relative humidity. Similarly, head wear was determined by measuring

the change in the heater touch-down power before and after 10 minute wear tests. After wear testing, selected recording heads were examined using atomic force microscopy to identify regions of wear or deposit formation on the slider surface, and the deposits were analyzed using time of flight secondary ion mass spectrometry (TOF-SIMS).

A new approach for predicting the touch-down power of a TFC slider is presented. The method utilizes the thermal contact sensor to sense head-disk proximity prior to actual head-disk contact. Impeding contact was predicted based on a change in dynamics from heater input to sensor output with decreasing flying height. The dynamics between the heater and the contact sensor were identified from experimental step response measurements using the step-based realization algorithm. The effect of step height was investigated and it is shown that the coefficients of the transfer function can be used to predict the onset of head-disk contact without having to perform a complete touch-down measurement.

Finally, an algorithm is proposed for minimizing low-frequency variations in flying height of thermal flying height control (TFC) sliders. The method utilizes the resistive heater element of a TFC sliders for spacing adjustment and the embedded thermal contact sensor for estimating changes in flying height. Data based modeling was carried out to identify the dynamics of the thermal actuator. The optimal feedforward heater input profile was calculate via convex optimization techniques. The feedforward approach was verified experimentally on a spin-stand tester.

Chapter 1

Introduction to digital data storage

1.1 Trends in the market of data storage

The ability to store, retrieve and distribute information has contributed majorly to the development of modern knowledge-based societies. Knowledge – the driver of technological and societal progress – could not have been developed to such an extent if there were no means for storing data. Up until the middle ages, the majority of the population in Europe was illiterate and knowledge was controlled by religious powers [3,4]. It was not until the invention of the printing press in 1439 by Johannes Gutenberg that mass production of printed book was possible [4, 5]. Gutenberg's invention introduced an era of *mass communication*, a sharp increase in literacy, and allowed the nearly unrestricted circulation of data – including revolutionary ideas – threatening the power of religious and political institutions [6]. The following centuries were marked by numerous scientific discoveries and inventions, known as the *scientific revolution*. Important achievements took place in astronomy, biology, mathematics and physics, for example, Copernicus' formulation of the universe and Sir Isaac Newton's publication *Principia* on the three laws of motion and the law of universal gravity [6].

The 20th century marks the start date of a new kind of era: The era of *digital mass communication*. Digital mass communication followed the invention of computers, the internet, and digital data storage (e.g., tape drives, hard disk drives, solid state drives). Fast-forward to the year 2013, humankind generated an astonishing amount of 4.4 Zettabyte (ZB)[1,2] of digital data within one calendar year alone [8]. From 2013 to 2020, this amount is predicted to increase tenfold to 44 ZB.

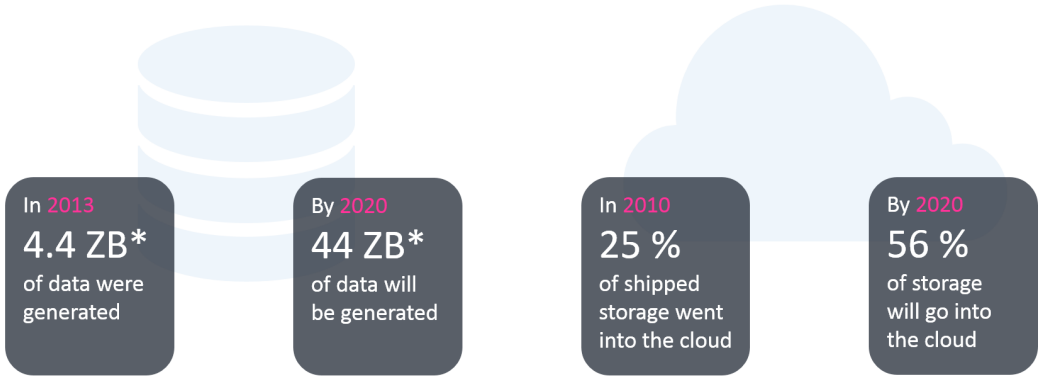

Figure 1.1: Future trends in the data storage market. Data from [8, 9].

Trends leading to such an enormous growth in data generation are related to digital entertainment (e.g., movies and TV), social media, scientific investigations (e.g., the Human Genome Project), and big data [10]. In recent years, there has also been a trend away from local data storage solutions to a more centralized approach: Cloud computing. Cloud computing is defined by the National Institute of Standards and Technologies (NIST) as a

"model for enabling ubiquitous, convenient, on-demand network access to a shared

[1] 1 ZB = 10^{21} bytes = 1 billion 1 TB hard disk drives = 100 billion high-definition (HD) movies at 1080 p resolution

[2] For comparison, a 500 page book in plain text format requires approximately 625 kbyte (kB) of digital storage. The library of congress has collected about 525 Terabyte (TB) of web archive data as of March 2014 [7], corresponding to 840 million books or 0.0000001 % of all data generated in 2013, respectively.

pool of configurable computing resources (e.g., networks, servers, storage, applications, and services) that can be rapidly provisioned and released with minimal management effort or service provider interaction" [11].

In 2013, about 25 % of storage devices shipped went into the cloud, which is expected to increase to 56 % by 2020 [9]. This tremendous growth in data generation calls for cheap, fast and reliable storage solutions.

Trends in data storage are summarized in Fig. 1.1 and an overview of current storage technology will be provided in the upcoming section.

1.2 Comparison of storage technologies

Data generation will continue to grow tremendously and a large portion of this data is expected to be stored in the cloud. In cloud computing, data is stored in data centers which handle both 'hot' and 'cold' data [10]. 'Hot' data refers to especially valuable information for which fast and reliable handling is needed. 'Cold' data on the other hand refers to less time critical data for which cost-effectiveness is a priority. In other words, the kind of data handled by the data center dictates the requirements on the storage devices being used. Desirable characteristics of digital storage devices are:

- High Performance: Fast writing and reading of data.
- Low cost: Low acquisition and operating cost (e.g., power consumption).
- Others: High storage capacity, secure data storage, and reliability.

In reality, there exists a trade-off between the above mentioned criteria, especially in terms of cost, storage capacity and performance [10]. Fig 1.2 compares the most commonly used storage devices in terms of their cost per Gigabyte (GB) and their relative performance.

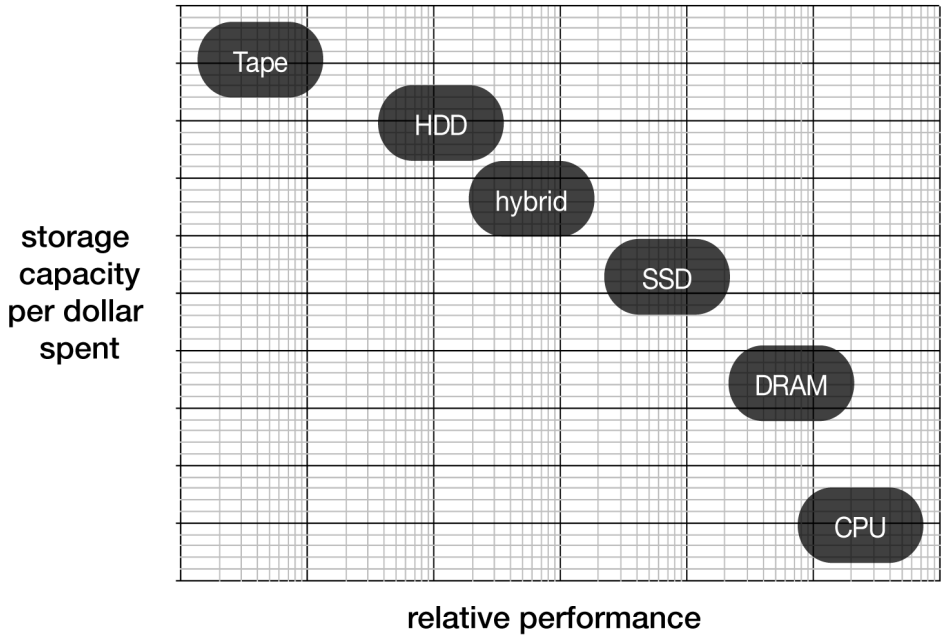

Figure 1.2: Comparison of relative cost and relative performance between tape drives, hard disk drives (HDDs), hybrid drives, solid-state drives (SSDs), dynamic random access memory (DRAM) and central processing unit (CPU).

It can be seen Fig 1.2 that *central processing units* (CPUs) are among the fastest but also the most expensive 'storage' devices. CPUs are electronic circuits carrying out the instructions of computer programs by performing basic operations. CPUs operate at speeds in the Gigahertz (GHz) range and only a few bytes are processed and stored at a time. *Dynamic random-access memory* (DRAM) provide fairly large memory blocks at much lower cost compared to CPUs. Both CPUs and DRAM are volatile, meaning that the data is lost after electrical power is withdrawn. *Tape drives* on the other hand provide extremely large capacities[3] at low cost. As tape drives are relatively slow, they are mainly used for backing up data. As of today, *hard disk drives* (HDDs) and *solid state drives* (SSDs) best bridge the gap in terms of cost and performance. HDDs are lower in cost and provide larger storage capacities compared to SSDs, which perform

[3] In 2014, Sony developed a tape drive with a storage capacity of 185 Terabyte (TB) provided by a single cartridge.

faster and are more reliable. To combine the advantages of HDDs and SSDs, *hybrid drives* were introduced. Hybrid drives are hard disk drives with an added on solid state portion. The SSD portion acts as a cache and keeps copies of the most frequently used data which significantly improves the overall performance.

1.3 Hard disk drives vs. solid state drives

There has been the perception that hard disk drives (HDDs) will eventually be replaced by the much faster and more reliable solid state drives (SSDs). However, the cost per bit of HDDs is significantly lower compared to that of SSDs. As of April 2015, 1 Terabyte (TB) of storage can be purchased for $40 in form of a HDD or for $230 in form of a SSD. This makes HDDs cheaper by a factor of 5.75 compared to SSDs. This comparison also highlights that SSDs have become inexpensive enough to replace HDDs in the mobile device market (e.g., laptops). The share of the mobile device market, however, constitutes less than 10 % of the revenue of the total storage market [9]. In recent years, the cost per GB has been falling steadily at a similar rate for both HDDs and SDDs. This trend is expected to continue [12], indicating that HDDs are not going to disappear from the market in the near future.

Historically, the number of HDDs shipped has been growing steadily starting from 1975 [13]. This trend started to reverse in recent years as SSDs are becoming more popular due to decreasing prices: HDD sales fell from 794 million units in 2012 to 755 million units in 2013 while the shipment of SSD grew by 82 % to 57 million units [14]. Still, SSDs only make up a small portion of the total number of units sold. This comparison becomes even more drastic when comparing the total capacity shipped rather than the number of units sold as HDDs provide significantly larger capacities compared to SSDs.

1.4 Conclusion

SSDs are clearly advantageous compared to HDDs in terms of performance but lack in providing large capacities at low cost. As of now and in the near future, it is less of a question of 'Who will win?' than a realization that both SSDs and HDDs have their own unique applications and can coexist. The choice between SSDs and HDDs depends on the type of data to be stored, the requirements by the end user, and the cost. It is already common praxis that data centers organize data into tiers. Top tear data is typically stored on DRAM or SSD whereas lower tier applications run on slow, typically 5400 revolutions per minute hard disk drives [10]. There are, however, companies which exclusively use SSD for their data storage solutions.

Overall, it is important that HDDs maintain their relative cost advantage compared to SSDs in order to stay relevant in the storage market. In order to do so, larger capacities need to be provided at lower cost while ensuring reliability.

Chapter 2

Introduction to hard disk drives

2.1 History of hard disk drives

On May 6th, 1955, IBM announced that a small team of engineers at their San Jose site had developed a new magnetic disk storage technology [15]. Sixteen months later, the first IBM 350 RAMAC disk file became commercially available. The disk file was part of the IBM 305 RAMAC system which also included a card reader, central processor and printer. RAMAC stands for *random access method of accounting and control* and its introduction to the market started a new era of interactive computer applications such as airline reservation systems, automated banking and personal computing [16]. To highlight the significance of this invention it shall be noted that prior to 1952, only punch cards, magnetic tapes and magnetic drums were available for storing information [15]. A photograph of the IBM 350 is shown in Fig. 2.1. The IBM 350 disk file consisted of fifty disks that were 24 inches in diameter, providing a total capacity of 5 million seven bit characters [15]. Mounted on a rotating shaft, the disks spun at 1,200 revolutions per minute (rpm). A single head assembly with two heads was used for accessing all 50 platters at an average head to media spacing of 20 micrometer

(µm) [15, 17]. The IBM 350 provided a data rate of 8800 bytes per second (bytes/s) and an access time of 600 milliseconds (ms) [18]. The RAMAC 350 file system was not for sale; one megabyte of storage could be rented for $130 a month which corresponds to $1,122 in 2015[1] [15].

Figure 2.1: 305 RAMAC system with 350 disk file, central processor, card reader and printer [15].

In June 1961, the IBM 1301 Disk Storage Unit was announced as the next generation disk storage technology. The IBM 1301 introduced the usage of self-flying sliders which 'fly' over the disk supported by an air bearing – a technology which is still used in today's hard disk drives. Furthermore, separate read/write heads for each disk surface were used for the first time. Each IBM 1301 module was comprised of 25 disks that provide a total storage capacity of 25-28 million characters [18, 19]. The disk stack spun at 1800 rpm and the head to media spacing was 6 µm.

With each following generation, hard drives became smaller, faster and had larger areal densities[2]. The most common form factors of modern hard drives are

[1] Accounted for inflation according to the Bureau of Labor Statistics, available at http://www.bls.gov/data/inflation_calculator.htm

[2] Areal density refers to the number of bits stored per unit area and is typically measured in bits per inch squared (Bit/in^2)

3.5 inch drives for desktop computers and 2.5 inch drives for laptop computers. In early 2007, the first 1 Terabyte (TB) hard drive was introduced by Hitachi GST [20] and in 2014, Western Digital Corporation announced a 10 TB helium filled hard drive [21].

2.2 The principle of magnetic recording

In hard disk drives, data is stored in the form of bits in the recording layer of a hard disk. The magnetic recording layer consists of very fine grains and several grains form one bit. The bits have either positive or negative magnetization and are written in circular data tracks on a rotating disk. Data is written onto the disk using a magnetic coil and read using a resistive element. This section discusses magnetic materials and the write and read process.

2.2.1 Magnetic materials

Since electrons carry a negative charge, they produce a magnetic field as they circle around the atom's nucleus. If a material is exposed to an external magnetic field, the magnetic field of the material's electrons will be affected. However, most atoms have electrons that occur in pairs. Paired electrons spin in opposite directions which causes their magnetic fields to cancel each other. Contrary, materials with unpaired electrons have a net magnetic field. Thus, external magnetic fields can have quite different effects on a material depending on whether or not the material's electrons occur in pairs. Depending on the induced magnetic field, materials can be categorized into diamagnetic, paramagnetic and ferromagnetic. *Diamagnetic materials* are slightly repelled by an external magnetic field and no changes in magnetic properties are retained after the external magnetic field is removed. The majority of elements in the periodic table such as copper, gold and silver are diamagnetic. *Paramagnetic materials* on the other

hand are slightly attracted by an external magnetic field. Similar to diamagnetic materials, no changes in magnetic properties are retained after the external magnetic field is removed. Examples for paramagnetic materials are magnesium, lithium and tantalum. *Ferromagnetic materials* exhibit a strong attraction to external magnetic fields and are able to retain their induced magnetic changes after the external field is removed. This is because ferromagnetic materials have unpaired electrons which allow the atoms to gain a net magnetic moment and also because ferromagnetic materials are organized in magnetic domains. When unmagnetized, the domains are organized randomly, resulting in a zero net magnetic field for the material as a whole. As ferromagnetic materials are exposed to an external magnetic field, the domains become aligned and produce a magnetic field within the material. The internal magnetic field becomes stronger, the more magnetic domains are aligned. Once all magnetic domains are aligned, the material is saturated and no additional amount of external magnetic field can increase the level of internal magnetization. Examples of ferromagnetic materials are iron, nickel and cobalt.

In hard disk drives, a single bit consists of several magnetic domains or grains and each bit has two stable states. The orientation of magnetization of the magnetic domains can be flipped by applying a proper external magnetic field. The process of demagnetization of ferromagnetic materials is not the inverse of the magnetization process, which is known as *hysteresis*. The hysteresis curve of ferromagnetic materials is shown in Fig. 2.2.

The magnetization M of a ferromagnetic material is zero before any external magnetic field H is applied. This state corresponds to point 0 in Fig. 2.2. Increasing the external magnetic field H increases the magnetization of the material until saturation level $+M_S$ is reached (point 1). Subsequent removal of the external magnetic field reduces the internal magnetization of the material to M_r (point 2), known as remanent magnetization. By reversing the magnetic field and slowly increasing its magnitude,

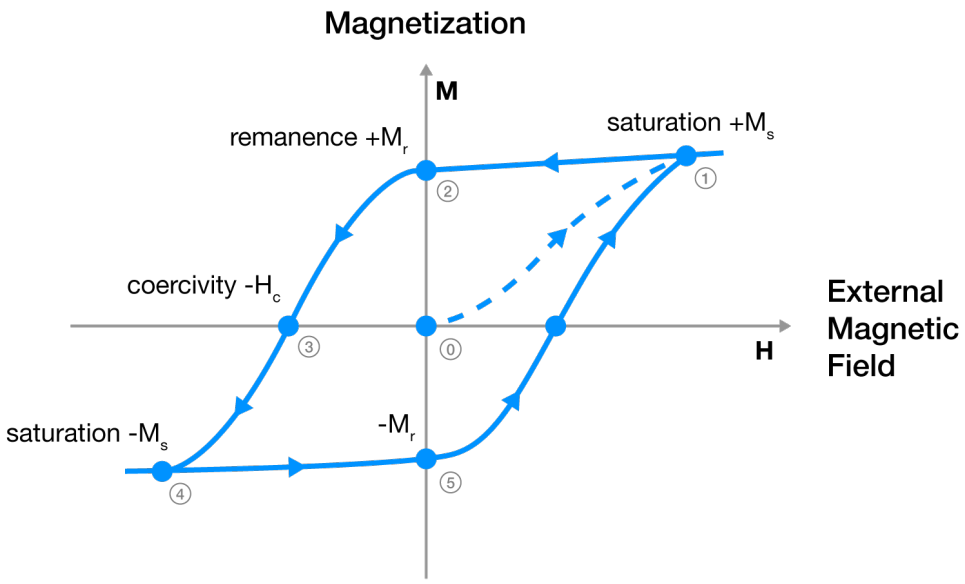

Figure 2.2: Hysteresis loop of magnetic materials. Binary recording as it is used in hard disk drives requires two stable states of magnetization which correspond to the two points of remanence $+M_R$ and $-M_R$.

zero magnetization is reached which corresponds to point 3 in Fig. 2.2. The external field needed for achieving zero magnetization is called the coercivity H_c of the material. If the reversed external field is further increased in magnitude, a negative state of saturation $-M_S$ is reached (point 4). Subsequent removal of the magnetic field increases the internal magnetization to $-M_R$ (point 5). The two points of remanent magnetization $+M_R$ and $-M_R$ represent the two stable states needed for binary recording.

For hard disk drives, it is important to choose materials with large enough coercivity H_C to ensure thermal stability. Thermal stability is needed for preventing spontaneous demagnetization and subsequent data loss. A detailed discussion on thermal stability of the magnetic grains is given in 2.6.1.

2.2.2 The write process

The magnetic orientation of a single bit can be either parallel or perpendicular to the disk surface; this is referred to as longitudinal or perpendicular magnetic recording,

respectively. Until 2005, the majority of hard disk drives used longitudinal magnetic recording (LMR) technology to store information [22–24]. However, soon the super paramagnetic limit in longitudinal magnetic recording was reached: If the grains in the recording layer become so small that they interfere with neighboring grains, they lose the ability to retain their magnetic orientation which results in data loss [25,26]. To overcome the super paramagnetic limit of longitudinal magnetic recording, the hard drive industry transitioned from longitudinal to perpendicular magnetic recording (PMR) technology starting in 2004 [23, 27]. Other advantages of perpendicular magnetic recording include a better signal to noise (SNR) ratio and a higher saturation magnetization which allows for thinner recording layers [23].

The fundamental differences between longitudinal magnetic recording and perpendicular magnetic recording are illustrated in Fig. 2.3 a) and b), respectively. A unique feature of perpendicular magnetic recording is the existence of a softmagnetic underlayer below the recording layer.

When writing data, the information to be recorded is received by the write channel in the form of '1's and '0's. This information is converted into an alternating current which is passed on to the write element. The write element consists of an inductive coil wrapped around a ferromagnetic yoke. Applying a current to the write coil produces a magnetic stray or fringe field in the gap of the yoke which is used to change the magnetic orientation of the bits in the recording layer. In longitudinal magnetic recording, the stray field passes through the magnetic medium below the gap of the magnetic core and magnetizes the bits parallel to the disk surface (see Fig. 2.3 a)). For perpendicular magnetic recording, a slightly different write head geometry is used which is similar to that of a horseshoe with one small and one large end (see Fig. 2.3 b)). When writing data, the magnetic flux passes through the small end, called the monopole, through the recording layer to magnetize bits perpendicular to the disk surface. The magnetic flux

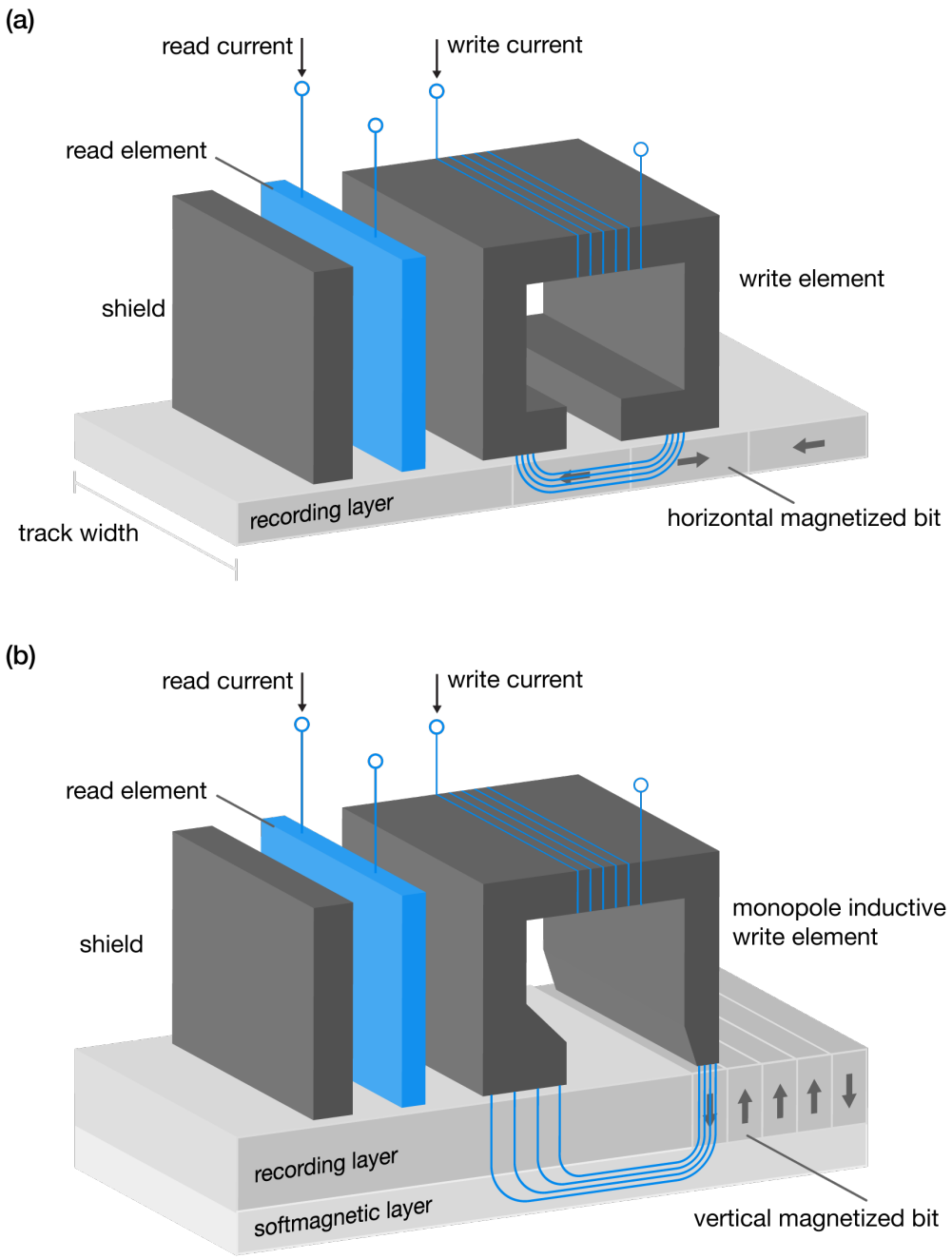

Figure 2.3: The principle of a) longitudinal magnetic recording (LMR), and b) perpendicular magnetic recording (PMR). In LMR, the orientation of the bits is parallel to the disk surface whereas the bit orientation in PMR is perpendicular to the disk surface. PMR allows for higher areal densities.

continues on through the softmagnetic underlayer back to the larger end of the horseshoe, the return pole. Because of the much larger return pole, the density of the magnetic flux returning to the magnetic coil is reduced so that no bit is re-magnetized.

Over the years, the technology of the write head has not changed fundamentally except for a significant reduction in size and the transition from longitudinal to perpendicular magnetic recording as described above.

2.2.3 The read process

In the early years of hard disk drive technology, the read and write elements were combined into a single ferrite inductive read/write head. When reading data, a change in magnetization seen by the read/write head causes a change in magnetic flux in the ferrite core. According to Faraday's law, a change in magnetic flux Φ induces a voltage V_{ind} as follows

$$V_{ind} = -N\frac{d\Phi}{dt} \tag{2.1}$$

where N is the number of windings.

As the bit size decreased over time to achieve higher storage densities, the read-back signal amplitude of inductive heads became so small that the signal-to-noise ratio (SNR) became too low. In the 1990s, magnetoresistive (MR) heads were introduced which use a different principle for reading data. Magnetoresistive heads contain a small electrical resistor whose resistance changes in the presence of an external magnetic field. There are three types of MR heads [28]: Anisotropic magnetoresistive (AMR) heads which were first introduced in 1990, giant magnetoresistive (GMR) heads which were introduced in 1997, and tunneling magnetoresistive (TMR) heads which were introduced in 2004. *Giant magnetoresistive heads* are multi-layered structures of magnetic and non-magnetic conductive materials. When neighboring layers are magnetized in

parallel, the resistance is decreased compared to the case where layers are magnetized in opposite directions. The effect of giant magnetoresistance was discovered by Albert Fert and Peter Grunberg in 1988, and they were recognized for their discovery by the Nobel Prize in Physics in 2007. The principle of *tunneling magnetoresistive heads* is based on tunneling magnetoresistance: Electrons move through an insulating layer between the magnetic layers which results in an even larger change in electrical resistance. Tunneling magnetoresistive heads are still used in today's hard disk drives.

2.3 Inside a hard disk drive

2.3.1 Component overview

A typical hard disk drive with its top cover removed is presented in Fig. 2.4.

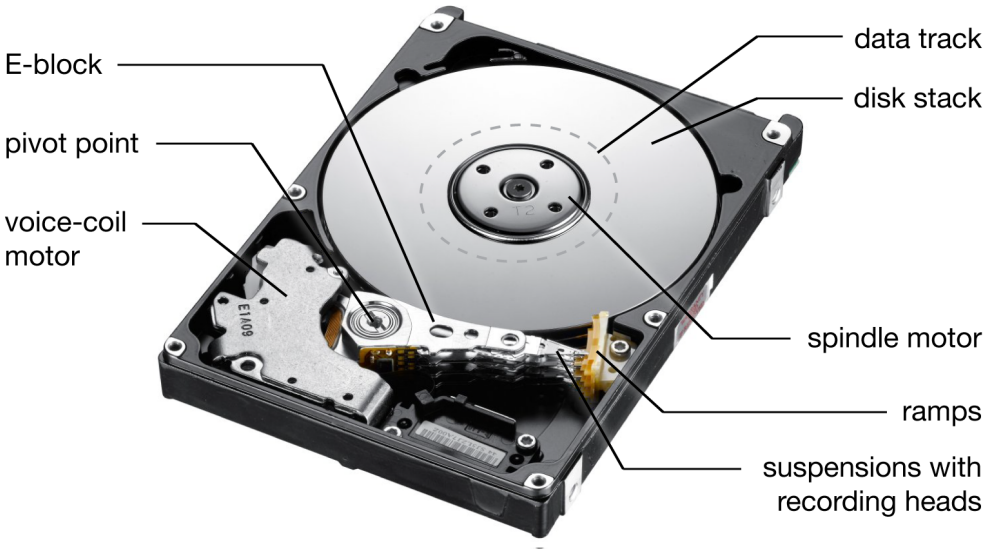

Figure 2.4: Typical commercially available hard disk drive [1] with its top cover removed. Data is stored in concentric tracks on both the top and bottom surface of the magnetic disks. Radial positioning of the recording heads is provided via a voice-coil motor. The sliders are parked on a ramp when no data is written or read to provide protection against accidental shock or vibration.

Hard disk drives usually contain a stack of disks which is spun by a spindle

motor. Data is written onto the disk in concentric tracks using a write coil and read from the disk using a read element. The write coil and read element are contained in the trailing edge of the slider which is also referred to as the slider. The slider hovers or 'flies' over the rotating disk supported by an air bearing. Since data is stored on both the top and the bottom surface of a magnetic disk, two recording heads per disk are used.

The slider is mounted to the suspension via the dimple-gimbal interface as shown in Fig. 2.5. The dimple is a spherical protrusion on the suspension that allows the slider to pitch and roll. The suspension applies a pre-load to the slider body in the vertical (z) direction that is in equilibrium with the air bearing pressure at the head-disk interface. The suspension is rigidly attached to the E-block as shown in Fig. 2.4. The E-block is moved radially across the disk using a voice-coil motor (VCM) whose position is controlled using a servo control loop.

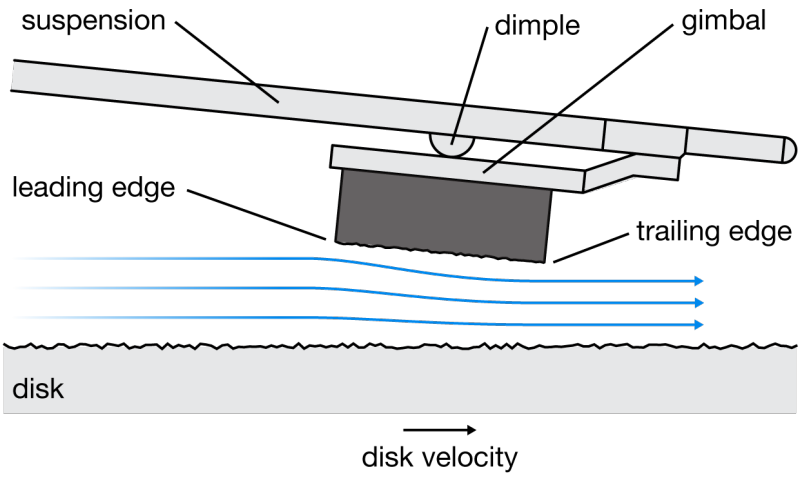

Figure 2.5: Dimpel-gimbal interface. The slider is attached to the suspension via the dimple gimbal interface. This interface allows the slider to pitch and roll independent of the suspension motion.

When a hard drive is not in operation, the sliders are 'parked' on a ramp as shown in Fig. 2.4). In earlier disk drive generations, the sliders were 'parked' at the inner diameter of the disk in the so-called landing zone [26]. The area of the landing

zone was solely reserved for parking the slider and could not be used for storing data. However, improvements in materials and manufacturing techniques lead to smoother surfaces which gave rise to larger stiction forces between the slider and the disk. Large stiction is undesirable during disk spin-up. To prevent these large stiction forces, laser textured landing zones were introduced to increase the surface roughness in the landing zone and hence decrease the real area of contact between the slider and disk when the slider was parked. It was found, however, that laser textured landing zones introduced friction induced tribo voltages during disk spin-up [29]. The presence of large voltage potential differences across the head-disk interface is undesirable because electrostatic damage of the sensitive read element may occur. For example, Wallash found that tunneling magneto resistive (TMR) read elements can be damaged at only 1 V [30]. To prevent voltage build-up during disk spin-up and maximize the disk area dedicated to disk storage, ramps were introduced.

The base cover of hard disk drives is sealed with a top cover. Small holes allow for equalization of air pressure between the inside and the outside of the hard disk drive. A filtration system prevents contaminants from entering the drive and controls moisture within the drive. In 2013, HGST introduced the first helium filled hard disk drive [31]. The advantage of helium is that its density is much less compared to that of air and that its Reynolds number is much smaller. As a consequence, spinning the disks causes less fluid friction and turbulence and hence, the drive runs cooler and less electrical power is required for spinning the disks stack. In addition, air-induced vibration of the slider and suspension are reduced which allows for higher track densities and for packing disks closer together, thus increasing the overall storage capacity of the drive. Helium-filled hard disk drives need to be sealed hermetically to prevent helium molecules from escaping the drive.

2.3.2 The head-disk interface

From a magnetic point of view, zero spacing between the read/write element and the magnetic recording layer is desired to achieve maximum strength in the read-back signal. However, from a tribological point of view, contact between the slider and the disk is undesirable as wear and degradation of the head-disk interface may occur. Hence, the question arises how low can one fly *safely* to ensure that data is read and written reliably while preventing damage to the slider and the disk.

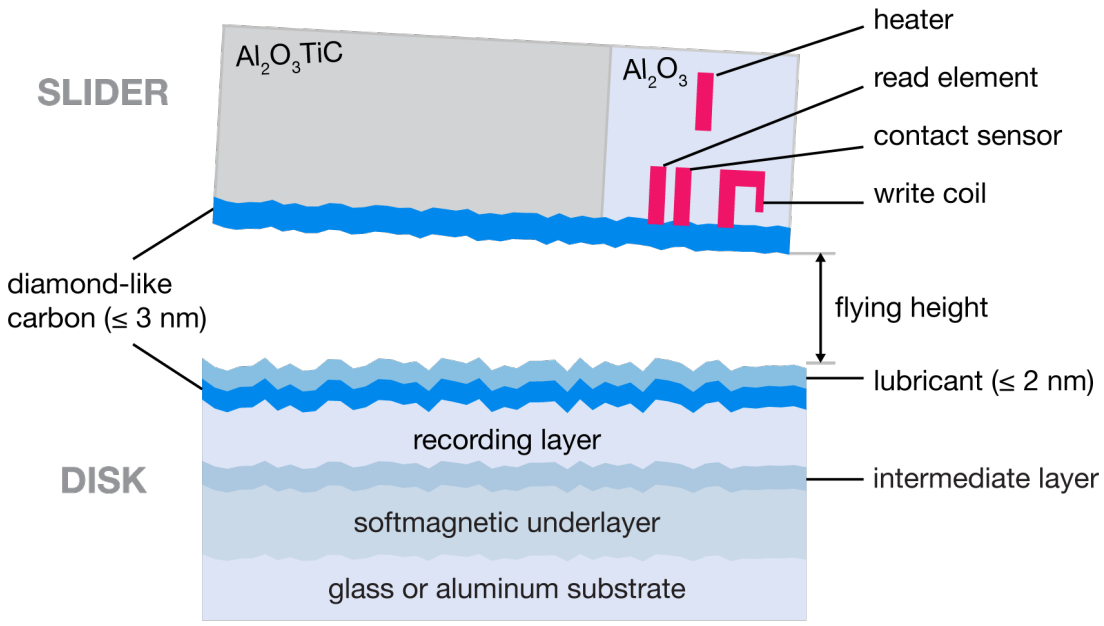

Figure 2.6: Head-disk interface (HDI). The slider flies over the disk supported by an air bearing. The nominal head-disk spacing, or flying height, is on the order of 10 nm. During reading and writing, the flying height is reduced to 1-2 nm. To minimize wear and friction during intermittent head-disk contacts, both the slider and the disk are coated with a thin layer of diamond-like carbon ($\leq$ 3 nm) and a thin lubricant layer is present on the disk ($\leq$ 2 nm).

In today's hard disk drives, the spacing between the read and write element and the magnetic disk is on the order of 1-2 nm during read and write operation. Such a low spacing is achieved using thermal flying height control (TFC) technology which will be discussed in section 2.3.3. When flying at 1–2 nm head-disk spacing, it may be

of no surprise that intermittent contacts between the recording head and the magnetic disk occur. To prevent corrosion and damage from intermittent head-disk contacts, the surface of the magnetic disk is covered with a molecularly thin layer of diamond-like carbon ($\leq$ 3 nm) and lubricant ($\leq$ 2 nm). Similarly, the bottom surface of the slider is coated with a thin film of diamond-like carbon ($\leq$ 3 nm) for wear and corrosion protection. A schematic of the recording head and the layered structure of the magnetic disk is presented in Fig. 2.6.

Diamond-like carbon coatings

In early hard disk drive generations, amorphous carbon (a-C) was sputtered onto the disk to provide protection against corrosion [32] and later, hydrogenated amorphous carbon (a-C:H) was used to also protect against mechanical wear [33]. In recent years, amorphous nitrogenated carbon (a-C:N) has been widely used since it provides high hardness, high wear resistance and low friction [34–41]. Amorphous carbon that contains nitrogen has an increased surface energy which improves bonding of the lubricant to the disk carbon [33,42]. Current diamond-like carbon (DLC) layers are less than 3 nm thick and their primary purpose is to provide a corrosion and diffusion barrier [33]. To fulfill this requirement, it is important that the deposited carbon layer is continuous. In recent years, tetrahedral amorphous DLC (ta-C) and hydrogenated tetrahedral amorphous DLC (ta-C:H) films were introduced because their deposition process allows for smoother films with higher densities [33].

He et al. [43] studied wear on the recording head resulting from a) contact with a single asperity on the disk surface and b) contact with the bulk surface of the disk. Contact with the disk asperities causes scratching on the recording head, whereas contact with the bulk surface results in smoothening or 'burnishing' of the the carbon film. It was shown that the scratched and burnished regions exhibit an increase in sp^2 bonds,

indicating that localized graphitization of the DLC film took place due to high contact stresses and frictional heating. A general introduction to DLC coatings and plastic deformation of surface coated materials is given in 2.4.7, respectively.

Disk lubricant

The disk lubricant plays a critical role in ensuring reliability and longevity of the head-disk interface. As the applied lubricant film is very thin ($\leq$ 1-2 nm), it is important to choose an adequate lubricant type and proper application method. Desired lubricant properties are [44]:

- **Good boundary lubrication** to prevent wear of the recording head and the disk.
- **Good surface affinity towards the disk** to prevent lubricant displacement via slider-disk contacts.
- **Mobility of lubricant molecules** to replenish disk areas depleted of lubricant.
- **Low volatility** to reduce lubricant evaporation.
- **Low surface tension** to reduce stiction forces in case of slider-disk contact and minimize the absorbtion of contaminants onto the lubricant.
- **Thermal and chemical stability** to prevent lubricant degradation.

Obviously, some of the criteria mentioned above are contradictory, hence, the main challenge lies in finding a lubricant that represents the best compromise for a particular head-disk combination. The most commonly used class of lubricants used for hard drive lubrication are perfluoropolyether (PFPE) type lubricants. The advantage of this type of lubricant is its high thermal stability, low viscosity and low vapor pressure [45]. Popular examples of PFPE lubricant are lubricants with Fomblin Z or Demnum

backbone [46]. The Fomblin Z backbones can be terminated with a variety of functional end groups at both ends, whereas the Demnum backbone can only be terminated with one functional end group [46]. Representatives of the Fomblin Z family are Fomblin Z-dol and Fomblin Z-tetraol which have two and four hydroxyl end groups, respectively [47]. The structure of Z-dol, Z-tetraol and Demnum is shown in Fig 2.7.

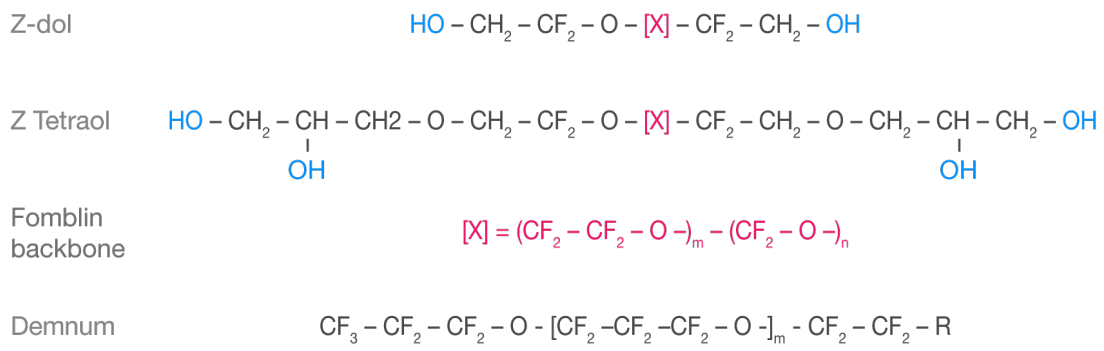

Figure 2.7: Chemical structure of Fomblin Z-dol, Fomblin Z-tetraol and Demnum. *R* denotes the (functional) end group to be added.

To simultaneously provide surface affinity and lubricant mobility, part of the lubricant is bonded onto the disk surface whereas the remaining part of the lubricant is said to be free or 'mobile'. Lubricant bonding is achieved by annealing the lubricant end-groups at elevated temperatures to the carbon overcoat on the disk. Bonding the lubricant to the disk carbon minimizes lubricant evaporation, disk spin-off and lubricant displacement during slider-disk contacts, respectively. The mobile portion of the lubricant is believed to reflow and replenish the lubricant depleted disk portions, thus 'repairing itself' [48]. The ratio between the bonded lubricant divided by the total amount of lubricant is defined as the *bonded lubricant ratio* (BLR). Typical bonding ratios are on the order of 60 % to 90 %.

It has been proposed that lubricants with a high lubricant diffusion coefficient improve the wear durability of hard drives [49]. A number of studies has been con-

ducted that investigate the effect of humidity and temperature on lubricant diffusivity and wear [48, 50–56]. For example, Min et al. [50] studied the effect of *relative humidity* on the diffusivity/spreading characteristics of thin liquid films of PFPE on silica surfaces. They found that the surface mobility of PFPE lubricants with functional hydroxyl end groups increases with increasing relative humidity. Nakazawa and Kawakubo [51] measured the decrease in head pad height using optical profilometry and found that head wear decreases with increasing relative humidity. Karis et al. [48] performed contact start/stop tests and found that the durability of disks increases with increasing relative humidity. It is known that water can be adsorbed onto the lubricant or the disk carbon, thus acting as a lubricant [52–54]. However, durability of PFPE lubricants was found to be decreased at very high levels of relative humidity (e.g., 80 %). It was suggested that water molecules might displace or permeate the lubricant film, thus resulting in a nonuniform lubricant layer [54,55]. Concerning the effect of *temperature*, Ma et al. [56] reported that temperature has little effect on the spreading characteristics of Fomblin lubricants. However, Nakazawa and Kawakubo [51] found that head wear increases with increasing temperature even though the diffusion coefficient was increased. They proposed that a change in the bonded lubricant characteristics leads to increased head wear at high temperatures.

Intermittent contact between slider and lubricant can result in lubricant rippling, lubricant pick-up and lubricant transfer from the disk to the slider and vice versa [57,58]. Lubricant can also transfer to the slider in the absence of slider-disk contacts [59, 60]. As lubricant is redistributed over the disk, the lubricant thickness becomes non-uniform [61]. It has also been found that lubricant contact excites vertical, down- and off-track vibrations of the slider with the largest displacement in the off-track direction [62–67].

It is critical that the disk remains fully lubricated at all times to reduce wear and friction. There are several mechanisms that contribute to degradation or loss of lubri-

cant. Lubricant loss or degradation may be initiated by mechanical shearing [68], high temperatures arising from mechanical friction [69] or laser heating [70, 71], catalytic reactions [68, 72], tribo-emission [73–75], and possibly electrostatic fields [76]. It has been suggested that lubricant degradation is dominated by triboelectrical reactions and mechanical scission [54, 68].

Sliders

The sliders are fabricated using a wafer process similar to that used for integrated circuits. During manufacturing, numerous layers of conductors and insulators are created to form the write coil, write shield, read element, read shield etc. The slider trailing edge consists of aluminum oxide (Al_2O_3) whereas the slider main body consists of aluminum oxide titanium carbide (Al_2O_3TiC, also called 'AlTiC') (see Fig. 2.6). Electrical access to the write coil and read element is provided via copper traces that are embedded in a laminated flexure. The flexure extends away from the trailing edge of the slider, runs along the suspension and terminates at electrical connection points at the flexure tail as shown in Fig. 2.8.

The bottom surface of the slider facing the disk is referred to as the air bearing surface (ABS). The air bearing surface in today's hard disk drives is fairly complex and consists of multiple recessed areas at various depths, generating high and low pressure regions as the slider flies over the disk. The air bearing surface of the slider is designed so that the slider flying height is independent from the radial position and the disk velocity. A typical air bearing surface is depicted in Fig. 2.9.

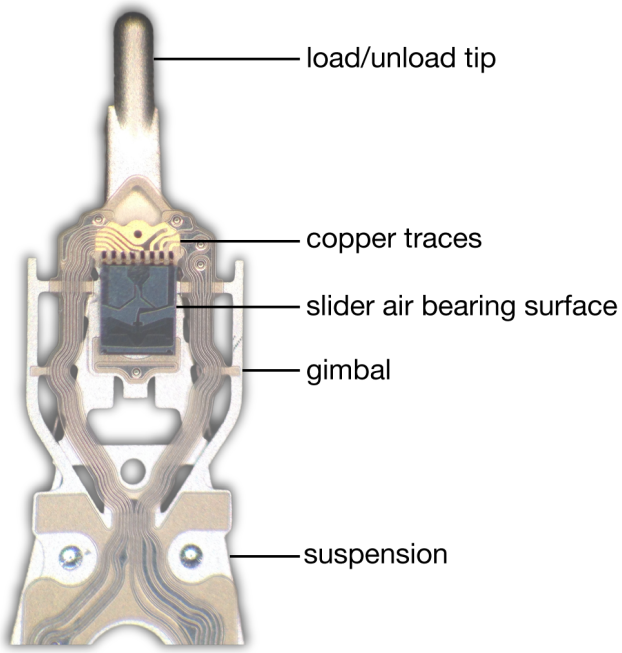

Figure 2.8: Close-up image of bottom surface of the slider, suspension, copper traces and flexure. The copper traces establish an electrical connection to the read and write element inside the slider.

2.3.3 Actuators in hard disk drives

Spindle motor for spinning the disk stack

The spindle motor spins the disk stack at disk velocities ranging from 5,400 rpm to 15,000 rpm. Hard drives spinning at 5,400 rpm are typically used in laptops, whereas 7,200 rpm hard drives are reserved for desktop applications. Higher spindle speeds allow for faster read/write access, but this advantage comes at a price: At high spindle speeds, more electrical power is required for spinning the disk stack, the drive runs louder, and out-of-plane suspension motion and slider off-track motion are increased [77].

The spindle motor plays a crucial role in the overall performance of a hard disk drive. It is important that the speed of the spindle motor is controlled precisely as variations in spindle speed affect the flying height and bit position during writing [26]. The motion of the spindle with respect to its center of rotation is defined as spindle

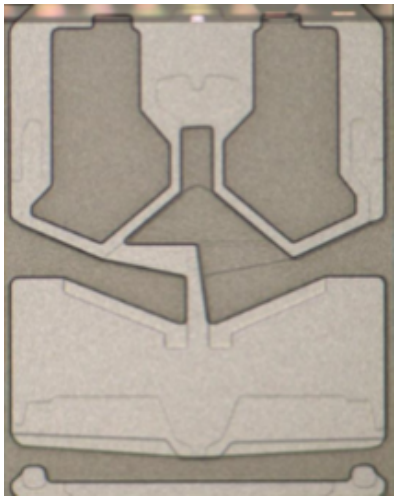

Figure 2.9: Air bearing surface of the slider showing the trailing edge at the top and the leading edge at the bottom. The air bearing surface is the bottom surface of the slider that faces the disk. The shields of the read and write element are located at the center of the trailing edge. Dark areas are recessed in height and result in sub-ambient air pressure as the slider flies over the disk compared to the elevated regions of the air bearing surface which result in above ambient air pressure.

run-out. Run-out can be repeatable (RRO) or non-repeatable (NRRO). Due to its deterministic nature, repeatable run-out can be compensated. Non-repeatable run-out on the other hand occurs randomly and can cause the recording head to go off-track, thus contributing to track mis-registration and limiting the overall achievable track density. Up until the early 2000s, ball bearing spindle motors were widely used in hard disk drives, but the need for increased spindle speeds, noise reduction and higher areal densities required a transition to fluid bearings [78–80]. A schematic of the cross-section of a ball bearing and a fluid bearing is presented in Fig. 2.10. Ball bearings produce non-repeatable run-out on the order of 2.5 nm (0.1 μ-inch) due to imperfections in the race ball interface geometry [79, 81]. By contrast, non-repeatable run-out in fluid bearings is 0.25 nm (0.01 μ-inch) due to higher viscosity of the lubricant between the stator and the sleeve [79]. Other advantages of fluid bearings are greater speed control, reduction in noise, improved shock resistance and reduced frequency resonance [78, 79].

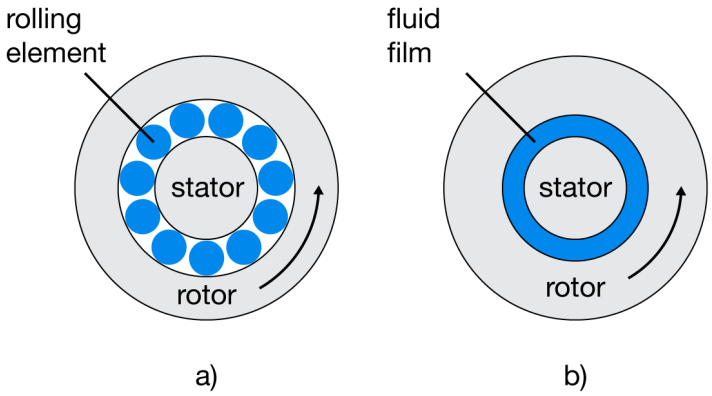

Figure 2.10: Cross-sectional view of a) ball bearing and b) fluid bearing. Compared to ball bearings, fluid bearings operate under less run-out, provide greater speed control, cause less acoustic noise and show improved shock resistance.

Voice coil motor for radial positioning of the recording head

Data tracks are accessed by radially moving the recording head over the disk surface. This is done using a rotary voice coil motor whose main functional principle is shown in Fig. 2.11. The coil of the actuator is surrounded by a magnetic field produced by a pair of permanent magnetics fixed to the casing of the hard drive. Applying a current to the coil causes the coil to move according to the Lorentz force law given by

$$\vec{F} = I \cdot (\vec{l} \times \vec{B}) \tag{2.2}$$

where $\vec{F}$ denotes the Lorentz force, I is the applied current, $\vec{l}$ refers to the vector of the coil wire exposed to the magnetic field, and $\vec{B}$ denotes the density of the magnetic flux. The direction of motion of the E-block is determined by the direction of the current I applied to the coil. Equation 2.2 shows that the generated force is proportional to the applied current.

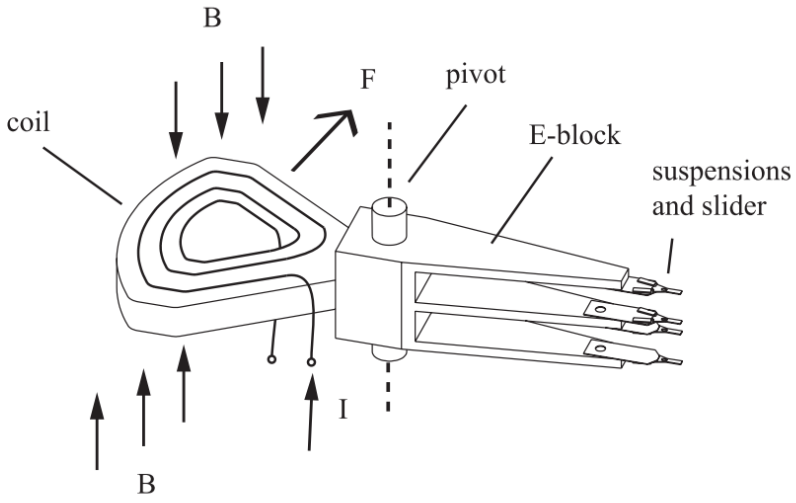

Figure 2.11: Working principle of a voice coil motor (VCM). The voice coil motor is used for radial positioning of the recording head to access different data tracks. Schematic courtesy of [82].

Thermal flying height control technology for flying height adjustment

Since the write element is comprised of a material with a higher thermal expansion coefficient, it expands and shrinks more rapidly compared to the remaining slider body as temperature changes. Thus, during writing when a high frequency current is applied to the write coil, the write element heats up and generates a protrusion towards the disk. This results in a lower head-to-media spacing during writing compared to reading. However, to ensure proper reading and writing of data, the spacing between the read element and the disk during reading needs to be the same as the spacing between the write coil and the disk during writing. Hence, a method is needed to rectify the static flying height loss due to write coil induced pole tip protrusion.

A reduction in clearance between the read or write element and disk surface can be achieved by lowering the flying height of the slider as a whole, for example by reducing the disk velocity or changing the air bearing design of the slider. It is also possible to reduce the head-to-media spacing *locally* only when needed, that is, during reading and

writing. The first proposals based on this idea were introduced in 1986 and involved the use of piezoelectric elements [83–86]. Integrated in the slider, these piezoelectric elements were used to adjust the position of the read and write element in the trailing edge of the slider (see Fig. 2.12 a)). However, sliders with integrated piezoelectric elements were difficult to fabricate at the time and therefore, their development was not pursued further.

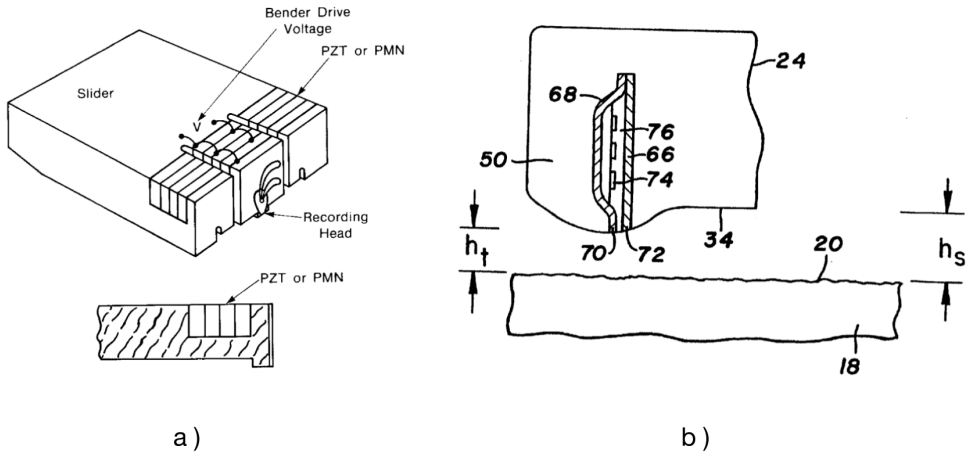

Figure 2.12: Early proposals for head-disk spacing adjustment using a) integrated piezoelectric actuators [84], and b) integrated heater element [87].

A different approach, based on an integrated resistive heater element, was first introduced by Meyer et al. [87] in 1999 (see Fig. 2.12 b)). The heater element is located in the trailing edge of the slider near the read and write element. Energizing the heater element heats up the nearby material and as a consequence, the bottom surface of the slider near the read and write element protrudes towards the disk, thus reducing the flying height locally. An increase in heater power increases this protrusion and a large enough heater power results in contact of this protrusion with the disk lubricant and/or the disk surface as illustrated in Fig. 2.13. The heater power at which contact occurs is commonly referred to as touch-down power (TDP). The nominal flying height of current slider designs without energizing the heater element is about 10-12 nm. Head-

disk spacings of 1-2 nm during reading and writing are achieved by setting the power input to the heater a few mW below the touch-down power.

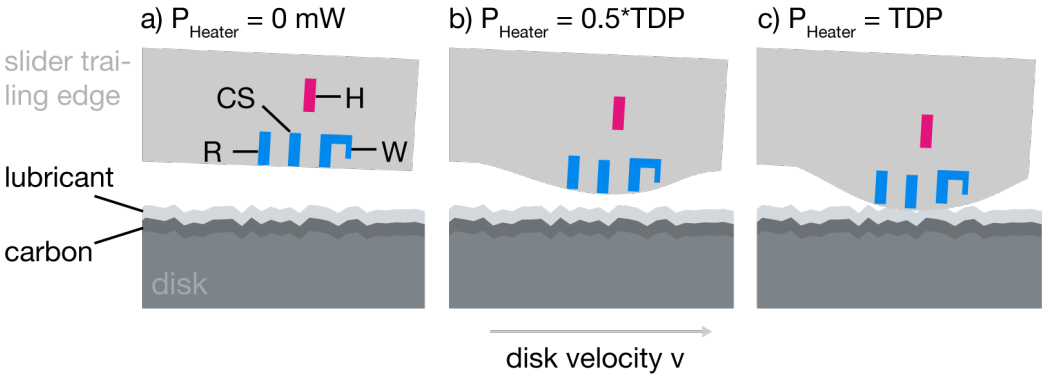

Figure 2.13: Schematic of thermal flying height control sliders for various heater powers expressed in terms of the touch-down power (TDP). An increase in heater power increases the slider protrusion. For a large enough heater power slider-disk contact occurs. This heater power is referred to as touch-down power. *H* denotes the heater element, *R* the read element, *W* the write coil and *CS* the contact sensor.

Sliders with micro heaters are commonly referred to as thermal flying height control (TFC) sliders [88, 89]. TFC slides were first implemented in 2007 with a linear actuator's stroke of 2.5 nm per 50 mW and a time constant of 1 ms [88, 90]. To improve performance, numerous investigations were carried out concluding that:

- A shorter distance between the heater and air bearing surface results in a larger temperature rise at the read element, larger stroke, and reduced time constant [91].
- The performance of TFC sliders can be improved using thermal insulator [92]. The thermal insulator should be as large as possible and should have a low thermal conductivity.
- TFC sliders with two heater elements, each of them with an insulator, show a better response time and allow for more accurate positioning of the read and write element [89].

TFC sliders are now a standard component in hard disk drives [88, 93]. As of today, thermal flying height control sliders are mainly used in a 'static' sense to achieve a consistent spacing during reading and writing independent from changes in environment (relative humidity, temperature) and disk operation (reading vs. writing).

2.3.4 Geometric aspects

Bit aspect ratio and linear, track and areal density

A single bit is typically much larger in width compared to its length due to limitations on the write head geometry (see 2.6.1 for more details). The number of bits per inch (BPI) in the down-track direction is a measure of the linear density and the number of tracks per inch (TPI) relates to the track density. The ratio between BPI and TPI is defined as the bit aspect ratio (BAR) and the areal density is determined by multiplying the linear density with the track density [26].

Over the years, areal densities have increased dramatically. The first disk storage system, the IBM 350 (see 2.1), provided areal densities of 3.1 Bit/mm^2 (2,000 bit/in^2) [26], compared to current densities on the order of 1.24 GBit/mm^2 (800 GBit/in^2) for perpendicular magnetic recording technology. This corresponds to an increase in areal densities by a factor of 400 million! Higher areal densities are achieved by increasing the track density, i.e., packing data tracks closer together, and reducing the bit size which allows for higher linear densities and smaller track width. Smaller bits require a reduction in head-disk spacing and precise head-positioning. Key elements that lead to a reduction in flying height are related to advances in manufacturing and material science (smoother surfaces, improved coatings and lubricants, smaller read and write head geometries), the invention of thermal flying height slider, better air bearing technology and improved read head sensitivity. The head-disk spacing of the IBM 1301 (see 2.1), the

first storage unit with self-flying heads, was 6 µm compared to 1-2 nm during reading and writing in today's hard-disk drives.

Skew angle

The skew angle is defined as the angle at which the recording head is oriented relative to the data track as shown in Fig. 2.14. The existence of such a skew angle is due to the use of rotational actuators for head positioning rather than linear actuators. The skew angle typically ranges from +15 ° at the inner diameter to -15 ° at the outer diameter. There are several undesired effects associated with skew angles such as read/write offset. During intermittent slider-disk contacts, slider vibration is found to be largest in the off-set direction [62] which is enhanced at large skew angles.

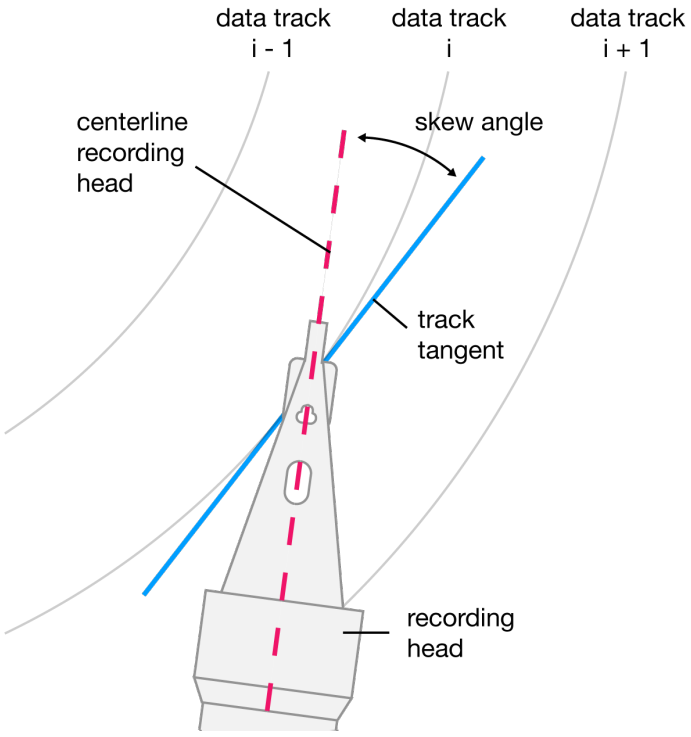

Figure 2.14: The skew angle is defined as the angle between the current track and the centerline of the recording head.

2.4 Tribological aspects

The term *tribology*, derived from the greek root *tribo* ('to rub'), was first introduced by British physicist Dr. H. Peter Jost in 1966 [94]. Jost was asked to form a committee to investigate the economic value of tribology to industry in a request made by Lord Bowden, the former british Minister of State for Science. In their final report, the committee stated that a better application of tribological principles could result in savings of over £515 million per year. In the Oxford dictionary, tribology is defined as "the study of friction, wear and lubrication; the science of interacting surfaces in relative motion". Tabor provides a more general definition by describing tribology as the study of "How surfaces interact when they are placed together and what happens when they slide".

Friction is the resistance that one surface or object encounters when moving over another [95]. *Wear* is the removal of material from either one of the two surfaces. There are several techniques available for reducing friction and wear such as the use of special materials, coatings, or lubricants. *Lubrication* refers to the practice of applying a lubricant such as oil or grease between two surfaces in relative motion to avoid direct contact, thus reducing friction and allowing smooth movement. The field of tribology is very interdisciplinary as it deals with surface and material science, contact mechanics, lubrication theory, etc.

At the head-disk interface in hard disk drives, tribological considerations are of uttermost importance and play a critical role in terms of reliability: As discussed in 2.3.2, zero spacing between the read and write element and the recording layer are desired from a magnetics point of view. However, such a configuration would result in accelerated wear and failure of the head-disk interface. Therefore, the slider is designed to fly over the disk at close proximity, thus preventing wear and degradation of the inter-

face. This situation is referred to as hydrodynamic lubrication. Nonetheless, intermittent head-disk contacts are likely to occur as the flying height is very small ($\leq$ 1-2 nm during reading and writing) compared to the surface roughness of the slider and the disk (2 nm peak-to-peak value). To reduce friction and wear during intermittent head-disk contacts, molecularly thin layers of diamond like carbon are applied to the slider and the disk and a thin layer of lubricant is present on the disk surface.

In the following, a brief historical perspective on tribology will be given, followed by a discussion on surface roughness, friction, wear and lubrication. Contact between rough surfaces and the effect of surface coatings are also discussed.

2.4.1 Historical perspective on tribology

Phenomena related to friction, wear and lubrication have been known since ancient times. However, as tribology is very complex in nature, its development as a scientific discipline was hindered until proper analytical and experimental tools became available. For example, quantitative surface roughness measurements via a stylus became available only in the 1940s [96]. The motion of the stylus was amplified electronically and provided a distorted cross-section of the surface. Atomic force microscopy used for imaging surface roughnesses on the micro scale was invented in 1986 [97]. Hence, early studies were based on intuition and macroscopic observations.

Da Vinci can be seen as the father of modern tribology. He studied numerous tribological subtopics such as friction, wear, lubrication and bearings [96]. Da Vinci discovered that friction is dependent on normal load and independent of the apparent contact area. However, his work had no historical influence as his findings remained unpublished.

Roughly 200 years later, Amontons rediscovered what da Vinci already knew and published his own theories on friction. Amontons believed that friction results from

dragging one surface over the roughness of the other, and from deforming and wearing the opposite surface. The idea that friction was caused by surface roughness shaped the theories of tribologists for many centuries.

Amontons findings were later confirmed by Euler and Coulomb. Euler studied the mechanics of a weight on an inclined plane and was the first to differentiate between static and kinetic friction [98]. He concluded from his experiments that static friction, i.e., the force needed to initiate sliding, is always larger than kinetic friction. Coulomb studied the sliding of materials under different sliding conditions [98]. He concluded that the friction force is also independent of the sliding velocity.

Da Vinci's, Amontons' and Coulomb's findings established the three macroscopic laws of friction[3] [98]:

1. **Independence of the area of contact:** Friction is independent of the contact area

2. **Amontons' Law:** The force of friction F_f is directly proportional to the applied normal load P_n: $F_f = \mu P_n$ where μ denotes the coefficient of friction.

3. **Coulomb's Law:** Kinetic friction is independent of the sliding velocity v.

Desaguliers proposed adhesion as an element of friction. Following Amontons' work he noted that "as surfaces are made smoother they ought to slide more easily, yet it is found by experience that the flat surfaces of metals or other bodies may be so far polished as to increase friction" [104]. He believed that this observation was caused by adhesion. However, Desaguliers was unable to relate the concept of adhesion to the laws of friction since molecular adhesion was known to be proportional to contact

[3] The classical laws of friction are remarkably true for most tribosystems. However, in 1981, Tabor changed our understanding of friction by realizing that the three main factors involved in friction are 1) the real area of contact, 2) the strength of the interfacial bonds, and 3) the deformation processes involved when these interfacial bonds are broken during sliding [99]. Today we know that classical laws of friction are only true for non-adhering surfaces and that they are invalid over a large range of loads [100]. Later work by Molinari et al. [101], Müser [102] and Braun [103] also showed that the friction force is indeed velocity dependent.

area whereas friction was not. It took nearly 200 years until Desaguliers observation on adhesion - which appeared to be contradicting at the time - could be explained by Bowden and Tabor.

It has been well known since ancient times that lubrication improves friction and wear. However, it was not until the 1880s when the theory of fluid film or hydrodynamic lubrication was established by Petrov and Reynolds. The effectiveness of the lubricant film is mainly determined by the ratio of the film thickness over the combined surface roughness. Depending on this ratio, different lubrication schemes can be distinguished which is expressed in the Stribeck curve, named after Richard Stribeck [105, 106]. For ultra-thin lubricant films, lubricants were found to behave solid-like which led to the theory of boundary lubrication proposed by Hardy in 1919.

Bowden and Tabor published their book on 'The friction and lubrication of solids' in 1950 which became the standard work for many decades [98]. Bowden and Tabor were the first who distinguished between the *real* area of contact versus the *apparent* area of contact. Given that engineering surfaces are rough, they realized that contact between two surfaces only occurs at the tips of the highest asperities. These regions define the *real* area of contact. The real area of contact is significantly smaller than the apparent area of contact, and the two are completely independent from each other. Bowden and Tabor suggested that the presence of a normal load causes the tips of the highest asperities to deform plastically. Plastic flow is believed to continue until the real area of contact was large enough to support the normal. Hence, Bowden and Tabor proposed that

$$A_r = \frac{P_n}{p} \tag{2.3}$$

where A_r denotes the real area of contact, P_n represent the normal load, and p is the compressive yield stress [96]. Equation 2.3 shows that the real area of contact is proportional to the normal load. Bowden and Tabor also proposed a model for explaining the origin

of friction. This model is known has the Bowden and Tabor adhesion model or plastic junction model [98]. Their model assumes that the friction force F_f is proportional to both the real area of contact A_r and the shear strength of the junctions formed σ, i.e., the mean lateral force per unit area, as expressed by

$$F_f = \sigma A_r \tag{2.4}$$

The term 'adhesion model' arises from the fact that friction force in equation 2.4 is proportional to the real area of contact, similar to adhesion. Friction is believed to originate from energy losses due to plastic deformation of the contacting asperities, hence the name plastic junction model. By distinguishing between the real and apparent contact area, Bowden and Tabor showed that both Amontons and Desaguliers were right: Friction and adhesion are proportional to the contact area, but it is the *real* contact area that they are proportional to.

Calculating the real area of contact is in general quite difficult. One of the first attempts were undertaken by Hertz who studied non-adhesive, elastic contact between two spherical lenses [107]. He formulated the well-known equations on the Hertzian contact stress [107] which provide the foundation for many problems in modern contact mechanics. However, the contact spot size depends on the radius of the asperity which is usually unknown.

Bowden and Tabor suggested that when two surfaces are in contact under loading, the individual contact regions increase in size via plastic flow until the contact pressure falls below the 'flow pressure' [108]. However, Archard pointed out two important facts: 1) An increase in load primarily increases the number of contact spots rather than just their size [109], and 2) the asperities may deform plastically at first but they must reach a steady state in which the load is supported more elastically [110]. Furthermore,

he went on and showed that the real contact area is proportional to the load even for purely elastic deformations [111].

In the 1960s, tools for quantitative surface roughness measurements emerged which allowed the description of 1) asperity distribution, 2) asperity heights, 3) radius of asperity tips, and 4) slope of asperities [96]. Greenwood and Williamson were among the first who took advantage of those tools. In their famous publication entitled 'Contact of Nominally Flat Surfaces' [110], Greenwood and Williamson showed that the real area of contact is indeed proportional to the applied normal load. It was demonstrated that contacting asperities may deform plastically (primarily rough surfaces) or elastically (primarily smooth surfaces) under normal load. Greenwood and Williamson introduced the plasticity index Φ which describes the transition from elastic to plastic flow. They showed that the deformation mode, i.e., elastic versus plastic deformation, is a function of material and topography properties and rather independent of load. From their surface studies Greenwood and Williamson concluded that 1) the height distribution of the higher parts of any nominally flat surface may be regarded as Gaussian, and 2) the asperities of any nominally flat surface may be treated as having spherical caps [108, 110].

2.4.2 Characterization of rough surfaces

Surface properties play a dominant role in tribological applications. All engineering surfaces are complex and have surface roughness as presented in Fig. 2.15. The high points of a surface are commonly referred to as asperities or protuberances. Typically, an oxide layer and contaminants are present on the surface, and the material properties near the surface are different from the bulk material properties away from the surface due to handling and manufacturing.

The interaction between surfaces is mainly characterized by the interaction of the surface asperities. The asperities' physical and chemical properties depend mainly

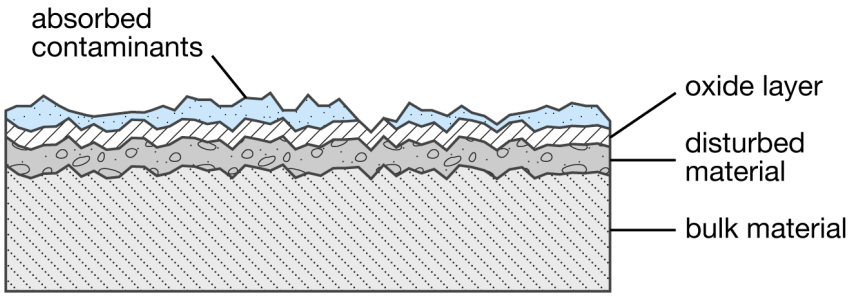

Figure 2.15: Example of an engineering surface. Surfaces are typically complex, i.e., they consist of multiple layers, and have surface roughness. Figure after [112].

on the manufacturing method and prior use. *Physical properties* of asperities refer to the hardness, the surface roughness on a macro level, e.g., waviness and shape, and the surface roughness on a micro level, e.g., asperity size and asperity distribution. The surface roughness dictates the contact area, contact stresses and lubricant or debris path and reservoirs when two surfaces are in contact. *Chemical surface properties* refer to the chemical compatibility and shear strength of the intervening layers, and the properties of the lubricant.

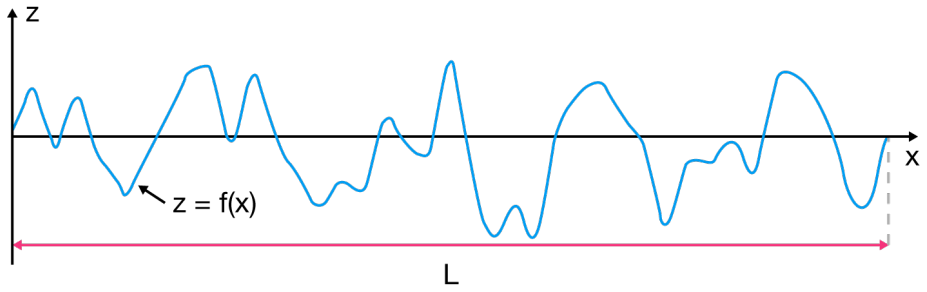

Figure 2.16: Height profile z of a rough surface with length L, showing asperities and valleys. Note that this is an exaggerated illustration; the vertical scale is typically smaller by a factor of 1000 compared to the horizontal scale for smooth surfaces.

Several statistical parameters exist for characterizing surfaces such as the peak-to-peak distance and the four central moments. A typical surface profile with length L is shown in Fig. 2.16.

With reference to Fig. 2.16., the *peak-to-peak distance* z_p is given by

$$z_p = |z_{max} - z_{min}| \tag{2.5}$$

where z_{max} and z_{min} denote the largest and smallest value of $z(x)$, respectively.

The *mean arithmetic surface roughness* R_a (1^{st} moment) of a given surface profile $z(x)$ is defined as

$$R_a = \frac{1}{L}\int_0^L |z(x) - z_{mean}|dx \tag{2.6}$$

where z_{mean} is the mean value of $z(x)$, i.e., $z_{mean} = \frac{1}{L}\int_0^L z(x)dx$.

The *root-mean-square surface roughness* R_q (2^{nd} moment) is given by

$$R_q = \sqrt{\frac{1}{L}\int_0^L (z(x) - z_{mean})^2 dx} \tag{2.7}$$

It shall be noted that R_a and R_q do not provide information regarding the lateral dimensions of the surface. It was also found that surfaces with different profiles can have similar R_a and R_q values [113]. Hence, additional characteristics are needed to properly describe surface characteristics. This can be done by means of the *skewness* R_{sk} (3^{rd} moment), and *kurtosis* R_{ku} (4^{th} moment) which are defined as

$$R_{sk} = \frac{1}{R_q^3} \cdot \frac{1}{L}\int_0^L |z(x)^3|dx \tag{2.8}$$

$$R_{ku} = \frac{1}{R_q^4} \cdot \frac{1}{L}\int_0^L |z(x)^4|dx \tag{2.9}$$

The skewness is a measure of the asymmetry of the distribution curve and the kurtosis represents the sharpness of peaks on a surface as indicated in Fig. 2.17. Sed-

lacek et al. suggested that surfaces with higher kurtosis and negative skew correlate with reduced friction [113].

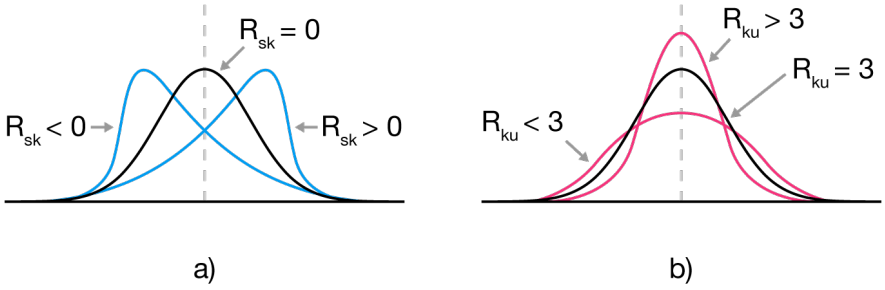

Figure 2.17: Skewness and kurtosis. Effect of a) the skewness on the asymmetry of the distribution peak ($R_{sk} = 0$ for the Gaussian distribution) and b) the kurtosis on the sharpness of the distribution peak ($R_{ku} = 3$ for the Gaussian distribution).

2.4.3 Friction

Friction is defined as the resistance that one surface or object encounters when moving over another [95]. Friction originates from microscopic forces of molecular adhesion (such as electrostatic forces, van der Waals forces and metallic bonds), microscopic forces of mechanical abrasion (elastic and plastic deformation), and contaminants present at the interface (such as oxides, absorbed films and gases, and foreign particles).

There are many mechanical components in hard disk drives that move relative to each other and give rise to friction. For example, friction is present during accidental slider-disk contact, in the fluid bearing of the spindle motor for spinning the disk stack, or when moving the head-gimbal assembly on or off the ramp. Furthermore, the voice-coil motor used for radial positioning of the recording head results in pivot friction [114, 115].

For dry friction, i.e., friction between two solids in the absence of lubrication, friction can be subdivided into kinetic and static friction. *Static* friction is friction between two bodies that do not move relative to each other, e.g., static friction can prevent

an object from sliding down an inclined surface. *Kinetic* friction occurs when two contacting objects are in relative motion. Kinetic friction is understood to be primarily caused by chemical bonding between surfaces, rather than interlocking asperities what Euler proposed. However, there are many cases in which roughness effects are dominant. Static friction is in general - but not always - larger than dynamic friction.

Bowden and Tabor [116] expressed the kinetic friction force F_k in terms of the real contact area A_r as

$$F_k = \tau A_r \tag{2.10}$$

where τ denotes the shear strength. A more general expression for kinetic friction is given by

$$F_k = \mu P_n + c_0 \tag{2.11}$$

where μ denotes the coefficient of force, P_n is the normal load and C_0 is a term that depends on the surface properties of both surfaces. The coefficient of friction is the sum of an adhesion component μ_a, a deformation component μ_d and an asperity summit deformation component μ_{dp} caused by particles [117] as expressed in the equation below

$$\mu = \mu_a + \mu_d + \mu_{dp} \tag{2.12}$$

2.4.4 Wear

Wear is the removal of material from either one of the two surfaces. As material is removed from either on of the two surfaces, the debris might form a lose wear particle or adhere to a surfaces depending on the surface energy of the surfaces involved. Similar to friction, wear is a system property. The wear rate depends on the wear mode which can occur simultaneously or sequentially. Principle types of wear are (1) adhesive wear, (2) abrasive wear, (3) fatigue wear, (4) erosive wear, (5) chemical or corrosive wear,

and (6) electrical-arc-induced wear [118]. The two most common types that occur at the head-disk interface are believed to be abrasive and adhesive wear. In the following, abrasive and adhesive wear under dry conditions and Archard's wear equation will be discussed.

Abrasive wear

During abrasive wear, the softer of the two surfaces undergoes material loss or deformation. On a microscopic level, the asperities of the harder surface cause plastic flow or cutting of the softer material. Abrasive wear can result in the formation of wear particles. There are two types of abrasive wear as indicated in Fig. 2.18: Two-body abrasion and three-body abrasion. Two-body abrasion refers to the case where the softer surface is damaged by the harder surface. Three-body abrasion involves a third body that is trapped at the interface such as small particles.

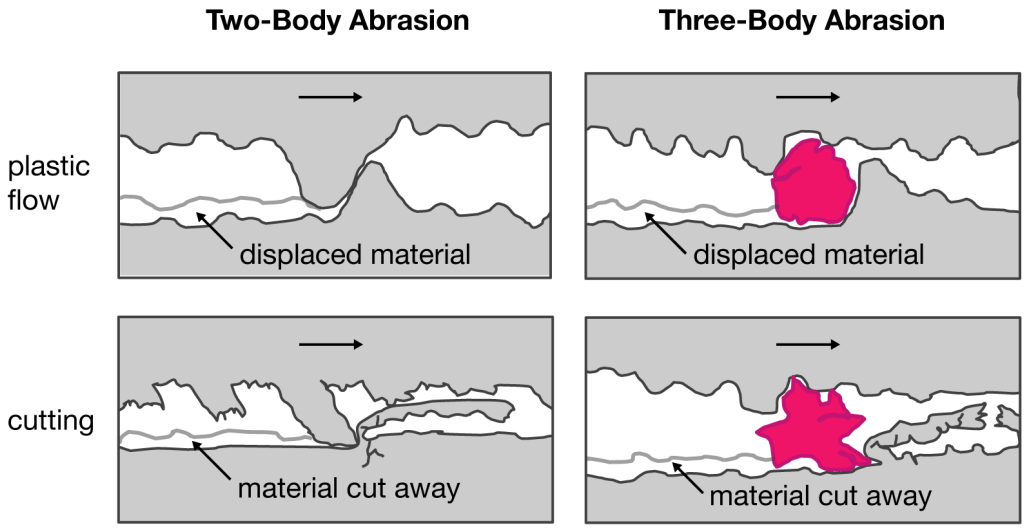

Figure 2.18: Types of abrasive wear. There are two-body abrasion and three-body abrasion. The later includes a foreign particle trapped at the interface. During abrasive wear, material deformation is caused by plastic flow or cutting. Schematic after [119, 120].

Adhesive wear

During adhesive wear, adhesive junctions are continuously being formed and broken off as two contacting surfaces are in relative motion under a normal load. Similar to abrasive wear, adhesive wear involves the plastic flow of the contacting surfaces. If the shear strength of the adhesive junctions are strong enough to resist sliding, cracks initiate and propagate.

Archard's wear equation

Wear mechanisms are generally quite complex and controlling wear is highly empirical [96]. Archard suggests that the volume of material loss Q due to abrasive and adhesive wear can be expressed via the following equation

$$Q = \frac{kP_n s}{H} \tag{2.13}$$

where k denotes the coefficient of wear, P_n is the normal load, s refers to the sliding distance, and H is the material hardness of the softer surface.

2.4.5 Lubrication

Lubrication is a technique employed for reducing friction and wear between two opposing surfaces in relative motion by means of lubricants. The lubricant can be a solid (e.g., bonded films such as graphite or compounds such as MoS_2), a liquid (e.g., oil, water), a liquid-liquid dispersion (e.g., grease), or a gas [121]. Examples of lubricants in hard disk drives are the lubricant applied to the disk surface (liquid lubricant) and the gas film at the head-disk interface (gaseous lubricant, typically air) as the slider flies over the disk.

Proper lubrication prevents or reduces contact between surface asperities which

reduces friction, wear and contact stresses, respectively. Furthermore, lubricants transport debris away from the interface and provide cooling. The effectiveness of the lubricant depends on the fluid shear properties (e.g., viscosity), the lubricant chemistry (e.g., surface reactivity and shear strength), and thermal properties (e.g., thermal conductivity and heat capacity) [112].

Lubrication regimes

Depending on the lubricant coverage, three basic lubrication regimes can be distinguished which are 1) full film lubrication (also called hydrodynamic lubrication), 2) mixed or thin film lubrication, and 3) boundary lubrication. In the case of *hydrodynamic lubrication*, the counter faces are completely separated by the lubricant film. Contacts between surface asperities are absent and load is entirely supported by viscous shear forces in the lubricant. During *boundary lubrication*, the solid surfaces are so close together that contact between the surface asperities is likely. The load is partly carried by the contacting asperities, and partly by the lubricant film.

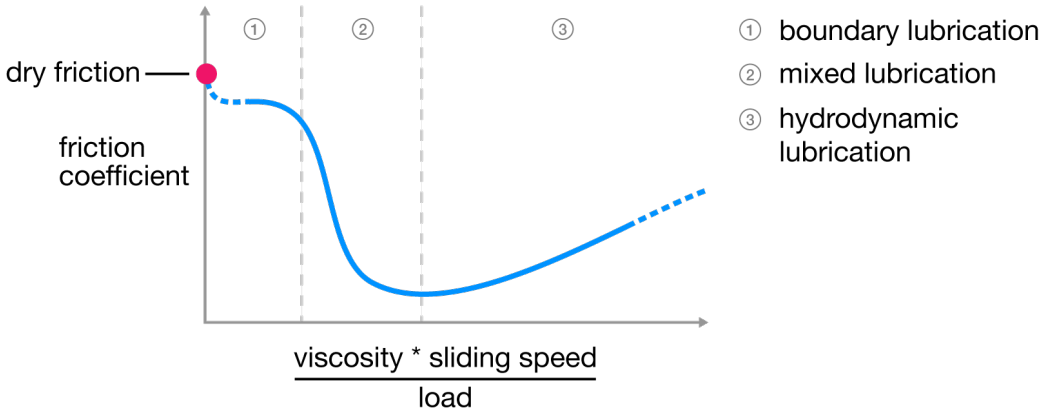

Figure 2.19: The Stribeck diagram describes the coefficient of friction for the three basic lubrication regimes. Friction is expressed in terms of lubricant viscosity, sliding speed and applied load. Schematic after [122].

The coefficient of friction of the three regimes is expressed in the Stribeck curve

(Fig. 2.19), named after Richard Stribeck (1861-1950). Stribeck studied friction in journal bearing as a function of lubricant viscosity, sliding speed and applied load and pointed out the existence of a point with minimum friction [123]. As shown in Fig. 2.19, friction is highest during boundary lubrication, and decreases to a minimum once the load is fully supported by the lubricant and asperity contacts are absent. In the regime of fluid film lubrication, friction increases again.

The next section discusses hydrodynamic lubrication and the Reynolds equation.

Hydrodynamic lubrication and the Reynolds equation

In hard disk drives, the slider flies over the rotation disk supported by an air bearing as described earlier in 2.3.1. The pressure distribution that carries the slider is generated from viscous forces within the air bearing and is in equilibrium with the normal load applied to the slider via the suspension. The fundamental equation that is widely used for describing the air flow at the head-disk interface is the Reynolds equation [124, 125]. The Reynolds equation is derived from the continuity equation and the Navier-Stokes equation and the following assumptions are made [126]:

- The flow is very thin, laminar and isothermal.
- The flow is Newtonian with constant viscosity.
- Inertia effects can be neglected.
- The gas is an ideal gas.

The two-dimensional Reynolds equation for compressible flow is given by [127]

$$\frac{\partial}{\partial x}\left(ph^3\frac{\partial p}{\partial x}\right)+\frac{\partial}{\partial y}\left(ph^3\frac{\partial p}{\partial y}\right)=6\mu\left(U\frac{\partial ph}{\partial x}+V\frac{\partial ph}{\partial y}\right)+12\mu\frac{\partial ph}{\partial t} \tag{2.14}$$

where p denotes the local pressure, h is the local spacing, μ is the viscosity of the fluid, and U and V are velocity components in the x- and y-direction, respectively, as shown in Fig. 2.20. It can be seen from equation 2.14 that the pressure forces on the left-hand side are in equilibrium with the shear forces on the right hand side.

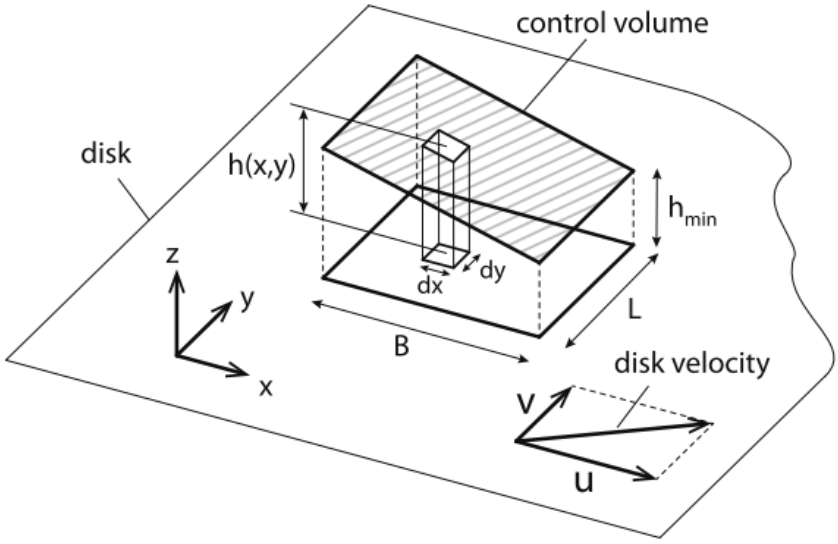

Figure 2.20: Governing channel in pivoted slider bearing. Schematic from [82].

For the derivation of equation 2.14, no-slip boundary conditions are applied at the head and disk surface. However, this assumption is no longer valid as the fluid film thickness h becomes smaller than the mean free path λ of the air molecules[4]. Hence, rarefaction effects need to be included. The degree of rarefaction is typically defined by the Knudsen number K_n which is defined as

$$K_n = \frac{\lambda}{h} \tag{2.15}$$

The various regimes observed in rarefied gas flow are: Continuum flow ($K_n < 0.01$), slip flow ($0.01 \leq K_n < 0.1$), transition flow ($0.1 \leq K_n < 10$) and free molecule flow

[4] The mean free path refers to the average distance traveled by moving particles between successive collisions. Collisions alter the direction and energy of the particle.

($K_n \geq 10$) [128]. Current head-disk spacings are on there order of 1-2 nm during reading and writing and the free-mean path of air is 65 nm. This corresponds to a Knudsen number of $K_n \geq 30$ which corresponds to highly rarefied flow. To accommodate for this situation, the modified Reynolds equation is used together with the energy equation using velocity slip and temperature jump boundary conditions. Fukui and Kaneko [129] proposed such a generalized Reynolds equation which is valid for any Knudsen number. The equation is derived from a linearized Boltzmann equation and given by

$$\frac{\partial}{\partial x}\left(\bar{Q}ph^3\frac{\partial p}{\partial x}\right)+\frac{\partial}{\partial y}\left(\bar{Q}ph^3\frac{\partial p}{\partial y}\right)=6\mu\left(U\frac{\partial ph}{\partial x}+V\frac{\partial ph}{\partial y}\right)+12\mu\frac{\partial ph}{\partial t} \tag{2.16}$$

where $Q = Q(K_n)$ is the so-called correction factor.

The slider air bearing surface (ABS) is rather complex (see Fig. 2.9) and hence, the pressure distribution of the ABS may be obtained using a finite element solution of the Reynolds equation [124]. For steady-state simulations, the time-dependent term in equations 2.14 and 2.16 can be neglected.

The steady-state slider position – or slider attitude – is calculated numerically by simultaneously solving the slider equilibrium equations with the Reynolds equation [130]. This approach ensures that the air bearing forces are in balance with the preload applied to the slider via the suspension. The slider equilibrium equations in the z-direction, pitch direction, and roll direction are given by [130]

$$\iint_A p(x,y)dA - F_z^{ext} = k_z dh \tag{2.17}$$

$$\iint_A p(x,y)(x-x_p)dA - M_\alpha^{ext} = k_\alpha d\alpha \tag{2.18}$$

$$\iint_A p(x,y)(x-y_p)dA - M_\beta^{ext} = k_\beta d\beta \tag{2.19}$$

where p represents the local pressure, F_z^{ext} is the suspension preload, α and β refer to

the pitch and roll angles, respectively, M_{α}^{ext} and M_{β}^{ext} denote the pitch and roll preload, respectively, and k_z, k_{α} and k_{β} are the stiffness values in the vertical, pitch and roll direction, respectively.

The slider attitude is commonly described in terms of its pivot flying height, minimum flying height, and slider pitch angle as illustrated in Fig. 2.21. The slider pitch angle is defined as the angle of the slider with respect to the horizontal and is typically on the order of 100 μrad. The flying height is smallest at the slider trailing edge near the location of the read and write element. State-of-the art hard disk drives are predominantly equipped with femto sliders [131]. Femto sliders are 850 μm by 700 μm large and their nominal flying height[5] is on the order of 10-12 nm. In the CMRR steady-state air bearing simulator, the pivot point is located at the geometric center of the air bearing surface. The slider can pitch and roll about the pivot point.

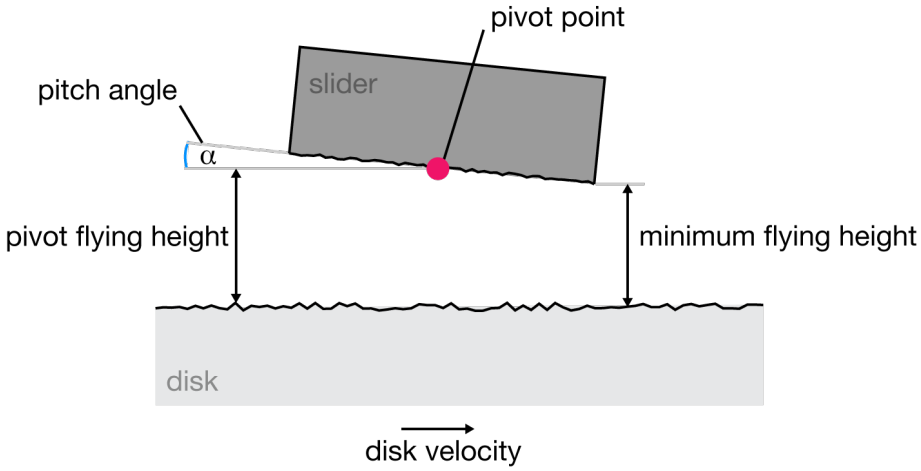

Figure 2.21: Steady-state slider attitude expressed in terms of its minimum flying height, slider pitch angle, and pivot flying height as defined in the CMRR steady-state air bearing simulator. Nominal flying heights and slider pitch angles are on the order of 10-12 nm and 100 μrad, respectively.

Using the CMRR steady-state ABS simulator [124], we calculated the pressure

[5] Nominal flying height refers to the case where the slider flies at its intended disk velocity and skew angle without actuating the heater element. See section 2.3.3 for more information on the heater element of thermal flying height control sliders.

distribution of the meshed slider surface shown in Fig. 2.22 a) without no heater actuation. The slider was meshed with triangular elements using HyperMesh, a commercially available finite element preprocessor. For the boundary conditions, ambient pressure was applied to the nodes along the edges of the slider surface. Figure 2.22 b) shows the calculated pressure distribution. It can be seen from Fig. 2.22 b) that the pressure is highest near the location of the read and write element and that several regions exist with sub-ambient pressure. The pressure at the location of the read and write element is roughly sixteen times larger than ambient pressure.

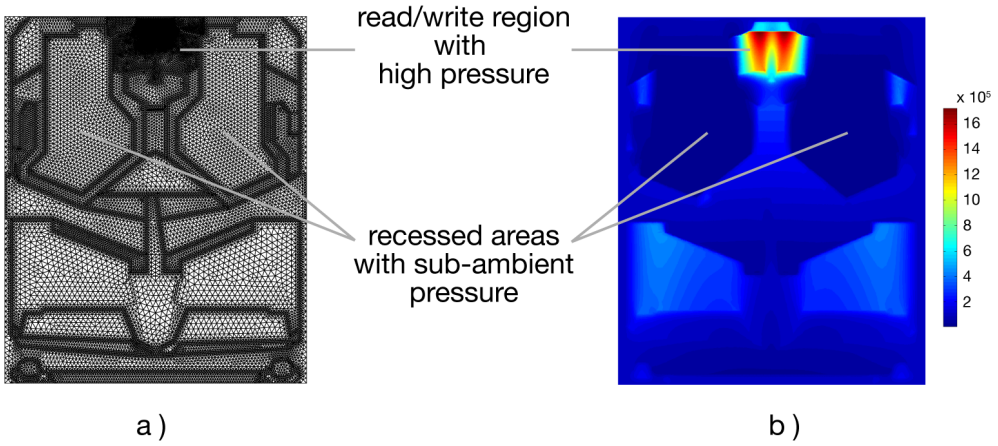

Figure 2.22: Slider air bearing surface (ABS) with trailing edge (top) and leading edge (bottom) showing a) meshed ABS and b) pressure distribution calculated numerically using the CMRR steady-state ABS simulator [124]. The pressure is highest near the read and write element. Note that the heater element was not actuated.

Changing the disk velocity affects the slider attitude. Figure 2.23 shows a) the minimum flying height, b) the pitch angle, and c) the pivot flying height versus disk velocity. It can be seen in Fig. 2.23 a) that the minimum flying height decreases with decreasing disk velocity. In fact, if the disk velocity is small enough, the slider will crash onto the disk. Fig. 2.23 b) and c) illustrate that both the pitch angle and pivot flying height decrease with increasing disk velocity for this particular air bearing surface.

To calculate the flying height as a function of heater power for thermal flying

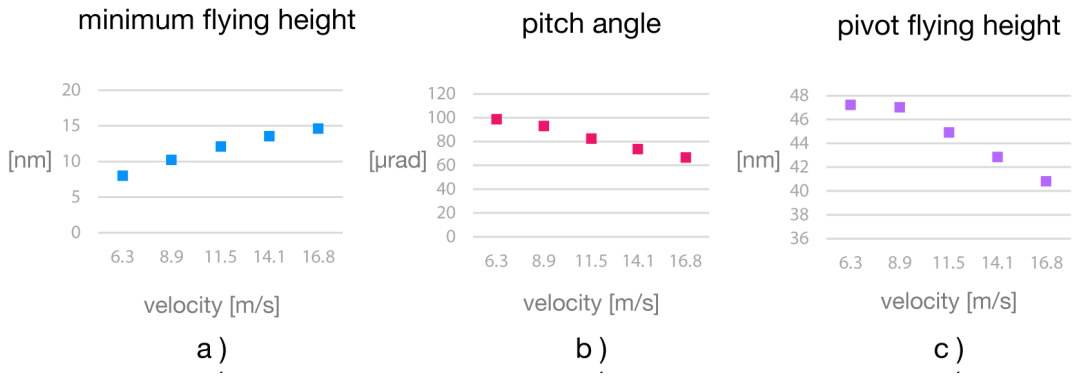

Figure 2.23: Slider attitude as a function of disk velocity, showing a) the minimum flying height, b) pitch angle, and c) pivot flying height.

height control sliders, an iterative approach is needed [132, 133]. Zheng et al. [133] used the following procedure: In step 1), the air bearing pressure was calculated across the entire air bearing surface using the CMRR steady-state air bearing simulator. In step 2), the heat transfer coefficient between the slider and the air bearing was calculated. These results served as boundary conditions for computing the thermal deformation of the slider due to heater actuation. Actuating the heater element in the slider trailing edge heats up the nearby material. The material expands due to the heat, forming a protrusion at the bottom surface of the slider. Once the new geometry of the air bearing surface is obtained, the pressure needs to be recalculated. Steps 1) and 2) are repeated until the flying height converges.

2.4.6 Contact between rough surfaces

When two surfaces are placed in contact, they will touch each other at their highest points. The sum of contact spots is referred to as the *real* or *true* area of contact. For most surfaces, the real area of contact is only a small fraction of the *nominal* or *apparent* surface area. The real area of contact depends on the surface topography, material properties and loading conditions. Under the presence of a normal load, the contact-

ing asperities deform plastically or elastically until the real area of contact A_r is large enough to support the normal load P_n. An increase in load primarily increases the number of contact spots and also – but to a lesser extend – their size [109]. Assuming that asperities are spherical in shape, it was found that $A_r \propto P_n^{2/3}$ for elastic deformation and $A_r \propto P_n^1$ for plastic deformation during single asperity contact. Asperities in close proximity result in adhesive contacts originating from interatomic interactions [117]. If the two surfaces are moved relative to each other, the adhesive contacts and other phenomena contribute to friction. Reoccurring surface interactions cause wear and degradation of the interface.

Greenwood and Williamson defined a plasticity index which describes if the deformation mode is plastic or elastic. Elastic deformation between two spheres was first described by Hertz. In the following, Hertz's theory of sphere-on-sphere contact, plastic deformation and the plasticity index by Greenwood and Williamson will be discussed.

Hertz's theory for elastic sphere-on-sphere contact

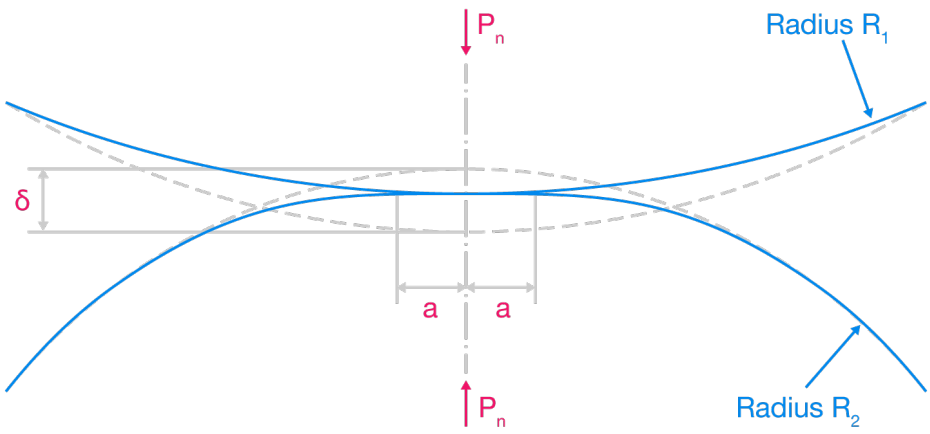

Figure 2.24: Cross-sectional view of two elastic, solid spheres under normal load P_n. The spheres have radii R_1 and R_2, respectively, and the radius of the resulting contact area and total compression are indicated by a and δ respectively.

Placing a spherical lens on top of a flat surface results in an interference pattern

due to the reflection of light. This phenomenon was first studied by Newton and known as Newton's rings. Motivated by Newton's findings, Hertz became interested in studying the optical properties of two lenses when stacked together under a normal load. In particular, he was interested in the contact area and the contact stresses. Hertz's work on non-adhesive, elastic contact between two ideal spheres lead to the formulation of the well-known equations on *Hertzian contact stress*. Published via "Über die Berührung fester elastischer Körper" (On the contact of elastic solids) by Hertz in 1881 [107], his theory provides the foundation for many problems in modern contact mechanics.

During Hertzian sphere-on-sphere contact, friction is neglected and the radius of the contact area a is assumed to be significantly smaller than the sphere radii R_1 and R_2 [134]. Based on these assumptions, the effective radius of curvature R^* and the effective modulus of elasticity E^* are defined as

$$\frac{1}{R^*} = \frac{1}{R_1} + \frac{1}{R_2} \tag{2.20}$$

$$\frac{1}{E^*} = \frac{1-\nu_1^2}{E_1} + \frac{1-\nu_2^2}{E_2} \tag{2.21}$$

where E_1 and E_2 are the moduli of elasticity and ν_1 and ν_2 the Poisson's ratios, respectively. Based on the above definitions, the radius of the contact area a is given as

$$a = \left(\frac{3P_nR^*}{4E^*}\right)^{\frac{1}{3}} \tag{2.22}$$

with P_n denoting the applied normal load which gives rise to a pressure distribution. The maximum pressure p_{max} occurs along a line at the center of the contact area and is given by

$$p_{max} = \frac{3P_n}{2\pi a^2} = \frac{3}{2}p_{mean} = \left(\frac{6P_nE^{*2}}{\pi^3R^{*2}}\right)^{\frac{1}{3}} \tag{2.23}$$

The total compression δ between the two spheres is given by

$$\delta = \frac{a^2}{R^*} \tag{2.24}$$

Fig. 2.24 illustrates contact between two spheres and shows the radius of the contact area a and the total compression δ. Since the total contact area A is given by $A = \pi a^2$, it follows that

$$A = \pi \left(\frac{3P_n R^*}{4E^*} \right)^{\frac{2}{3}} = kP_n^{\frac{2}{3}} \tag{2.25}$$

In other words, the contact area for a single contact is proportional to $P_n^{\frac{2}{3}}$ where P_n denotes the normal load.

Plastic deformation

Tabor [135] studied plastic deformation during sphere-on-plane contact experimentally. It was shown that the material starts deforming plastically when the maximum contact pressure p_{max} between the sphere and the plane reaches a value of $0.6H$, where H denotes the material hardness. Based on this finding, Greenwood and Williamson derived a critical displacement value ω_c which describes the onset of plastic deformation during sphere-on-plane contact

$$\omega_c = \left(\frac{\pi}{2} \right)^2 \left(\frac{0.6H}{E} \right)^2 R \approx 0.89 \left(\frac{H}{E} \right)^2 R \tag{2.26}$$

where E denotes Young's modulus and R is the sphere radius.

Chang et al [136] took volume conservation into account for the plastic deformation of asperities. For displacements $\omega > \omega_c$, the contact area A and contact load P

of a plastically deformed asperity are given by

$$A = \pi R\omega \left(2 - \frac{\omega_c}{\omega}\right) \tag{2.27}$$

$$P = \pi R\omega \left(2 - \frac{\omega_c}{\omega} KH\right) \tag{2.28}$$

Kogut and Etsion studied elastic-plastic contact of a deformable sphere pressed by a rigid flat [137]. Three distinct stages of elastic-plastic contact were identified based on the ratio ω/ω_c: The contact area is elastic for $1 \leq \omega/\omega_c \leq 6$, plastic-elastic for $6 \leq \omega/\omega_c \leq 68$, and fully plastic for $\omega/\omega_c > 68$.

Plasticity index by Greenwood and Williamson

The Greenwood-Williamson (GW) model [110] is a classical approach for studying plastic-elastic contacts between rough surfaces. The mode of contact, i.e., predominantly plastic vs. predominantly elastic deformation, is described by the plasticity index Φ.

For their statistical model, Greenwood and Williamson [110] assume that surfaces possess the following properties:

- Surface asperities are spherical in shape near their summits.
- All asperity summits have identical radius R.
- The asperity heights vary randomly; the probability that the height of a particular asperity is between z and $z+dz$ with respect to some reference plane expressed in terms of $\Phi(z)dz$.

Considering two rough surfaces at an initial separation distance d. The separation distance d is reduced so that the surfaces touch each other. For this situation,

contact will occur at asperities with heights z taller than d. Hence, the probability of making contact at asperities with height z is given by [110]

$$P(z > d) = \int_{d}^{\infty} \Phi(z) dz \tag{2.29}$$

and the expected number of contact spots is given by

$$n = N \int_{d}^{\infty} \Phi(z) dz \tag{2.30}$$

where N denotes the total number of asperities. Combining the above equations with the results from Hertz' theory on contact between a sphere and a plane, the expected total area of contact A and the expected total load F_t are given by

$$A = \pi N R \int_{d}^{\infty} (z-d) \Phi(z) dz \tag{2.31}$$

$$F_t = \frac{4}{3} N E^* R^{\frac{1}{2}} \int_{d}^{\infty} (z-d)^{\frac{3}{2}} \Phi(z) dz \tag{2.32}$$

E^* refers to the effective Young's modulus as defined in 2.21.

Greenwood and Williamson [110] also studied the properties of numerous surfaces and concluded that most engineering surfaces adhere to the following two properties:

1. The height distribution of the higher parts of any nominally flat surface may be regarded as Gaussian.

2. The asperities of any nominally flat surface may be treated as having spherical caps with radii R.

Based on such a surface, they defined the plasticity index Φ as

$$\Phi = \sqrt{\frac{\sigma}{\delta_p}} = \frac{E^*}{H}\sqrt{\frac{\sigma}{R}} \tag{2.33}$$

where σ denotes the standard deviation of the asperity height distribution, δ_p refers to the criterion for detectable plastic flow at the asperity according to the yield point of the material, E^* is the effective Young's modulus as defined in 2.21, H is the hardness of the material, and R the radius of the asperity summits. Greenwood and Williamson suggest that a significant degree of plasticity is reached when 2 % of deforming asperities deform plastically. For this situation, the plasticity index Φ can be interpreted as follows:

- Contacts are largely plastic if $\Phi > 1.0$
- Contacts are largely elastic if $\Phi < 0.6$

Most surfaces are found to have plasticity indices larger than 1 suggesting that the asperities will flow plastically even under very small normal loads. Equation 2.33 demonstrates that the mode of deformation at the asperities depends only on surface parameters rather than applied normal load.

In the following, the plasticity index will be estimated for the head-disk interface. Figure 2.25 shows the height image of the read/write region of a new, unused head obtained using atomic force microscopy (AFM). The bright regions on the left and right in Fig. 2.25 a) identify the write and read shields, respectively. Dark areas are recessed in height and bright areas are elevated in height. A three-dimensional topography image of the region marked by the black rectangle is shown in Fig. 2.25 b). The following surface properties were identified: Arithmetic mean of $R_a = 0.20\ nm$, root-mean-square roughness of $R_q = 0.25\ nm$ and an average asperity radius of $R = 0.15\ nm$. Lu et al. [138] characterized disk surfaces experimentally and determined an average

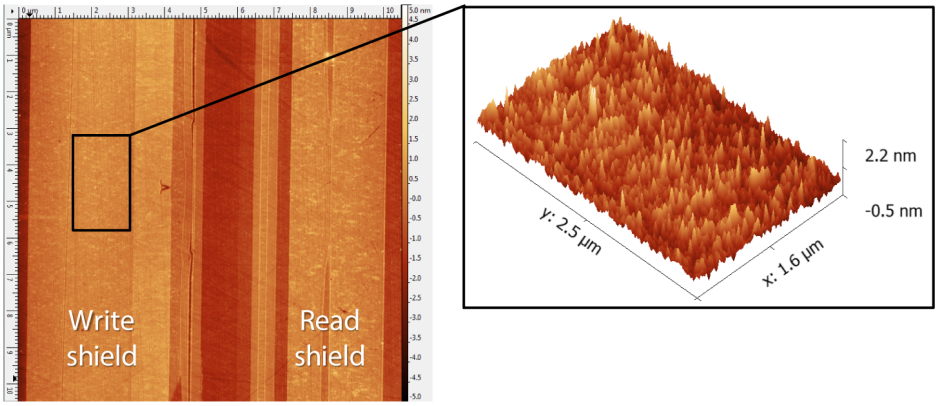

Figure 2.25: Topography of read/write region of a new, unused head measured using atomic force microscopy.

hardness and Young's modulus of 14 GPa and 100 GPa, respectively. The average root-mean-square roughness of disks is on the order of $R_q = 0.20\ nm$ [139]. Hence, the plasticity index is calculated to be $\Phi = 0.87$, suggesting that the deformation of surface asperities on the slider and the disk is in the elastic-plastic range.

2.4.7 Effect of surface coatings on tribological performance

Diamond-like carbon coatings

Carbon may exist in many different configurations as its four valence electrons are capable of forming either sp, sp^2, or sp^3 hybridization bonds[6] [33]. Well-known examples of carbon are diamond and graphite. In diamond (sp^3 configuration[7]), each carbon atom is covalently bonded to four other carbon atoms, forming a tetrahedron. The

[6] During hybridization, subshells or orbitals of multiple atoms combine to hybrid orbitals. For carbon, hybridization involves the s orbitals and p orbitals. Carbon (^{6}C) has six electrons of which two electrons occupy the s orbital in the first shell ('1s'), two electrons occupy the s orbital in the second shell ('2s') and the last two electrons occupy the p_x and p_y orbitals of the second shell ('$2p_x$', '$2p_y$').

[7] Each sp^3 bond involves the electrons of one 2s orbital and three 2p orbitals. The sp^3 orbitals are arranged in the form of a tetrahedron at angles of 109.5°

crystalline structure gives diamond its great hardness. Graphite (sp^2 configuration[8]) is structurally comprised of parallel layers. In each layer, carbon atoms are arranged in a honeycomb lattice via covalent bonds and in between the layers, weaker van der Waals forces are present. This special configuration allows graphite layers to easily slide past one another.

Diamond-like carbon (DLC) is a type of amorphous carbon possessing some of the desired properties of diamond, such as hardness. DLC can be manufactured into many different structures or forms, and different structures correlate with different tribological properties. In general, DLC coatings possess high hardness, chemical inertness and excellent tribological, adhesive and corrosion properties [33, 38, 41, 43, 140–142]. Critical parameters that control the tribological properties of DLC are [41, 140–142]:

- The bonding structure or the carbon **hybridization states**. DLC is composed of sp^3, sp^2 and – to a lesser extend – sp bonds. Hardness of DLC films strictly correlates with sp^3 content [38, 41, 43]. On the other hand, the properties of DLC films with high sp^2 content will be more similar to that of graphite. Hence, the sp^3/sp^2 ratio is an important parameter for characterizing mechanical properties of DLC coatings. DLC contains about 20-50 % of sp^3 bonds [141]. When exposed to high temperatures, DLC films may undergo a graphitization process, thus reducing the hardness and sp^3 content of the film [143–145]. High temperatures may develop during unlubricated sliding as a result of frictional heating [146].

- The **deposition method** and **deposition parameters**. Common deposition methods are [33, 38, 139] filtered cathodic vacuum arc (FCVA), chemical vapor deposition (CVD), ion beam deposition, pulsed laser deposition, and magnetron sputtering.

[8] sp^2 bonds involve the electrons of one 2s orbital and two 2p orbitals. The orbitals are oriented in a plane at angles of 120°

- The use of **dopants**. During the deposition process, DLC may be doped with nitrogen, hydrogen or other elements.

- **Surface properties** such as surface termination and surface roughness. The surface roughness depends on the deposition method [33] and the surface roughness of the underlaying substrate as DLC films typically grow conformal to the substrate surface [142].

- **Environmental conditions** such as atmosphere, temperature and humidity.

- **Test conditions** such as the type of motion or counter material.

The wear behavior of DLC films depends on the adhesion strength of the film to the substrate, the mechanical properties of the film such as hardness and elastic modules, and the film thickness. Deposition of the DLC film leads to high internal stresses and these stresses are known to vary with deposition parameters [142]. High internal stresses results in poor *adhesion* of the DLC film to the underlaying substrate [140]. In hard disk drives, a thin layer of silicon is employed between the magnetic layer and the carbon layer to improve adhesion of the DLC to the substrate material. The *hardness* of the DLC coating does not only depend on the sp^3/sp^2 ratio, but also on the deposition method and parameters, the source of carbon, the type and amount of dopants used and the underlaying substrate. The deposition method affects the density of the DLC film [147]. It was suggested that the hardness of the DLC film correlates with an increase in density [41]. It was also found that an increase in nitrogen content results in decreased hardness, decreased internal stresses, and an increase in critical load for fracturing [39, 140, 148]. The elastic properties of DLC films correlate with the films' density and hybridization [41]. For very *thin* coatings, the mechanical properties are greatly determined by the underlaying substrate.

Friction of DLC coatings [40] may be attributed to adhesive, abrasive and shear mechanisms. *Adhesive friction* is related to the microsctructure of the DLC film, the counterface, and environmental conditions. *Abrasive friction* is closely related to the surface roughness of the DLC films. It has been found that wear debris may build up and form a transfer layer at the interface (the interested reader may refer to [142,143] for an overview). *Friction caused by shearing* is related to the shear strength of the transfer layer and is largely affected by the presence of environmental species, e.g., water, which might react with the transfer layer [142].

Plastic deformation of surface coated materials

When a single asperity is in contact with a flat surface, the asperity can either indent the opposing surface or be flattened by it. During contact between coated rough surfaces, it is generally of interest to know the onset of plastic yield and its location. Plastic yield can occur either within the coating, in the underlaying substrate, or at the interface between the coating and the substrate [149].

Chang et al. [150] noted that the tribological performance of surface coatings is greatly determined by the thickness of the coating and the roughness of the substrate. McCool [151] extended the Greenwood Williamson model by including the effect of surface coatings. It was found that the average load at asperities correlates with an increase in coating thickness for the case when the coating is stiffer than the substrate; when the coating is more compliant with respect to the substrate, the average load decreases with an increase in coating thickness.

Goltsberg et al. [149] studied the onset of plastic yielding in a coated sphere that is compressed by a rigid flat. The effect of coating thickness and material properties was investigated for the special case of $\nu = 0.32$ and $E_{su}/Y_{su} = 952$ where ν denotes Poisson's ratio and E_{su} and Y_{su} represent Young's modulus and the yield strength of

the substrate, respectively. Goltsberg et al. [149] identified the dimensionless coating parameter λ' given by

$$\lambda' = (\frac{t}{R})(\frac{P_{c_{co}}}{P_{c_{su}}})^{-0.507} \tag{2.34}$$

where t denotes the coating thickness, R refers to the radius of the coated sphere, and $P_{c_{co}}$ and $P_{c_{su}}$ refer to the critical load of the coating and the substrate material, respectively. The existence of an optimum coating parameter value λ'_p was found: for $\lambda' = \lambda'_p$, the system's resistance to failure was maximized. Furthermore, three possible locations of plastic yield inceptions were identified depending on the ratio of λ'/λ'_p. For $\lambda'/\lambda'_p > 1$, i.e., relatively thick coatings, yield inception takes place within the coating slightly below the contact area. For very thin coatings, yield inception takes place within the substrate.

Song et al. [152] studied plastic yield inception of a hard coated half sphere which is indented by a rigid sphere. A dimensionless 'hard coating parameter' λ_h was introduced given by

$$\lambda_h = (\frac{t}{R})(\frac{P_{c_{co}}}{P_{c_{su}}})^{-0.474}(\frac{E_{su}}{Y_{su}})^{1.003} \tag{2.35}$$

where t denotes the coating thickness, R refers to the radius of the coated sphere, $P_{c_{co}}$ and $P_{c_{su}}$ refer to the critical load of the coating and the substrate material, respectively, and E_{su} and Y_{su} represent Young's modulus and the yield strength of the substrate, respectively. Similar to Goltberg et al. [149] who studied flattening of a coated sphere, an optimal coating thickness $(\lambda_h)_p$ and three different locations at which plastic yield inception may occur were identified. Depending on the ratio of $\lambda_h/(\lambda_h)_p$, the onset of plastic yield may occur within the coating (for relatively thick coatings), at the interface on the substrate side, or within the substrate (for relatively thin coatings).

2.5 Controls aspects

To reliably read and write data, the slider must follow the data tracks on the recording surface closely enough while maintaining a near constant spacing. More precisely, variations in clearance between the head and the track center need to be minimized in both the vertical and the horizontal direction.

As indicated in section 2.3.3, hard disk drives are exposed to a variety of disturbances that introduce vertical and off-track motion of the recording head [26, 153–157]. Hence, the position of the head relative to the data tracks needs to be actively controlled. Controls problems in hard disk drives can be divided into two main areas:

1. Radial positioning of the recording head: Track seeking and track following.

2. Vertical positioning of the recording head: Flying height control.

In hard disk drives, the position error in the off-track direction is obtained from special magnetic patterns. These patterns are hard coded in the magnetic layer and known as *servo sectors*. In the following, servo sectors, radial head positioning and flying height control will be discussed.

2.5.1 Servo sectors

Special magnetic patterns are used to identify the radial and circumferential position of the recording head on the disk. In earlier hard disk drive generations, this special pattern was written on one disk surface only, meaning that one head was responsible for the position estimate of all the other heads. This technique is referred to as *dedicated servo* [26]. This approach, however, is only feasible for low track densities as each slider has its own dynamics.

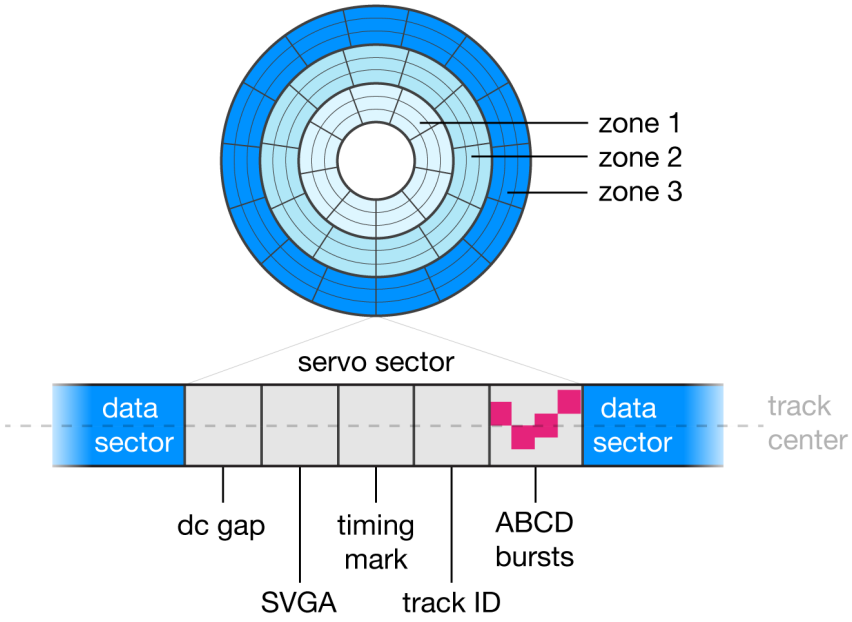

Figure 2.26: Schematic of data zones and servo sectors. Tracks are divided into data sectors in which data is stored and servo sectors which contain control related information. In order to have all data sectors be equal in length, the tracks are organized into data zones. Each zone has a different number of servo sectors.

In state-of-the art hard disk drives, data tracks are divided into data sectors and servo sectors along the circumference of the disk as indicated in Fig. 2.26. This technique is referred to as *embedded servo* [26]. While data is stored in the data sectors, servo sectors contain control related information such as a DC gap field, a servo-variable gain amplifier (SVGA) field, a timing mark, track identification number (ID) and a special burst pattern [26]. The burst pattern contains an A, B C and D burst from which the position error signal (PES) is generated [26]. Towards the outer diameter of the disk, data tracks become longer and can hold more data. In order to fully utilize disk space and increase storage capacities, data tracks are grouped into zones. Each zone is assigned a certain number of servo sectors which increases from the inner to the outer disk diameter as shown in Fig. 2.26. This technique is called zone bit recording (ZBR).

Servo information is available at discrete time intervals only. The PES sampling rate is a function of the spindle speed and the number of servo sectors. Modern hard disk drives typically contain between 100 and 300 servo sectors. The percentage of the storage area dedicated to servo sectors is defined as the servo overhead. Clearly, a trade-off exists between high PES sampling frequency and high storage capacities.

The servo sectors can also be used for calculating variations in flying height. Boettcher et al. [158] proposed a novel method for estimating changes in flying height Δz based on the servo sector. Using a modified version of the Wallace spacing loss formula [159], the following equation was derived

$$\Delta z = \frac{\lambda_1}{16\pi}(\ln(\Phi_{A1} + \Phi_{B1}) - 3 \cdot \ln(\Phi_{A3} + \Phi_{B3})) \tag{2.36}$$

where λ_1 denotes the wavelength of the first harmonic of the read-back signal, and $\Phi_{A,Bi}$ is the amplitude of the i^{th} harmonic of the read-back signal of the A and B burst, respectively.

2.5.2 Radial head positioning: Track seeking and track following

As discussed in 2.3.3, the recording head is moved radially across the disk surface using a voice coil motor (VCM). During track seeking, the head needs to be moved from one track to another within less than one disk revolution. Once the new track is reached, the recording head must follow the data track within 10 % of the track width to prevent read and write errors.

During track seeking, the non-linarities of the VCM (i.e., limits on the input and output) pose a major challenge [160]. A number of different control schemes have been proposed to address this issue such as:

- Proximate time-optimal servo (PTOS) control [161].

- Mode switching control with initial value compensation [162, 163].
- Composite nonlinear feedback (CNF) [164].
- Shaped time-optimal servo (STOS) control [165].
- Reference signal shaping [166].

In future hard disk drives the track densities will increase to 1 million tracks per inch [167]. At such high densities, the head cannot deviate more than 2-3 nm from the track center in order to prevent track mis-registration (TMR) [167]. Hence, advanced techniques are required to compensate for repeatable and non-repeatable run-out in the off-track direction (the interested reader may refer to [82] for an overview). It shall be noted that the (large) VCM is limited in bandwidth due to its inertia and constraints on the control input. These limitations illustrate why the VCM is incapable of compensating for high frequency disturbances acting on the recording head. Suspensions with dual-stage actuators (DSA) were hence introduced to increase the bandwidth and improve track following. Dual-stage suspensions are equipped with a secondary (faster) micro-actuator, typically a piezoelectric transducer. This micro-actuator is embedded either in the suspension base (*suspension-based design*) or close to the recording head (*collocated design*) [168]. Dual-stage suspensions are primarily used in high-performance hard disk drives. High-performance hard disk drives operate at higher than usual disk speeds and thus, windage induced vibration and disk flutter are of concern.

2.5.3 Vertical head positioning: Flying height control

As the slider flies over the disk, the head-disk spacing is non-uniform — dynamic and static variations in head-disk spacing can be observed. *Dynamic flying height variations* cause the flying height to be different on different positions on the disk. Disk

waviness, disk deformation due to clamping, and slider vibration induced by turbulence or external shock and vibration contribute to dynamic variations in head-disk spacing [169]. *Static flying height losses* cause the flying height to be reduced by a constant amount independent of the disk position. Manufacturing tolerances and environmental variations such as altitude drop [170], changes in temperature [171] and changes in humidity [172] affect the head-disk spacing in a static fashion.

As discussed in 2.3.3, the head-disk spacing can be controlled using thermal flying height control (TFC) technology. State-of-the art hard disk drives use TFC technology in a *static* fashion, meaning that the heater input is statically controlled by a constant power supply to the heater [173]. Desired flying heights of 1-2 nm during reading and writing are achieved by setting the heater input to a power level a few mW below the point at which the onset of slider-disk contact occurs.

Several techniques have been proposed for minimizing variations in flying height that utilize the read-back signal of the read element [93, 173–175]. Some authors [93, 173] suggested to write a special magnetic pattern onto the disk and to control the heater input based on the read-back signal of this special magnetic pattern . Other authors [175] propose controlling the heater input via an adjustment value generated from the position error signal. Boettcher et al. [93] proposed a feedforward control algorithm where the optimal heater input is calculated using convex optimization. The method computes the optimal heater input based on the read-back signal. The convex optimization procedure requires knowledge of the dynamics from the heater input to the read-back signal. The system dynamics are identified from experimental data via the step-realization algorithm [176].

It shall be noted that using the read-back signal has several drawbacks including:

- The magnetic spacing, i.e., the distance between the read/write element and the recording layer of the disk, may not be proportional to the actual flying height due

to thickness variations of the disk lubricant and the carbon overcoat on the slider and the disk, respectively. Hence, topography effects are neglected.

- Variations in the magnetic properties of the recording layer which affect the read-back signal.
- Disk space dedicated to servo sectors for control purposes results in less space for storing data.
- Head-position information via the read-back signal is available at discrete events only, i.e., the sampling frequency is limited to the number of servo sectors and disk velocity.

2.6 Current and future technologies

2.6.1 Limitations on perpendicular magnetic recording

The magnetic orientation of a single bit in today's hard disk drives is perpendicular to the disk surface (see section 2.2.2,). This technology is referred to as perpendicular magnetic recording (PMR). Current areal densities of PMR are on the order of 1.24 GBit/mm^2 (800 GBit/in^2) and the maximum achievable areal density is estimated to be 1.55 GBit/mm^2 (1 Tbit/in^2) on a continuous medium [177,178]. This barrier arises from a phenomenon known as the superparamagnetic effect. The super paramagnetic effect commonly refers to a combination of write field limitations and thermal stability requirements of the magnetic grains in the recording layer [22, 179–182].

A key strategy for increasing the areal density is making data tracks narrower and packing them closer together. Thinner data tracks can be achieved by reducing the width of the main pole of the write element and by using side shields. For writing data, however, a certain minimum *write field* is required which in turn dictates the minimum

write head dimensions. This restriction makes it difficult to reduce the track width below 50 nm [178], thus limiting the overall achievable areal density.

Another key strategy for increasing areal density is reducing the bit size. One bit consists of several grains and a reduction in bit size also requires the grain size to be reduced [22]. The *thermal stability* of a single grain is a function of the expression KV/k_BT, where K denotes the anisotropy constant of the magnetic material, V is the grain volume, k_B represents the Boltzmann's constant, and T the absolute temperature [179]. This relation shows that the thermal stability decreases with a decrease in grain volume. It follows that for constant temperature and anisotropy, a certain minimum grain volume is required in order to guarantee thermal stability.

To overcome the areal densities limitations in perpendicular magnetic recording, new approaches are needed. Over the years, many technologies have been proposed and partially realized such as shingled magnetic recording (SMR), two-dimensional magnetic recording (TDMR), bit patterned media (BPM), heat assisted magnetic recording (HAMR), and microwave assisted magnetic recording (MAMR). In terms of maximum achievable areal density, bit patterned media and heat assisted magnetic recording show the greatest potential. In fact, storage densities up to 50-300 Terabit per square inch are theoretically possible from a thermal stability point of view by combining patterned media for storing data with HAMR for writing data [183]. However, while both technologies were demonstrated to work successfully, BPM and HAMR pose major challenges in terms of cost-effectiveness and long-term reliability, respectively [182, 184–186]. From that perspective, SMR and TDMR, which are both technologies that barely require modifications from conventional hard drives, are seen as temporary solutions to further ensure areal density growth until the technologies of BPM and HAMR are fully developed.

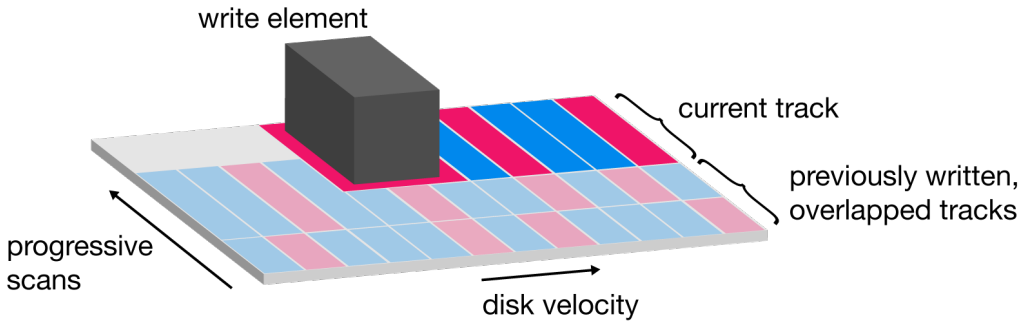

Figure 2.27: In shingled magnetic recording, data tracks are written sequentially and overlapped in order to minimize the spacing in between the data tracks. This increases the overall storage density.

2.6.2 Shingled magnetic recording

In shingled magnetic recording (SMR), higher areal densities are achieved by slightly overlapping neighboring data tracks and thus eliminating the space in between them, similar to shingles on a roof (see Fig. 2.27). To ensure high write fields and large magnetic field gradients in the down-track and off-track direction, corner edge write elements are used [187, 188]. As a new track is written in shingled magnetic recording, the old adjacent track is partially overwritten or 'trimmed'. The information stored in the trimmed data tracks can still be read since the read element is smaller in width compared to the write element.

When updating or rewriting already existing information, however, not only the requested data but also the data in all of the following tracks need to be rewritten. This is because the write element is wider than the trimmed tracks and therefore, overwriting one track will harm the subsequent track. To better deal with the issue of rewriting data, data tracks in shingled magnetic recording are organized in data bands. The shingled track layout is interrupted between the bands, i.e., the bands do not overlap. By organizing the tracks in bands, rewriting data requires at most a rewrite of one band as opposed to re-writing the entire disk.

Seagate was the first hard drive manufacturer to introduce shingled magnetic recording technology in late 2014 [189]. Compared to conventional hard drives, areal densities of singled magnetic recording hard drives are 25 % larger.

2.6.3 Two-dimensional magnetic recording

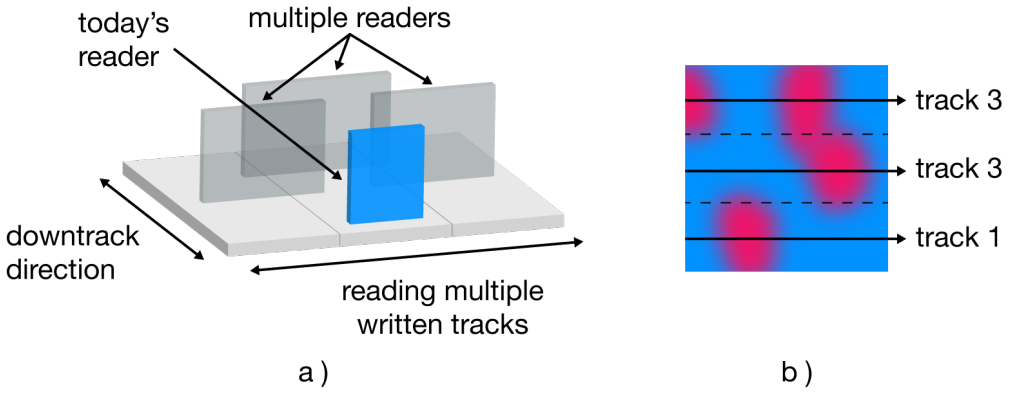

Figure 2.28: Two-dimensional magnetic recording (TDMR) sliders are equipped with multiple read elements, allowing for a complete read-back image of multiple neighboring tracks at once. Combined with advanced signal processing, this technology allows identifying stored in a shingled track layout at extremely small track widths. Schematic b) after [187].

Two-dimensional magnetic recording (TDMR) combines shingled magnetic recording (SMR) with two-dimensional read-back. As discussed in the previous subsection (2.6.2), data tracks in shingled magnetic recording overlap each other and are therefore smaller in width compared to conventional data tracks. As the width of the data tracks becomes smaller than the width of the read element, the read element will pick up more noise from neighboring tracks which negatively affects the signal to noise (SNR) ratio. To counteract this effect, a two-dimensional read-back image of multiple neighboring tracks is created. This is done by either scanning multiple tracks sequentially using a conventional slider or by scanning multiple tracks at once using a TDMR slider [182]. TDMR sliders are sliders that contain two or more read heads arranged in parallel as

shown in Fig 2.28. However, the realization of TDMR technology poses huge challenges from a signal processing point of view because of difficulties related to combining the signals from multiple read channels [187].

By combining shingled writing and two-dimensional read back, areal densities up to 10 Terabits per square inch may be possible [187].

2.6.4 Bit patterned media

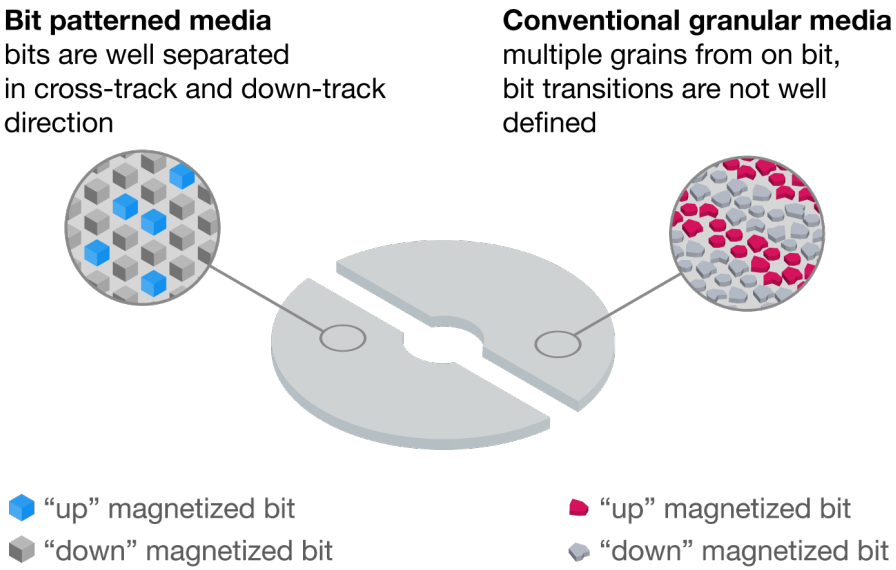

Figure 2.29: Bit patterned media. In bit patterned media (BPM) recording, data is stored in predefined islands compared to conventional magnetic recording where data is stored in randomly organized domains. BPM enables higher recording densities and lower signal to noise ratios.

The fundamental idea of bit patterned media (BPM) is that one bit is represented by a single pre-defined unit or island, as opposed to multiple smaller grains representing one bit as shown in Fig 2.29 [25, 181, 190, 191]. In conventional media, the magnetic layer is continuous and composed of very small, randomly organized single grains as shown in Fig 2.29 a). Several grains form one bit and the transition between the bits is not well defined. In bit patterned media (Fig 2.29 b)), the magnetic recording layer

is composed of well defined, physically isolated islands which are lithographically patterned into a regular array. Since the volume of the individual islands is much larger than the grain volume in conventional media, thermal stability is ensured as larger grains are more resistant towards thermal agitation (as discussed in 2.6.1). Thus, the super paramagnetic limit can be pushed to higher recording densities on patterned media. Another advantage of bit patterned media over conventional media is that the transition from one bit to the next is well defined, which results in reduced transition noise and improved signal-to-noise ratio [190, 192].

There are a number of challenges associated with bit patterned media. The recording performance of bit patterned media is very sensitive towards variations in spacing between the bits and variations in magnetic properties of the bits [25]. Hence, creating a media with well-arranged bits and consistent magnetic properties is of importance. As of today, researchers have been able to produce media with densities up to 5.12 GBit/mm^2 (3.3 Tbit/in^2) [193]. In order to be used in commercial products, practicality and cost-effectiveness of the fabrication process for patterned media is crucial [192].

2.6.5 Energy assisted magnetic recording

Another approach to increase areal density are magnetic materials that possess a very high magnetic anisotropy. As outlined in 2.6.1, thermal stability of the grains in the magnetic recording layer is proportional to the media anisotropy. Hence, high media anisotropy allows for smaller grain sizes while ensuring thermal stability. Materials with high anisotropy usually have a high coercivity, meaning that additional external energy is required for bit reversal [184]. To overcome this issue, heat assisted magnetic recording (HAMR) and microwave assisted magnetic recording (MAMR) have been proposed [184, 194].

In *heat assisted magnetic recording*, the additional energy required for writing

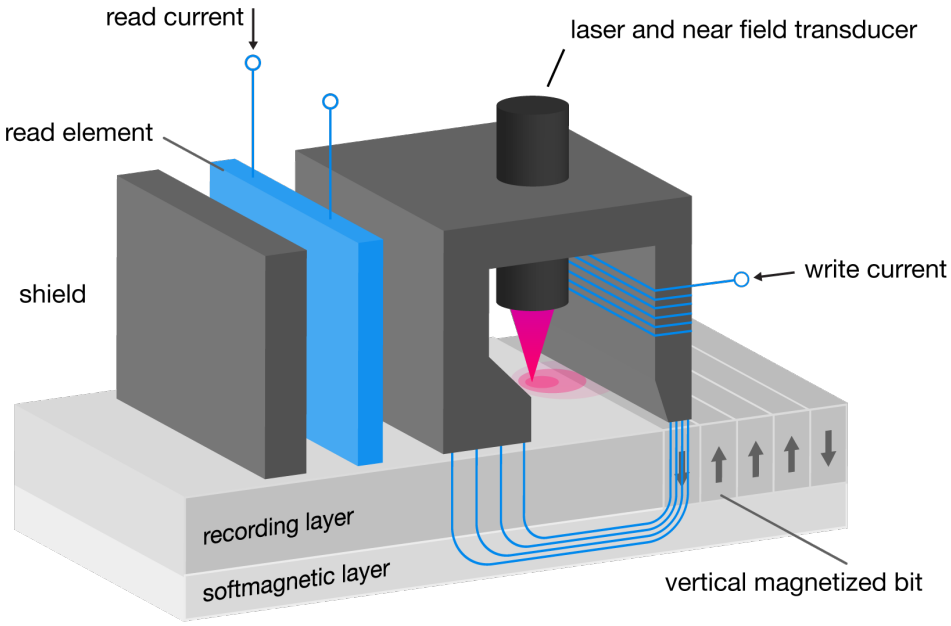

Figure 2.30: In heat-assisted magnetic recording (HAMR), the write process is enabled by temporarily lowering the media anisotropy via laser heating. High-anisotropy media allows for higher areal densities.

is provided by a laser which is integrated in the slider. The main principle behind heat assisted magnetic recording is presented in Fig 2.30. Before writing, the laser is turned on to temporarily lower the media coercivity by locally heating the media to a temperature just below the Curie temperature. Next, the bit is written. As the media cools down quickly after writing, the intended magnetization of the bit is maintained.

A small laser spot size is desired so that neighboring bits are not affected during laser heating. The high temperatures from operating the laser are associated with various challenges at the head-disk interface such as damage of the lubricant [70,184,195], large thermal stresses [184], and damage of the disk surface due to graphitization and oxidation of the disk carbon. [196–198]. As of today, researchers have been able to demonstrate areal densities of 1.55+ GBit/mm^2 (1+ Tbit/in^2) experimentally with longterm reliability remaining a challenge [199].

In *microwave assisted magnetic recording* (see Fig 2.31), a microwave field is

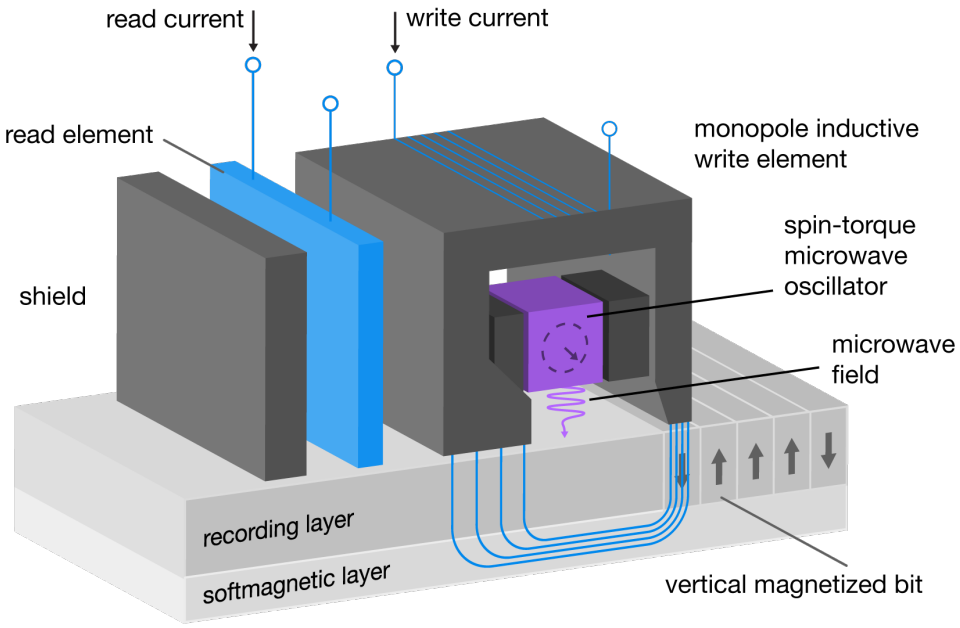

Figure 2.31: In microwave-assisted magnetic recording (MAMR), the write process is enabled by temporarily lowering the media anisotropy via microwaves. High-anisotropy media allows for higher areal densities.

applied so that the magnetization of the grains precesses at ever larger angles, thus temporarily lowering the coercivity of the material or even reversing the magnetic orientation of the bit [200, 201]. The microwave field is generated by a spin tunnel oscillator located in the slider between the read and write element. An advantage of MAMR compared to HAMR is that microwaves do not produce any heat in the head and the media, thus preventing reliability issues as seen in HAMR. So far, the feasibility of microwave assisted magnetic recording has been studied theoretically by several researchers [201, 202]. In 2011, Matsubara et al demonstrated experimentally that microwaves could be generated in the magnetic media using a spin tunnel oscillator [203].

2.7 Organization of the dissertation

This dissertation focuses on the head-disk interface with an emphasis on experimental work. The interface between the recording head and the disk is studied from a tribological and controls point of view. Of special interest are wear on the recording head and interfacial temperature rise upon head-disk contact. Furthermore, novel methods for head-disk proximity detection and control approaches for vertical positing of the recording head are proposed.

Chapter 1 is an introduction to data storage and current trends in the (digital) data storage market. Currently available technologies for data storage are discussed with an emphasis on hard disk drives and solid state drives.

In *chapter 2*, hard disk drive technology is introduced. A strong emphasis is given to tribological and control aspects as these lie within the main scope of this dissertation.

Chapter 3 gives background information with respect to the experimental work carried out in this dissertation. Methodologies for monitoring slider-disk interactions and surface analysis tools are discussed.

In *chapter 4* we investigate contact and interfacial temperature rise upon head-disk contacts of thermal flying height control sliders. The temperature rise during slider-disk contacts is estimated from the resistance change of the read element via auxiliary calibration measurements. The motion of the slider is investigated using laser Doppler vibrometry.

In *chapter 5*, we study wear of recording heads as a function of lubricant properties, temperature and relative humidity. Head wear is determined by measuring the wear induced spacing changes on the recording head by comparing the touch-down power before and after wear testing. After wear testing, selected heads are examined using

scanning electron microscopy and atomic force microscopy measurements to evaluated wear of the write shields and changes in surface roughness.

Chapter 6 discusses the effect of applying a DC bias across the head-disk interface on wear of the recording head. Wear tests are carried out for three different levels in relative humidity. Similar to chapter 5, head-wear is determined by measuring the change in the heater touch-down power before and after wear testing. Atomic force microscope (AFM) and electrostatic force microscope (EFM) measurements of the recording head are taken to identify regions of wear or deposit formation on the slider surface.

Chapter 7 presents a new approach for predicting the touch-down power (i.e., the heater power at which the onset of head-disk contact occurs) of a thermal flying height control slider. Utilizing the contact sensor, head-disk proximity is 'sensed' prior to actual head-disk contact. The transfer function between heater input and sensor output is estimated as a function of head-disk spacing from experimental step-response data using step-realization. Impeding head-disk contact is predicted based on a change in the coefficients of the transfer function

Chapter 8 proposes an algorithm for minimizing low-frequency variations in flying height of thermal flying height control (TFC) sliders. The method utilizes the resistive heater element of a TFC sliders for spacing adjustment and the embedded contact sensor for estimating changes in flying height. Data based modeling is carried out to identify the dynamics of the thermal actuator. The optimal feedforward heater input profile is calculate via convex optimization techniques.

A summary and concluding remarks are given in *chapter 9*.

2.8 Acknowledgement

Chapter 2, in part, is a reprint of the material as it appears in "Head wear of thermal flying height control sliders as a function of bonded-lubricant ratio, temperature and relative humidity", Liane M. Matthes, Ralf Brunner, Bernhard E. Knigge, and Frank E. Talke, *Tribology Letters*, vol. 60, no. 3, p. 39 (2015). The dissertation author was the primary investigator and author of this paper.

Chapter 3

Experimental techniques

As outlined in chapter 2, intermittent contacts between the recording head and the disk are inevitable if the spacing decreases to the order of nanometers. Intermittent contacts are undesirable as they can result in wear and degradation of the head-disk interface. It may hence be of no surprise that numerous publications exist that are concerned with wear of the recording head and how wear is affected by the disk lubricant, changes in environment, and the diamond like carbon (DLC) coatings on both the slider and the disk [35, 49, 54, 204–214]. The durability of recording heads is commonly investigated by deliberately bringing the recording head into contact with the magnetic disk. For this purpose, methodologies for monitoring contact between the recording head and the magnetic disk are needed. After wear testing, the wear induced damage on the recording heads is assessed via surface analysis techniques.

In the following, a brief discussion on methodologies for monitoring of head-disk interactions and common surface roughness analysis techniques is presented.

3.1 Methodologies for monitoring head-disk interactions

With the introduction of thermal flying height control (TFC) sliders (see 2.3.3), it has been of interest to know the heater power at which the onset of slider-disk contact occurs. This heater power is commonly referred to as touch-down power (TDP).

Head-disk contacts need to be detected reliably and on time. That is, no contact event shall be missed and contact needs to be detected at heater powers neither larger nor smaller than the touch-down power. If head-disk contact is detected at heater powers larger than the actual touch-down power, the resulting spacing during reading and writing will be smaller than intended and the likelihood of intermittent head-disk contacts and subsequent damage increases. If head-disk contact is detected at heater powers smaller than actual head-disk contact, the resulting spacing during reading and writing will be larger than intended which results in an increased bit-error rate during reading and writing.

Common methodologies for detecting head-disk interactions involve acoustic emission (AE) sensors, Laser Doppler Vibrometry (LDV), and contact sensors (CS). Whereas contact sensors are embedded in the recording head and thus suitable for in-drive testing, acoustic emission and Laser Doppler Vibrometry need to be employed externally.

3.1.1 Acoustic emission (AE)

On a micro scale, deformation of physical structures causes transient elastic waves inside the structure. These waves are generated by the rapid release of energy from a localized source within the material [215]. To detect elastic waves in physical structures, acoustic emission (AE) sensors are widely used. An AE sensor contains a piezoelectric element that picks up surface movements caused by elastic waves in the

object that the sensor is attached to. The mechanical vibration of the piezoelectric element is then converted into an electric voltage signal according to the principle of piezoelectricity.

AE sensors have been used for studying contacts between the recording head and the magnetic disk for more than two decades [204, 216–218]. AE sensors are typically attached to the suspension or mounted onto the suspension holding tool. Head-disk contacts are detected by monitoring the standard deviation of the acoustic emission sensor. The standard deviation of an acoustic emission sensor is approximately constant in the absence of slider-disk contacts when the slider flies stably but shows a steep rise with the onset of slider-disk contacts.

3.1.2 Thermal contact sensors (TCS)

In recent years, contact sensors have been embedded in thermal flying height (TFC) sliders which allow detection of head-disk contacts and mapping of disk topography or disk defects [219]. The contact sensor is located between the read and write element. A contact sensor is a resistive element which is sensitive to temperature changes. It has been shown that the sensitivity of contact sensors for detecting head-disk contact is similar to that of conventional acoustic emission (AE) sensors [220]. Head-disk contact is usually detected by monitoring the standard deviation of the contact sensor voltage. Similar to acoustic emission sensors, the standard deviation of a contact sensor is approximately constant in the absence of slider-disk contacts when the slider flies stably but increases suddenly with the onset of slider-disk contacts.

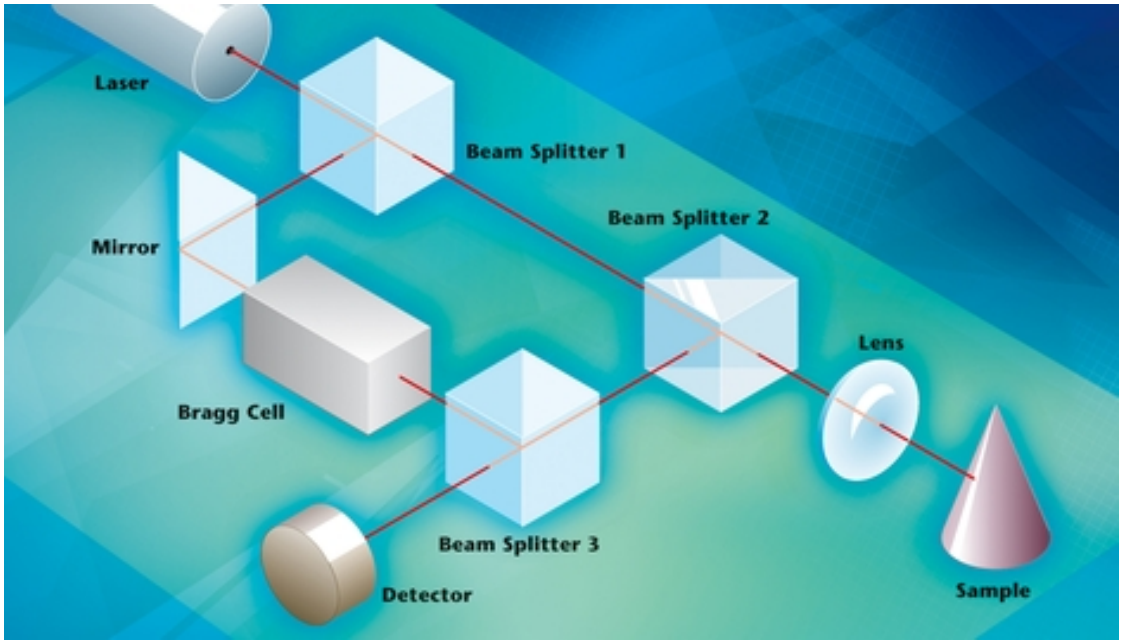

Figure 3.1: Operating principle of laser Dopppler vibrometry (LDV). LDV is a non-contact vibration measurement technique. Measurements are taken by focusing the laser beam of an LDV on the object of interest. The vibration amplitude and frequency are determined based on the Doppler effect and the principles of interferometry. Schematic from [221].

3.1.3 Laser Doppler vibrometry (LDV)

Laser Doppler vibrometry (LDV) is an optical, non-contact measurement technique for determining the velocity of a vibrating object. Measurements are taken by focusing the laser beam of an LDV onto the object of interest as shown in Fig. 3.1. The object reflects or scatters the light from the laser beam. Information about the vibration amplitude and frequency of the object are obtained using the principles of interferometry and the Doppler effect.

The Doppler effect states that monochromatic laser light undergoes a frequency shift as it is backscattered from a vibrating target. The frequency shift as measured by the LDV is

$$f_{Doppler} = 2\frac{v}{\lambda} \tag{3.1}$$

where v is the velocity of the vibrating object and λ is the wavelength of the emitted wave [221].

To determine the velocity of an object, the frequency at which the Doppler shift occurs needs to be known. This is done via laser interferometry inside the LDV by overlapping an internal laser bream with the reflected laser beam that experienced the Doppler shift. The intensity of two overlapping coherent light beams with light intensities I_1 and I_2 is given by

$$I_{total} = I_1 + I_2 + 2 \cdot \sqrt{I_1 I_2} \cdot \cos(2\pi \frac{r_1 - r_2}{\lambda}) \tag{3.2}$$

where r_1 and r_2 denote the path length of the internal beam and the reflected beam, respectively [221]. Equation 3.2 shows that the resulting intensity is the sum of the single intensities I_1 and I_2, plus an interference term which relates to the difference in path length between the two laser beams. Constructive interference occurs if the path length difference is an integer multiple of the wave length *lambda*. If the path length difference is equal to half the wavelength, destructive interference occurs.

As shown in equation 3.1, the output voltage of the LDV is directly proportional to the velocity at which the surface is moving along the direction of the laser beam. The non-contact nature of Laser Doppler Vibrometry is advantageous in a sense that no mass-loading of the object of interest occurs during the measurement (i.e., no sensor needs to be attached). Laser Doppler Vibrometry is capable of measuring displacements less than 1 nm from near DC to several MHz [222].

Laser Doppler Vibrometry has been used for hard-disk drive related experimental investigations since the 1980s [62,154,167,223–227]. For example, Zeng et al. [154] used Laser Doppler Vibrometry to measure flying height modulation of sliders with flying heights less than 10 nm. Pit and Marchon studied lubricant-slider interactions [226]

and Canchi and Bogy [62] investigated slider dynamics using Laser Doppler Vibrometry.

3.2 Surface analysis techniques

Head-disk contacts can result in both slider and disk wear. However, the area of the slider that contacts the disk is much smaller than the wear track on the disk: Assuming a track radius of 20 mm and a contact area of 50 μm^2, the ratio of contact area between the disk and the slider is $2 \cdot 10^4$, suggesting that more wear occurs on the slider compared to the disk. Hence, it is primarily of interest to study wear induced surface changes on the recording head rather than the disk.

Commonly used techniques for high-resolution surface analysis are scanning electron microscopy (SEM) and atomic force microscopy (AFM). Both measurement techniques allow lateral resolution on the nanoscale, with AFM generally being superior [228]. SEM provides a two-dimensional projection of a specimen surface, whereas AFM produces three-dimensional surface profiles. Electrostatic force microscopy is a technique closely related to AFM and capable of distinguishing between conducting and non-conducting regions on a sample. In the following, the principles of atomic force microscopy, electrostatic force microscopy and scanning electron microscopy, will be discussed.

3.2.1 Atomic force microscopy (AFM)

Atomic force microscopy (AFM), or scanning force microscopy (SFM), is a high-resolution surface characterization technique developed in the 1980s [97, 229]. A height profile is gathered by scanning the specimen surface line by line via a cantilever with a sharp probe tip at its end (see Fig. 3.2). The scanning motion is carried out by

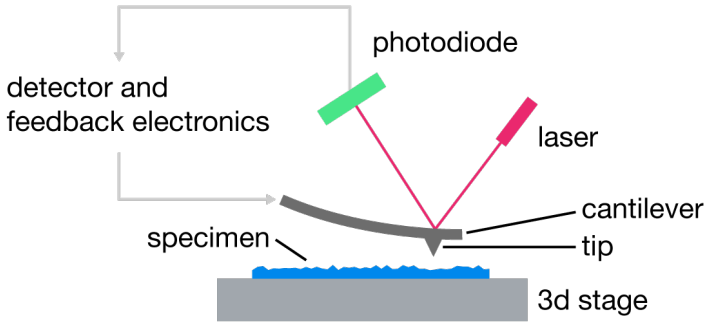

Figure 3.2: Operating principle of an atomic force microscope. A cantilever beam with a sharp tip at its end scans the sample surface at close proximity. Near-range forces (e.g., van der Waals forces) deflect the cantilever towards the sample. The surface topography is determined from the deflection of the cantilever which is measured via a laser and a photodiode.

a piezoelectric tube scanner. The scanner moves either the tip relative to the sample or the sample relative to the tip. Interactions between the surface and the cantilever tip are monitored by focusing a laser on the back of the cantilever and capturing the reflected laser light by an array of photodiodes. The change in the photodetector output is a measure of the cantilever deflection or oscillation amplitude.

The specimen surface can be scanned using contact, tapping or non-contact mode (see Fig. 3.3). In *contact mode*, the cantilever tip is dragged across the sample surface while monitoring the deflection of the cantilever. There are two scanning modes: Constant height and constant force. In constant height mode, the topography image of the sample is created from the cantilever deflection. In constant force mode, the cantilever deflection is kept constant via a feedback loop by moving the scanner up or down. The vertical motion of the scanner is captured to deliver a height image of the specimen surface. In *non-contact mode*, the cantilever beam oscillates close to its resonance frequency up and down along the z-direction (typically several hundred kHz) above the sample surface. As the cantilever tip moves closer towards the sample surface, forces at the interface – such as van der Waals, electrostatic, magnetic or capillary forces – reduce the oscillation amplitude [229]. A feedback loop maintains a constant

oscillation amplitude. By imaging the forces between the tip and sample surface, surface information of the specimen is gathered. *Tapping mode* is similar to non-contact mode, except that the cantilever tip taps the sample surface.

Whereas contact mode delivers the most accurate scanning results, it suffers from tip and sample degradation. Contrary, sample or tip degradation does not occur in non-contact mode, making this technique suitable for studying soft specimens such as biological samples. Tapping mode combines the advantages of both techniques.

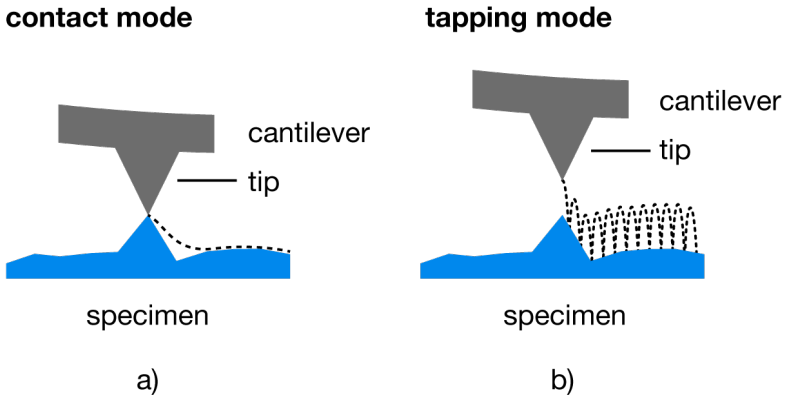

Figure 3.3: Atomic force microscopy (AFM): a) contact mode during which the cantilever tip is dragged across the sample surface, and b) tapping mode during which the cantilever oscillates at a frequency near its resonance frequency while tapping the sample surface. Contact mode is more accurate but also more destructive to the sample surface and/or the tip.

A secondary imaging technique for tapping mode is *phase imaging*. Phase imaging monitors the phase lag between the driving signal for oscillating the tip and the cantilever oscillation output. As the tip touches the sample, the elastic properties of the material and adhesion forces may affect the movement of the tip, causing a phase lag [230–232]. Hence, phase imaging can be used to assess the elastic, adhesive and frictional properties of the specimen. By combining height images with phase images, surface topography and surface properties can be directly correlated.

Using AFM, cantilever deflections up to 0.1 Å can be measured and typical

forces between cantilever tip and specimen surface range from 10^{-11} to 10^{-6} N [229]. Due to scanning artifacts, the acquired surface topography does not always correspond to actual surface features, a fact which needs to be taken in consideration when interpreting AFM results. There are "profile broadening' artifacts due to tip-sample convolutions and 'height lowering' artifacts due to elastic deformation of the specimen.

AFM has been used for hard-disk drive related research for more than two decades [30, 34, 205, 208, 209, 214, 233–237]. Several researchers used AFM to measure wear on the recording head [214, 235]. AFM has also been used to study surface features on the magnetic disk such as laser bumps [34] and disk asperities [235]. Furthermore, surface roughness of magnetic disks has been studied using AFM [209].

3.2.2 Electrostatic force microscopy (EFM)

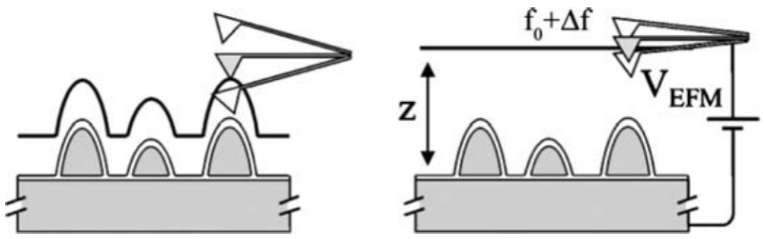

Figure 3.4: Electrostatic force microscopy (EFM) measurements are carried out in a two step measurement procedure. First (left image), the topography is measured using atomic force microscopy (AFM) tapping mode in one scan line. Next (right image), the EFM scan is carried with the tip biased at voltage V_{EFM}. The cantilever oscillates at a controlled distance z away from the sample surface. Schematic from [238].

Electrostatic force microscopy (EFM) is a type of atomic force microscopy (AFM, see 3.2.1) where the electrostatic force between the sample and cantilever tip is probed. EFM makes it possible to identify *conducting regions* on a specimen surface compared to AFM which provides a pure height image.

EFM measurements are typically carried out in a two-step measurements procedure in which each EFM scan line is interleaved between AFM topography scan lines

as indicated in Fig. 3.4 [238]. First, one scan line is measured in AFM tapping mode to obtain information about the topography. Next, the tip is lifted off the sample surface and the scan is repeated at a controlled distance z_0 (e.g., 10 nm). This time the tip is biased at the detection voltage V_{EFM} (e.g., 3 V) while oscillating near its resonance frequency. Two measurement modes are available for measuring the electrostatic force: 1) The cantilever is excited mechanically at a fixed frequency f' and the phase shift $\Delta\phi$ of the cantilever oscillation is recorded as the EFM signal; 2) Alternatively, the phase shift $\Delta\phi$ is kept constant by adjusting the excitation frequency f_0' via a feedback loop. Both measurement modes result in qualitatively similar images [238].

EFM measurements are based on electrostatic force gradients [238]. The basic relation between the cantilever frequency shift Δf and the force gradient $\frac{\delta F(z_0)}{\delta z}$ acting on the tip is given by

$$\frac{\Delta f}{f_0} = -\frac{1}{2k}\frac{\delta F(z_0)}{\delta z} \tag{3.3}$$

where k denotes the cantilever spring constant and f_0 the resonance eigenfrequency [238].

3.2.3 Scanning electron microscopy (SEM)

Scanning electron microscopy (SEM) is a technique used for imaging solid samples using an electron beam. The basic principles of SEM were first established in the 1930s by Knoll and later in the early 1940s by von Ardenne [239]. Surface information is gathered by scanning the specimen surface with a focused beam of electrons. The electrons interact with the atoms in the sample surface, producing various signals that provide information about the surface topography and composition. The type of signals produced are secondary electrons, back-scattered electrons, transmitted elec-

trons, cathodoluminescent light, specimen current and X-rays. Secondary electrons are most commonly used for imaging. On flat surfaces, the emitted secondary electrons are mostly contained by the sample, whereas more electrons are emitted if the surface is tilted. Thus, a topography image of the sample surface can be created by scanning the sample with an electron beam and detecting the emitted secondary electrons.

In SEM, the electron beam is guided to the sample by a series of electromagnetic lenses [228]. The depth of field and resolution of SEM images is determined by the final spot size and the current of the electron beam. The electrons interact with the specimen up to a few micrometers below the surface. Using SEM, lateral resolutions better than 1 nm can be achieved.

The very thin carbon layer on the slider is not visible in SEM images as it is penetrated by the high energy electron beam. Hence, SEM cannot be used to study carbon wear. However, SEM can be used to study wear of the underlying write shield [209, 214, 236, 237, 240]. Furthermore, SEM has been used to study damage of the read element after electrostatic discharge-events or severe slider disk [30].

3.2.4 Discussion

The combination of AFM height images, AFM phase images and EFM phase images allows for in-depth study and comparison of both surface properties and surface profiles. AFM phase provides information regarding the elastic properties of the specimen and EFM phase identifies conducting regions. Combined, these three techniques are excellent tools for studying build-up or depletion of material during wear processes.

Both SEM and AFM provide lateral resolution on the nanometer-scale. As the underlying principles of SEM and AFM are quite different, each method provides different information about the surface structure. SEM provides a two-dimensional projection of a specimen surface with scan sizes up to several mm^2. AFM on the other hand pro-

duces three-dimensional surface profiles with scan sizes up to 150 x 150 μm.

AFM provides higher resolution scans compared to SEM and scans can be taken in ambient or fluid environments. SEM on the other hand requires a vacuum environment during scanning. Image acquisition in AFM, however, is much slower compared to SEM. Slow scanning speeds become problematic if the sample or sample mount undergo thermal drifting. Furthermore, the piezoelectric tube scanner suffers from nonlinearities, hysteresis, creep and cross-talk between the x, y and z directions. The resolution of AFM in tapping mode is determined by the oscillation frequency of the cantilever, the scan speed and the scan size, and the tip radius. Accurate imaging requires the radius of the cantilever tip to be smaller than the radius of the features to be scanned. Contaminated tips result in scan artifacts and the cantilever tip has difficulties following steep walls.

SEM produces images in almost real-time. However, charging artifacts might affect the final image and very thin surface coatings are not 'visible' in SEM images as they are penetrated by the high energy electron beam of the SEM. Thus, DLC wear on the slider surface cannot be studied using SEM.

Chapter 4

Contact and temperature rise of thermal flying height control sliders

The flying height in hard disk drives (HDDs) has decreased to only a few nanometers and intermittent contacts between slider and disk are likely to occur. Currently, the head-disk spacing in commercially available HDDs is on the order of 2 nm during read and write operation [220]. To achieve an areal density of 5–10 Terabit per square inch, a physical spacing on the order of 0.25 nm is required [241]. Intermittent contact between slider and disk could result in wear, frictional heating, read/write element degradation or lubricant interactions at the head-disk interface (HDI). Furthermore, local temperature rise exceeding the Curie temperature due to frictional heating might result in the erasure of magnetic information and are therefore of concern [146]. The temperature rise during contact is of very short duration and generally referred to the term flash temperature [242]. In numerical studies, flash temperatures on the order of 1,000 K have been simulated [243, 244].

Since the resistance of the read and write element is temperature dependent, frictional heating due to slider-disk contact causes a change in the resistance of the read

and write element as well. The read element is a very sensitive sensor and has also been used for the detection of slider/disk contacts [64, 67, 245]. Hence, the question is raised, can local temperature rises due to slider-disk contact be estimated by measuring the change in read element resistance?

As discussed in 2.3.3, thermal flying height control (TFC) sliders have been implemented in commercial HDDs since 2007 [88]. TFC sliders contain a heater element close to the read and write element in the trailing edge of the slider. Energizing the heater element causes a thermal deformation of the bottom surface of the slider, thereby reducing the flying height between the read and write element and the disk. TFC sliders have allowed a reduction of the head- disk spacing to the order of several nanometers.

In the present study, we investigate contact between a commercially available TFC slider and a magnetic disk. To achieve contact, the heater element of the TFC slider is energized with constant and square wave input profiles with increasing bias. Laser Doppler vibrometry is used to study the dynamics of the vertical gimbal velocity. The temperature rise during slider-disk contact is estimated from the resistance change at the read element using auxiliary calibration measurements.

4.1 Experimental set-up and procedure

A schematic of the experimental set-up used in this investigation is shown in Fig. 4.1. The set-up consists of a commercially available HDD with a cutout in the top cover, a 3D laser Doppler vibrometer (3-D LDV) and an oscilloscope for high-speed data acquisition. A printed pre-amp circuit board was designed and built to access the read, write and heater element. To measure the respective resistance values, the write element was biased with a current of 20 mA, whereas the read element was biased with a voltage of 100 mV. The input to the heater of the TFC slider was generated

using a dynamic signal generator. To monitor the resistance of the heater, the voltage over a known resistance in series with the heater element was measured as indicated in Fig. 4.1. For the investigation of the vertical gimbal vibrations and the resistance change at the read and write element, constant and square wave voltage profiles were applied to the heater. The resistance changes of the read and write element as a function of heater power were measured along with the vertical gimbal velocity using an LDV. In addition, the resistance change of the read element was measured for the following three cases: a) the slider was removed from the disk, b) the slider was loaded on the stationary disk and c) the slider was flying over the disk. To estimate the temperature rise during contact, auxiliary resistance calibration measurements were carried out in a temperature-controlled environment.

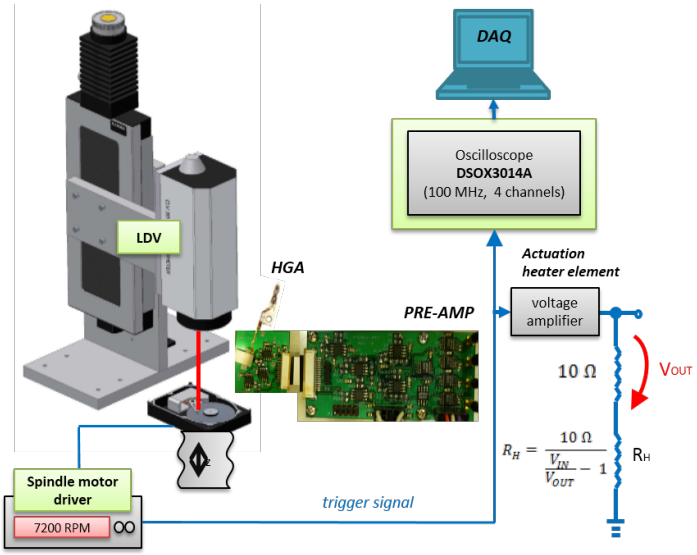

Figure 4.1: Experimental set-up.

4.2 Experimental results

4.2.1 Contact for constant and square wave heater input profiles

Contact for constant heater input profile

A constant voltage input profile was applied to the heater element of a TFC slider and increased in small increments. The results for a power input to the heater of 0 mW (1st column), 82 mW (2nd column), 103 mW (3rd column) and 126 mW (last column) are depicted in Fig. 4.2. The first and second row of Fig. 4.2 show the resistance of the write and read element, respectively, as a function of power input to the heater. Figure 4.2 c) shows the change in the amplitude spectrum of the read element resistance |Y|, obtained by subtracting the spectrum observed at zero heater power $|Y_0|$. The frequency spectrum of the write element is not shown since no significant changes were observed with increasing heater input. The vertical gimbal velocity is depicted in Fig. 4.2 d) and the last row, Fig. 4.2 e), shows the change in the amplitude spectrum of the vertical gimbal velocity after subtracting the spectrum for the heater input of 0 mW.

We observe from Fig. 4.2 a) and b) that the write and read element resistance increases with increasing power input to the heater. Furthermore, we observe that the standard deviation of the read element resistance increases with increasing heater power (Fig. 4.2 b)). Figure 4.2 c) shows that the spectrum of the read element resistance does not exhibit any isolated resonance frequencies for a power input to the heater of 0 and 82 mW, while a well-defined frequency peak at 144 kHz is present for a heater input of 103 and 126 mW, respectively. Looking at the frequency spectrum of the vertical gimbal velocity in Fig. 2e, we observe that frequencies in the 144 kHz range are also absent for a heater power of 0 and 82 mW, while a well-defined peak is present in the frequency spectrum at 144 kHz for a heater power of 103 and 126 mW. It is apparent that the slider is vibrating and that contacts between slider and disk occurs. The amplitude of

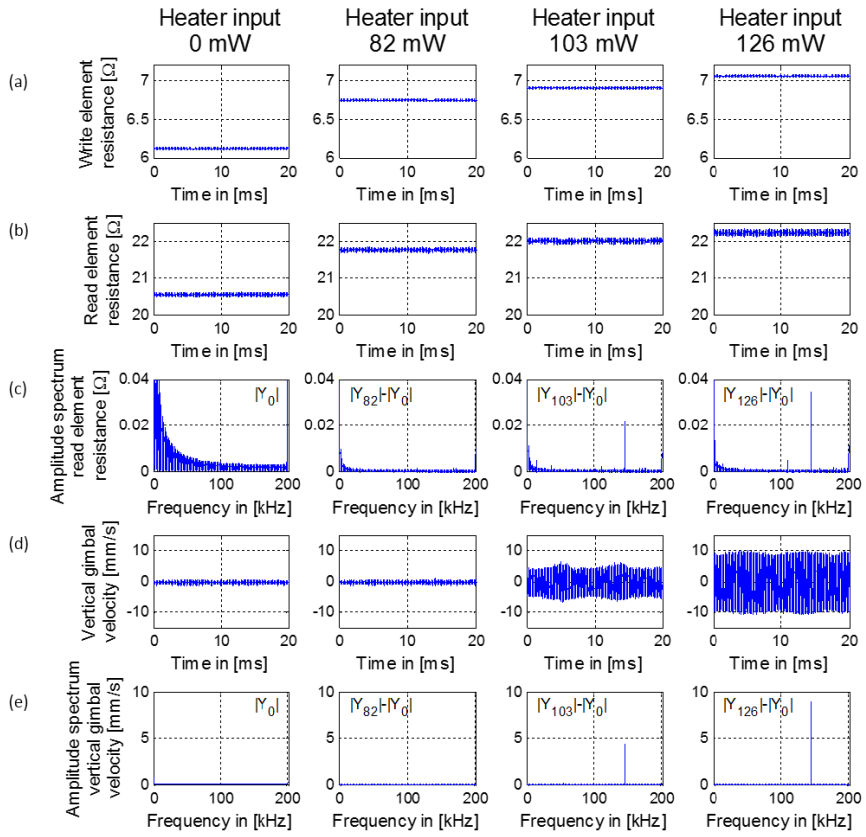

Figure 4.2: a) Write element resistance, b) read element resistance, c) change in frequency spectrum of the read element resistance after subtracting the resistance spectrum $|Y_0|$ at 0 mW, d) vertical gimbal velocity and e) change in frequency spectrum of the vertical gimbal velocity after subtracting the spectrum $|Y_0|$ at 0 mW for a constant heater input of 0 mW (1st column), 82 mW (2nd column), 103 mW (3rd column) and 126 mW (last column).

the read element resistance and the vertical gimbal velocity at 144 kHz are summarized as a function of heater power in Fig. 4.3. We observe from Fig. 4.3 that the read element resistance increases at the same heater power (102 mW) at which a strong increase in the amplitude of the vertical gimbal velocity is observed (102 mW). It is likely that the occurrence of a peak in the spectrum of the vertical gimbal velocity is related to contacts between slider and disk. A frequency of 144 kHz could correspond to the first pitch mode frequency of the air bearing of the slider or to higher order gimbal vibrations. The observation that the read element resistance and the vertical gimbal velocity are

correlated suggests that the resistance change is related to contacts between slider and disk. Clearly, if the slider makes contact with the disk, frictional heating is expected to occur which would result in an increase in resistance.

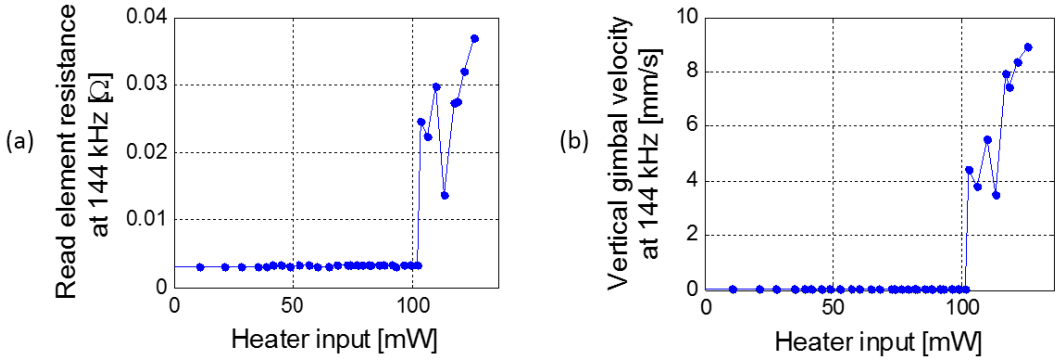

Figure 4.3: Amplitude of the read element resistance and vertical gimbal velocity at 144 kHz as a function of power in put to the heater for a constant heater input profile.

Contact for square wave heater input profile

In a second experiment, a square wave voltage profile with a step size of 1 V was applied to the heater element and the bias voltage was increased in small increments. The results for a mean power input to the heater of 5 mW (1st column), 83 mW (2nd column), 104 mW (3rd column) and 125 mW (last column), respectively, are depicted in Fig. 4.4. The first and second row of Fig. 4.4 show the resistance of the write and read element, respectively, as a function of power input to the heater. Figure 4.4 c) shows the change in amplitude spectrum of the read element resistance obtained by subtracting the spectrum at 5 mW heater power, denoted as |Y0|. The vertical gimbal velocity is depicted in Fig. 4.4 d). Figure 4.4 e) shows the change in the amplitude spectrum of the vertical gimbal velocity after subtracting the spectrum for a heater input of 5 mW. In the last row, Fig. 4.4 f), the time frequency plot of the vertical gimbal velocity is shown.

Similar to the experiment with constant heater input, we observe an increase in the write and read element resistance with increasing power input to the heater (Fig. 4.4

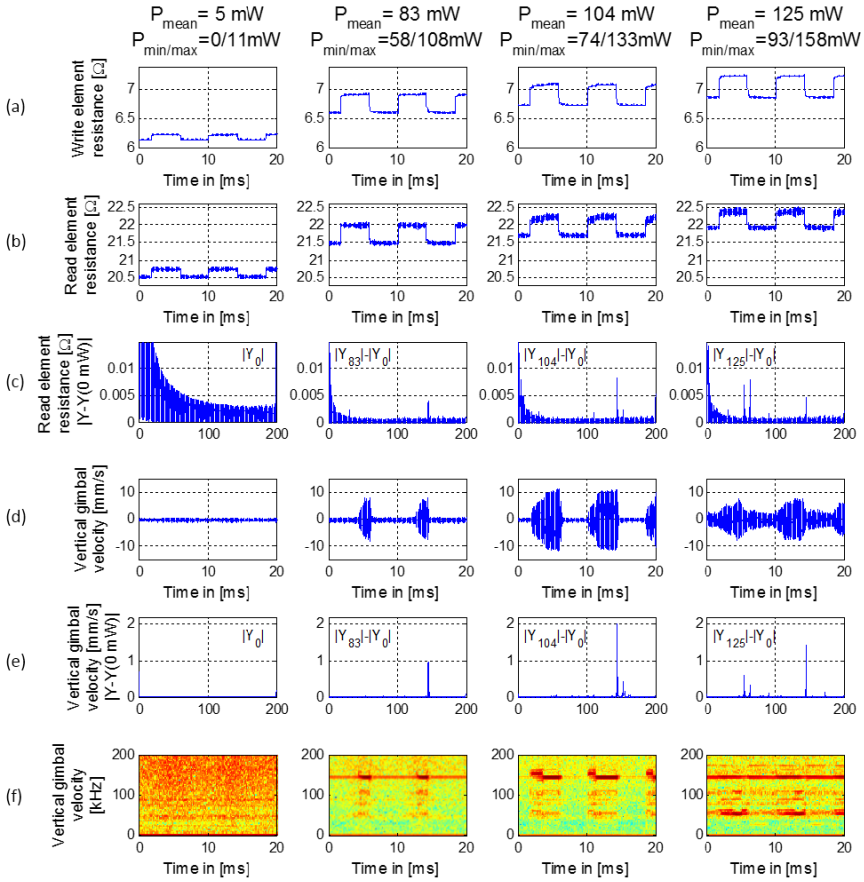

Figure 4.4: a) Write element resistance, b) read element resistance, c) change in frequency spectrum of the read element resistance after subtracting the resistance spectrum $|Y_0|$ at 5 mW, d) vertical gimbal velocity, e) change in frequency spectrum of the vertical gimbal velocity after subtracting the spectrum $|Y_0|$ at 5 mW, and f) time frequency plot of the gimbal velocity for a square wave heater input of 5 mW (1st column), 83 mW (2nd column), 104 mW (3rd column) and 125 mW (last column).

a), b). Also, the standard deviation of the read element resistance increases with increasing heater input (Fig. 4.4 b). In Fig. 4.4 c) we see that frequency peaks are absent for a heater input of 5 mW, while a well-defined frequency peak at 144 kHz occurs in the spectrum of the read element resistance for a heater power of 83 mW or higher. From Fig. 4.4 e) we observe that the same frequency at 144 kHz is also present in the frequency spectrum of the vertical gimbal velocity. For a heater input of 104 mW, the gimbal is excited at both 144 and 155 kHz, which can be seen in the third column of

Fig. 4.4 e). Looking at the time-frequency plot of the vertical gimbal velocity for a mean heater power of 104 mW (Fig. 4.4 f), we see that the gimbal is first excited at 155 kHz and then at 144 kHz. It can be seen in Fig. 4.4 d) that the amplitude of vibrations at 144 kHz is larger than the amplitude of vibrations at 155 kHz. For a heater input of 104 mW, we observe from Fig. 4.4 a), b) that stronger vibrations of the gimbal correlate with an increase in the resistance of the write and read element resistance, respectively. Frequencies of 144 and 155 kHz can also be seen in the spectrum of the read element resistance as shown in Fig. 4.4 c). If the heater input is increased to 125 mW, vertical gimbal vibrations at 55, 63 and 144 kHz are observed (last picture of Fig. 4.4 e), f). All three frequencies can also be seen in the frequency spectrum of the read element resistance as depicted in Fig. 4.4 c).

The amplitudes of the frequencies at 54, 63, 144 and 155 kHz as a function of power input to the heater are shown in Fig. 4.5. The first row shows the amplitudes spectrum of the read element resistance while the second row shows the amplitude spectrum of the vertical gimbal velocity. We observe from Fig. 4.5 a), b) that frequencies at 54 and 63 kHz occur in the read element resistance if the mean power input to the heater exceeds 122 mW. Figure 5c shows that a frequency at 144 kHz appears in the amplitude spectrum of the read element resistance for a heater power larger than 79 mW. This frequency decreases in amplitude for a heater input above 113 mW. From Fig. 4.5 d) we observe that a new peak at 155 kHz appears in the resistance of the read head for a mean heater power between 79 and 122 mW. The second row of Fig. 4.5 shows that the same frequencies occur in the LDV measurement of the vertical gimbal velocity for the same range of heater power as observed for the read head resistance. Again, this correlation of frequencies in the resistance and velocity spectrum leads us to the conjecture that the increase of the read head resistance is related to frictional heating due to slider-disk contact.

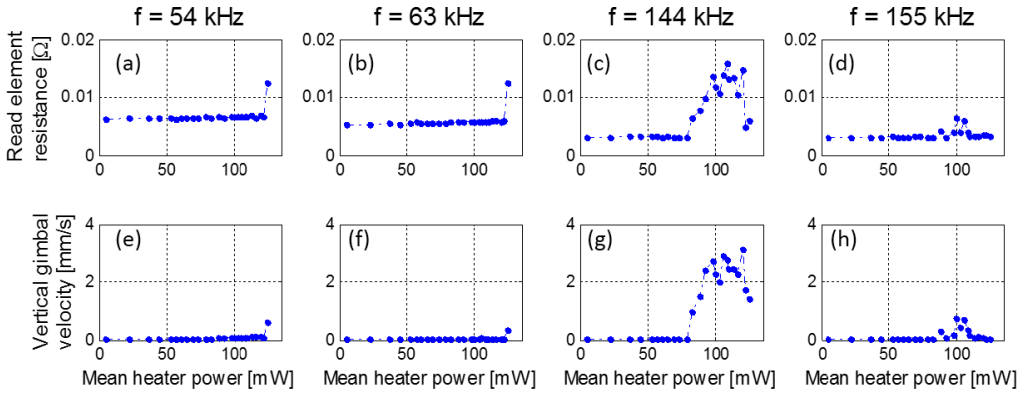

Figure 4.5: Amplitude of frequencies at 55, 63, 144 and 155 kHz as a function of heater power for a square wave heater input profile.

4.2.2 Temperature calibration measurement

Figure 6 shows the resistance change of the read and write element as a function of temperature. The resistance changes are normalized by the initial resistance of 20.9 Ω for the read element and 6.1 Ω for the write element, respectively, measured at 25 °C room temperature.

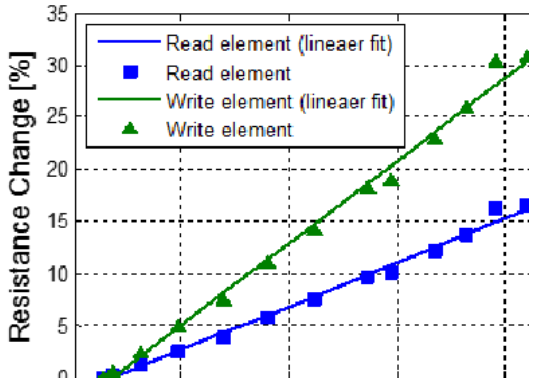

Figure 4.6: Resistance change of the read and write element as a function of temperature.

We observe from Fig. 4.6, that a linear relationship exists between resistance change and temperature for both the read and write element. Furthermore, we observe that the resistance change in percent is larger for the write element than the read element. This is related to the different material properties of the read and write elements.

4.2.3 Read element resistance and temperature rise for unloaded, loaded and flying slider

Prior to determining the temperature rise at the read element from resistance measurements, we have studied the resistance change of the read element as a function of heater power for the following three cases: a) the slider is removed from the disk, b) the slider is loaded on a stationary disk and c) the slider is flying over the disk. The results for these resistance measurements are shown in Fig. 4.7.

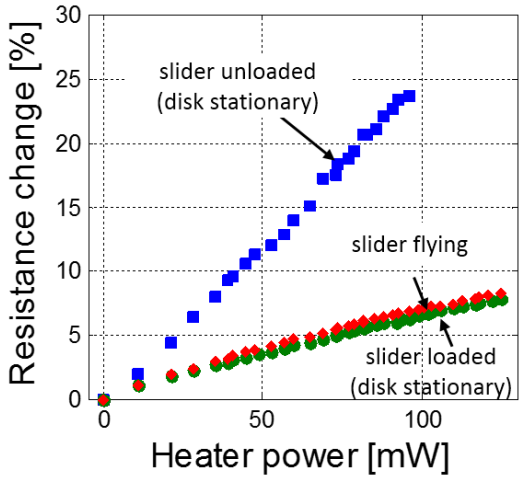

Figure 4.7: Resistance change of the read element as a function of heater power for a) unloaded slider, b) loaded slider on a stationary disk and c) flying slider.

From Fig. 4.7 we observe that the resistance change in percent is largest for the unloaded slider case, when the slider is removed from the disk. The resistance of the read element increases nearly linearly as a function of heater power. If the slider is loaded against the stationary disk or is flying over the rotating disk, the resistance increase is substantially less than for the unloaded case. If the slider is removed from the disk (unloaded case), a major part of the heat generated by the heater element is conducted through the slider body to the read element. This temperature increase results in a resistance increase of the read element. If the slider is in contact with the stationary

disk or flies over the disk, the slider is cooled by the disk or the air bearing, respectively. Thus, the resistance increase of the flying slider is smaller than for the unloaded slider. From the results of Fig. 4.7 we conclude that the cooling effect due to the air bearing and due to heat conduction into the disk is on the same order. Figure 8 shows the estimated temperature change of the read element for the unloaded, loaded and flying slider case. The temperature change of the read element was obtained by dividing the normalized resistance change measurements shown in Fig. 4.7 by the results from Fig. 4.6. As shown in Fig. 4.8, the temperature increases 115 K at the read element for the unloaded case if the heater is energized to 95 mW. If the slider is loaded onto the stationary disk, the disk acts as a heat sink and the temperature increases only about 38 K. During flying, the slider is cooled by the air bearing and the resistance of the read element increases by 39 K.

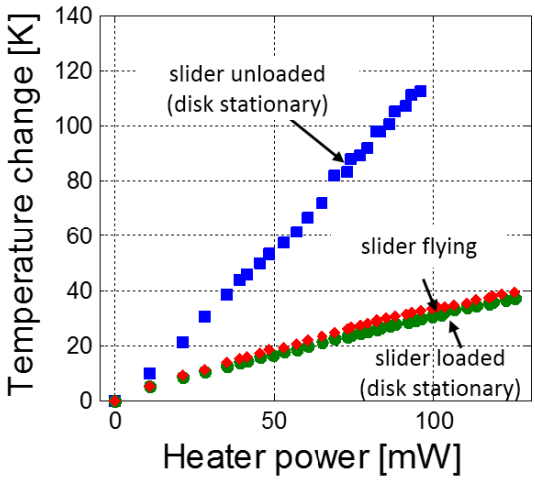

Figure 4.8: Temperature change of the read element as a function of heater power for a) unloaded slider, b) loaded slider on a stationary disk and c) flying slider.

4.2.4 Temperature rise for a constant and a square wave heater input profile

Temperature increase for a constant heater input profile

In Fig. 4.9, the maximum temperature rise at the read element during stable flying conditions is plotted as a function of heater power for a constant heater input profile.

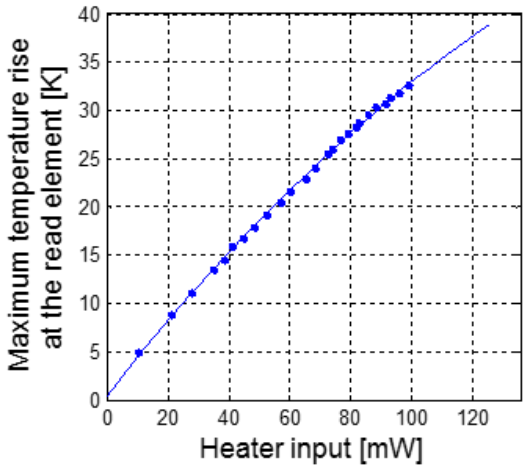

Figure 4.9: Estimated temperature at the read element as a function of heater power when the slider was flying stably.

As presented earlier, at a heater power below 99 mW, the slider was flying stably, i.e., the temperature increase at the read element was entirely caused by heat dissipation due to energizing the heater. At heater powers above 99 mW, an increase in the LDV measurement of the vertical gimbal velocity was detected, i.e., the slider was contacting the disk. If the slider makes contact with the disk, the temperature increase at the read element is caused not only by energy dissipated in the heater, but also by frictional heating during slider-disk contact. In order to estimate the temperature increase due to frictional heating during slider-disk contacts, we proceeded as follows: We first extrapolated the temperature increase from the stable flying region to the unstable flying region (P [99

mW) using a second order polynomial curve fit. The temperature increase obtained using this procedure can be assumed to correspond to the temperature increase caused by heat dissipation from the heater only. We then compared the extrapolated temperature increase to the actual measured temperatures that were obtained when the slider was contacting the disk, i.e., when heat dissipation and frictional heating effects were present. The difference between the extrapolated curve and the actual measurements represents an estimate of the temperature increase due to frictional heating (Fig. 4.10). From Fig. 4.10 we observe that the temperature increase due to frictional heating that is measured by the read element is only on the order of 1 or 2 K. In other words, the temperatures measured by the read element are only slightly larger than the extrapolated temperature increase without slider-disk contact. Therefore, we conclude that the temperature change at the read element is mainly caused by Joule heating due to the heater element and not by frictional heating. Clearly, flash temperatures are not measurable using the resistance change of the read element.

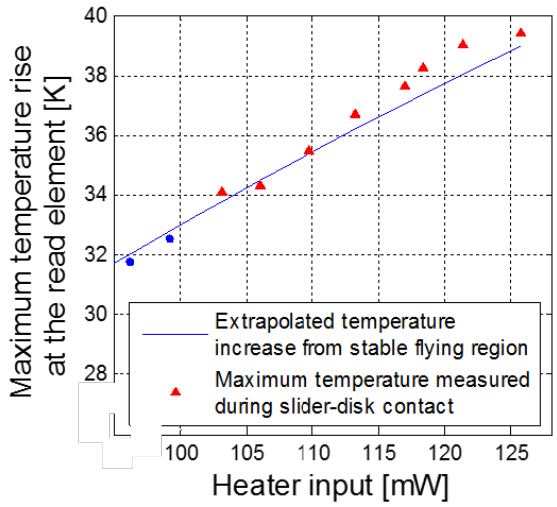

Figure 4.10: Maximum temperatures measured during slider-disk contact and extrapolated temperature increase from the stable flying region below 103 mW to the unstable flying region above 99 mW for a constant heater input profile.

Temperature increase for a square wave heater input profile

The same procedure as the previous section for estimating the temperature increase due to frictional heating was applied to the experiments with the square wave heater input profile (Fig. 4.11). From Fig. 4.11 we observe that the temperature increase at the read element due to frictional heating during slider-disk contacts is, again, only one or two degrees Kelvin. This value is far below the expected flash temperatures that occur during slider-disk contacts. Thus, we conclude again that flash temperatures cannot be obtained from the resistance change at the read element.

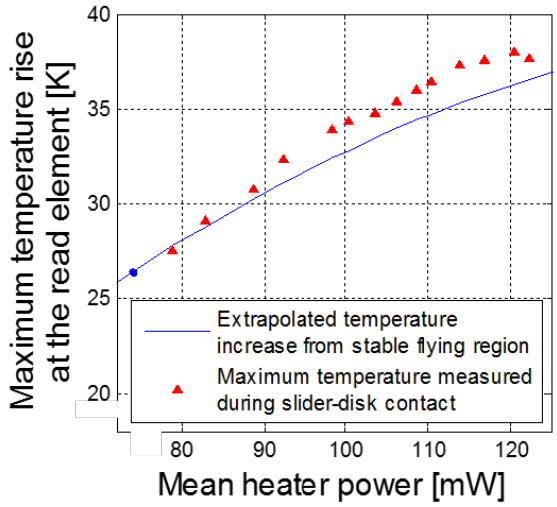

Figure 4.11: Maximum temperatures measured during slider-disk contact and extrapolated temperature increase from the stable flying region below 74 mW to the unstable flying region above 74 mW for a square wave heater input profile.

4.3 Discussion

Comparing Figs. 3 and 5, we observe that the gimbal is excited at only one frequency in the case of a constant heater input profile while additional frequencies are excited for a square wave heater input profile. In particular, we observe that the gimbal is excited at 144 kHz for a constant heater input profile if the power input to the heater

exceeds a critical level. On the other hand, for a square wave input profile the gimbal exhibits vibrations at 54, 63, 144 and 155 kHz. In addition, we observe from Fig. 4.3 and Fig. 4.5 that the critical heater power that results in vertical gimbal vibrations at 144 kHz is smaller for a square wave profile than for a constant heater input. This is apparently related to the time dependent changes in the heater power input. Further investigations of this effect are desirable since time-dependent heater input power changes will be needed for active flying height control of TFC sliders [93].

In our experiments, we did not observe a sharp resistance increase at the read or write element that could indicate the occurrence of flash temperatures. There are several reasons why flash temperatures could not be observed experimentally using the resistance change of the read or the write element. First, at high disk speeds, flash temperatures occur only for very short time duration on the order of nano-seconds. The detecting of very short temperature spikes is limited by the sampling frequency at which the data was acquired. In our experiments, data was acquired at 400 kHz which corresponds to a time resolution of 2.5 μs. Clearly, this sampling rate is too low to capture a short temperature rise in the nano second range. To capture flash temperatures, sampling frequencies on the order of GHz are required. Secondly, it is apparent that flash temperatures occur at the peaks of contacting asperities. Thus, the area over which flash temperatures are present is very small [246]. If the read element is not exactly at the position where contact occurs, the read element 'sees' a smaller increase in temperature compared to the temperature rise at the contact spot. Thus, in addition to the time resolution issue there is a spatial resolution issue related to the spatial separation between the read element and the location of contact.

An approximate expression for the temperature decay over time and space for an instantaneous heat source was presented by Carslaw and Jaeger (1947) who treated the case of a finite amount of heat Q being liberated over a vanishingly small volume at

position (x', y', z') at time $t = 0$. They showed that the temperature T as a function of time t and distance r to the heat source can be expressed as

$$T(r,t) = \frac{Q}{8(\pi\kappa t)^{3/2}} e^{-\frac{r^2}{4\kappa t}} \tag{4.1}$$

where λ is defined as

$$\lambda = \frac{k}{\rho c} \tag{4.2}$$

with k representing the thermal conductivity, ρ the density and c the specific heat of the substrate. It can be seen from equation 4.1 that the temperature decays quickly with time and distance from the heat source.

Thus, the resistance change at the read element cannot be used for estimating the interfacial temperature rise if the contact spot is not exactly at the position of the read element or for sampling rates below the GHz range. Furthermore, the volume of the contacting asperities at which flash temperatures occur is likely to be much smaller compared to the volume of the read element. Therefore, the thermal energy that is generated when flash temperatures occur is most likely too small to cause a sufficiently large response of the read element.

4.4 Conclusion

Experiments have been performed to investigate contacts and temperature changes between a TFC slider and a magnetic disk. To achieve contacts, the heater element of a TFC slider was energized with constant and square wave input profiles with increasing bias. To estimate the temperature rise during contacts, auxiliary resistance calibration measurements were carried out in a temperature controlled environment. Using this relationship we estimated the temperature rise at the read and write element as a function

of heater power. We conclude that:

- Slider disk contacts and vertical gimbal vibrations are detected by LDV measurements if the heater input exceeds a critical level.

- For a square wave heater input profile, gimbal vibrations at 144 kHz were observed for a smaller heater power compared to a constant heater input profile; furthermore, it was found that additional frequencies were excited compared to the experiment with a constant heater input profile.

- The resistance of the read and write element increases as a function of temperature. The temperature rise at the read element is mainly caused by power dissipation in the heater of the TFC slider.

- The resistance change at the read element cannot be used to estimate the interfacial temperature rise due to frictional heating during contact due to limited time response of the read element and the spatial separation between the contact spot and the read element. In addition, the thermal energy at contacting asperities is too small to cause a sufficiently strong response of the read element.

4.5 Acknowledgement

Chapter 4, in part, is a reprint of the material as it appears in "Contact and temperature rise of thermal flying height control sliders in hard disk drives", Liane M. Matthes, Uwe Boettcher, Raymond A. de Callafon, Bernhard E. Knigge, Frank E. Talke, *Microsystem Technologies*, vol. 18, no. 9-10, pp. 1693-1701 (2012). The dissertation author was the primary investigator and author of this investigation.

Chapter 5

Effect of bonded lubricant ratio, temperature and relative humidity on head wear of thermal flying height control sliders

Thermal flying height control (TFC) sliders are presently used in hard disk drives to control the spacing between the slider and the disk. As discussed in 2.3.3, actuating the heater element of a TFC slider locally protrudes the bottom surface of the slider towards the disk at the location of the read and write element. Using this technology, flying heights of 1–2 nm are realized during reading and writing which are needed to guarantee a low bit error rate. However, at such low spacings, intermittent contacts between the head and the disk are likely to occur. Head-disk contacts are undesired as they can result in both wear of the slider and wear of the disk.

In this chapter, head wear of thermal flying height control sliders is studied experimentally by (a) comparing the touch-down power before and after a wear test

consisting of 300 consecutive touch-down cycles, (b) examining scanning electron microscopy (SEM) images, and (c) investigating atomic force microscopy (AFM) measurements of unworn and worn heads. The effect of bonded lubricant ratio, relative humidity, temperature, and heater power on head wear is investigated. The experiments were carried out on a commercial load/unload tester inside an environmental test chamber. A detailed discussion of the head-disk interface including the DLC coating and the lubricant on the disk is given in sections 2.3.2 and 2.3.2, respectively. In the following, a brief overview on head wear will be given.

5.1 Head wear and the role of disk lubrication

During contact between the slider and disk lubricant, adhesion forces are present and shearing of the lubricant film occurs [61, 247]. It has been suggested that adhesion is dominated by meniscus forces arising from lubricant bridges between slider and disk [247]. Occasional contacts between slider and disk can result in elastic and/or plastic deformation and the generation of wear particles. In the event of un-lubricated sliding, high temperatures might develop from frictional heating. Li et al. [240] studied head wear for different contact states and reported that head wear is absent if the slider is in contact with the lubricant and that head wear occurs if the slider is in occasional contact with disk asperities or during continuous slider-disk contact. Contact between TFC sliders and so-called thermal disk asperities that are several nm in height can result in slider wear and high local temperature rise [213, 237, 248, 249]. Singh et al. [234] proposed a wear-in-pad approach for minimal head-media separation by wearing off the overcoat and recession of the recording head in a controlled fashion.

The area of the slider that contacts the disk is much smaller than the area of the wear track on the disk. Assuming a protrusion radius of 2.5 μm and a track radius of

25 mm, the ratio of the apparent contact area between the wear track area on the disk and the slider is 10^4. Consequently, the wear depth on the slider is expected to be much larger compared to the wear depth on the disk.

Several researchers studied head wear by comparing the change in touch-down power before and after wear testing [214, 250]. Wang et al. [214] performed a sequence of 1-min wear tests with constant heater power while measuring the touch-down power on an adjacent track every minute. Kobayashi et al. [250] studied the effect of lubricant molecular weight on head wear. Their wear test was composed of four 10 min tests on separate disk radii with different levels of constant heater power. Although TFC sliders are now in common use, few results have been published on the effect of bonded lubricant ratio and environmental conditions on head wear. TFC sliders allow the measurement of changes in the head-disk spacing by determining the change in touch-down power before and after a wear test. Scanning electron microscopy (SEM) and atomic force microscopy (AFM) measurements are important tools to correlate the measured changes in head-disk spacing with actual wear on the recording head.

5.2 Experiments

5.2.1 Experimental set-up

A commercially available load/unload tester was used for the head wear study. The load/unload tester was placed inside an environmental test chamber to control relative humidity and temperature (see Fig. 5.1). The disk rotated at 5400 rotations per minute (rpm), and head-disk contact was detected in real time using an acoustic emission (AE) sensor.

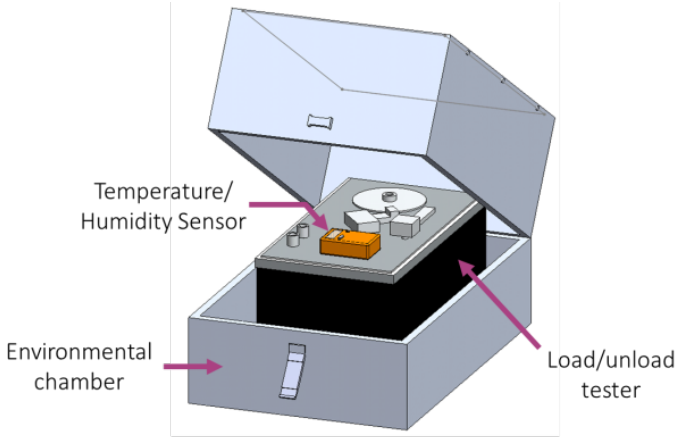

Figure 5.1: Experimental set-up with load/unload tester and environmental test chamber.

5.2.2 Disks and slider

Two specially made sets of disks were used for the experiments. Set 1 was coated with a 1.6 nm thick layer of amorphous nitrogenated carbon (a-CN_x) and used to study the effect of bonded lubricant ratio on head wear. Set 2 was coated with a 1.9 nm thick layer of a-CN_x and used to investigate the effect of relative humidity and temperature. Both sets were covered with a 1.2 nm thick layer of Z-tetraol. The lubricant was applied by dip coating the disks and exposing the lubricants to UV light. The disks were evaluated about two weeks after UV exposure, i.e., the touch-down power was measured and wear testing was performed. A commercially available 'femto' slider [131] was used for this study. An image of the air bearing surface of the slider is presented in Fig. 2.9. The read and write shields consist of nickel cobalt iron (NiCoFe), and the material surrounding the shields is Al_2O_3. The bottom surface of the slider was coated with a 20-30 Åthin carbon film deposited by filtered cathodic arc (FCA) deposition.

5.2.3 Experimental procedure

To investigate head wear, the following procedure was used (see Fig. 5.2). First, the head was positioned on track A and the average touch-down power TDP_{before} was measured. In step 2, the head was moved to a neighboring track, track B, on which the wear test was performed. The wear test consisted of 300 consecutive touch-down cycles. For each touch-down cycle, the heater input was gradually increased in steps of 1 mW per disk revolution until head-disk contact was detected as shown in Fig. 5.3. Once touch- down was detected, the heater input was further increased in steps of 1 mW per disk revolution until a specific additional heater power (AHP), or 'over-push power', was reached. The time duration between each touch-down cycle was 300 ms, and the heater input during this time period was 0 mW. Finally, in step 3, the head was moved back to track A, and the average touch-down power TDP_{after} was measured.

We then computed the change in touch down-power ΔTDP before and after 300 consecutive touch-down cycles, which is defined as

$$\Delta TDP = TDP_{after} - TDP_{before} \tag{5.1}$$

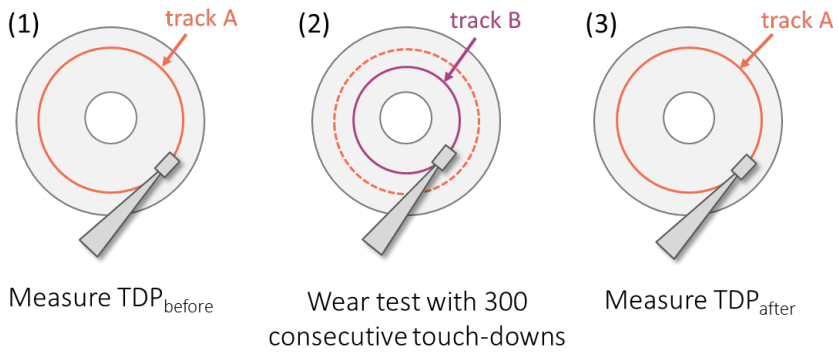

Figure 5.2: Wear test procedure. Step 1: Measure touch-down power; step 2: conduct 300 consecutive touch-down cycles; step 3: measure touch-down power.

If wear occurs during the 300 consecutive touch-down cycles, the head-disk

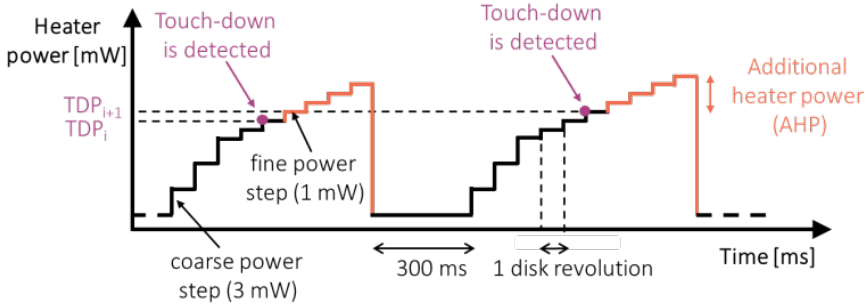

Figure 5.3: Heater input profile during the 300 consecutive touch-down cycles.

spacing will increase and thus, the heater power at which head-disk contact occurs will increase as well. Consequently, we hypothesize that a positive change in touch-down power (ΔTDP>0) indicates that head wear occurred during the 300 consecutive touch-down cycles. In order to verify whether or not wear of the shields occurred, SEM and AFM images of selected heads were taken. In this study, we focused on damage of the recording head rather than disk, and hence, we did not perform optical disk roughness measurements to examine the damage on the disk. It is important to note that the touch-down power change was measured on a disk radius different from the disk radius on which the wear test was performed. If the same disk radius was used for steps 1, 2, and 3, the change in touch-down power would be the result of wear on both the head and the disk. The experiments were carried out about half an hour after the desired temperature and humidity conditions were reached inside the chamber. Initial experiments showed that DTDP increases with an increase in touch-down cycles and an increasing time interval. Because we wanted to study the effect of temperature, humidity, and bonding lubricant ratio on ΔTDP, we chose 300 touch-down cycles and 300 ms time interval since this combination resulted in a change in ΔTDP large enough to be measured.

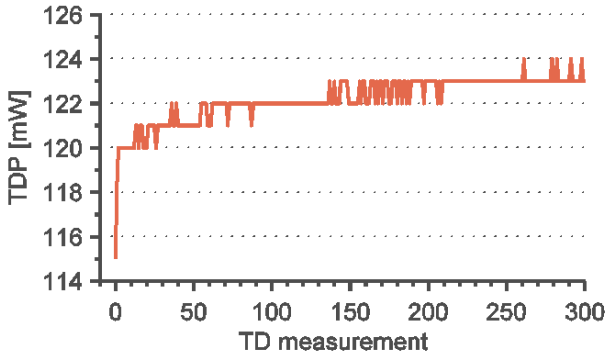

Figure 5.4: Typical experimental result showing the change in touch-down power over 300 consecutive touch-down cycles.

5.3 Experimental results

Fig. 5.4 shows a typical measurement for the change in touch-down power as a function of touch-down cycles. The additional heater power during the 300 consecutive touch- down cycles was 30 mW. Z-tetraol lubricant with 90 % bonding ratio was used (30 řC and 25 % relative humidity). The touch-down power measurement and the wear test were performed at a radius of 0.95” (24.1 mm) and 0.96” (24.4 mm), respectively. The average touch-down power before the wear test was 114 mW. We observe from Fig. 5.4 that the touch-down power increases initially and reaches an asymptotic behavior after approximately 60 touch-down cycles. This behavior is typical for a wear-in process. After the wear test, TDP_{after} was determined to be 121 mW, corresponding to a change in touch-down power of 7 mW.

Fig. 5.5 shows an SEM image of the protrusion area of the slider with write shield (top) and read shield (bottom). The thin layer of carbon on the slider is not visible in the SEM image since it is penetrated by the electron beam. Therefore, SEM cannot be used to study carbon wear. Instead, SEM can be used to study whether or not wear of the write shield occurred. An accelerating voltage of 0.5 kV was used for all SEM measurements in this study.

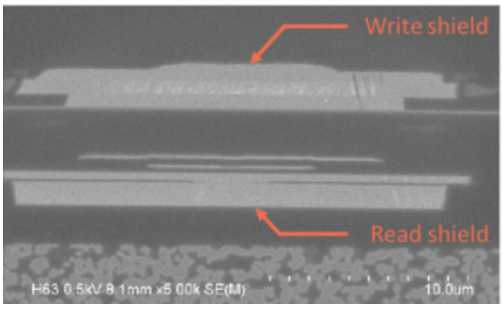

Figure 5.5: SEM image of the head operated at an additional heater power of 30 mW during the 300 consecutive touch-down cycles. SEM image shows the protrusion area with write shield (top), read shield (bottom). Bright areas indicate wear.

In Fig. 5.5, we observe bright areas and scratches on the write shield. Bright and shiny areas in SEM images indicate wear of the shield. In order to estimate the portion of the write shield that is worn, the SEM image was analyzed by performing a pixel count of the write shield and a pixel count of the shiny part of the write shield. Then, the ratio of pixels of the shiny over the total area was computed. The result of our image analysis is presented in Fig. 5.6. The shiny area is shown in white and the unworn portion of the write shield in gray. The ratio of the shiny over the total area is 0.057, suggesting that roughly 6 % of the write shield is worn.

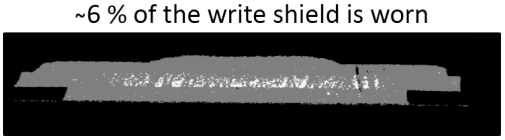

Figure 5.6: Post-processed SEM image of the head with 30 mW AHP. Our analysis suggests that 6 % of the write shield is worn.

5.3.1 Effect of lubricant bonding ratio on change in touch-down power

Fig. 5.7 shows the change in touch-down power as a func- tion of additional heater power for lubricant bonding ratios of 75 % (squares), 85 % (circles), and 90 %

(diamonds) (at 25 % relative humidity and 30 °C). In addition, Fig. 5.7 shows the corresponding flying height change displayed along a second y-axis (on the right side) assuming an actuation efficiency of 0.1 nm per 1 mW. Each data point in Fig. 5.7 represents the average of two or three wear tests. It can be seen in Fig. 5.7 that the change in touch-down power increases with an increase in additional heater power. Furthermore, we observe that the change in touch-down power increases with an increase in bonded lubricant ratio. The maximum observed change in touch-down power for this set of wear tests is 7 mW, which corresponds to a change in flying height of approximately 0.7 nm.

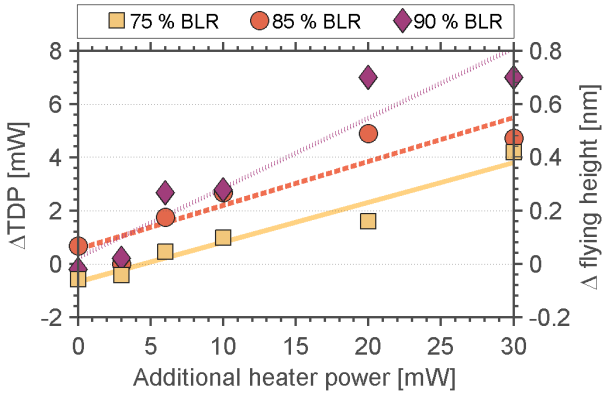

Figure 5.7: Change in touch-down power versus additional heater power for 75 % (squares), 85 % (circles) and 90 % (diamonds) bonded-lubricant ratio (temperature of 30 °C and 25 % relative humidity).

5.3.2 Effect of relative humidity on change in touch-down power

Our environmental chamber allowed investigating levels of relative humidity ranging from 12 to 65 %. We performed our wear tests at 15, 25, 35, and 60 % relative humidity. Fig. 5.8 shows the effect of relative humidity on the change in touch-down power. The additional heater power during this wear test was 30 mW and each data point represents the average of two or three experiments (75 % bonded-lubricant ratio, 40 °C). As shown in Fig. 5.8, the change in touch-down power is nearly the same for 25 %, 35 %

and 60 % relative humidity. However, for 15 % relative humidity, a significant increase in the change in touch-down power is observed.

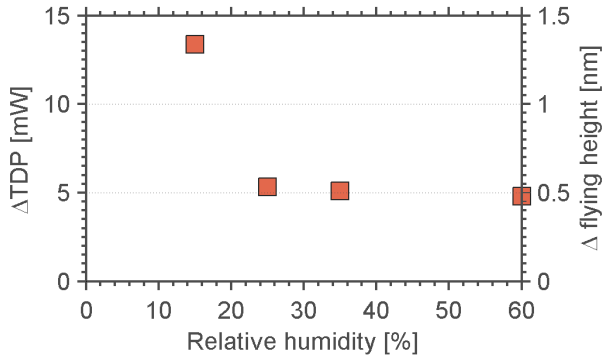

Figure 5.8: Change in touch-down power for 15 %, 25 %, 35 % and 60 % relative humidity at 40 °C with an additional heater power of 30 mW after 300 consecutive touch-down cycles.

5.3.3 Effect of temperature on change in touch-down power

The effect of temperature on the change in touch-down power versus additional heater power is illustrated in Fig. 5.9 for a temperature of 30 °C (squares), 40 °C (circles) and 50 °C (diamonds) (25 % relative humidity and 75 % bonded lubricant ratio). This temperature range lies within the operating range of hard disk drives. Each data point represents the average result of two or three experiments. We observe from Fig. 5.9 that the change in touch-down power increases with an increase in additional heater power. However, the effect of temperature on the change in touch-down power is small.

5.4 SEM measurements

After the wear test, SEM images of selected heads were taken and post-processed as discussed earlier to estimate the size of the shiny portion of the write shield. Fig. 5.10

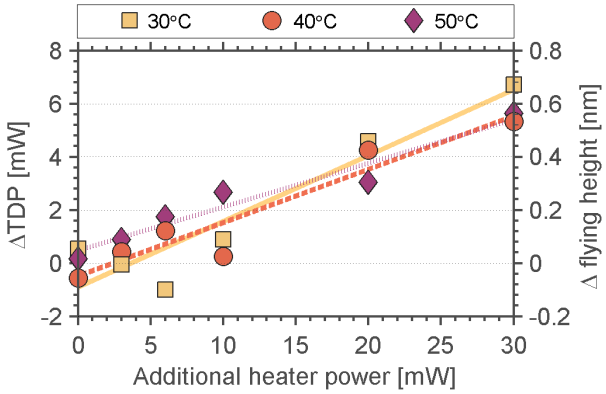

Figure 5.9: Change in touch-down power versus additional heater power for 30 °C (squares), 40 °C (circles) and 50 °C (diamonds) at 25 % relative humidity.

shows selected post-processed SEM images for 90 % bonded-lubricant ratio and additional heater powers of 0, 6, 20 and 30 mW, respectively. It can be seen in Fig. 5.10 that shiny regions on the write shield are absent for additional heater powers of 0 mW and 6 mW (Fig. 5.10 a) and b)). For these two heads, a change in touch-down power of 0 and 2.7 mW was measured after the wear test, respectively. For additional heater powers of 20 and 30 mW (both (ΔTDP = 7.0 mW), shiny portions and scratches are present on the write shield as shown in Fig. 5.10 c) and d). The shiny portion of the write shield was estimated to be 6 % for both heads.

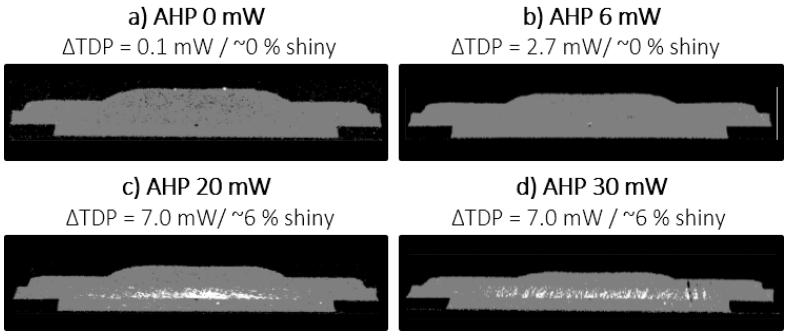

Figure 5.10: Post-processed SEM images of the write shield for various additional heater powers (90 % bonded-lubricant ratio). During post-processing the size of the 'shiny' portion of the write shield was estimated and plotted in white.

Fig. 5.11 shows the results for 75 % bonded lubricant ratio and additional heater

powers of 0, 6, 20 and 30 mW, respectively. We observe from Fig. 5.11 that visible wear of the write shield is absent for 0 mW, 6 mW and 30 mW additional heater power. For these heads, a change in touch-down power of 0, 1, and 5 mW was measured after the wear test, respectively. However, for an additional heater power of 20 mW (ΔTDP = 1.9 mW), the post-processed SEM image shows that approximately 4 % of the write shield is shiny (Fig. 5.11 c)).

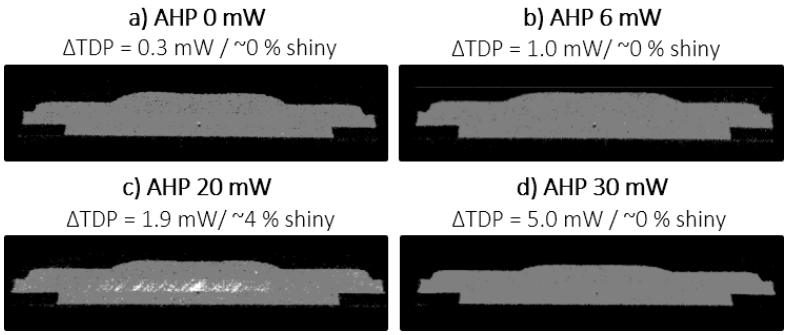

Figure 5.11: Post-processed SEM images of the write shield for various additional heater powers (75 % bonded-lubricant ratio). During post-processing the size of the 'shiny' portion of the write shield was estimated and plotted in white.

Fig. 5.12 shows the post-processed SEM images for 15, 25, and 35 % relative humidity. Figure 5.12 a) and b) show that shiny areas on the write shield are absent for 35 % and 25 % relative humidity for which a change in touch-down power of 4 and 4.2 mW was measured after the wear test, respectively. For 15 % relative humidity (ΔTDP = 13.7 mW), the post-processed SEM images indicate wear and scratching of the write shield.

Fig. 5.13 shows the post-processed SEM images for 30, 40, and 50 °C with an additional heater power of 30 mW. For 30 °C (ΔTDP = 7.2 mW), approximately 1 % of the write shield is shiny (Fig. 5.13 a)). For 40 °C (ΔTDP = 4.2 mW), shiny areas are absent on the write shield (Fig. 5.13 b)). For 50 °C (ΔTDP = 6 mW), about 1 % of the write shield is shiny as shown in Fig. 5.13 c).

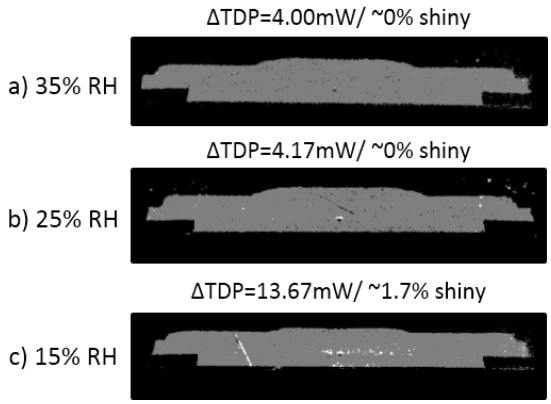

Figure 5.12: Post-processed SEM images for a) 35 % b) 25 %, and c) 15 % relative humidity. During post-processing the size of the 'shiny' portion of the write shield was estimated and plotted in white.

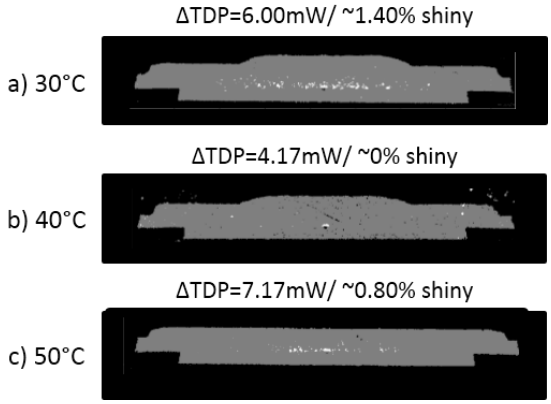

Figure 5.13: Post-processed SEM images for a) 30 °C, b) 40 °C, and c) 50 °C. During post-processing the size of the 'shiny' portion of the write shield was estimated and plotted in white.

5.5 AFM measurements

In order to assess how the surface roughness of the recording head is affected by head wear, atomic force microscope (AFM) measurements of unused and used heads were examined using atomic force microscopy (AFM). For this purpose, additional experiments were conducted on a spin stand using a similar wear test procedure. However, instead of performing 300 consecutive touch-down cycles, a constant heater power was applied during the wear test. The wear test track and the reference track for measuring

the touch-down power before and after the wear test were 0.8 mm apart. An overview over the wear test parameters and the measured change in touch- down power is presented in 5.1. As given in 5.1, the change in touch-down power increases with increasing test duration and increasing additional heater power.

Table 5.1: Wear test parameters and measured change in touch-down power ΔTDP of the wear test conducted for the AFM measurements

Test #	AHP [mW]	Wear test duration	ΔTDP [mW]
1	6	20 s	1.3
2	10	20 s	2
3	6	1 min	1.8
5	6	5 min	3.8
6	10	5 min	5
7	20	5 min	5.8
8	30	5 min	8
9	10	25 min	6.8
10	30	25 min	9

After the wear test, AFM measurements of each head were taken and the AFM measurements were post-processed using leveling, background subtraction and removal of small defects. Then, cross-sectional profiles were extracted from the center of the recording head as shown in Fig. 5.14. The cross-sectional profile represents the average of 40 neighboring pixels. Furthermore, the arithmetic mean R_a of the surface roughness was calculated for regions W1, W2, CS, R1, and R2 as indicated by the white boxes in Fig. 5.14.

Typical cross-sectional profiles of an unused head and two worn heads are presented in Fig. 5.15 a)–c), respectively. We observe in Fig. 5.15 a) that the cross-sectional profile of a new, unused head has peaks on the contact sensor shield and on the right end of the write shield. These peaks are partially worn off for the worn head shown in Fig. 5.15 b) for which a change in touch-down power of 1.8 mW was measured. Furthermore, the write shield appears overall smoother compared to the unworn head in

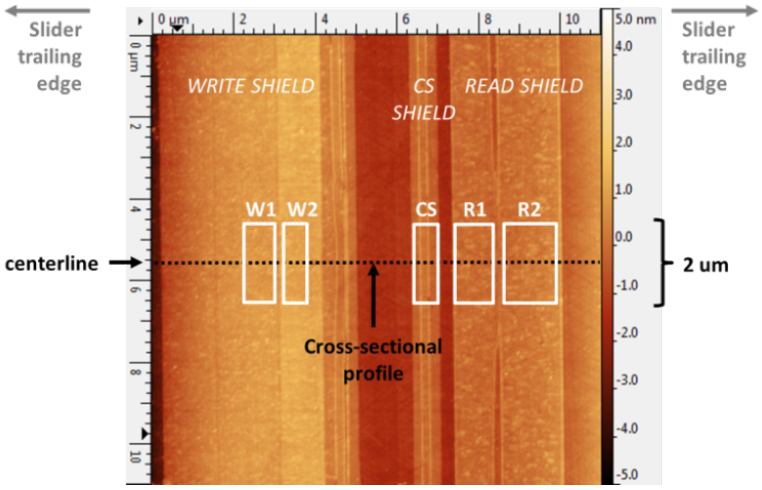

Figure 5.14: AFM image of a recording head showing write shield (left), contact sensor (CS) shield (middle), and read shield (right). This image indicates from which region the cross-sectional profile (black dashed line) and arithmetic mean of the surface roughness were extracted (white boxes).

Fig. 5.15 a). In Fig. 5.15 c) the cross-sectional profile of a head is shown for which a change in touch-down power of 6.8 mW was measured after the wear test. Clearly, the peaks on the write and contact sensor shield are worn off. Furthermore, the write shield and the left region of the read shield appear smoother compared to the profiles shown in Fig. 5.15 a) and b).

The arithmetic mean of the surface roughness of various heads with different changes in touch-down power is presented in Fig. 5.16 a) – e) for regions W1, W2, CS, R1, and R2. The enlarged data points at $\Delta TDP = 0$ mW represent the average R_a value of four new, unused heads. It can be seen in Fig. 5.16 a) that the R_a value in region W1 of worn heads is smaller compared to a typical unworn head.

In fact, the R_a value of a head for which a change in touch-down power of 1.3 mW was measured is half the average R_a value of unused heads (0.10 vs. 0.21 nm). Similarly, the R_a value of worn heads is clearly smaller compared to the R_a value unworn heads for region W2 (0.06–0.10 vs. 0.20 nm), region CS (0.08–0.20 vs. 0.34 nm), and region R1 (0.08–0.16 vs. 0.25 nm). On the other hand, there is no significant difference

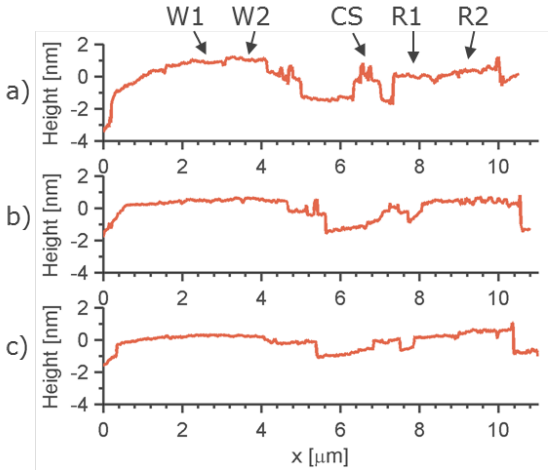

Figure 5.15: Cross-sectional profiles through the center of the shields of a) a new, unused head, b) a worn head with ΔTDP=1.8 mW, and c) a worn head with ΔTDP=6.8 mW.

in the R_a value between worn and unworn heads in region R2 (0.18–0.26 vs. 0.29 nm), indicating that the disk was not in contact with this region of the head during slider-disk contact.

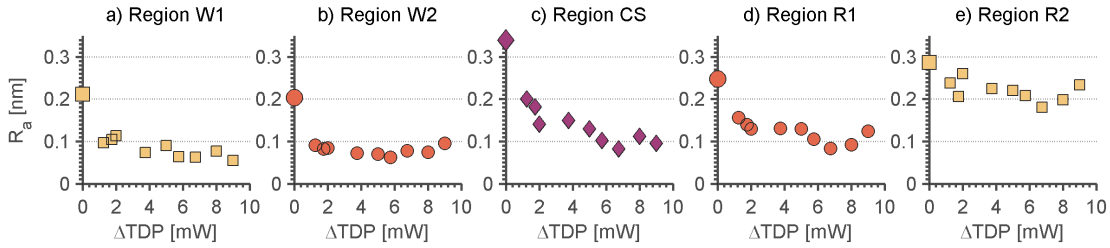

Figure 5.16: Arithmetic mean R_a of the surface roughness vs measured change in touch-down power ΔTDP for a) region W1, b) region W2, c) region CS, d) region R1, and e) region R2. The enlarged data point at ΔTDP=0 mW represents the average Ra value of four unused heads.

5.6 Discussion

5.6.1 Effect of bonded lubricant ratio and relative humidity on head wear

We observe in Fig. 5.7 that the change in touch-down power increases with an increase in bonded lubricant ratio. These findings are in accordance with [48]. Lubricants with high bonding ratio have less mobile lubricant that can replenish depleted lubricant areas. Since mobile lubricant can replenish depleted lubricant areas, lubricants with high bonding ratio are expected to result in increased wear compared to lubricants with lower bonding ratios. We observe in Fig. 5.8 that the change in touch-down power is increased at low relative humidity, indicating increased wear at low relative humidity. Nakazawa and Kawakubo [51] and Karis et al. [48] also found that head wear increases with decreasing relative humidity. This observation might be related to the presence of additional water molecules in the air at high relative humidity. Water molecules can be absorbed on the lubricant or on the disk carbon [52, 53]. For example, PFPE lubricants have the ability to retain water molecules at their functional end groups, thus leading to an increased fraction of mobile lubricant at high relative humidity [251]. Hence, the effective lubricant thickness increases at high relative humidity, which enhances lubrication and reduces wear. High humidity, however, may not be desirable from a corrosion point of view. Stirniman [252] found that the bonded lubricant ratio of Z-tetraol coated disks exposed to ambient conditions increases within the first 50 days and decreases thereafter. It has also been shown that the bonding ratio of lubricants increases over time at elevated temperature [48] and with decreasing relative humidity [253]. On the other hand, lubricants that are initially fully bonded gradually de- bond over time at ambient temperature and ambient relative humidity [48]. These findings suggest that the increased change in touch-down power at 15 % relative humidity observed in Fig. 5.8

could also be related to an increase in bonding ratio of the lubricant. From our experimental results, we concluded that a small change in temperature does not affect ΔTDP for the investigated head-disk combination in the temperature range from 30 to 50 °C. It is likely that a larger change in temperature causes a change in ΔTDP. However, hard disk drives typically operate at temperatures between 30 and 50 °C. In addition, the accuracy of the touch-down power measurement of our load/unload tester is limited to approximately 1 mW, making very small changes in DTDP difficult to observe.

5.6.2 Changes in touch-down power versus SEM images

On-track head wear is largely controlled by disk roughness. The authors believe that the observed behavior in Fig. 5.11 may be attributed to disk-to-disk variations in surface roughness and asperity distribution. These subtle part-to-part differences may not be measurable by the mean arithmetic surface roughness, R_a, nor the root mean square roughness, R_q, but by studying down-track roughness in the frequency or spatial domain. In addition to disk variations, there are head variations which may explain discrepancies between the measured change in touch-down power and the size of the wear scars of the SEM images.

5.6.3 Wear coefficient

Our experimental investigations have shown that wear of the recording head is a complicated process and that the wear rate depends on many factors including contact force, lubricant properties, material properties of slider and disk, sliding distance, sliding speed, as well as environmental conditions and tribochemical processes. In an attempt to estimate the coefficient of wear for our wear tests, we use Archard's wear equation [254]

given by

$$Q = \frac{kPs}{H} \tag{5.2}$$

where Q represents the wear volume, k is the coefficient of wear, P_n is the normal load, s is the sliding distance and H is the hardness of the softer surface.

The head shown in Fig. 5.15 c) underwent a wear test of 25 min duration with an additional heater power of 30 mW at a radial position of 21.8 mm and a disk velocity of 12.3 m/s (5400 rpm). A change in touch-down power of 6.8 mW was measured, and the sliding distance was calculated to be 18,500 m. The hardness and normal load can be assumed to be within the range of 5-20 GPa [138] and 1-10 mN [255], respectively. Based on numerical simulations of thermal flying height control sliders and published literature [255, 256], we assume a slider protrusion with ellipsoidal cross section. Fig. 5.17 shows the cross-sectional profile of a typical slider protrusion in (a) the down-track direction and (b) the cross-track direction [255, 256]. The wear volume is estimated by fitting the wear scar from SEM images into the cross section of the thermal protrusion at a depth that matches the wear scar dimensions best. For a head with ΔTDP = 7 mW, the width of a typical wear scar on the write shield as measured from SEM images is approximately 17 µm in the cross-track direction (see Fig. 5.10). The wear volume, wear depth, and contact area can then be estimated to be $2.2 \cdot 10^{-20}$ m^3, 1.1 nm, and 47.8 µm, respectively.

Using the above values for the sliding distance s, the wear volume Q, hardness H, contact load range P, we obtain a wear coefficient on the order of 10^{-11} to 10^{-13} for the head shown in Fig. 5.15 c). This value is very small and indicative of the fact that wear of thermal flying height control sliders is a nanoscale phenomenon. Machcha et al. [35] studied nano-wear of contact recording sliders and found Archard's wear coefficient likewise to be very small, on the order of 10^{-10} for drag and sweep testing.

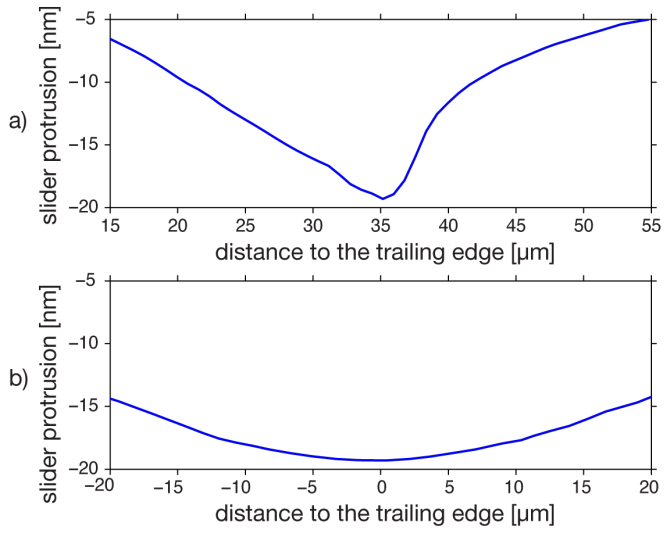

Figure 5.17: Profile of the slider protrusion along a) the down-track direction and b) the off-track direction.

5.7 Conclusion

We conclude that

1. The change in touch-down power increases with increasing bonded lubricant ratio.

2. Temperature has a minor effect on the change in touch-down power for the temperature range of 30-50 °C.

3. The change in touch-down power increases with decreasing relative humidity.

4. AFM analysis revealed noticeable changes in surface roughness of heads with changes in touch-down power as little as 1.3 mW compared to unworn heads. These changes in surface roughness are observed across the write shield, contact sensor shield, and small portions of the read shield.

5. SEM analysis showed wear of the write shield for changes in touch-down power that are typically larger than 6 mW.

6. The wear coefficient was estimated to be on the order of 10^{-11} to 10^{-13}

5.8 Acknowledgement

The authors would like to thank Susan Lee, J.P. Peng, Jian Xu, and Kaynam Chung from Western Digital for their help and support during the experiments.

Chapter 5, in part, is a reprint of the material as it appears in "Head wear of thermal flying height control sliders as a function of bonded-lubricant ratio, temperature and relative humidity", Liane M. Matthes, Ralf Brunner, Bernhard E. Knigge, and Frank E. Talke, *Tribology Letters*, vol. 60, no. 3, p. 39 (2015). The dissertation author was the primary investigator and author of this paper.

Chapter 6

Effect of head-disk interface biasing and relative humidity on wear of thermal flying height control sliders

As the physical spacing between the recording head, or slider, and the magnetic disk decreases, intermittent slider-disk contacts become of increasing concern. Slider-disk contact may occur during slider disk-asperity contacts, or during spacing calibration of thermal flying height control sliders [257]. Slider-disk contacts are undesirable since they can result in wear and damage of the head-disk interface (HDI), and, in particular, the read and write elements.

It has been reported [211,258,259] that the wear rate of the slider can be reduced by voltage biasing of the HDI. Knigge et al. [211] state that wear occurs primarily on the disk surface rather than the slider surface when a negative voltage of -0.3 V was applied to the slider with respect to the disk, compared to +0.3 V or 0 V slider bias. This result is interesting although it is unclear *a priori* why a negative slider bias should result in diminished slider wear. One possibility is the electrochemical action on diamond

like carbon (DLC) protected overcoat surfaces when positively biased [259]. On the other hand, if slider wear is enhanced by increased slider-disk attraction arising from electrostatic forces, wear should be independent of the polarity applied to a particular surface and depend only on the potential difference across the HDI.

Potential differences at the HDI can also affect the slider flying height [227,260], and cause damage to the sensitive read element [30] or the thermal contact sensor via electrostatic discharge. Electron bombardment [74] and exposure to electrostatic fields [76] have also been reported to cause lubricant degradation. This is undesirable since the lubricant is supposed to protect the HDI against corrosion and minimize damage from intermittent slider-disk contacts. The presence of an electric field at the HDI might also affect the competition between bondable disk lubricants, such as Z-tetraol and Demnum [46, 76], and polarizable species such as water for the reactive groups in the protective diamond-like carbon (DLC) layer on the slider and the disk surfaces. These considerations motivated us to extend the previous wear studies described in [211] and [258] by investigating HDI biasing effects over a range of relative humidity using disks with different types of lubricant.

6.1 Background on electrostatic forces across the head-disk interface

A 'natural' potential difference exists between the slider and the disk due to differences in slider-disk material properties. This inherent potential difference between the slider and the disk is generally referred to as the contact potential, V_c [227,261,262]. Although both slider and disk are coated with a thin protective layer of DLC ($\leq$ 2-3 nm), the protective coatings on these two surfaces may be dissimilar due to, for example, different manufacturing procedures. Furthermore, a thin layer of lubricant ($\leq$ 2 nm) is

present on the disk surface.

To obtain a first order estimate of the electrostatic force F_{el} acting across the HDI, one can approximate the HDI by two conducting plates. For this case, the electrostatic force is given by

$$F_{el} = \varepsilon_0 \varepsilon_r (V_c + d_{dc})^2 \iint \frac{1}{2h^2} \, dx \, dy \tag{6.1}$$

where ε_0 is the dielectric constant of vacuum or absolute vacuum permittivity, ε_r is relative dielectric constant or relative permittivity of the gas mixture in the hard disk drive, V_c is the contact potential, V_{dc} is the applied DC bias voltage, and h denotes the distances between the plates. To obtain the exact value of the electrostatic force, a numerical integration of the force over the air bearing surface is needed. We see from equation (6.1) that the presence of a potential difference across the HDI creates an electrostatic force which could decrease the slider-disk spacing, and that the electrostatic force is zero if the applied DC bias voltage is set to $V_{dc} = -V_c$.

6.2 Approach and Experimental set-up

The effect of HDI biasing, relative humidity (RH) and disk lubricant type on slider wear was investigated using two different experimental set-ups, a load/unload tester to confirm the findings reported in [211, 258], and a spin-stand tester (Micro-Physics [2]) with RH control. For both experimental set-ups, slider-disk contacts were monitored by observing the standard deviation of the amplified voltage output of an acoustic emission (AE) sensor. A pre-amplifier was used to amplify the AE output voltage by 60 dB. After wear testing on the spin-stand tester, the read and write region of selected sliders were examined using atomic force microscopy (AFM) to identify regions of wear and deposit formation. The deposits were analyzed thereafter using time

of flight secondary ion mass spectrometry (TOF-SIMS).

6.2.1 Load/Unload tester experiments

Preliminary wear tests were performed at 20 °C and 25 % RH while applying a DC HDI bias voltage to the slider relative to the spindle using a voltage source. The motor spindle was electrically isolated from the tester ground. This biasing scheme was opposite to that used during wear testing on the spin-stand tester described in the following section. Details of the wear test procedure with the load/unload tester are provided in section 6.2.2 .

6.2.2 Spin-stand experiments

The spin-stand tester was enclosed in an environmental chamber and Faraday cage as shown in Fig. 6.1. Experiments were performed at 27 °C and RH levels of $\leq$ 8 %, 30 %, and 52 %. The RH in the chamber was controlled by mixing filtered clean dry air with water saturated air. Disks were mounted on a pressurized air bearing spindle which was electrically isolated from both spin-stand instrument ground and earth ground. The head gimbal assembly (HGA), which was also isolated from spin-stand instrument ground, was operated on the bottom surface of the disk.

DC voltages across the HDI during the spin stand experiments were supplied by a source meter (Keithley model 2400 [263]), with the meter 'HI' lead attached to the spindle, and the 'LO' lead attached to both leads of the read element; the shorted reader leads are denoted 'common read' in this paper. For all spin-stand experiments, the disk was biased relative to the slider, in contrast to the biasing scheme used during load/unload tester experiments and the wear tests described in [211] where the slider was biased relative to the disk.

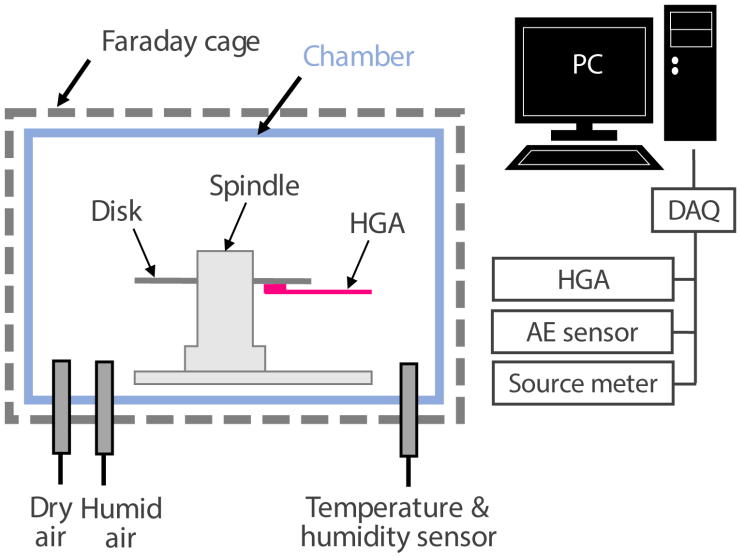

Figure 6.1: Schematic of spin-stand (MicroPhysics [2]) enclosed in environmental chamber.

6.2.3 Disks and sliders

For the load/unload tester experiments, commercially available disks with Z-tetraol lubricant were used. For the spin-stand test, three different types of disks were used: two with Demnum based lubricants (lubricant A and B), and one with a Z-tetraol lubricant (lubricant C). Wear tests were conducted with disks spinning at 5400 rotations per minute (rpm).

The same type of commercially available slider was used for all wear tests (see Fig. 6.2). The main body of the slider consisted of Al_2O_3TiC (AlTiC). The read and write shields were comprised of nickel cobalt iron (NiCoFe), and sputtered aluminum oxide (Al_2O_3) surrounded the read and write shields. The air bearing surface of the slider was coated with a protective DLC layer of approximately 2-3 nm thickness.

The effects of disk velocity and suspension preload on the flying height for this particular slider were calculated using a finite element based air bearing simulator (CMRR air bearing simulator, [124]). As shown in Fig. 6.3, the slider flying height

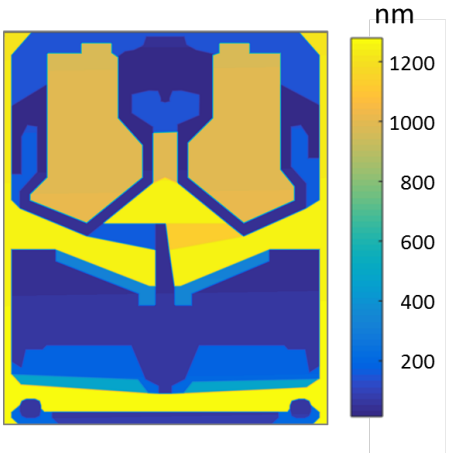

Figure 6.2: Air bearing contour of the slider. The read/write region is located at the center of the trailing edge (top). The color bar indicates the recess height.

at zero degree skew angle increases with increasing disk velocity and decreasing suspension preload. At a rotational speed of 5400 rotations per minute (rpm) and a disk radius of 25 mm, the slider flying height and pitch angle are on the order of 13.6 nm and 73.9 micro radians.

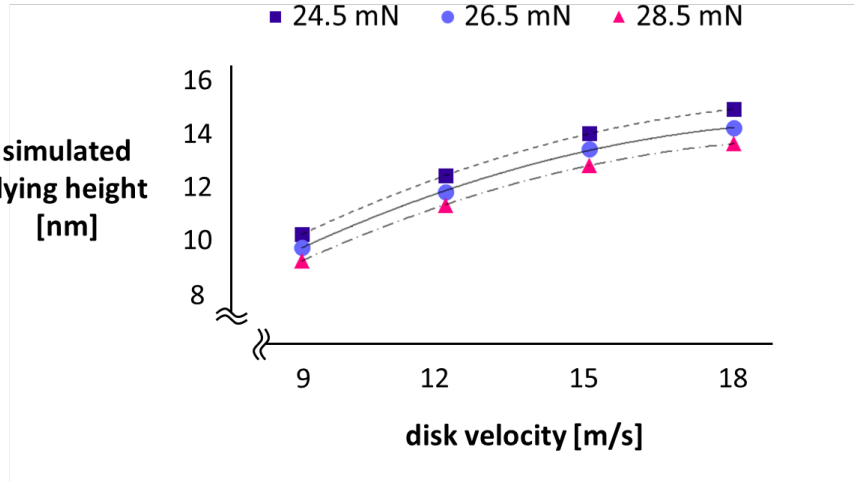

Figure 6.3: Flying height as a function of disk velocity and various suspension preloads (zero degree skew angle).

6.3 Wear test procedure

Prior to wear testing, the disks were cleaned by sweeping a new slider from the inner to the outer diameter several times without actuating the heater. Our wear test procedure involved using two different disk radii, reference track 'A' and wear track 'B', similar to the test procedure used in [264]. Slider wear was determined at reference track A by measuring and comparing the heater touch-down power (TDP) before and after wear testing. The touch-down power (TDP) in thermal flying height control sliders denotes the heater input at which the onset of slider-disk contact occurs. TDP was determined by increasing the power input to the heater in steps of 0.5 mW or 1 mW per disk revolution until the onset of slider-disk contact was detected using the AE sensor. The average touch-down power was first measured on reference track A ($\overline{TDP}_{A,before}$). Then, the wear test was performed on neighboring track B (see sections 6.3.1 and 6.3.2). After completing the wear test, the slider was moved back to reference track A to determine the average touch-down power ($\overline{TDP}_{A,after}$). Slider wear was estimated by computing the average change in touch-down power ΔTDP via:

$$\Delta TDP = \overline{TDP}_{A,after} - \overline{TDP}_{A,before} \tag{6.2}$$

Wear tests were performed for various HDI bias voltages, as described below, using a new slider for each new bias voltage.

6.3.1 Load/Unload tester experiments

The slider was biased at +0.5 V, 0 V, or -0.5 V during wear testing on track B. Wear tests consisted of 300 consecutive touch-down cycles. During each touch-down cycle, the power input to the heater was increased in steps of 1 mW per disk revolution until the onset of slider-disk contact was detected. Once slider-disk contact was detected,

the power input to the heater was further increased in steps of 1 mW per disk revolution until attaining 30 mW additional heater power beyond the point of slider-disk contact. The heater power was then set back to zero, and the next touch-down cycle was initiated after a 300 ms time delay.

6.3.2 Spin-stand experiments

Prior to measuring $\overline{TDP}_{A,before}$, the touch-down power was measured on track A as a function of HDI DC bias voltage. A second order polynomial curve fit was applied to the data and the peak of the curve, corresponding to $V_{dc} = -V_c$, was denoted V^*. The slider was then moved to track B and the average touch-down power was determined ($\overline{TDP}_B$). Wear testing on track B was performed for 10 minutes with the heater power set to $\overline{TDP}_B$ + 30 mW while biasing the HDI at either V^* + 1 V, 0 V, V^*, and V^* - 1 V.

Fig. 6.4 shows a typical result for the variation of touch-down power as a function of HDI DC bias voltage. The solid line represents a second order polynomial fit to the experimental data. It can be seen in Fig. 6.4 that the touch-down power is largest for a DC disk bias voltage of V^* = 0.11 V. In our experiments we observed slider-to-slider and disk-to-disk variations in V^* from 0.05 V to 0.5 V. These values are in agreement with results of other researchers [261, 262]. Both Feng et al. [261] and Zhang and Liu [262] studied the effect of electrostatic forces on slider flying height by measuring the read-back signal vs HDI voltage. Feng et al. [261] isolated the slider from ground and applied a voltage to the slider with respect to the disk. They found that the slider -disk spacing was largest for HDI voltages ranging from -0.9 V to -0.2 V (slider relative to disk), depending on the slider -disk combination. Zhang and Liu [262] grounded the slider and applied a voltage to the disk relative to the slider. They found that the slider-disk spacing was largest for an HDI voltage of +0.25 V (disk relative to slider). Fig. 6.4 illustrates how the presence of an electrostatic force across the HDI reduces the slider-disk spacing

and hence the touch-down power, which is also expressed in equation 6.1.

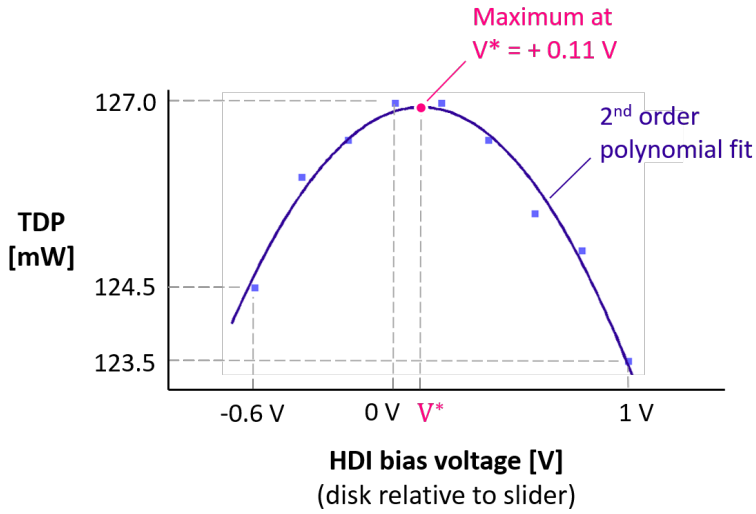

Figure 6.4: Touch-down power (TDP) as a function of HDI bias voltage.

We observe from Fig. 6.4 that the touch-down power decreases from 127 mW to 124.5 mW for an HDI bias of -0.6 V (disk relative to slider). For the slider attitude calculated earlier and an HDI bias voltage of -0.6 V, the electrostatic force is estimated to be on the order of 0.73 mN using equation 6.1, corresponding to a reduction in flying height of approximately 0.25 nm.

6.4 Wear test results

6.4.1 Load/unload tester experiments

A wear test was first performed at -0.5 V DC slider bias at 19 mm disk radius, followed by wear tests at 0 V and +0.5 V slider bias at 19.8 mm and 20.6 mm disk radii, respectively. All three wear tests were performed on the same disk at 22 °C and 25 % RH. As shown in Fig. 6.5, the change in touch-down power is smallest for negative slider bias relative to the disk.

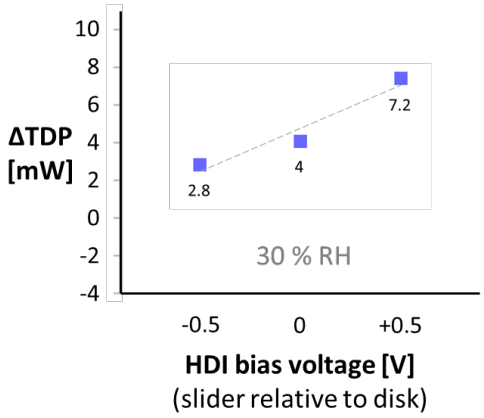

Figure 6.5: ΔTDP vs HDI bias voltage (22 °C, 25 % RH).

6.4.2 Spin-stand experiments

The effect of HDI bias voltage on ΔTDP for disks with lubricant A (30 % RH) is shown in Fig. 6.7. It can be seen in Fig. 6.7 that ΔTDP is smallest for V^* + 1 V DC disk bias. This result is in agreement with the load/unload tester results (Fig. 6.5) where the opposite biasing scheme was used.

ΔTDP results obtained with lubricant B disks are shown in Fig. 6.7 a) and b) for $\leq$ 6 % RH and 30 % RH, respectively. In the 30 % RH environment, ΔTDP is smallest for V^* + 1 V DC disk bias as observed previously with lubricant A disks. However, at relative humidity $\leq$ 6 %, ΔTDP is found to be smallest for V^* - 1 V DC disk bias (Fig. 6.7 a)).

Fig. 6.9 shows that disks with lubricant C produced results similar to those obtained with lubricant A and B disks: ΔTDP is smallest for V^* - 1 V at low RH ($\leq$ 8 % RH), but ΔTDP is smallest for V^* + 1 V DC disk bias when tests are conducted in high RH environments (30 % and 52 % RH).

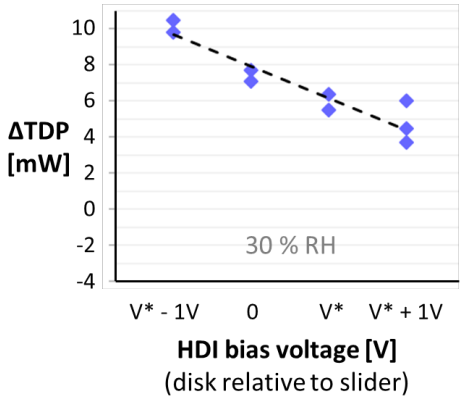

Figure 6.6: ΔTDP vs HDI bias voltage for lubricant A disks (30 % RH).

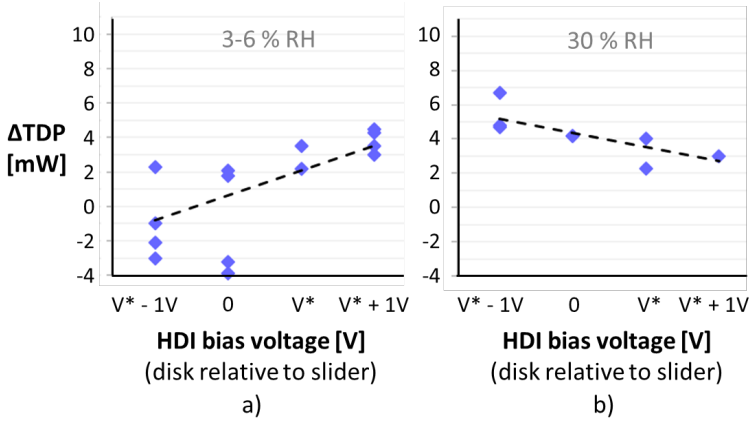

Figure 6.7: ΔTDP vs HDI bias voltage for lubricant B disks at a) $\leq$ 6 % RH and b) 30 % RH.

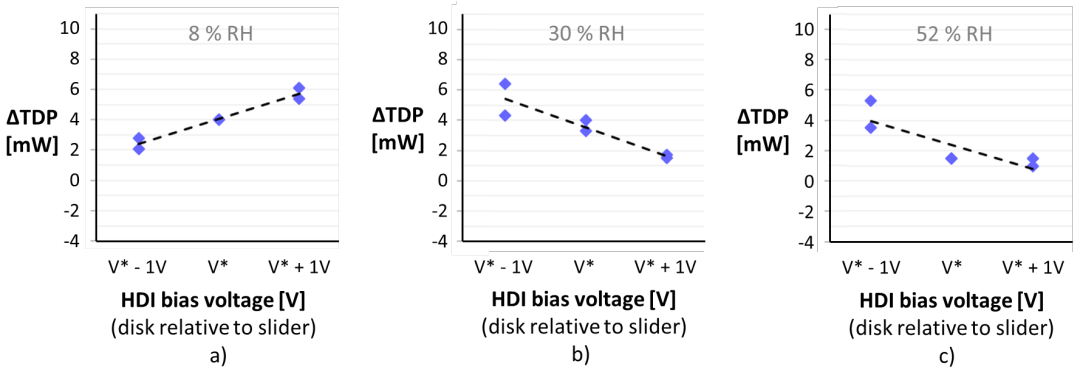

Figure 6.8: ΔTDP vs HDI bias voltage for lubricant C disks at a) 8 % RH, b) 30 % RH and c) 52 % RH.

6.5 AFM measurements

After wear testing, the read and write (R/W) regions of selected sliders were examined using AFM. Images were obtained with the fast-scan axis parallel to both the down-track direction (0° AFM images) and the cross-track direction (90° AFM images). The fast scan direction is along the trace and retrace movement of the AFM cantilever, which is parallel to the horizontal axis of the AFM images. Using different scan directions helps to identify scan artifacts or loose objects on the specimen surface. Cross-sectional height profiles were always taken parallel to the fast scan directions.

6.5.1 Unused slider

For reference, an AFM image of a new, unused slider is presented in Fig. 6.9. In this figure the write shield (W) is on the left, the read shield (R) is near the center and the Al_2O_3TiC slider substrate is on the right. The read and write shield protrude about 1-2 nm above the sputtered Al_2O_3 surrounding the shields.

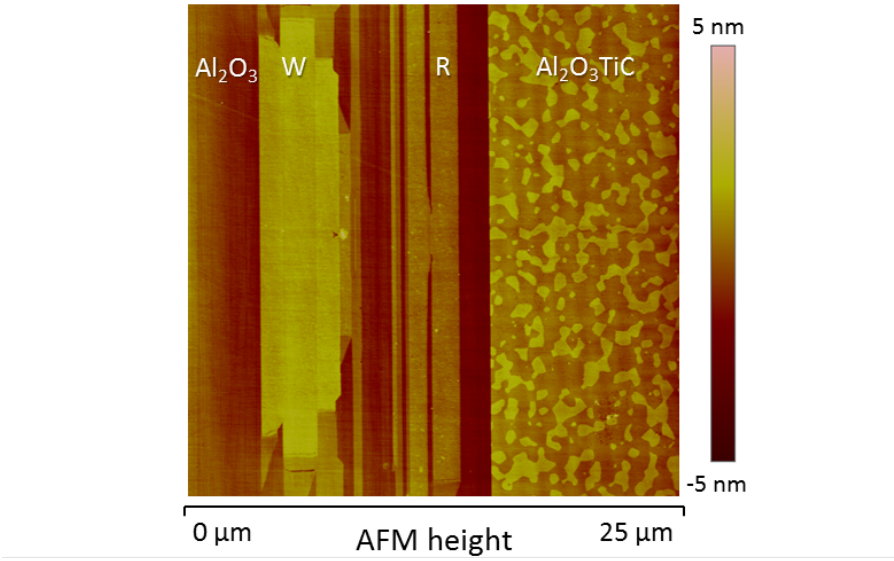

Figure 6.9: AFM height image of a new, unused slider.

6.5.2 Wear tests with lubricant A disks

Fig. 6.10 shows AFM height images of typical sliders after wear testing with lubricant A disks at 30 % RH for various DC disk bias voltages. The scratch diagonally across the write shield in Fig. 6.10 a) was likely introduced during manufacturing or post-production testing, and not during wear testing, because its angle is much larger than the slider skew angle during wear testing. The regions between the write shield (W) and the read shield (R) centered around the write pole in Fig. 6.10 a)-d) are recessed compared to the same region on the unused slider in Fig. 6.9, indicating wear of the DLC and write shield during wear testing. We observe that neither the 0° nor 90° AFM images show deposits in the read/write (R/W) regions, except for some deposits for the slider tested at V^* - 1 V DC disk bias voltage (Fig. 6.10 a)). As shown in Fig. 6.11, the deposits on the latter slider are parallel to the skew angle direction.

6.5.3 Wear tests with lubricant B disks

AFM images showed no significant deposits on the slider surfaces after wear testing with lubricant B disks at 30 % RH, similar to the results obtained with lubricant A disks. However, at $\leq$ 8 % RH, deposits were observed as can be seen in Fig. 6.12. All six AFM height images in Fig. 6.12 show deposits on top of the write shield and on the sputtered alumina on the trailing edge side of the write shield. The orientation of the streaks of the deposits in Fig. 6.12 b)-e) coincides with the skew angle during wear testing, suggesting that the deposits are a direct result of the wear test. Fig. 6.12 a)-c) also shows that a DC disk bias voltage of V^* - 1 V results in a greater amount of deposits compared to V^* + 1 V DC disk bias (Fig. 6.12 d)-f)). This result is unexpected because a previous study on the effect of HDI bias voltage on slider wear did not mention any formation of deposits on the slider at low RH [259].

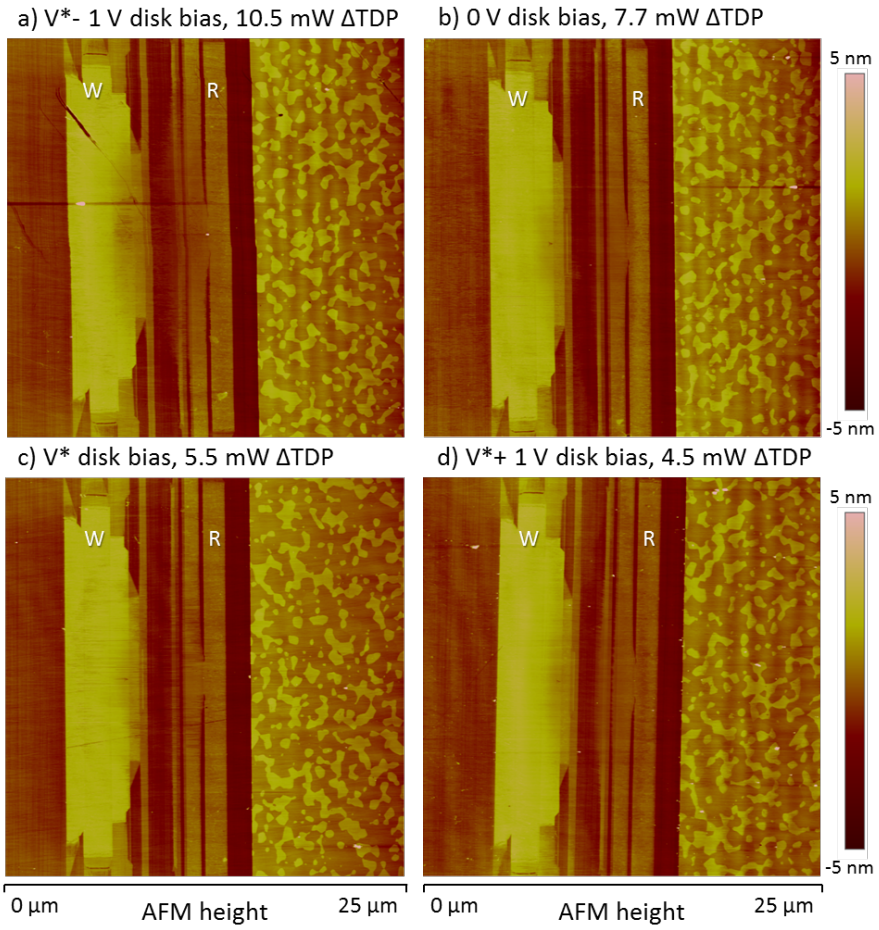

Figure 6.10: AFM height images of selected slider after wear testing on lubricant A disks (30 % RH) for various HDI bias voltages.

The height of the deposit on the trailing edge side of the write shield in Fig. 6.12 a) (see dotted line 'A') is approximately 3-4 nm thick as shown in Fig. 6.13. The section shown in Fig. 6.14 was obtained from the corresponding 90° AFM image.

6.5.4 Wear tests with lubricant C disks

Fig. 6.14 a) and b) show AFM height images of a slider after wear testing with a lubricant C disk at 8 % RH using V^* - 1 V DC disk bias voltage. Deposits on the R/W shields are clearly visible, similar to the sliders tested with lubricant B disks at low

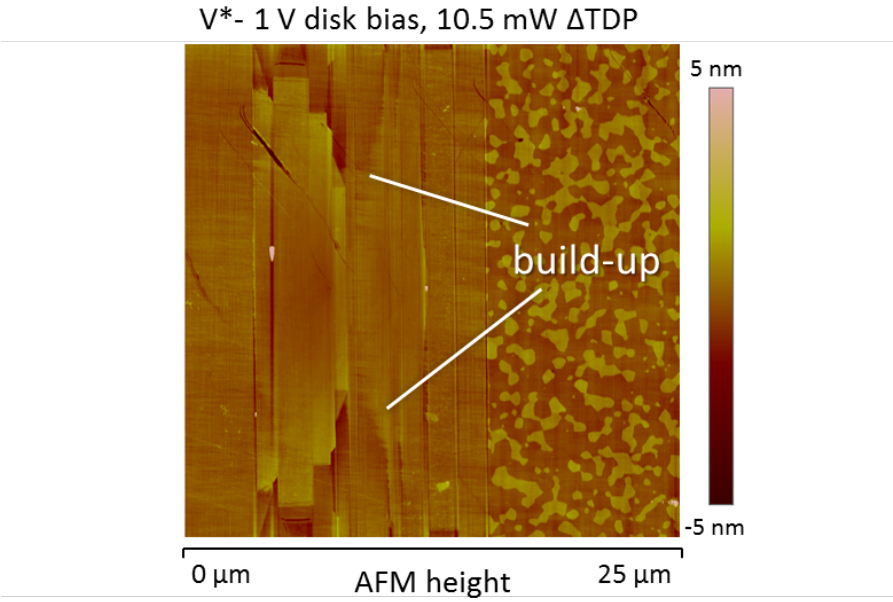

Figure 6.11: 90° AFM height scan of the slider shown in Fig. 6.10 a) (rotated 90° counter-clockwise w.r.t. the standard orientation).

RH. The large number of particles in both figures is likely due to external contamination because the wear tests and AFM measurements were not performed in a cleanroom environment.

Height profiles of the deposits (transverse and parallel to the shields) are shown in Fig. 6.14 c) and d), respectively. Deposits on the read shield are approximately 1 nm thick (Fig. 6.14 c)), based on a comparison of shield areas with no deposits. Deposits on the alumina at the trailing edge side of the write shield ('C' in Fig. 6.14 d)) are approximately 2 nm thick.

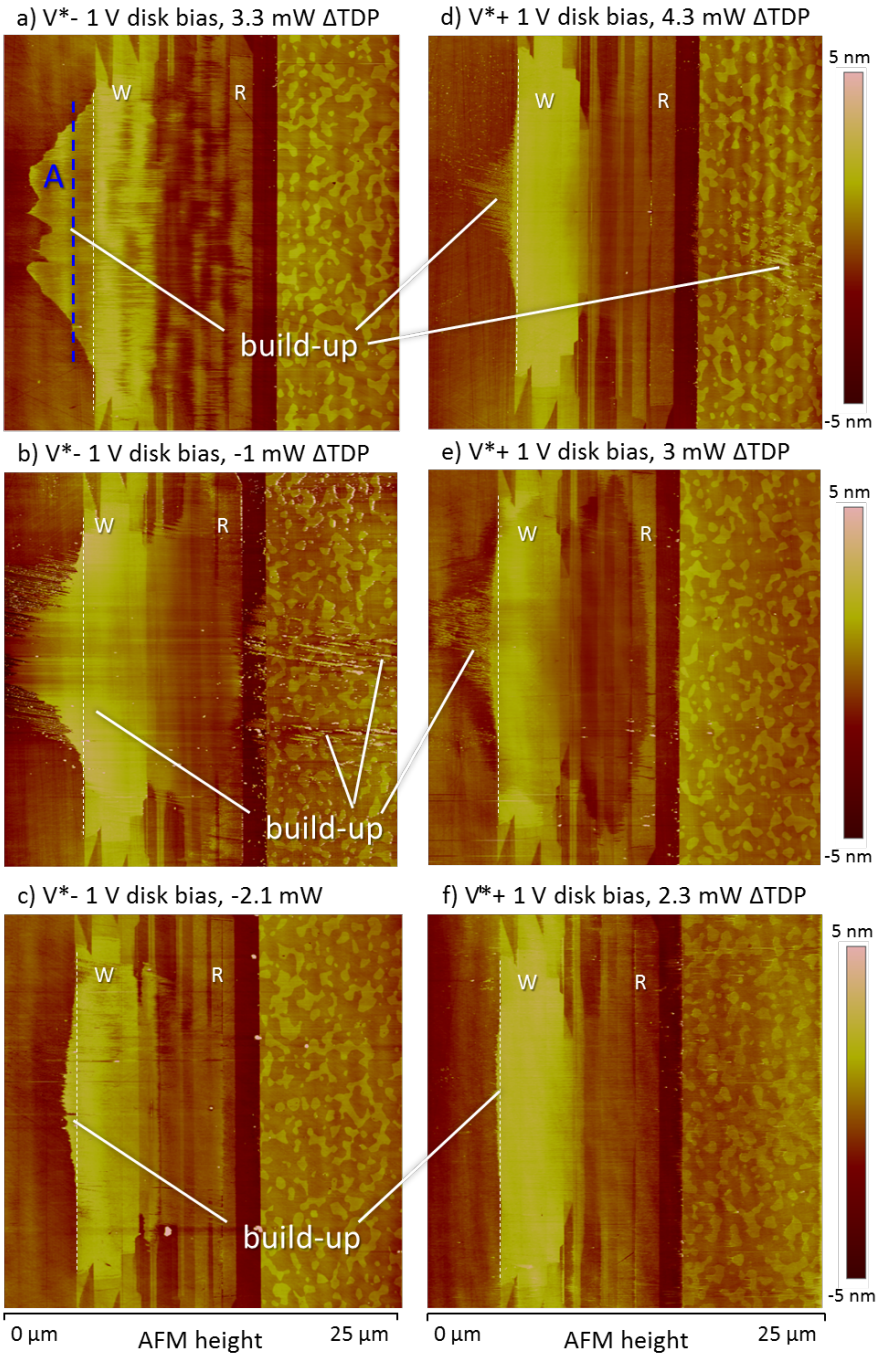

Figure 6.12: AFM height images of selected slider after wear testing on lubricant B disks ($\leq$ 6 % RH) for various HDI bias voltages.

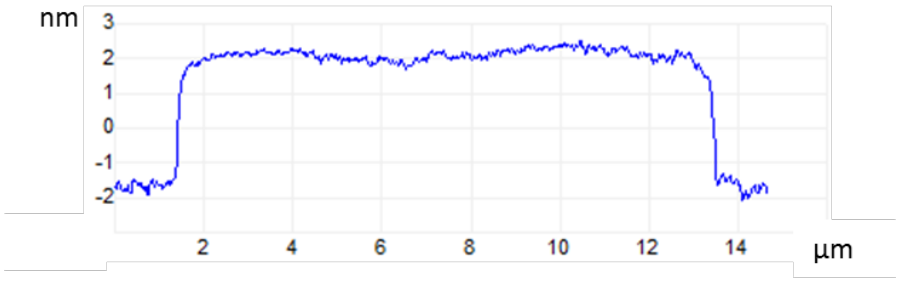

Figure 6.13: Height cross-section of the deposit along the dotted line in Fig. 6.12 a) from the corresponding 90° AFM image.

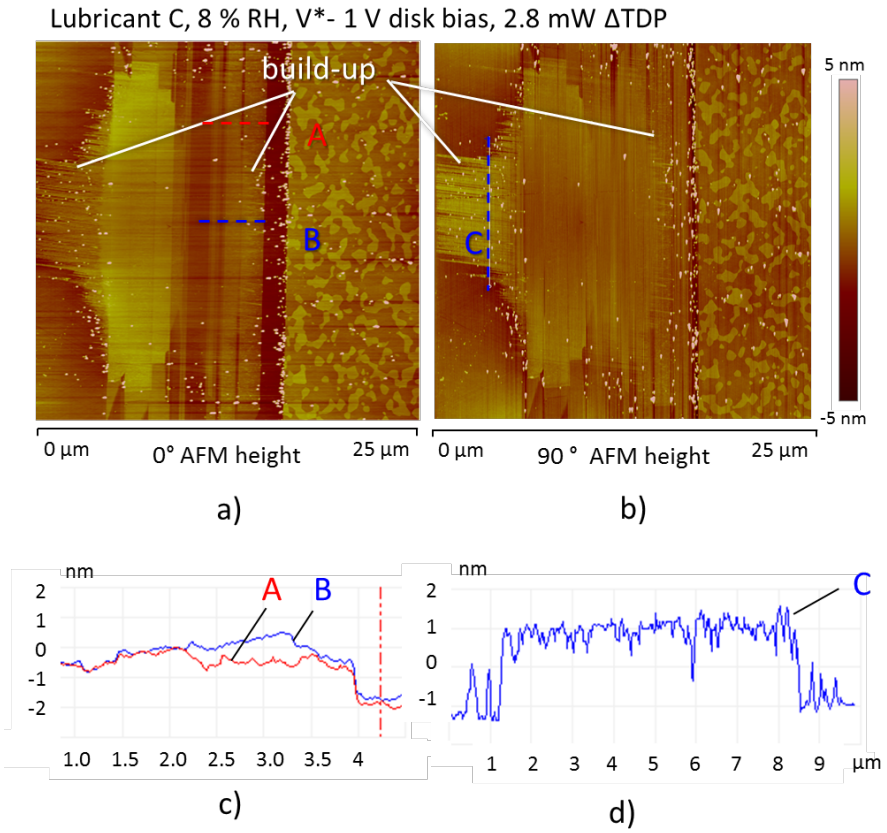

Figure 6.14: AFM height images and associated height profiles of a slider after wear testing on lubricant C disks (8 % RH). a) 0° AFM image, b) 90° AFM image (rotated 90° counter-clockwise from the standard orientation), c) height profiles 'A' and 'B' from 0° AFM image, and d) height profile 'C' from 90° AFM image.

6.6 TOF-SIMS measurements

6.6.1 Analysis of deposits in the read/write region

TOF-SIMS was used to analyze the deposits and carbon wear in the pole region of the sliders. Because the intensity scale in each TOF-SIMS image is normalized with respect to the maximum absolute intensity in each image, intensities from multiple TOF-SIMS images are not comparable.

Fig. 6.15 a) and b) shows the TOF-SIMS fluorine maps of the worn slider from Fig. 6.12 a) and the unused slider from Fig. 6.9, respectively. The deposit in the AFM height image from Fig. 6.12 a) coincides with the presence of $C_2F_5^+$ and CF^+ ions in the TOF-SIMS image (Fig. 6.15 a)), whereas $C_2F_5^+$ and CF^+ ions were absent at the pole region of the unused slider (Fig. 6.15 b)). This clearly shows that the deposits consist of either fluorocarbon lubricants or, more likely, degraded fluorocarbon lubricant fragments.

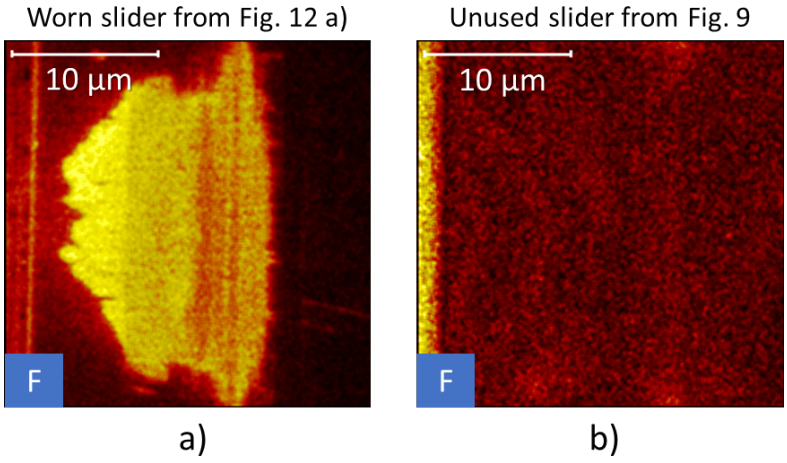

Figure 6.15: TOF-SIMS fluorine maps of a) the worn slider from Fig. 6.12 a), and b) the unused slider from Fig. 6.9.

The TOF-SIMS nickel iron (Fe + Ni) maps of the worn slider from Fig. 6.12 a) and the unused slider from Fig. 6.9 are shown in Fig. 6.16 a) and b), respectively. We

observe a high intensity of Fe and Ni on parts of the write and read shields of the worn slider (see Fig. 6.16 a)), whereas the intensity of Fe and Ni is uniform across both shields for the unused slider (Fig. 6.16 b)). Both iron and nickel originate from the read and write shields which consist of NiCoFe. Because the iron and nickel from the shields mix with the DLC during deposition of the thin DLC layer onto the slider, the Fe and Ni intensity is increased at the location of the read and write shields for unused sliders (see Fig. 6.16 b)). If the DLC protecting the read and write shields is worn, an increase in Fe and Ni intensity can be observed in the TOF-SIMS image corresponding to the location of the carbon wear scar. Hence, the regions of high Fe and Ni intensity in the TOF-SIMS image in Fig. 6.16 a) identifies regions on the slider with worn DLC.

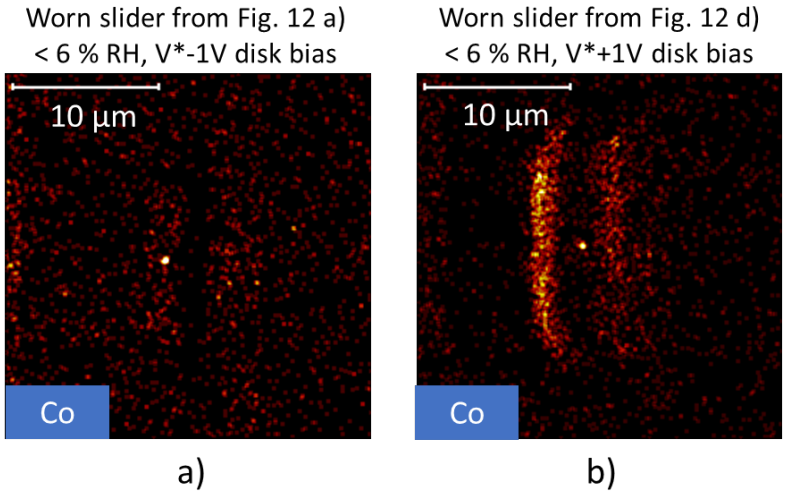

Figure 6.16: TOF-SIMS iron nickel maps of a) the worn slider from Fig. 6.12 a), and b) the unused slider from Fig. 6.9.

Fig. 6.17 a) and b) show the TOF-SIMS cobalt (Co) maps of the worn slider from Fig. 6.12 a) and the worn slider from Fig. 6.12 d), respectively. We observe a uniform intensity distribution of cobalt in Fig. 6.17 a) with a small spot of increased intensity of cobalt at the center of the image corresponding to the write pole. This slider was biased at a DC voltage of V^* - 1 V during wear testing. In contrast, the slider tested at V^* + 1 V

DC disk bias (Fig. 6.17 b)), shows an increase in cobalt intensity around the write pole region. The cobalt most likely originates from the magnetic layer in the disk, suggesting increased wear of the disk DLC during wear testing at V^* + 1 V DC disk bias compared to V^* - 1 V DC disk bias.

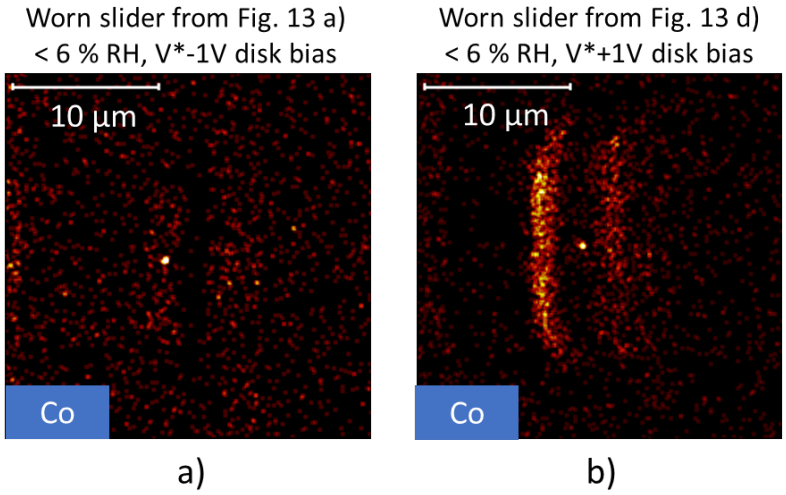

Figure 6.17: TOF-SIMS iron nickel maps of a) the worn slider from Fig. 6.12 a), and b) the worn slider from Fig. 6.12 d).

6.6.2 Effect of HDI DC bias on lubricant transfer

To understand the effect of HDI DC bias on lubricant transfer from the disk to the slider, two 'sweep tests' using different HDI DC bias voltages were performed. For test 1, we used -1 V disk bias relative to the slider and a sweep range from 22.5 mm to 24.4 mm (14.9-11.9° skew angle); for test 2, we used +1 V disk bias relative to the slider and a sweep range of 25.4-27.2 mm (10.6-7.8° skew angle). During both sweep tests the heater of the TFC slider was not activated. Each sweep test was performed at 30 % RH, at a temperature of 27 °C, and lasted 54 hours. TOF-SIMS was also used to characterize the amount of fluorocarbon based lubricant or lubricant fragments present on the air bearing surface following the sweep tests.

Fig. 6.18 shows that disk lubricant or lubricant fragments are transferred from the disk to the slider even at nominal flying heights of 12-13 nm. However, biasing the disk at -1 V showed a larger amount of transferred lubricant or lubricant fragments to the air bearing surface of the slider than biasing the disk at +1V.

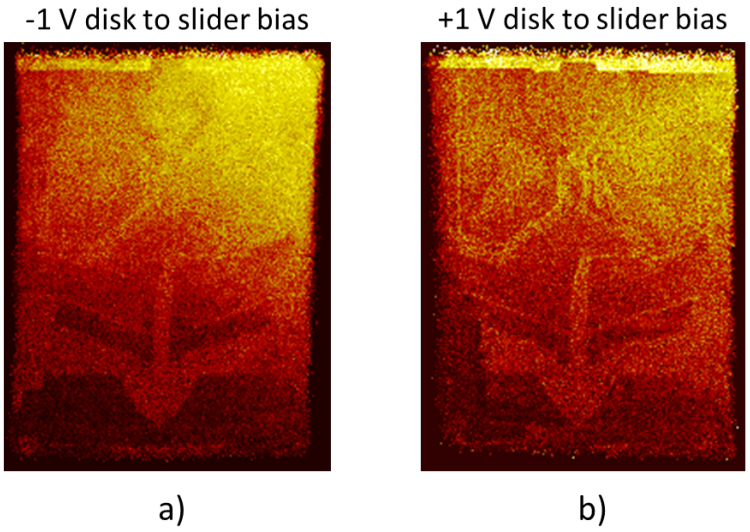

Figure 6.18: TOF-SIMS images of lubricant fragments $C_2F_5^+$ and CF^+ on the slider for a) Ú1 V disk bias , b) +1 V disk bias (intensity plot with red and yellow denoting low and high intensity of $C_2F_5^+$ and CF^+, respectively).

6.7 Discussion

Wear tests conducted at RH > 25 % showed that ΔTDP decreases as the disk potential becomes more positive relative to the slider (i.e., as the slider bias becomes more negative relative to the disk), independent of whether the slider or the disk is biased. These observation are consistent with previous reports [211, 259] of diminished slider wear at negative slider potentials. However, at low relative humidity (e.g., RH $\leq$ 8 %), the trend in ΔTDP vs HDI bias voltage is reversed and we even observe negative ΔTDP values for some sliders (see Fig. 6.7). AFM and TOF-SIMS investigations revealed the

presence of up to 4 nm thick deposits consisting of degraded lubricant fragments in the pole region of sliders tested at RH $\leq$ 8 %. Substantially less or no deposits were observed on sliders tested at RH > 25 %. Electrostatic force microscopy (EFM) measurements also showed that the deposits are non-conducting. Deposits on the pole region may decrease the head-disk spacing, hence resulting in a lower ΔTDP, giving the impression of less wear. Our results hence demonstrate that ΔTDP as a measure of slider wear for RH $\leq$ 8 % should be treated with caution since wear and deposit formation may occur simultaneously. In contrast, a previous study by Rajauria et al. [259] did not report any deposit formation on sliders. This may be due to a shorter wear test duration of 3 seconds [259] compared to our wear tests which lasted 10 min.

For wear tests conducted at 6 % RH, TOF-SIMS analysis suggests increased DLC wear on the disk for positive disk bias (negative slider bias) compared to negative disk bias (positive slider bias). A previous study by Rajauria et al. [259] which uses ΔTDP as a measure of carbon wear found similar results for tests conducted at 45 % RH; however, at 7 % RH, they note high rates of carbon wear for both positive and negative sider bias. We have already noted that ΔTDP as a measure of wear at low relative humidity ($\leq$ 8 % RH) should be treated with caution due to deposit formation on the slider. The differences between Rajauria et al. [259] and our results may again may be due to different wear test durations (3 seconds in [259] versus 10 min in our study). Rajauria et al. attribute carbon wear at 45 % RH to the electrochemical oxidation of the carbon overcoat, and that the applied polarity governs whether the slider or the disk undergo oxidation [259]. Oxygen in the environment can chemi-absorb onto DLC surfaces, resulting in the formation of surface oxides [32]. These surface oxides may then desorb under heat, producing CO and CO_2 and hence deplete the carbon surface of carbon atoms [32].

The most interesting aspects of our results are the effects of relative humidity

and HDI bias on the extent of deposit formation in the R/W region on the slider. Our studies have not addressed the issue of whether or not the deposits primarily consist of unaltered lubricants or their degradation products, but it is reasonable to assume that the deposits on the slider surface are strongly bonded at the deposit locations because there was no evidence of spreading while performing multiple AFM measurements in different scan directions and during the time period between the first AFM measurements and subsequent TOF-SIMS analysis. Sliders tested with disks having the Demnum based lubricants and Fomblin Z-tetraol produced very similar results, suggesting that relative humidity and HDI bias influence these two types of bondable lubricants in similar manners. At RH > 25 %, deposit formation on the slider appears to be inhibited, but is not entirely suppressed when the disk has a negative bias with respect to the slider (i.e., positive slider bias) as shown in Fig. 6.11. At RH $\leq$ 8 %, deposit formation is observed for both positive and negative disk bias (negative and positive slider bias, respectively) but the deposits are much greater for negative disk bias (positive slider bias). HDI bias polarity and humidity are therefore both important factors which influence the accumulation of lubricant or degraded lubricant fragments on the slider. This effect is relevant for HDI reliability because the elevated internal temperatures in operating commercial disk drive products create a reduced relative humidity environment at the HDI.

Clearly, our wear tests created direct contact between the slider and the disk which can promote transfer of lubricant from the disk to the slider surface by mechanical means. However, purely mechanical transfer mechanisms cannot readily account for the strong influences of HDI bias polarity and RH on deposit formation in the R/W region reported in this paper. Tani et al. [265] showed that lubricant transfer to the entire air bearing surface is enhanced by a positive slider bias in the range of 41-52 % RH. These authors suggest that airflow over the disk surface produces a negative charge on perfluorinated polyether disk lubricant molecules which are then attracted to a positively biased

slider surface. Our results also show that negative disk bias (positive slider bias) results in a greater amount of deposits and, notably, that deposit formation in the R/W region is significantly increased in low relative humidity environments. One possible reason for increased deposit formation at low humidity may be enhanced electrostatic charging of the lubricant molecules in the dry environment, creating more charged species which respond to the electric field between slider and disk. A reduction in the number of water molecules in the HDI environment may also increase the number of bonding sites on the slider DLC surface available for bonding with the lubricant end groups. In contrast, the greater number of water molecules present in the air at high RH would compete with lubricant or lubricant degradation products for bonding sites on the carbon surface on either the slider or the disk [52, 53, 253, 266]. Water molecules can be absorbed onto the lubricant or carbon overcoat of either the slider or the disk and may displace lubricant [52, 53, 253, 266]. Hence, in high humidity environments in combination with E-fields, the presence of water in the air may prevent large accumulations of lubricant or lubricant degradation products onto the slider surface compared to low humidity environments.

Our AFM measurements indicate that deposit formation occurs primarily in close proximity to the portion of the slider that contacts the disk during wear testing. Nakayama et al. [267] discussed tribochemical reactions at the HDI, distinguishing three different regions: 1) inside the contact area, 2) near the contact area, and 3) far away from contact area. Nakayama et al. [267] suggest that inside the contact area, acid-based reactions take place, perhaps leading to wear; in close proximity to the contact area in the near contact region, very large E-fields are presents that may decompose the lubricants via electrons, ions, or radicals; and regions far away from the contact region usually undergo a limited amount of reactions, perhaps resulting in deposition on bondable sites of the slider carbon. Spada et al. [268] investigated deposit formation on the surfaces of

magnetic tape recording heads. Their work suggests that tribochemical reactions need to be considered in tribological systems in addition to mechanical wear.

Further investigations are required to better understand the mechanisms responsible for the strong influences of HDI bias polarity and relative humidity on deposit formation both with and without direct slider-disk contact.

Regarding our experimental set-up and the choice of biasing the disk instead of the slider, it shall be mentioned that the design of our spin-stand tester made it easier to access and bias the spindle. This is because the spin-stand electronics share the same electrical ground as the slider, and because the spin-stand electronics cannot be easily modified without affecting the functionality of the spin-stand. In a hard disk drive, both the slider and the disk can be individually accessed for biasing. It is, however, more desirable to bias the slider rather than the spindle in order to avoid an electrical contact to the spindle with a moving interface.

6.8 Summary

The following observations were made:

1. The change in touch-down power before and after wear testing (ΔTDP) decreases with increasing disk bias (decreasing slider bias) for levels in RH larger than 25 %, independent of the tester being used (load/unload vs spin-stand tester), lubricant type and whether the slider or the disk was biased. For 8 % RH, the measured change in touch-down power was found to increase with increasing disk bias (decreasing slider bias).

2. AFM images showed deposits in the R/W region for sliders tested at low relative humidity (RH $\leq$ 8 %), and when biasing the disk with a negative bias voltage independent of humidity. Deposits were found next to the write shield towards the

slider trailing edge, on top of the write shield, or on top of the read shields. TOF-SIMS analysis revealed that the deposits consist of either fluorocarbon lubricant or, more likely, degraded fluorocarbon lubricant fragments.

3. AFM analysis revealed that ΔTDP may not be suitable as an indicator of slider wear because material removal and deposit formation may occur simultaneously. The latter is expected to reduce the measured change in touch-down power.

4. TOF-SIMS analysis suggests increased wear on the disk for positive disk bias (negative slider bias) and that lubricant transfer from the disk to the slider is enhanced for -1 V disk bias compared to + 1 V disk bias during sweep testing in the absence of slider-disk contacts.

The results presented in this paper indicate that both the relative polarity of the HDI voltage and relative humidity affect wear and deposit formation on the slider.

6.9 Acknowledgements

We would like to thank Daniel K. Bilich for conducting the TOF-SIMS measurements and valuable discussions.

Chapter 6, in part, is a reprint of "Effect of head-disk interface biasing and relative humidity on wear of thermal flying height control sliders", Liane M. Matthes, Frederick E. Spada, Andrey Ovcharenko, Bernhard E. Knigge, and Frank E. Talke (currently being prepared for submission for publication). The dissertation author was the primary investigator and author of this paper.

Chapter 7

Head-disk proximity sensing of thermal flying height control sliders

As discussed in 2.3.3, it is crucial to know the touch-down power (TDP) of a thermal flying height control (TFC) slider accurately to achieve the correct spacing during read and write operations. The touch-down power refers to the heater power at which contact between the thermal slider protrusion and the disk occurs. During reading and writing, the head-disk spacings is set to 1-2nm which is achieved by setting the power input to the heater a few mW below the touch-down power. If the resulting spacing is too large, the likelihood of read and write errors is increased. If the resulting spacing is too small, intermittent head-disk contacts are likely to occur. Head-disk contacts are undesirable as they are associated with wear and degradation of the head-disk interface. Consequently, it would be useful if one could predict the touch-down power by sensing proximity several milliwatt before actual head-disk contact occurs.

In this chapter, we present a new approach for predicting the touch-down power of a thermal flying height control slider. The method utilizes the contact sensor to sense head-disk proximity prior to actual head-disk contact. Impeding contact is predicted

based on a change in dynamics from heater input to sensor output. A step in heater power with varying DC bias is applied to the heater element and the corresponding sensor voltage output is measured. An increase in DC bias reduces the flying height. The transfer function from heater power to sensor voltage output is estimated via the step realization algorithm. It is shown that the coefficients of the transfer function can be used to predict the touch-down power without having to perform a complete touch-down measurement. The effect of step height is investigated and an alternative approach involving sinusoidal heater modulation is presented.

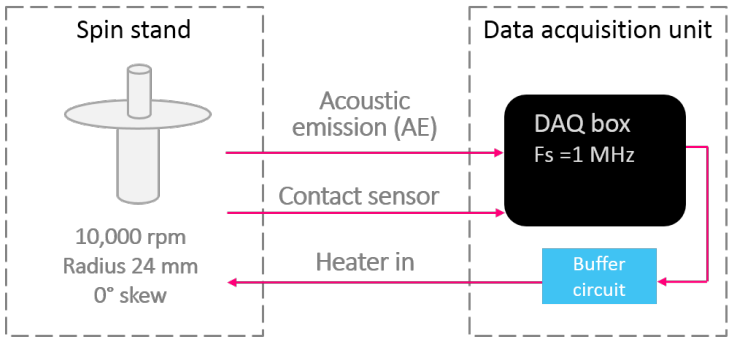

Figure 7.1: Experimental set-up for predicting impeding head-disk contact. Spindle speed, radial position and slider skew angle was controlled by the spin-stand system. A personal computer (PC) and data acquisition box were used for generating the heater input and acquiring various voltage signals.

7.1 Experimental set-up

A figure of the experimental set-up is shown in Fig. 7.1. The experimental setup consists of a spin-stand and data acquisition unit. The spin-stand controls spindle speed, the radial position of the slider, and slider skew angle. The data acquisition unit consists of a personal computer and a data acquisition box used for acquiring the voltage across the contact sensor. Data were acquired using a sampling frequency of 1 MHz. The data acquisition unit was also used to generate the power input to the heater element to adjust

the flying height of the slider. The contact sensor was biased with a constant current of 1.5 mA.

Commercially available femto [131] TFC sliders and 65 mm glass disks were used for the experiments. The suspension was a dual-stage suspension designed for disk speeds of 10000 rpm. The experiments were performed at a radial position of 24 mm with a slider skew angle of 0 °.

7.2 Experimental results

7.2.1 Prediction of touch-down power using the standard deviation of the contact sensor

The touch-down power of the TFC slider used in this paper was determined by increasing the power input to the heater in steps of 1 mW/disk revolution. For each power level, the standard deviation and mean value of the sensor voltage were calculated. Figure 7.2 shows the standard deviation (dotted line) and mean value (solid line) of the contact sensor voltage versus heater power.

We observe from Fig. 7.2 that the standard deviation (dotted line) is nearly constant for heater powers up to 97 mW. For heater powers larger than 97 mW, the standard deviation of the contact sensor increases significantly. Head-disk contact is detected at a critical heater power of 99 mW, which is indicated by the black dotted vertical line in Fig. 7.2. In addition to the standard deviation of the contact sensor voltage, Fig. 7.2 also shows the mean of the contact sensor voltage (solid line), as a function of heater power. This curve increases initially, reaches a local maximum at 91 mW, and then decreases thereafter. For heater powers larger than 103 mW, the mean sensor voltage increases again which appears to be caused by frictional heating during slider-disk contact.

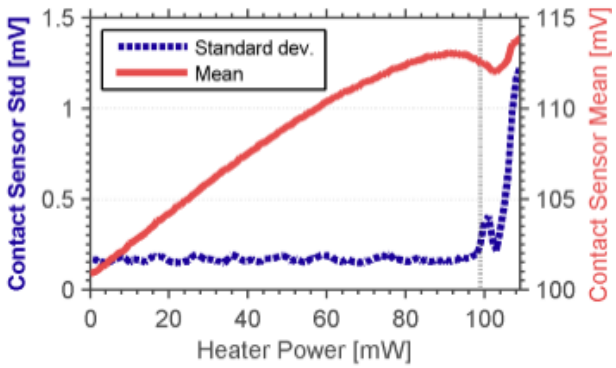

Figure 7.2: Contact sensor voltage standard deviation (solid line) and mean (dashed line) versus heater power.

7.2.2 Prediction of touch-down power using transfer function approach

The step realization algorithm can be used to estimate the transfer function of a system from step response data [176]. Because of measurement noise, it is expedient to perform multiple step response measurements and use averaged step response data to estimate the transfer function. For the purpose of averaging, we apply rectangular pulses as power input to the heater element rather than steps in heater power.

The procedure for determining the transfer function as a function of DC level in heater power is shown in Fig. 7.3. The transfer function from heater power to sensor voltage is determined by first measuring the average sensor voltage in response to rectangular pulses in heater power as a function of flying height. Different flying heights were realized by increasing the DC level of the heater pulses. Thereafter, the averaged sensor voltage response was normalized. From this data, we estimated the corresponding discrete-time transfer function of the contact sensor using the step realization algorithm. The coefficients of a first-order discrete-time transfer function were determined

as a function of the DC level in heater power as shown below

$$G(z, H_{Heater}) = \frac{b_0(P_{Heater})}{z + a_0(P_{Heater})} \tag{7.1}$$

where the time constant and DC gain of the system are given by $1/a_0$ and b_0/a_0, respectively. For this paper, pulse widths of 0.5 ms and pulse amplitudes of 4, 6, 8, 10, or 12 mW were used.

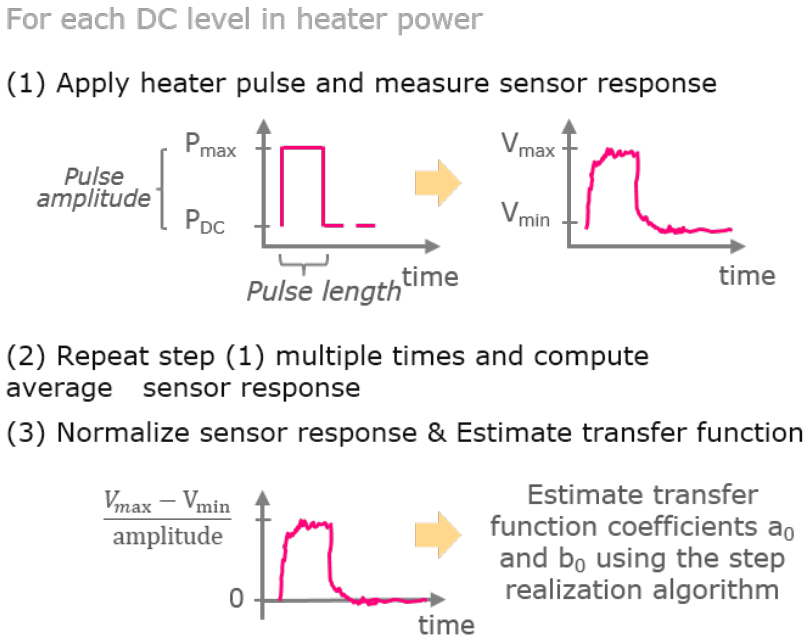

Figure 7.3: Procedure used to determine the heater power to contact sensor transfer function as a function of DC level in heater power.

Fig. 7.4 shows the normalized and averaged sensor voltage response with different DC levels in heater power. It can be observed in Fig. 7.4 that the amplitude and time constant of the measured sensor response is different for different DC levels in heater power. This observation suggests that the voltage response of the contact sensor to a step in heater power is different for different flying heights.

Fig. 7.5 shows the coefficients of the estimated first-order discrete-time transfer functions versus maximum heater power. Here, the maximum heater power denotes the

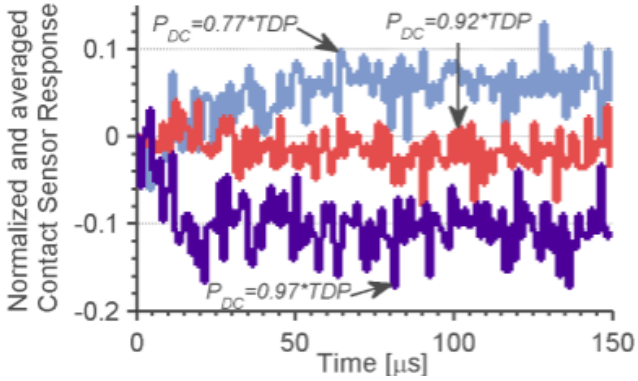

Figure 7.4: Normalized and averaged sensor voltage in response to a positive 4 mW step in heater power starting from DC level in heater powers of a) 77 % of the touch-down power, b) 92 % of the touch-down power, and c) 97 % of the touch-down power.

maximum power input applied to the heater that results from the pulse, as indicated in step (1) in Fig. 7.3.

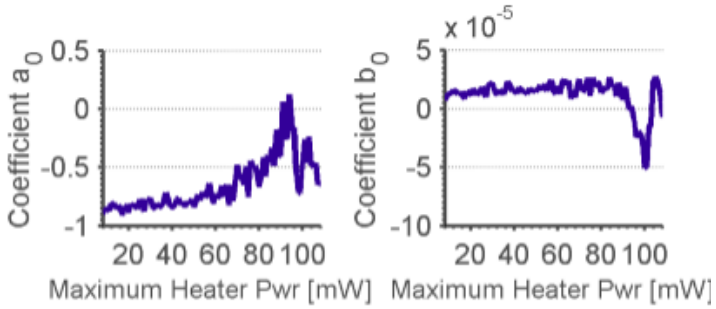

Figure 7.5: Coefficients of the identified first-order discrete time transfer function of the contact sensor voltage in response to a 4 mW step in heater power versus maximum heater power.

From Fig. 7.5, we observe that the coefficient a_0 is constant for small heater powers but increases very strongly for heater powers larger than ∼60 mW. The coefficient a_0 reaches a maximum at 94 mW, followed by a dip at 98 mW maximum heater power. The coefficient b_0 remains approximately constant for heater powers up to 90 mW. For heater powers larger than 90 mW, the coefficient b_0 decreases initially in value but increases again strongly as the heater power exceeds 101 mW.

In Fig. 7.6, we compare the standard deviation of the sensor voltage and the

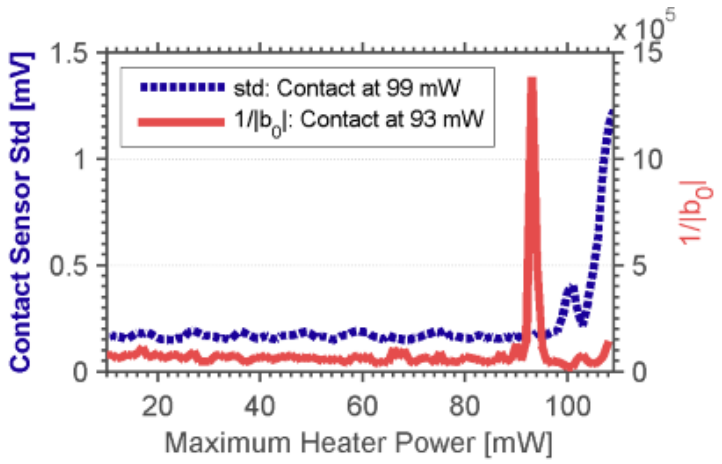

Figure 7.6: Standard deviation of the contact sensor voltage (dotted line) and inverse of the absolute value of coefficient b_0 (solid line) versus maximum heater power.

inverse of the absolute value of the coefficient b_0. As discussed earlier in Fig. 7.2, head-disk contact is detected at a heater power of approximately 99 mW if the standard deviation of the contact sensor voltage (dotted line) is used. In comparison, the curve $1/|b_0|$ shows a peak at 93 mW heater power which is lower than the touch-down power of 99 mW.

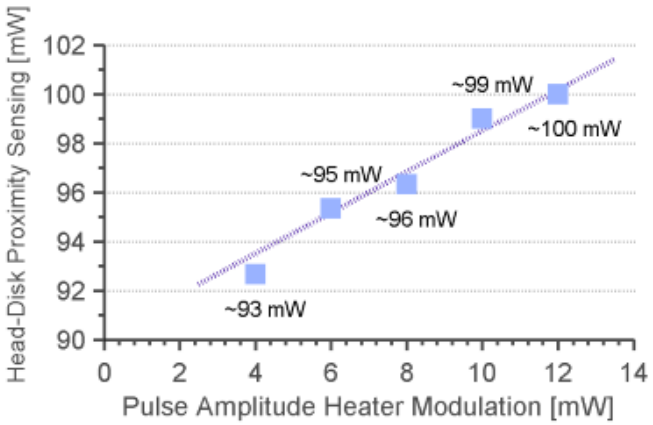

Figure 7.7: Maximum heater power (average of three measurements) at which head-disk proximity is sensed using the inverse of the absolute value of coefficient b_0 versus pulse amplitude during heater modulation.

Fig. 7.7 shows the average power levels at which head- disk contact would be detected when using different pulse amplitudes. Pulse amplitudes of 4, 6, 8, 10, and

12 mW were used and three measurements were taken for each amplitude. It can be observed in Fig. 7.7 that the power level at which head-disk proximity is sensed using $1/|b_0|$ increases with increasing pulse amplitude. The maximum heater power is amplitude dependent due to the local maximum of the sensor mean curve, as shown earlier in Fig. 7.2.

7.3 Alternative method using sinusoidal input

Step-realization involves performing the singular value decomposition of the shifted Hankel matrix. The shifted Hankel contains the step response of the sensor voltage of length N and the matrix is of size N by N. Hence, the proposed method is fairly 'expensive' from a computational point of view.

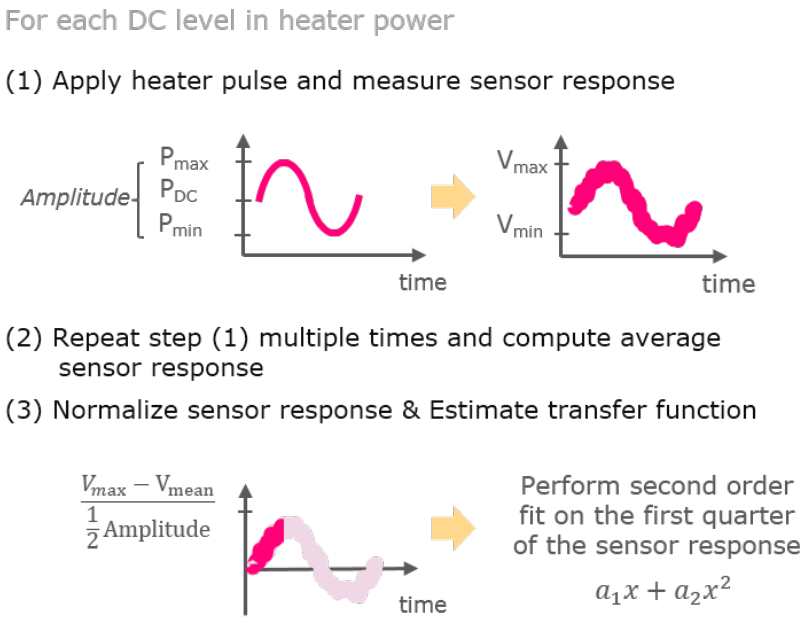

Figure 7.8: Procedure for determining the transfer function from heater power to contact sensor as a function of DC level in heater power using sinusoidal heater modulation.

Alternatively, the touch-down power can be predicted by modulating the heater

input with a sinusoid of amplitude A as shown in Fig. 7.8. Next, the corresponding sensor voltage output is measured multiple times and the average is computed. In step 3), the first quarter period of the sensor response is normalized and a second order polynomial curve fit is applied given by

$$y_{fit} = a_1 x + a_2 x^2 \tag{7.2}$$

Fig. 7.9 shows coefficients a_1 and a_2 of the second order polynomial curve fit of the sensor response as a function of maximum heater power. The maximum heater power denotes the maximum power input applied to the heater resulting from the sinusoidal heater modulation as indicated in Fig. 7.8.

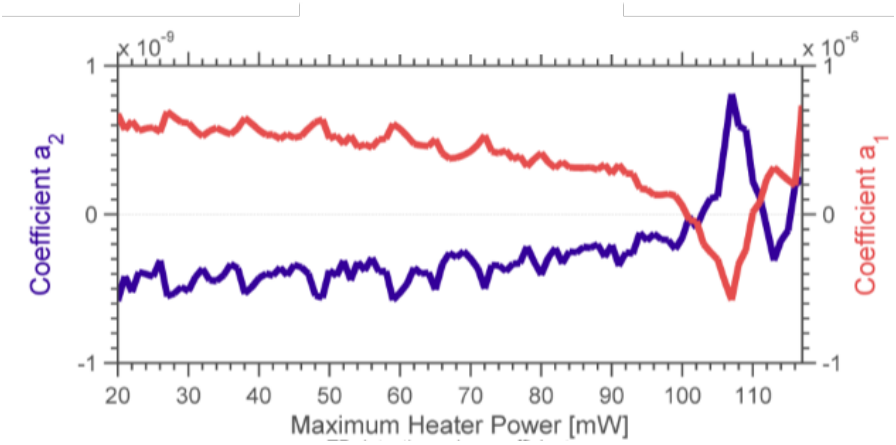

Figure 7.9: Coefficients of the second order polynomial curve fit of the contact sensor voltage in response to a sinusoidal heater modulation with an amplitude 4 mW.

From Fig. 7.9 we observe that coefficient a_1 is constant for small heater powers but starts decreasing for heater powers larger than 96 mW. Coefficient a_1 reaches at minimum at around 108 mW heater power and increases thereafter. Coefficient a_2 is also approximately constant for small heater powers and shows a noticeable increase for heater powers larger than 99 mW. A maximum is reached at 108 mW heater power and thereafter, coefficient a_2 decreases. Similar to the case of rectangular heater modulation,

we found that the inverse of the absolute value of coefficient a_1 can be used to 'sense' impeding head-disk contact.

Fig. 7.10 shows the average heater power at which head-disk contact would be sensed when using different amplitudes of sinusoidal heater modulation. Amplitudes of 4 mW, 6 mW, 8 mW, 10 mW and 12 mW were used and two measurements were taken for each amplitude. From Fig. 7.10 we observe that the heater power at which head-disk proximity is sensed using $1/|a_1|$ increases with increasing modulation amplitude, except for an amplitude of 8 mW.

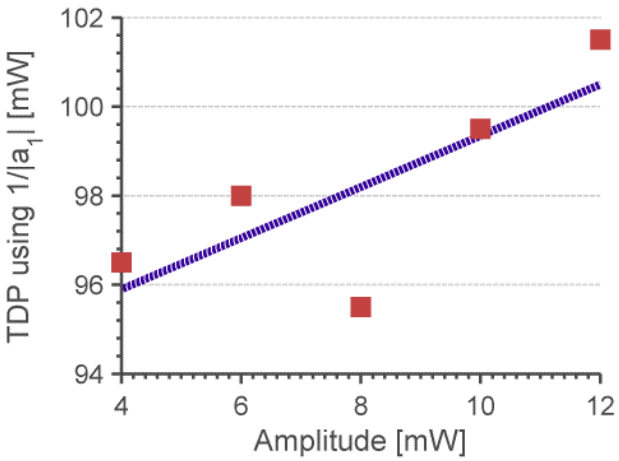

Figure 7.10: Maximum heater power (average of two measurements) at which head-disk proximity is sensed using the inverse of the absolute value of coefficient a_1 versus amplitude of sinusoid during heater modulation.

7.4 Discussion

We have shown that the touch-down power can be predicted before actual head-disk contact using the coefficient b_0 of the heater to sensor voltage transfer function. The coefficient b_0 of the first order, discrete-time transfer function given in equation 7.1 is a measure of the DC gain divided by the time constant. Since the sensor voltage is proportional to the sensor resistance, which in turn is proportional to the sensor temper-

ature, we can conclude that changes in the coefficient b_0 are related to changes in the mean temperature of the sensor (dc gain) and changes in the cooling rate of the contact sensor (time constant). Consequently, the question arises why the cooling of the contact sensor changes as the slider approaches the disk surface.

Fig. 7.11 compares the resistance change of the sensor versus heater power for the case that the slider is positioned away from the disk a), and that the slider flies over the disk b).

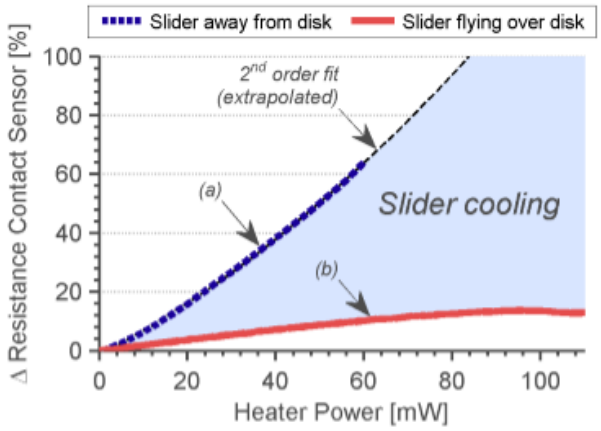

Figure 7.11: Change in contact sensor resistance versus heater power for a) slider away and not in contact with the disk and b) slider flying over the disk.

In case a) as indicated by the dotted line, the increase in contact sensor resistance was solely caused by increasing the power input to the heater. When increasing the power input to the heater, more heat is generated by the heater element which causes a change in the resistance of the contact sensor. In case b) (solid line), the resistance change of the contact sensor is smaller when the slider flies over the disk compared with the case when the slider is positioned away from the disk. Clearly, the difference between the two curves is caused by cooling due to the presence of the disk and the air flow between slider and disk. Possible mechanisms of heat transfer at the head- disk interface are heat conduction from the slider to the disk through the air film, slider cooling through heat convection by the air film, slider heating through viscous dissipation in the

air film, and possibly heat radiation from the slider to the disk.

A schematic of the head-disk interface indicating the relative location of the contact sensor and heater element for different heater powers is shown in Fig. 7.12. For increasingly larger heater power, the slider protrusion will approach the disk until it makes contact with the disk lubricant. As the heater power is further increased, contact between the slider protrusion and disk asperities will occur which should result in a temperature increase at the air bearing surface (ABS) caused by frictional heating.

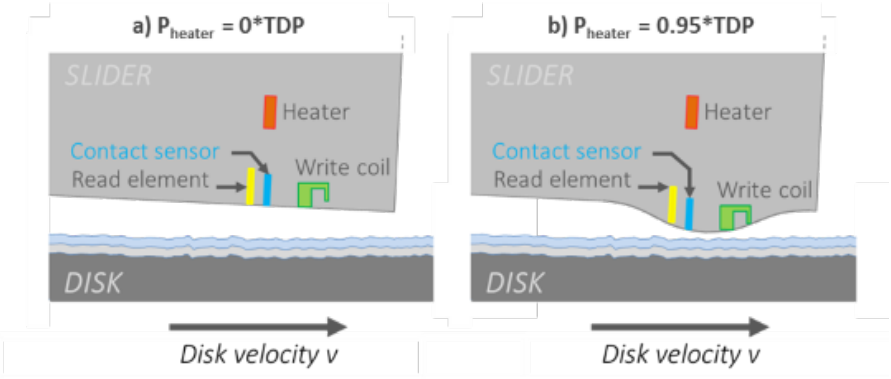

Figure 7.12: Schematic of the head-disk interface with relative location of the contact sensor and heater element for heater powers of a) P_{Heater} = 0*touch-down power, and b) P_{Heater} = 0.95*touch-down power.

When calculating the heat flux on the ABS of the slider one has to consider that the airflow between slider and disk is highly rarified. Traditional continuum computational techniques fail as the thickness of the flow becomes smaller than the mean free path of the air molecules. The Knudsen number, which is defined as the ratio of the free mean path λ over the slider-disk spacing, is used to describe the various regimes observed in rarefied gas flow: continuum flow (Kn < 0.01), slip flow ($0.01 \leq$ Kn < 0.1), transition flow ($0.1 \leq$ Kn < 10), and free molecule flow (Kn $\geq$ 10) [128]. For current flying heights of 1–2 nm during reading and writing and a free mean path of 65 nm for air, we obtain a Knudsen number of Kn $\geq$ 30 that is far beyond the continuum region. Thus, the modified Reynolds equation must be used together with the energy equation,

including velocity slip and temperature jump boundary conditions. Following this approach, Zhang and Bogy [269] derived an analytical expression for the heat flux q that includes heat conduction and viscous dissipation as follows

$$q = q_{conduction} + q_{dissipation} = -k\frac{T_{slider} - T_{disk}}{h + \frac{2-\sigma_T}{\sigma_T}\frac{4\sigma}{\gamma+1}\frac{1}{Pr}\lambda} + q_{dissipation} \tag{7.3}$$

where k is the thermal conductivity of air, T_{slider} and T_{disk} are the temperature of slider and disk, respectively; h denotes the local flying height of the slider; σ_T is the thermal accommodation coefficient; γ is the heat capacity ratio of the air, and Pr the Prandtl number. In order to improve accuracy of the heat conduction term in equation 7.3, several researchers proposed modified expressions for the mean free path [8-9]. The viscous dissipation term in equation 7.3 is small compared to the heat conduction term and has therefore been neglected in many studies [241, 270, 271]. However, Chen et al. [272] showed that viscous heating is no longer negligible for near-contact sliders by deriving an expression for viscous dissipation in the gas film through the energy conservation equation. Another approach to study heat transfer at the head-disk interface is based on the Boltzmann equation which assumes that collisions between molecules in the flow are absent. Shen and Chen [273] analyzed heat transfer using the linearized Boltzmann equation and showed that heat transfer at the head- disk interface is composed of heat conduction and viscous dissipation from Couette and Poiseuille flow. All objects loose energy through the emission of electromagnetic waves. The spectrum of thermal radiation of electromagnetic waves from a black body in thermal equilibrium at a specific temperature is given by Planck's law. However, Planck's law is not valid between bodies that are maintained at different temperatures if the distance is smaller than a few characteristic wavelengths of the thermally radiated electromagnetic waves. In fact, it was found that the radiative transport at the nano-scale can be orders of magnitudes larger

than Planck's law of black body radiation [274]. Motivated by these findings, Budaev and Bogy derived an analytical expression for the heat transport coefficient across a nano-scale vacuum gap [275].

In most heat transfer studies of the head-disk interface the temperature difference between slider and disk is assumed to be small which allows the assumption of isothermal flow at the head- disk interface which simplifies derivation of analytical expressions. The temperature at the ABS can be estimated from the resistance change of the contact sensor. Assuming that the relationship between the contact sensor resistance and temperature is linear, we have

$$\Delta R = \alpha \Delta T \tag{7.4}$$

where R and T are the change in resistance and temperature, respectively, and α denotes the temperature coefficient of resistance. A common material for contact sensors is NiFe which has a temperature coefficient of resistance of 0.2 %–0.3 % per °C. From Fig. 7.11, we observe that the contact sensor resistance increases by about 15 %. Thus, we estimate the temperature increase at the contact sensor to be 50 to 75 K using equation 7.4. This result suggests that the temperature distribution of the slider and the disk may not be uniform.

Fig. 7.13 shows the effect of disk velocity on the mean sensor resistance versus heater power. It can be seen that head-disk contact occurs at smaller heater power as the disk velocity decreases. Furthermore, we observe from Fig. 7.13 that the decrease in contact sensor resistance after the local maximum is largest for large disk velocities.

Theoretically, the transfer function describing the sensor voltage in response to a step in heater power should be of second order. However, we found that the coefficients of the corresponding second-order discrete-time transfer function are not suited to

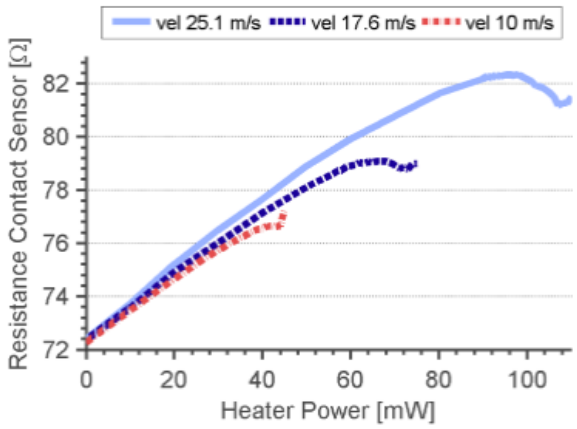

Figure 7.13: Effect of disk velocity on the resistance of the contact sensor versus heater power.

sense head-disk proximity using the proposed transfer function method. In general, our approach for sensing head-disk proximity is based on the change in DC gain and time constant of the contact sensor transfer function which can be described sufficiently via a first-order system. The transfer function approach described in the previous section was also performed on a different disk type. Similarly, we found that the touch-down power could be predicted before actual head-disk contact. This result suggests that the transfer function approach is not limited to a particular head-media combination.

7.5 Conclusion

A new approach was investigated for predicting the touch-down power of a TFC slider. A first-order discrete-time transfer function describing the contact sensor voltage in response to a step in heater power was estimated as a function of DC level in heater power. We conclude that:

1. The coefficient b_0 of the first-order transfer function can be used to predict the touch-down power several milliwatt before actual head-disk contact.

2. The proposed transfer function approach was used on different media and is not

restricted to a particular head- disk combination.

3. Knowledge of the transfer function of the contact sensor could be useful for optimizing the heater input to minimize flying height variations.

7.6 Acknowledgement

We would like to thank Prof. de Callafon for valuable discussions.

Chapter 7, in part, is a reprint of the material as it appears in "Head-Disk Proximity Sensing using Contact Sensors in Hard Disk Drives", Liane M. Matthes, Bernhard E. Knigge, and Frank E. Talke, *IEEE Transactions on Magnetics*, vol. 50, no. 11, 2014. The dissertation author was the primary investigator and author of this investigation.

Chapter 8

Flying height control using contact sensors in hard-disk drives

As discussed in 2.3.3, thermal flying height control sliders were originally introduced to correct for the write coil induced pole tip protrusion. Since the write element is comprised of a material with a higher thermal expansion coefficient compared to the remaining slider body, it expands and shrinks with a larger magnitude as temperature changes. Thus, during writing when a large high frequency current is applied to the write coil, the write element heats up and generates a protrusion toward the disk. This results in a lower head-to-media spacing during writing compared to reading. A similar phenomenon is observed during reading, however, the electrical power applied to the read element during reading is significantly smaller compared to the 'write power'. There are other factors that affect the flying height in a static fashion, for example, manufacturing tolerances and environmental variations such as ambient pressure changes [169], changes in temperature [171] and changes in humidity [172]. Typically, thermal flying height control sliders are being used in a quasi-static fashion by supplying the heater with a constant level of heater power to compensate for static spacing variations. The

level of heater power is adjusted according to changes in environment and disk operation (i.e., reading vs writing). There are, however, several factors that cause the flying height to change more dynamically around the circumference of the disk. These dynamic flying height changes result from disk waviness, disk distortions due to clamping, and slider vibrations induced by turbulence or even external shocks [169]. Since the read-back signal amplitude decreases exponentially with increasing magnetic spacing, flying height variations need to be minimized to ensure a low bit error rate [234]. Flying heights smaller than a particular 'target' flying height, on the other hand, increase the likelihood of slider-disk contacts, that also need to be avoided to reduce wear. It is clear that a dynamically controlled TFC slider can be used to optimally tune magnetic spacing while avoiding slider-disk contacts.

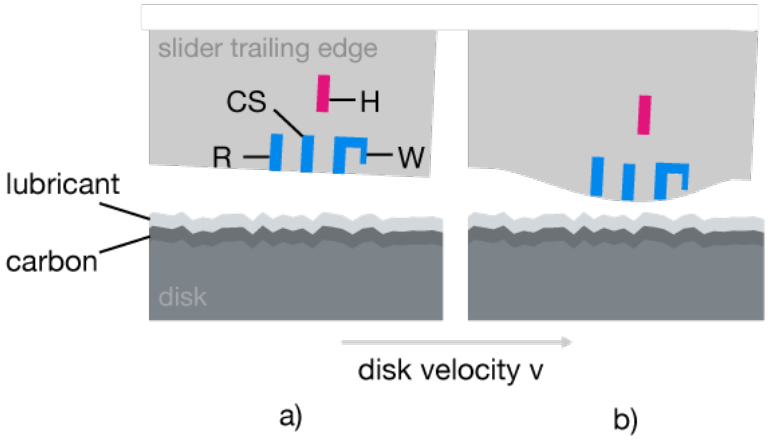

Figure 8.1: Schematic depiction of the operation of a thermal flying height control (TFC) slider. Head-disk interface showing the trailing edge of a thermal flying height control slider and the disk in a) its default state, and b) under heater actuation. The schematic depiction shows the resistive heater element (H), the contact sensor (TCS), the read element (R), and the write coil (W).

Several researchers [93, 173] have proposed methods for compensating dynamic variations in flying height. Shiramatsu et al. [173] proposed two different feedforward control schemes to compensate for modulations in the magnetic signal seen by the read element. One of the methods was based on the average read-back signal and the other

method involved the transfer function of the thermal actuator. However, little information was provided regarding the exact procedure and target flying heights were significantly larger (> 10 nm) compared to today's hard disk drives. Boettcher et. al [93] proposed a feedforward approach in which the optimal heater input profile is calculated using convex optimization techniques. The flying height modulation was estimated from the read-back signal via the modified Wallace spacing loss formula [93, 276]. The convex optimization procedure required knowledge of the relationship between heater input and the induced changes in flying height. To identify the dynamics of the system, the step-based realization algorithm was applied to experimentally obtained step-response excitation data applied to the TFC slider.

In recent years, thermal contact sensors (TCS), or touch-down sensors (TDS), have been implemented in TFC sliders, allowing detection of head-disk contacts and mapping of disk topography or disk defects [219, 249]. Thermal contact sensors are temperature sensitive resistive elements and located between the read and write element as indicated in Fig. 8.1. It has been shown that the sensitivity of thermal contact sensors for detecting head-disk contacts is similar to that of conventional acoustic emission (AE) sensors [220].

The read-back signal is a measure of the magnetic spacing, i.e., the spacing between the read element and the magnetic layer on the disk. Dynamic flying height adjustment based on the magnetic spacing may have potential drawbacks if there are variations in the thickness of the layers above the magnetic layer (e.g. the carbon overcoat and the lubricant). Furthermore, variations in the magnetic properties of the magnetic layer affect the amplitude of the read-back signal. The algorithm proposed by Boettcher et al. [93] greatly minimized flying height variations for mean flying heights in the range of 5 - 9 nm. As the relationship between the thermal actuator and the read-back signal was found to be non-linear for flying heights less than 2 nm, the method proposed by

Boettcher et al. may need to be modified for extremely small spacings in the range less than 2 nm. Thus, dynamic flying height control involving a sensor different than the read element is warranted.

In this study, we propose a method for minimizing flying height variations of TFC sliders. The method utilizes the embedded thermal contact sensor to estimate the flying height error, and model the dynamics of the TFC slider. First, we identify the static and dynamic behavior of the thermal contact sensor as a function of heater power. Based on the static and dynamic behavior of the system, the optimal power input profile to the heater is calculated using a convex optimization technique similar to Boettcher et al. [93]. The proposed approach is verified experimentally on a spin-stand tester and used to illustrate how flying height variations can be reduced dynamically.

8.1 Approach and experimental set-up

The paper is organized as follows: First, the static behavior of the thermal contact sensor (TCS; referred to as 'sensor' in the remainder of this paper) is discussed in section 8.2. Here, we address the operating range of the sensor, estimate the flying height error from the voltage output of the sensor by subtracting the effect of heater power, and determine the sensor gain based on voltage measurements from the sensor. In section 8.3, we identify the dynamics of the TFC slider based on measurements from the sensor. The dynamics of the TFC and sensor system is modeled from experimental step-excitation data using the step-based realization algorithm [93]. In section 8.4.1, the optimal power input profile to the heater is computed using convex optimization techniques [93] based on the static and dynamic behavior of the sensor, followed by experimental verification of the proposed algorithm in section 8.4.2.

The experiments were performed on a commercially available spin-stand tester

(MicroPhysics, Inc. [2]) as shown in Fig. 8.2. The disk rotates at 10,000 rotation per minute (rpm) using a pressurized air bearing spindle. Commercially available disks (90 mm in diameter) and recording heads were used for the experiments. Fig. 8.3 shows the bottom surface of the slider that faces the disk, also called air bearing surface (ABS), with the slider trailing edge at the top and the slider leading edge at the bottom. The read/write region is located at the center of the slider trailing edge. The head gimbal assembly (HGA) was operated on the bottom surface of the disk. The skew angle was approximately +13 ° and -13 ° for radial positions of 21 mm and 43 mm, respectively.

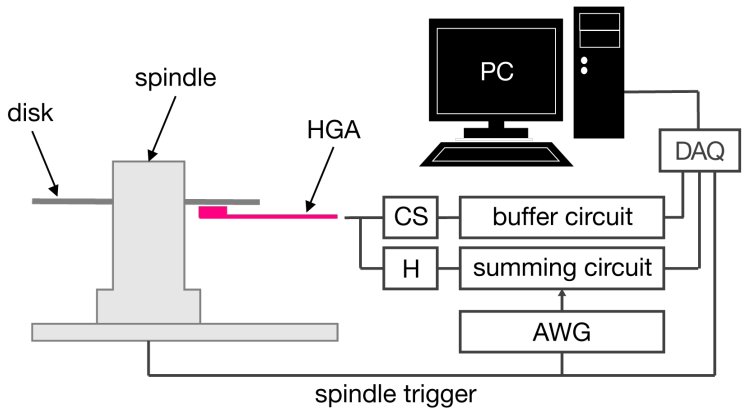

Figure 8.2: Experimental set-up. The input to the heater (H) in the TFC slider was generated using a data acquisition (DAQ) system and an arbitrary waveform generator (AWG). A constant bias current of 1.5 mA was applied to the thermal contact sensor (TCS) to measure the sensor voltage signal for detecting resistor variations in the TCS.

Heater actuation was accomplished by supplying a voltage across the heater corresponding to the desired heater power. Boettcher et al. [93] demonstrated that the resistance of the heater is not a strong function of the applied power and hence, a constant heater resistance was assumed for calculating the voltage input to the heater. The DC and AC component of the heater input were generated using the analog output of a data acquisition (DAQ) system and an arbitrary waveform generator (AWG), respectively. Both voltage signals were added using a buffering and summing amplifier circuit with

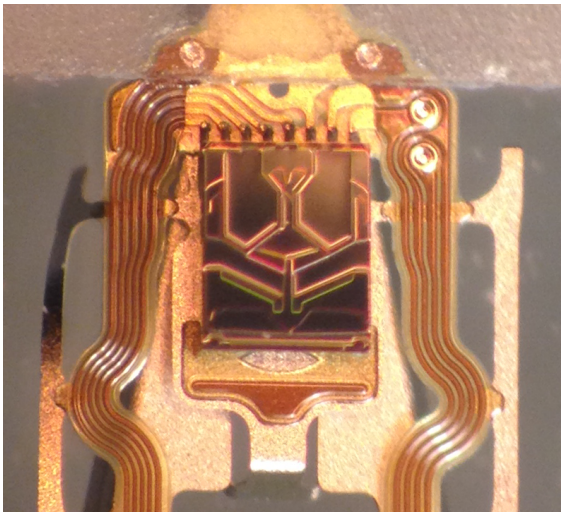

Figure 8.3: Air bearing surface (ABS) of the recording head used for flying height control.

a unity gain and a dynamic response characterized by a settling time of approximately 0.5 ns. The output of both instruments is triggered with the once-around trigger signal of the spindle.

The thermal contact sensor was biased with a constant current of 1.5 mA and the resulting voltage across the sensor was acquired using the DAQ device at a sampling frequency of 1 MHz.

8.2 Static characterization of thermal contact sensors

8.2.1 Mean and standard deviation trends

To illustrate the sensitivity of the TCS, we show the sensor voltage as a function of heater power in Fig. 8.4 at a radial position of 27 mm on the disk. We observe from Fig. 8.4 that the standard deviation of the sensor voltage (solid curve) is nearly constant for heater powers up to 130 mW. For heater powers larger than 130 mW, a sudden increase in the sensor standard deviation is observed. The onset of slider-disk contact

occurs at 134.5 mW. This is indicated by the vertical dashed line in Fig. 8.4. The dashed curve in Fig. 8.4 represents the mean of the sensor voltage. The sensor mean voltage increases initially, reaches a local maximum at 122.5 mW, and decreases thereafter.

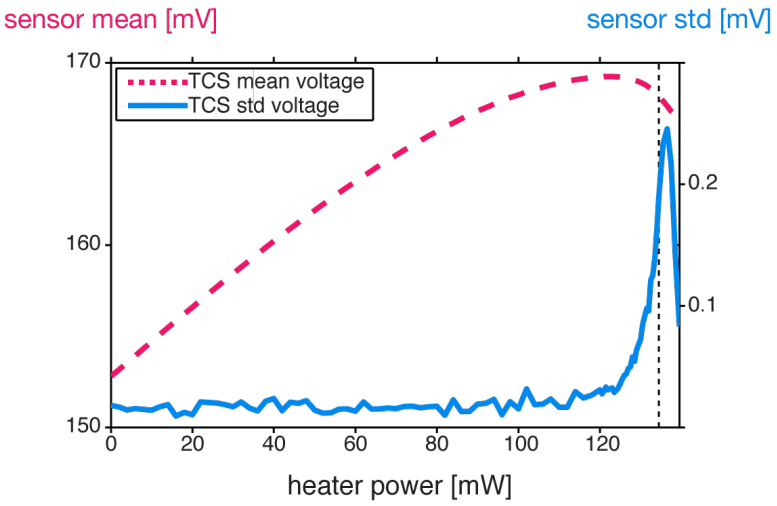

Figure 8.4: TCS voltage output versus heater input power. Head-disk contact is detected at 134.5 mW according to the sensor standard deviation (std) as indicated by the vertical dashed line.

Fig. 8.4 illustrates that the mean sensor voltage creates a measurable signal and becomes 'active' in close proximity with the disk – the exact operating condition where the flying height should be for minimal magnetic spacing and largest read-back signals. However, spacing variations need to be reduced as much as possible to avoid intermittent contact at these spacing levels. The resistance and hence voltage output of the sensor are temperature dependent. The voltage output of the sensor, V_{TCS}, may therefore be expressed as a function of

$$V_{TCS} = f(I_{TCS}, P_{heater}, q) \tag{8.1}$$

in which I_{TCS} denotes the bias current for driving the sensor, P_{heater} is the electrical power applied to the heater for adjusting the head-disk spacing, and q refers to the heat flux in the neighborhood of the sensor which is a function of the head-disk spacing.

Clearly, the sensor voltage is a function of the sensor temperature ('heating') and the heat flux at the interface ('cooling').

8.2.2 Estimation of flying height changes

To use the sensor as an estimate for changes in flying height, we apply a third order polynomial curve fit to the sensor mean voltage over a specified curve fit range and subtract the curve fit from the sensor mean voltage. The curve fit y_{fit} is described by

$$y_{fit} = a_0 + a_1 P_{heater} + a_2 P_{heater}^2 + a_3 P_{heater}^3, \qquad P_{heater} \in [0, k \cdot TDP]\ mW \tag{8.2}$$

in which a_0, a_1, a_2, a_3 are the coefficient of the third order polynomial curve fit and k denotes the curve fit range expressed as a percentage of the touch-down power TDP (i.e., the onset of slider-disk contact indicated by the vertical dashed line in Fig. 8.4).

Fig. 8.5 a) shows the sensor mean voltage (dashed line) as a function of heater power for various third order polynomial curve fits. Curve fitting was performed over a range starting from 0 mW up to heater powers of $k = 70$ %, 80 %, 85 %, or 90 % with respect to the TDP in equation (8.2). Subtracting the extrapolated third order polynomial curve fit from the sensor mean voltage yields the control curve shown in Fig. 8.5 b). The control curve compensates for the effect of heater power and as a result is nearly zero for a heater power up to 122.5 mW and decreases thereafter. The decrease is caused by cooling of the TCS when reducing the head-disk spacing. The region between 122.5 mW and the touch-down power at 134.5 mW outlines the operating region suitable for flying height control. To use the sensor as an estimate for changes in flying height, we investigated polynomial curve fits of several orders. Since we desire a control curve

that is zero for small heater powers and increases strongly prior to the onset of head-disk contact, we chose a cubic polynomial curve fit instead of a linear or quadratic fit.

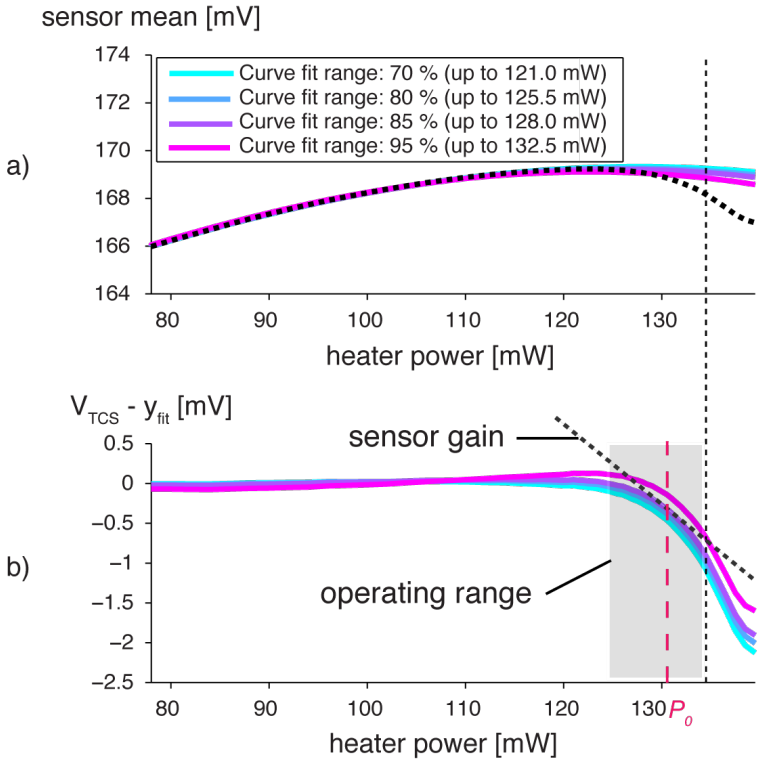

Figure 8.5: a) sensor mean voltage (dashed line) versus heater power and various third order polynomial curve fits (solid lines) of the sensor mean data; b) control curve which is obtained be subtracting a third order polynomial curve fit from the sensor mean voltage. The onset of slider-disk contacts is indicated by the vertical dashed line.

For control purposes it is of interest to know the slope of the control curve (which is indicated as the sensor gain) at the desired operating power P_o (see Fig. 8.5). The sensor gain is determined by applying a linear fit to the control curve in the range -1 mW $\leq P_0 \leq +1$ mW. Clearly, the sensor gain will depend on the curve fitting results of equation (8.2) used to eliminate the effect of heater power from equation (8.1), where k in (2) determines the curve fitting range. Fig. 8.6 shows the sensor gain at an operating power 4 mW below the onset of slider-disk contact, i.e., $P_0 = 130.5$ mW, at a radial position of 27 mm. We observe that the magnitude of the slope is not a strong

function of the curve fit range.

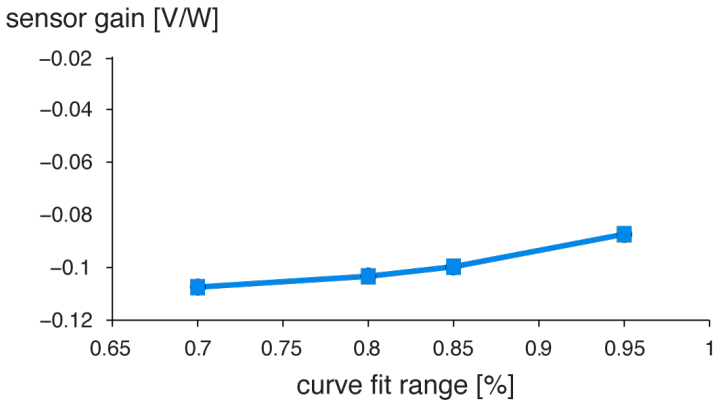

Figure 8.6: Sensor gain at operating power P_0 as a function of curve fit range (R = 27 mm).

For this study, a curve fit range of 85 % is used as this curve fit range appears to best describe the sensor mean voltage.

8.2.3 Effect of radial position on the disk

The radial position of the recording head over the disk affects the TDP, i.e., the heater power at which the onset of slider-disk contact occurs indicated earlier by the vertical dashed line in Fig. 8.4. This is because the flying height of the slider and hence the touch-down power increase with increasing disk velocity. As the air bearing surface of the slider is asymmetric, the flying height and touch-down power are also skew angle dependent. As a consequence, both the TDP and the coefficients of the third order polynomial curve fit as defined in equation (8.2) and the sensor gain at the operating point P_0 are also disk radius dependent. With changes in the TDP and thus changes in the sensor mean and control curves depicted earlier in Fig. 8.5, changes in the sensor gain are expected. To show this dependency, measurements of TDP were obtained at different radii on the disk and the results are summarized in Fig. 8.7. In can be observed that the TDP increases, as expected, toward the outer diameter of the disk.

It may therefore be necessary to create look-up tables in order to compensate for the effect of radial position for flying height control.

Fig. 8.8 shows the effect of disk radius on the sensor gain at operating powers 4 mW below the onset of head-disk contact, illustrating that the magnitude of the sensor gain is largest close to the middle diameter of the disk.

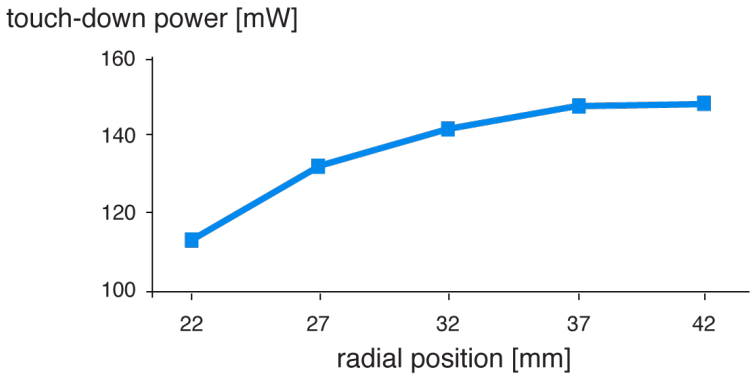

Figure 8.7: Measured dependency of touch-down power (TDP) on the radial position of the slider along the disk rotating at the same rpm.

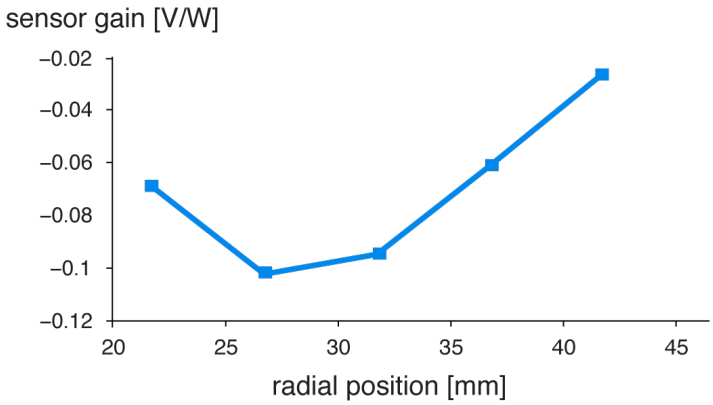

Figure 8.8: Sensor gain at operating power P_0 as a function of disk radius.

A change in disk velocity and skew angle causes a change in flying height and slider pitch angle and thus, the thermal response of the contact sensor. Hence, the observation that the sensor gain is largest at the middle diameter appears to be related to a combination of changes in flying height, pitch angle and skew angle of the slider.

8.3 Dynamic modeling

In order to compute the optimal feedforward heater profile via convex optimization, a dynamic model of the thermal actuator is needed. The step-based realization algorithm [93] allows the estimation of a linear time invariant discrete time model of the thermal actuator from experimentally obtained step-response data. The step response data is created via a step wise excitation signal applied to the TFC and measuring the TCS signal around the operating condition of P_0.

As discussed in section 8.2.1, the flying height error is estimated from the voltage output of the thermal contact sensor. Fig. 8.9 shows again the control curve at a radial position of 27 mm obtained using a curve fit range of 85 %. P_0 denotes the desired operating power and the dashed horizontal line indicates the corresponding set-point r_{cc} of the control curve. In this paper, we focus on an operating power 4 mW below the onset of slider-disk contacts, i.e., $P_0 = 130.5$ mW.

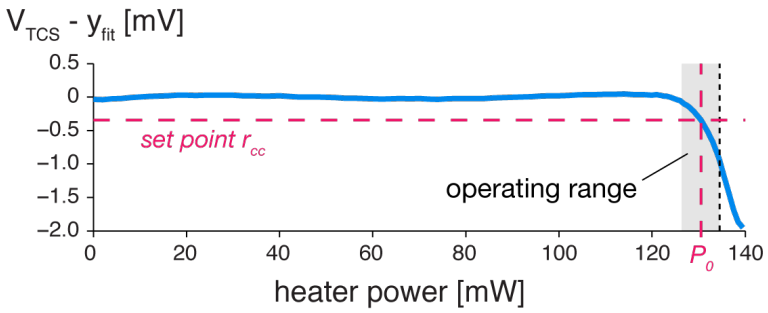

Figure 8.9: Control curve vs heater power with desired operating power P_0 and corresponding set-point.

To obtain a measure of the flying height error over one disk revolution, the following procedure was used: First, the average sensor voltage V_{TCS} of 20 disk revolutions was acquired. Thereafter, the curve fit y_{fit} of the mean voltage (see Fig. 8.6 a)) was subtracted from the instantaneous sensor voltage V_{TCS} via linear interpolation. The resulting curve was then compared to the control curve set-point r_{cc} (see Fig. 8.9), yielding error

signal ε

$$\varepsilon = r_{cc} - (V_{TCS} - y_{fit}) \tag{8.3}$$

The error signal ε of 20 disk revolutions (down-sampled from 1 MHz to at 16.67 kHz) is shown in Fig. 8.10. The dots represent the average of 20 continuous disk revolutions and the solid lines indicate the corresponding standard deviation. It can be seen that the error signal varies repetetively with every disk revolution.

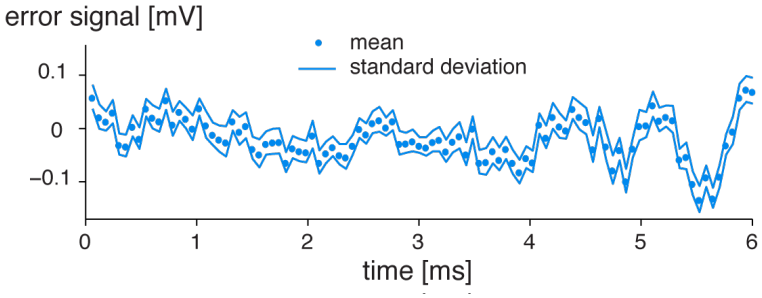

Figure 8.10: Error signal versus time for one disk revolution (average of 20 consecutive disk revolutions).

Next, we estimate the dynamics between heater power and error signal in state space form

$$\begin{aligned} \mathbf{x}(k+1) &= \mathbf{A}\mathbf{x}(k) + \mathbf{B}u(k) \\ \Delta\varepsilon(k) &= \mathbf{C}\mathbf{x}(k) \end{aligned} \tag{8.4}$$

where $\mathbf{x}(k) \in \mathbb{R}^{2\times 1}$ denotes the state vector and the state-space matrices $\mathbf{A}$, $\mathbf{B}$, and $\mathbf{C}$ are obtained via the identification procedure described in section 8.3. The following procedure is used for estimating the state space model: First, the average error signal of 20 disk revolutions, denoted ε_0, is acquired while supplying the heater with the desired DC operating power P_0 = 130.5 mW. Next, the experiment is repeated while modulating the heater input with rectangular pulses, yielding ε^*. We then subtract ε_0 rom ε^* to obtain the change in error signal due to applying a step in heater power. Fig. 8.11 shows

the error signal vs time for various steps in heater power. The time duration of each step was 3 ms. Using the realization algorithm in [93], a second order discrete time model was identified for each set of step response data. The simulated system response is indicated by black dashed lines in Fig. 8.11. We observe that the identified second order systems are in good agreement with the measured step response data. Moreover, the dynamics of the model characterized by the time constants of the identified systems appear to be on the same order.

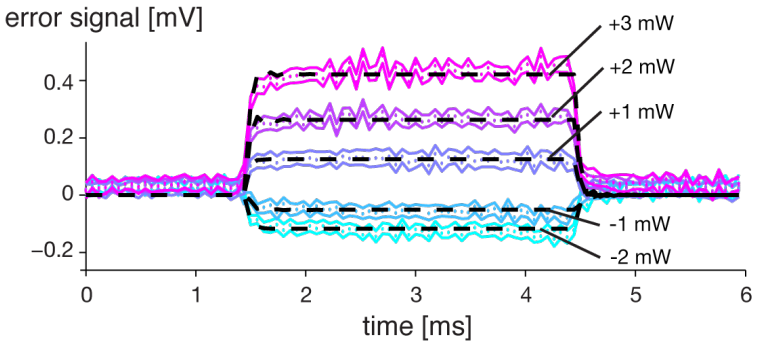

Figure 8.11: Comparison between measured and dynamic simulated error signal resulting from rectangular pulses in heater power (average of 20 consecutive disk revolutions).

Fig. 8.12 shows the Bode plot of the identified second order discrete time models that follow from applying +2 mW (dashed line) and +3 mW (solid line) steps in heater power, normalized by the step size for heater modulation. The time constants for the +2 mW system are 1.7×10^{-4} s and 9.1×10^{-4} s and for the +3 mW system 2.3×10^{-4} s and 10.1×10^{-4} s. The dynamics of the TFC actuator are similar for 2 mW and 3 mW step sizes in the power applied to the TFC, simplifying the control to linear (optimal) algorithms, as used in this paper, to reduce flying height variations.

The second order discrete time model can be represented in transfer function form as follows

$$G(z) = \frac{b_1 z + b_0}{z^2 + a_1 z + a_0} \tag{8.5}$$

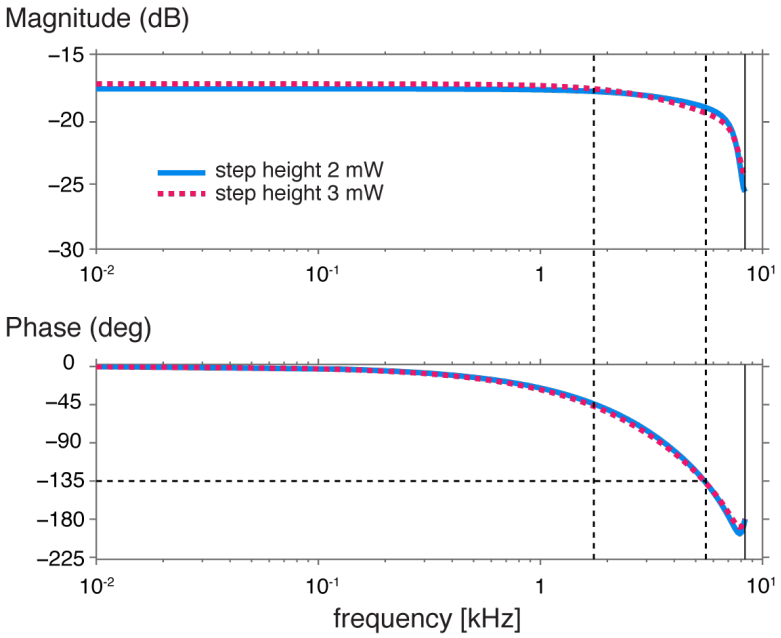

Figure 8.12: Bode plot of the identified second order discrete time models that follow from applying +2 mW (dashed line) and +3 mW (solid line) steps in heater power, normalized by the step size for heater modulation.

where the model parameters b_1, b_0, a_1 and a_0 are given in Table 8.1 for the identified models.

Table 8.1: Parameters of second order discrete time models

Step height [mW]	b_1	b_0	a_1	a_0
-2 mW	0.0444	0.0332	0.5079	-0.1899
-1 mW	0.0193	0.0349	0.3302	-0.2871
1 mW	0.1067	0.0999	0.7911	-0.1362
2 mW	0.1046	0.0900	0.5546	-0.0712
3 mW	0.1052	0.0871	0.4952	-0.1269

8.4 Computing the optimal heater input profile

The flying height error can be eliminated by actuating the heater element in a way so that the induced flying height changes match the inverse of the flying height

error. As Boettcher et al. [93] pointed out, this problem can be stated as a convex optimization problem where the flying height modulation is minimized in a 2-norm sense. In the following, the optimization algorithm will be discussed and thereafter, experimental results will be presented.

8.4.1 Optimization algorithm – theory

Equation (8.4) can be rewritten recursively as

$$\begin{aligned}
\Delta\varepsilon(0) &= \mathbf{C}\mathbf{x}(0) \\
\Delta\varepsilon(1) &= \mathbf{C}\mathbf{A}\mathbf{x}(0) + \mathbf{C}\mathbf{B}u(0) \\
\Delta\varepsilon(2) &= \mathbf{C}\mathbf{A}^2\mathbf{x}(0) + \mathbf{C}\mathbf{A}\mathbf{B}u(0) + \mathbf{C}\mathbf{B}u(1) \\
&\vdots \\
\Delta\varepsilon(2N) &= \mathbf{C}\mathbf{A}^{2N}\mathbf{x}(0) + \sum_{j=1}^{2N} \mathbf{C}\mathbf{A}^{2N-j}\mathbf{B}u(j-1)
\end{aligned} \tag{8.6}$$

Setting the initial state to zero, i.e., $\mathbf{x}(0) = 0$, we can express equation (8.4) in matrix form as

$$\boldsymbol{\Delta\varepsilon} = \boldsymbol{\Psi}\mathbf{u} \tag{8.7}$$

in which

$$\boldsymbol{\Psi} = \begin{bmatrix}
0 & 0 & 0 & \cdots & 0 \\
\mathbf{CB} & 0 & 0 & \cdots & 0 \\
\mathbf{CAB} & \mathbf{CB} & 0 & \cdots & 0 \\
\vdots & \vdots & \vdots & & \vdots \\
\mathbf{CA}^{2N-1}\mathbf{B} & \mathbf{CA}^{2N-2}\mathbf{B} & \mathbf{CA}^{2N-3}\mathbf{B} & \cdots & 0 \\
\mathbf{CA}^{2N}\mathbf{B} & \mathbf{CA}^{2N-1}\mathbf{B} & \mathbf{CA}^{2N-2}\mathbf{B} & \cdots & \mathbf{CB}
\end{bmatrix} \tag{8.8}$$

Based on this definition, the objective function of the optimization problem can

be stated as

$$\begin{aligned} \underset{\mathbf{u}}{\text{minimize}} \quad & \left\| \varepsilon_{target} - (\boldsymbol{\varepsilon_0} + \boldsymbol{\Psi}\mathbf{u}) \right\| \\ \text{subject to} \quad & \mathbf{u} \leq u_{max} \\ & \mathbf{u} \geq u_{min} \end{aligned} \tag{8.9}$$

In equation (8.9), ε_{target} denotes the target value of the error signal, $\boldsymbol{\varepsilon_0}$ is the error signal when supplying the heater with the desired DC operating power P_0, and $\boldsymbol{\Psi}\mathbf{u}$ are the contributions of heater modulation on the error signal. Limitations on the heater modulation are imposed via u_{min} and u_{max} to ensure that the electrical power supplied to the heater remains within the operating range.

8.4.2 Optimization algorithm – application

The average error signal of 20 disk revolutions in Fig. 8.10 shows significant high-frequency variations in flying height. As the bandwidth of the thermal actuator is limited (see Fig. 8.12), accounting for these high frequency variations in the error signal would result in large high frequency control inputs to the thermal actuator which is undesirable. A non-causal low-pass filter is therefore applied to limit the bandwidth of the error signal to 5 kHz as shown in Fig. 8.13.

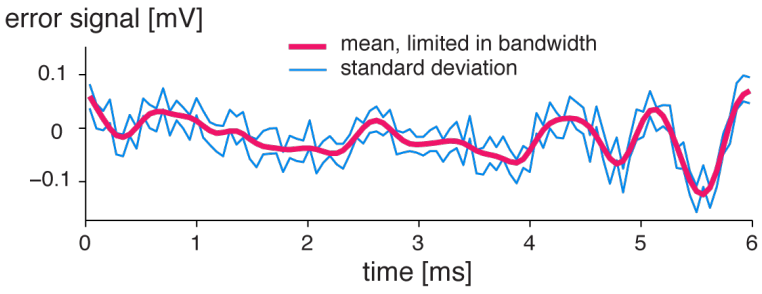

Figure 8.13: A non-causal filter was applied to the average error signal of 20 disk revolutions to limit the bandwidth of the signal to 5 kHz in order to avoid large high frequency control signals.

The optimal feedforward heater input profile for minimizing flying height vari-

ations was computed after equation (8.9) using the CVX software package [277, 278]. For the optimization procedure, we used the bandwidth limited error signal (Fig. 8.13) as $\boldsymbol{\varepsilon_0}$ and the mean value of $\boldsymbol{\varepsilon_0}$ was chosen to be ε_{target}. The state-space matrices **A**, **B** and **C** followed from applying a 2 mW step in heater power. The operating DC power was chosen to be 4 mW below the onset of slider-disk contact, i.e., $P_0 = 130.5$ mW. The nominal flying height without heater actuation is on the order of 10 - 12 nm. If we assume a linear relationship between heater actuation and flying height change, a 4 mW back-off power would correspond to a flying height of less than 0.5 nm.

After completing the optimization procedure, the calculated power profile was applied to the heater element and the corresponding error signal of 20 disk revolutions was measured. Fig. 8.14 shows a) the heater power versus time, and b) the error signal versus time over the duration of one disk revolution. The dots in Fig. 8.14 b) represent the mean of the error signal of 20 continuous disk revolutions, and the solid lines represent the standard deviation of the error signal.

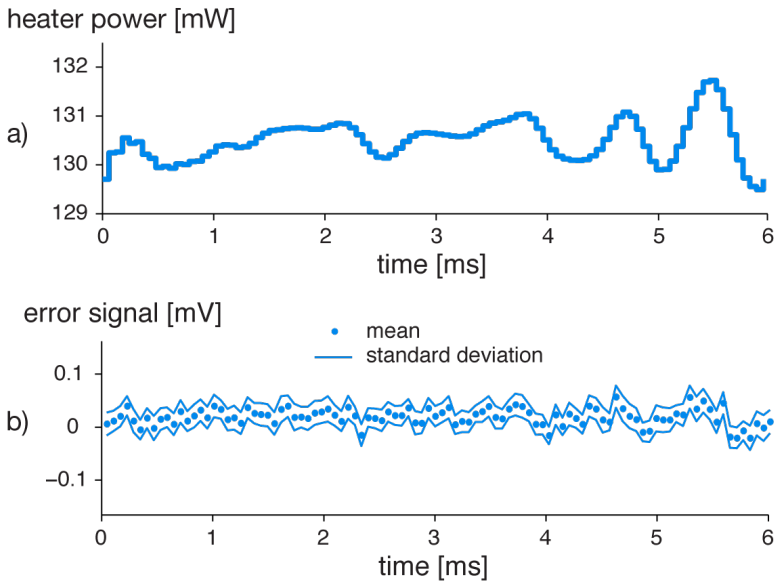

Figure 8.14: a) Heater power versus time, and b) error signal versus time while applying the optimal feedforward profile to the heater (average of 20 consecutive disk revolutions).

Our feedforward compensation targets the repeatable variations in flying height up to frequencies of 5 kHz. In fact, the error signal shown in Fig. 8.14 b) shows significantly less variations compared to the uncontrolled case shown in Fig. 8.10. In particular, the difference between the maximum and the minimum value is reduced from $2.1 \cdot 10^{-4}$ V to $1 \cdot 10^{-4}$ V and the standard deviation of the mean error signal is reduced from $4.1 \cdot 10^{-5}$ V to $1.8 \cdot 10^{-5}$ V. These results demonstrate that the proposed method is a promising technique for reducing variations in flying height in close proximity utilizing the embedded thermal contact sensor.

Fig. 8.15 shows the simulated amplitude of the step response of the identified models versus step height in heater input. We observe from Fig. 8.15 that the amplitude of the simulated step response increases with increasing step size in heater modulation, but the relationship is not linear. Hence, we performed experiments in which we scaled the heater input according to the curve shown in Fig. 8.15 to minimize flying height variations rather than using different models (e.g. 1 mW, 2 mW and 3 mW). However, our experiments did not show any performance improvements (i.e., reduced standard deviation or reduced min to max value) of the scaled heater input compared to an unscaled heater input.

In addition to the feedforward control approach presented in this paper, simulations were carried out to investigate the feasibility of real-time feedback control. Our simulation results showed that the additional performance improvements due to feedback were negligible compared to our proposed feedforward approach which can be traced back to the noisy nature of the sensor signal. Due to the noisy sensor signal, averaging of the sensor signal is required for minimizing flying height variations which makes feedforward control a suitable choice for our current set-up.

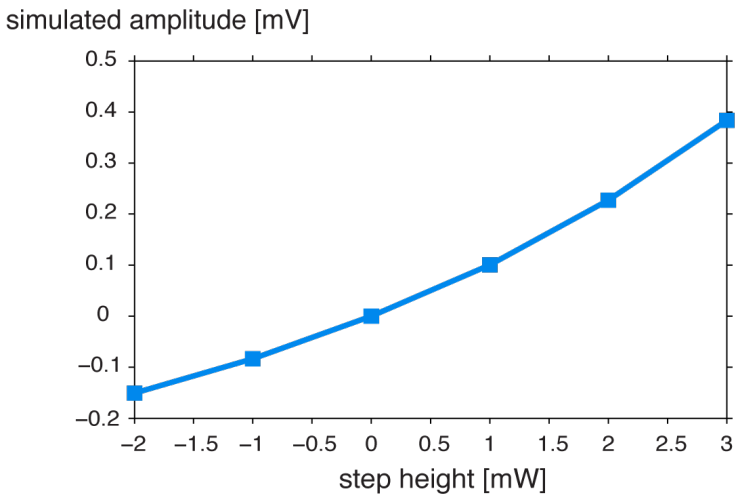

Figure 8.15: Simulated amplitude of the step response of the identified models versus step height in heater input.

8.5 Summary and conclusions

A modeling and optimization method was proposed and implemented for computing the optimal feedforward heater profile to minimize variations of flying height in hard disk drives. The method utilizes the resistive heater element of TFC sliders for adjustment of flying height at the read and write element and the embedded thermal contact sensor (TCS) as a relative measurement for changes in flying height. The flying height error is approximated by 1) applying a third order polynomial curve fit to the sensor mean versus heater power curve; 2) measuring the average sensor voltage over one disk revolution at the desired DC operating power; 3) subtracting the curve fit obtained in step 1) from 2); and 4) comparing the result to a desired set-point, yielding the error signal. A model of the system was identified from experimental step excitation data via a realization algorithm utilizing the full dynamic potential of the thermal flying height actuator. We found that the dynamics can be described using a second order model. The optimal heater input for minimizing flying height variations was obtained using convex optimization techniques. The optimization approach was verified

experimentally, showing that the proposed approach reduces the difference between the maximum and the minimum value of the TFC measurements by a factor of two, indication a twofold reduction of flying height variations. The touch-down power and voltage outputs of the thermal contact sensor was shown to depend on the radial position of the slider over the disk. Look-up tables may therefore be necessary to compensate for radial and skew effects on the proposed algorithm. The TCS only provides a reliable signal in close proximity of the disk in the sub-nanometer range. Controlling the variations of the TCS implies that flying height variations have been reduced at the sub-nanometer range. Future work will involve independent measurements of the sub-nanometer flying height variations to verify the validity of using the TCS and control of the TFC for sub-nanometer flying height control.

8.6 Acknowledgements

We would like to thank Dr. Uwe Boettcher for his help and comments during this work and the preparation of this manuscript.

Chapter 8, in part, is a reprint of "Near contact thermal flying height control in hard disk drives", Liane M. Matthes, Raymond A. de Callafon, Bernhard E. Knigge, and Frank E. Talke, *IEEE Transactions on Control Systems Technology*, vol. PP, no. 99, pp. 1-8 (2016). The dissertation author was the primary investigator and author of this paper.

Chapter 9

Summary and conclusions

In this dissertation, we focus on experimental investigations of the head-disk interface from both a tribological and controls point of view.

First, experiments were performed to investigate contact and temperature rise between a thermal flying height control (TFC) slider and a magnetic disk. To achieve head-disk contact, the heater element of a TFC slider was energized with constant and square wave input profiles with increasing bias. Laser Doppler vibrometry (LDV) was employed to measure the vertical motion of the gimbal. The temperature rise due to contacts was estimated via auxiliary resistance calibration measurements. It was found that the resistance change at the read element cannot be used to estimate the interfacial temperature rise due to frictional heating during contact, which can be attributed to the spatial separation between the contact spot and the read element, and limitations in the sampling frequency during data acquisition. In addition, the thermal energy generated at the contacting asperities is too small to cause a sufficiently strong response of the read element.

Next, the effect of bonded-lubricant ratio, relative humidity and temperature on head wear of TFC sliders were investigated. Head wear was studied by measuring the

change in the heater touch-down power before and after wear testing. The touch-down power denotes the heater power at which the onset of slider-disk contact occurs. In addition, scanning electron microscopy (SEM) and atomic force microscopy (AFM) images of selected heads were taken. It was found that head wear increases with increasing bonded-lubricant ratio, temperature has a minor effect on head wear for the temperature range of 30 °C to 50 °C, and head wear was increased at low relative humidity. SEM analysis showed wear of the write shield for changes in touch-down power typically larger than 6 mW. AFM analysis revealed noticeable changes in surface roughness of heads with changes in touch-down power as little as 1.3 mW compared to unworn heads.

In addition, head wear was examined as a function of DC disk bias voltage, relative humidity (RH), and lubricant type. Two different experimental set-ups were used: First, preliminary experiments were carried out on a load/unload tester under ambient conditions (22 °C and 25 % RH). Second, experiments were performed on a spin-stand tester at <8 %, 30 % and 52 % relative humidity and 27 °C, and three types of disk lubricants (two Demnum and one Z-tetraol lubricant). Similarly, head-wear was determined by measuring the change in the heater touch-down power, ΔTDP, before and after wear testing. After wear testing, selected recording heads were examined using atomic force microscope (AFM) to identify regions of wear or deposit formation on the slider surface. It is found that the measured change in touch-down power, ΔTDP, is smallest when applying a positive DC disk bias voltage for levels in relative humidity larger than 25 %, independent of the tester being used, the disk lubricant and if the head or the disk was biased. For the <8 % RH wear tests, the measured change in touch-down power, ΔTDP, was found to be smallest for negative disk DC bias voltages. The AFM height images show build-up in the read/write region of heads tested at <8 % RH. Except for heads tested at negative DC disk bias voltages which showed very small amounts of

deposit, no deposit was observed on the recording heads tested at 30 % and 52 % RH. Preliminary electrostatic force microscope images (EFM) suggest that the build-up is non-conducting. In summary, the results indicate that both the relative polarity of the voltage across the HDI and relative humidity affect head wear.

A new approach was investigated for predicting the touch-down power of a TFC slider, i.e., the onset of slider disk-contact. The method utilizes the contact sensor to sense head-disk proximity prior to actual head-disk contact. Impeding contact was predicted based on a change in dynamics from heater input to sensor output with decreasing flying height. A first-order discrete-time transfer function of the thermal actuator was estimated form experimentally obtained step-response data using the step-based realization algorithm. We concluded that the coefficient b_0 of the first-order transfer function can be used to predict the touch-down power several milliwatt prior to actual head-disk contact. The proposed transfer function approach was experimentally verified using two different types of disks and hence does not appear to be restricted to a particular head-disk combination.

Lastly, a method was proposed for computing the optimal feedforward heater profile to minimize low-frequency variations in flying height. The method utilized the embedded contact sensor (CS) as a spacing estimate. The flying height error was approximated by 1) applying a third order polynomial curve fit to the CS mean versus heater power curve; 2) measuring the sensor voltage over one disk revolution at the desired DC operating power; 3) subtracting the curve fit obtained in step 1) from 2) via linear interpolation; and 4) comparing the result to a desired set-point, yielding the error signal. The relationship between heater modulation and error signal was modeled from experimental step-response data via step-based realization. The optimal heater input for minimizing flying height variations was obtained using convex optimization techniques. Experiments showed that the standard deviation of the sensor error was reduced by a

factor of two when using the optimized heater power compared to the case where a constant level in DC power was applied to the heater.

In summary, hard disk drives have evolved into highly complex products. Extremely low flying heights of 1-2 nm during reading and writing give rise to many challenging and interdisciplinary problems. The work presented in this dissertation suggests that wear of the recording head is not only driven by purely mechanical phenomena but also by tribochemistry and electrochemistry. The proposed flying height control method may reduce the likelihood of intermittent contact events by enabling constant flying heights, thus improving reliability of hard disk drives. In recent years, the hard disk drive industry has been threatened by the emergence of the much faster and possibly more reliable solid state drives. It is hence important that hard disk drives maintain their relative cost advantage compared to solid state drives in order to stay relevant in the storage market. In order to do so, larger capacities need to be provided at lower cost while ensuring reliability, warranting further research on this topic.

Appendix A

Step-based realization algorithm

The step-based realization algorithm [93, 176, 279] allows identifying a discrete time model of a system from experimentally obtained step-response data. In the following, the step-based realization is briefly reviewed.

The input-output relationship of a time-invariant, single-input single-output (SISO) system in state-space form is given by

$$\begin{aligned} \mathbf{x}(k+1) &= \mathbf{A}\mathbf{x}(k) + \mathbf{B}u(k) \\ y(k) &= \mathbf{C}\mathbf{x}(k) + \mathbf{D}u(k) \end{aligned} \tag{A.1}$$

where $\mathbf{x}(k) \in \mathbb{R}^{n\times 1}$ denotes the n-dimensional state vector, $u(k) \in \mathbb{R}^{1\times 1}$ is the input, $y(k) \in \mathbb{R}^{1\times 1}$ is measurement output, k refers to the input and output samples at discrete time events $t = k\Delta T$ with constant sampling interval ΔT (k = 0, 1, ..., $2N$), $\mathbf{A} \in \mathbb{R}^{n\times n}$ is the state matrix, $\mathbf{B} \in \mathbb{R}^{n\times 1}$ is the input matrix, $\mathbf{C} \in \mathbb{R}^{1\times n}$ is the output matrix, and $\mathbf{D} \in \mathbb{R}^{1\times 1}$ denotes the feed-through term.

The output y due to arbitrary inputs u in equation (A.1) can also be rewritten as

$$y(k) = \sum_{j=0}^{\infty} \mathbf{g}(j)u(k-j) \tag{A.2}$$

where $\mathbf{g}(j)$ denote the impulse response coefficients (or Markov parameters) given by

$$\mathbf{g}(j) = \begin{cases} \mathbf{D}, & j = 0 \\ \mathbf{CA^{j-1}B}, & j > 0 \end{cases} \tag{A.3}$$

Alternatively, the input-output relationship in equation (A.1) can be expressed via the following Hankel matrix based representation

$$\mathbf{H_Y} = \mathbf{HU} + \mathbf{E} \tag{A.4}$$

in which $\mathbf{H_Y}$ denotes the Hankel matrix of the output signals

$$\mathbf{H_Y} = \begin{bmatrix} y(1) & y(2) & \cdots & y(N) \\ y(2) & y(3) & \cdots & y(N+1) \\ \vdots & \vdots & & \vdots \\ y(N) & y(N+1) & \cdots & y(2N-1) \end{bmatrix}_{N \times N} \tag{A.5}$$

$\mathbf{H}$ is the Hankel matrix of the Markov parameters

$$\mathbf{H} = \begin{bmatrix} g(1) & g(2) & \cdots & g(N) \\ g(2) & g(3) & \cdots & g(N+1) \\ \vdots & \vdots & & \vdots \\ g(N) & g(N+1) & \cdots & g(2N-1) \end{bmatrix}_{N \times N} \tag{A.6}$$

U denotes the input matrix

$$\mathbf{U} = \begin{bmatrix} u(0) & u(1) & \cdots & u(N-1) \\ 0 & u(0) & \cdots & u(N-2) \\ \vdots & \vdots & & \vdots \\ 0 & 0 & \cdots & u(0) \end{bmatrix}_{N \times N} \tag{A.7}$$

and **E** is a row-wise listing of output signals given by

$$\mathbf{E} = \begin{bmatrix} y(0) & y(0) & \cdots & y(0) \\ y(1) & y(1) & \cdots & y(1) \\ \vdots & \vdots & & \vdots \\ y(N-1) & y(N-1) & \cdots & y(N-1) \end{bmatrix}_{N \times N} \tag{A.8}$$

The Hankel matrix of the Markov parameters can be expressed as

$$\mathbf{H} = \mathbf{Q}\boldsymbol{\zeta} \tag{A.9}$$

where **Q** and ζ denote the observability and controllability matrices, respectively

$$\mathbf{Q} = \begin{bmatrix} \mathbf{C} \\ \mathbf{CA} \\ \mathbf{CA^2} \\ \vdots \\ \mathbf{CA^{j-1}} \end{bmatrix}, \qquad \boldsymbol{\zeta} = \begin{bmatrix} \mathbf{B} & \mathbf{AB} & \mathbf{A^2B} & \cdots & \mathbf{A^{j-1}B} \end{bmatrix}. \tag{A.10}$$

The generalized realization algorithm allows estimating the state-space matrices **A**, **B**, **C**, and **D** by performing a realization on the weighted Hankel matrix **R**. The

weighted Hankel matrix $\mathbf{R}$ is defined as

$$\mathbf{R} = \mathbf{Y} - \mathbf{E} = \mathbf{HU}. \tag{A.11}$$

For unit step inputs, the matrix $\mathbf{U}$ is an upper triangular matrix containing only ones. Hence, $\mathbf{U}$ has full rank from which follows that rank($\mathbf{R}$) = rank($\mathbf{H}$). For noise-free measurements, the rank of $\mathbf{R}$ is on the same order as the order of the system to be identified. Step response measurements, however, are rarely noise-free and therefore, rank($\mathbf{R}$)$> n$ where n denotes the order of the system. To choose the rank of the model, the singular value decomposition (SVD) is applied to $\mathbf{R}$ yielding

$$\mathbf{R} = \mathbf{U\Sigma V^T} = \begin{bmatrix} \mathbf{U}_n & \mathbf{U}_s \end{bmatrix} \begin{bmatrix} \mathbf{\Sigma}_n & 0 \\ 0 & \mathbf{\Sigma}_s \end{bmatrix} \begin{bmatrix} \mathbf{V_n^T} \\ \mathbf{V_s^T} \end{bmatrix}. \tag{A.12}$$

The matrices $\mathbf{U}$ and $\mathbf{V}$ are unitary, and $\mathbf{\Sigma}$ is a diagonal matrix containing the (non-negative) singular values of matrix $\mathbf{R}$ in descending order. $\mathbf{\Sigma}$ and is split up into $\mathbf{\Sigma}_n$ and $\mathbf{\Sigma}_s$, with $\mathbf{\Sigma}_n$ containing the large singular values, and $\mathbf{\Sigma}_s$ containing the small singular values. In the case of noise-free measurements, $\mathbf{\Sigma}_n$ is non-zero and all entries in $\mathbf{\Sigma}_s$ are zero.

After applying the singular value decomposition to $\mathbf{R}$ and determining the order n of the system, the matrix $\mathbf{R}$ can be reduced in rank resulting in

$$\mathbf{R}_n = \mathbf{R_1 R_2} \tag{A.13}$$

where

$$\begin{aligned} \mathbf{R_1} &= \mathbf{U_n}\, \mathbf{\Sigma}_n^{1/2} \\ \mathbf{R_2} &= \mathbf{\Sigma}_n^{1/2}\, \mathbf{V_n^T} \end{aligned} \tag{A.14}$$

with expression for the left and right inverse of $\mathbf{R_1}$ and $\mathbf{R_2}$, respectively, given by

$$\begin{aligned} \mathbf{R_1^{\dagger}} &= \mathbf{\Sigma}_n^{-1/2}\mathbf{U_n^T} \\ \mathbf{R_1^{\dagger}} &= \mathbf{V_n}\mathbf{\Sigma}_n^{-1/2}. \end{aligned} \tag{A.15}$$

Comparison with equations (A.10) and (A.13) shows that $\mathbf{R_1} = \mathbf{Q}$ and $\mathbf{R_2} = \boldsymbol{\zeta}\mathbf{U}$.

It can be shown that the matrix $\mathbf{R}$ has the shift property so that

$$\bar{\mathbf{R}} = \mathbf{R_1}\,\mathbf{A}\,\mathbf{R_2} \tag{A.16}$$

where $\bar{\mathbf{R}}$ denotes the shifted Hankel matrix in which each element is shifted forward in time by one sample. $\bar{\mathbf{R}}$ is defined as $\bar{\mathbf{R}} = \bar{\mathbf{H}}_\mathbf{Y} - \bar{\mathbf{E}}$ in which

$$\bar{\mathbf{H}} = \begin{bmatrix} g(2) & g(3) & \cdots & g(N+1) \\ g(3) & g(4) & \cdots & g(N+2) \\ \vdots & \vdots & & \vdots \\ g(N+1) & g(N+2) & \cdots & g(2N) \end{bmatrix}_{N\times N} \tag{A.17}$$

$$\bar{\mathbf{H}}_\mathbf{Y} = \begin{bmatrix} y(2) & y(3) & \cdots & y(N+1) \\ y(3) & y(4) & \cdots & y(N+2) \\ \vdots & \vdots & & \vdots \\ y(N+1) & y(N+2) & \cdots & y(2N) \end{bmatrix}_{N\times N} \tag{A.18}$$

$$\bar{\mathbf{E}} = \begin{bmatrix} y(1) & y(1) & \cdots & y(1) \\ y(2) & y(2) & \cdots & y(2) \\ \vdots & \vdots & & \vdots \\ y(N) & y(N) & \cdots & y(N) \end{bmatrix}_{N\times N} \tag{A.19}$$

It follows from equations (A.13) and (A.16) that the state-space matrices $\mathbf{A}$, $\mathbf{B}$ and $\mathbf{C}$

can be estimated as follows

$$\begin{aligned} \mathbf{A} &= \mathbf{R_1^{\dagger}}\,\bar{\mathbf{R}}\,\mathbf{R_2^{\dagger}} \\ \mathbf{B} &= \mathbf{R_1}(1,:) \\ \mathbf{C} &= \mathbf{R_2}(:,1) \end{aligned} \tag{A.20}$$

with the left and right inverse as defined in (A.15) and $(\cdot)(1,:)$ and $(\cdot)(:,1)$ denoting the first row and first column of a matrix, respectively.

The feedthrough **D** can be estimated from the first output sample after applying a unit step input, i.e. $\mathbf{D} = y(0)$. This, however, may not be a good estimate if the noise on the system is large. Improved estimates of both **B** and **D** may instead be obtained via least-squares optimization [279]. In the work presented in chapters 7 and 8, one sample of time delay between heater input and the change in output of the sensor error is assumed and hence, the **D** is set to zero.

Bibliography

[1] "NETIABI Data recovery." [Online]. Available: http://www.recovery-estonia.ee/userfiles/kovaketas.jpg

[2] C. Lacey, "MicroPhysics, Inc." 1992. [Online]. Available: http://www.microphysics.com/

[3] P. Scaruffi, "A Brief History of Knowledge," p. 72, 2011. [Online]. Available: http://scaruffi.com/know/history.html

[4] L. Howsam, K. Attar, T. Loughran, S. Shep, P. Stoicheff, M. J. M. Ezell, A. Johns, C. Clegg, J. Raven, A. McCleery, J. Bath, S. Schofield, M. F. Suarez, S.J., K. Bode, R. Osborne, and M. Hammond, *The Cambridge Companion to the History of the Book*, L. Howsam, Ed. Cambridge University Press, 2014.

[5] A. V. D. Weel, *Changing our textual minds: Towards a digital order of knowledge*. Manchester University Press, 2011.

[6] T. Breverton, *Encyclopedia of Inventions: A Compendium of Technological Leaps, Groundbreaking Discoveries and Scientific Breakthroughs that Changed the World*. Quercus Publishing, 2012.

[7] "The Library of Congress." [Online]. Available: http://goo.gl/zi7Ymb

[8] V. Turner, J. F. Gantz, D. Reinsel, and S. Minton, "The Digital Universe of Opportunities: Rich Data and Increasing Value of the Internet of Things," International Data Corporation (IDC), Tech. Rep. April, 2014. [Online]. Available: http://www.emc.com/collateral/analyst-reports/idc-digital-universe-2014.pdf

[9] Seagate, "UCSC-ISM: Seagate Overview," Seagate Technologies, Tech. Rep. January, 2015. [Online]. Available: https://courses.soe.ucsc.edu/courses/tim101/Winter15/01/pages/attachments/attachments/30543

[10] W. Digital, "Elemental Storage Building Blocks For Every Datacenter," Western Digital, Tech. Rep., 2013. [Online]. Available: http://www.slideshare.net/WesternDigital/elemental-storage-building

[11] P. Mell and T. Grance, "The NIST Definition of Cloud Computing Recommendations of the National Institute of Standards and Technology," NIST, Tech. Rep., 2011. [Online]. Available: http://nvlpubs.nist.gov/nistpubs/Legacy/SP/nistspecialpublication800-145.pdf

[12] "Cease Fire in HDD vs. SSD Price War," 2013. [Online]. Available: http://www.storagenewsletter.com/rubriques/market-reportsresearch/cease-fire-in-hdd-vs-ssd-price-war-priceg2/

[13] "564 Million HDDs Shipped in 2014 - Trendfocus," 2015. [Online]. Available: http://www.storagenewsletter.com/rubriques/market-reportsresearch/564-million-hdds-shipped-in-2014-trendfocus/

[14] N. Kobie, "SSD sales almost doubled last year," 2014. [Online]. Available: http://www.pcpro.co.uk/news/386938/ssd-sales-almost-doubled-last-year

[15] IBM, "The IBM 350 RAMAC Disk File," 1984. [Online]. Available: https://www.asme.org/getmedia/17666e1b-8c69-4028-9227-b6d04ca4375e/90-IBM-350-RAMAC-Disk-File.aspx

[16] A. S. Hoagland, "History of Magnetic Disk Storage Based on Perpendicular Magnetic Recording," *IEEE Transactions on Magnetics*, vol. 39, no. 4, pp. 1871–1875, 2003.

[17] IBM Inc, "IBM Archives: IBM 350 disk storage unit," 2003. [Online]. Available: https://www-03.ibm.com/ibm/history/exhibits/storage/storage{_}350.html

[18] J. M. Harker, D. W. Brede, R. E. Pattison, G. R. Santana, and L. G. Taft, "A Quarter Century of Disk File Innovation," *IBM Journal of Research and Development*, vol. 25, no. 5, pp. 677–690, 1981.

[19] IBM, "IBM 1301 disk storage unit." [Online]. Available: http://www-03.ibm.com/ibm/history/exhibits/storage/storage{_}1301.html

[20] D. Grabham, "CES 2007: World's first 1TB hard drive," jan 2007. [Online]. Available: http://www.techradar.com/us/news/digital-home/home-networking/ces-2007-world-s-first-1tb-hard-drive-148723

[21] S. Anthony, "Western Digital unveils world's first 10TB hard drive: Helium-filled, shingled recording," sep 2014. [Online]. Available: http://goo.gl/PmfJ8b

[22] I. McFadyen, E. Fullerton, and M. Carey, "State-of-the-Art Magnetic Hard Disk Drives," *MRS Bulletin*, vol. 31, no. 05, pp. 379–383, jan 2006.

[23] H. J. Richter, "The transition from longitudinal to perpendicular recording," *Journal of Physics D: Applied Physics*, vol. 40, no. 9, pp. R149–R177, may 2007.

[24] S. N. Piramanayagam, "Perpendicular recording media for hard disk drives," *Journal of Applied Physics*, vol. 102, no. 1, pp. 0 113 011–22, 2007.

[25] H. J. Richter, a. Y. Dobin, K. Gao, O. Heinonen, R. J. Van De Veerdonk, R. T. Lynch, J. Xue, D. K. Weller, P. Asselin, M. F. Erden, and R. M. Brockie, "Recording on bit-patterned media at densities of 1Tb/in2 and beyond," *INTERMAG 2006 - IEEE International Magnetics Conference*, vol. 42, no. 10, p. 721, 2006.

[26] G. Guo, A. Al Mamun, and C. Bi, *Hard Disk Drive - Mechatronics and Control*, ser. Automation and Control Engineering. CRC Press, 2006.

[27] Toshiba, "Toshiba Leads Industry in Bringing Perpendicular Data Recording to HDD–Sets New Record for Storage Capacity With Two New HDDs," 2004. [Online]. Available: https://www.toshiba.co.jp/about/press/2004{_}12/pr1401.htm

[28] Christopher H. Bajorek, "Magnetoresistive (MR) heads and the earliest MR head-based disk drives: Sawmill and Corsair," Computer History Museum, Mountain View, CA, Tech. Rep., 2014.

[29] Z. Feng, C. Shih, V. Gubbi, and F. Poon, "A study of tribo-charge/emission at the head-disk interface," *Journal of Applied Physics*, vol. 85, no. 8, p. 5615, 1999.

[30] A. J. Wallash, "Electrostatic discharge and electrical breakdown study of the head-disk interface in a hard disk drive," *IEEE Transactions on Magnetics*, vol. 40, no. 3, pp. 1751–1755, 2004.

[31] HGST, "Ultrastar He6 3.5-Inch Helium Platform Enterprise Hard Disk Drives," pp. 5–6, 2013.

[32] B. Marchon, M. R. Khan, N. Heiman, P. Pereira, and A. Lautie, "Tribochemical wear on amorphous carbon thin films," *IEEE Transactions on Magnetics*, vol. 26, no. 5, pp. 2670–2675, 1990.

[33] J. Robertson, "Diamond-like amorphous carbon," *Materials Science and Engineering: R: Reports*, vol. 37, no. 4-6, pp. 129–281, 2002.

[34] B. Wei, B. Zhang, and K. E. Johnson, "Nitrogen-induced modifications in microstructure and wear durability of ultrathin amorphous-carbon films," *Journal of Applied Physics*, vol. 83, no. 5, pp. 2491–2499, 1998.

[35] A. R. Machcha, M. H. Azarian, and F. E. Talke, "An investigation of nano-wear during contact recording," *Wear*, vol. 197, pp. 211–220, 1996.

[36] A. Grill, "Tribology of diamondlike carbon and related materials: an updated review," *Surface and Coatings Technology*, vol. 94-95, pp. 507–513, oct 1997.

[37] T. W. Scharf, R. D. Ott, D. Yang, and J. a. Barnard, "Structural and tribological characterization of protective amorphous diamond-like carbon and amorphous CN[sub x] overcoats for next generation hard disks," *Journal of Applied Physics*, vol. 85, no. 6, pp. 3142–3154, 1999.

[38] E. Riedo, "Structural properties and surface morphology of laser-deposited amorphous carbon and carbon nitride films," *Surface and Coatings Technology*, vol. 125, no. 1-3, pp. 124–128, 2000.

[39] A. Tan, "Corrosion and tribological properties of ultra-thin DLC films with different nitrogen contents in magnetic recording media," *Diamond and Related Materials*, vol. 16, no. 3, pp. 467–472, 2007.

[40] C. Donnet and A. Erdemir, *Tribology of Diamond-Like Carbon Films*, C. Donnet and A. Erdemir, Eds. Boston, MA: Springer US, 2008.

[41] C. A. Charitidis, "Nanomechanical and nanotribological properties of carbon-based thin films: A review," *International Journal of Refractory Metals and Hard Materials*, vol. 28, no. 1, pp. 51–70, 2010.

[42] M. Grischke, K. Bewilogua, K. Trojan, and H. Dimigen, "Application-oriented modifications of deposition processes for diamond-like-carbon-based coatings," *Surface and Coatings Technology*, vol. 74-75, pp. 739–745, 1995.

[43] M. He, S. Lee, and C.-D. Yeo, "Investigating atomic structure of thin carbon film under mechanical stress and frictional heat generation," *Surface and Coatings Technology*, vol. 261, pp. 79–85, 2015.

[44] C. Mathew Mate, "Molecular tribology of disk drives," *Tribology Letters*, vol. 4, no. 2, pp. 119–123, 2000.

[45] R. Z. Lei, A. J. Gellman, P. Jones, and Ryan Z. Lei; Andrew J. Gellman; Paul Jones, "Thermal stability of Fomblin Z and Fomblin Zdol thin Films on amorphous hydrogenated Carbon," *Tribology Letters*, vol. 11, no. 1, pp. 1–5, 2001.

[46] G. W. Tyndall, P. B. Leezenberg, R. J. Waltman, and J. Castenada, "Interfacial interactions of perfluoropolyether lubricants with magnetic recording media," *Tribology Letters*, vol. 4, no. 2, pp. 103–108, 1998.

[47] P. H. Kasai and V. Raman, "Lubricant Transfer in Disk Drives," *Tribology Letters*, vol. 48, no. 3, pp. 367–374, aug 2012.

[48] T. E. Karis, G. W. Tyndall, and R. J. Waltman, "Lubricant Bonding Effects on Thin Film Disk Tribology," *Tribology Transactions*, vol. 44, no. 2, pp. 249–255, jan 2001.

[49] X. Ma, J. Gui, B. Marchon, M. Jhon, C. Bauer, and G. Rauch, "Lubricant replenishment on carbon coated discs," *IEEE Transactions on Magnetics*, vol. 35, no. 5, pp. 2454–2456, 1999.

[50] B. G. Min, J. W. Choi, H. R. Brown, and D. Y. Yoon, "Spreading characteristics of thin liquid films of PFPE on solid surfaces." *Tribology Letters*, vol. 1, pp. 225–232, 1995.

[51] S. Nakazawa and Y. Kawakubo, "Effects of Humidity and Temperature on Head Wear on Thin-Film Disk." in *Proceedings of the INTERMAG 2006 Conference*, vol. 1, no. 1995, 2006, p. 2001.

[52] M. Yanagisawa, "Water Adsorption on Lubricated Surfaces for Magnetic Storage Devices," *Tribology Transactions*, vol. 44, no. 2, pp. 197–202, jan 2001.

[53] N. Shukla, E. Svedberg, R. J. M. van de Verdonk, X. Ma, J. Gui, and A. J. Gellman, "Water Adsorption on Lubricated a-CHx in Humid Environments," *Tribology Letters*, vol. 15, no. 1, pp. 9–14, 2003.

[54] Z. Tao and B. Bhushan, "Bonding, degradation, and environmental effects on novel perfluoropolyether lubricants," *Wear*, vol. 259, no. 7-12, pp. 1352–1361, jul 2005.

[55] Z. Zhao and B. Bhushan, "Humidity effect on friction/stiction and durability of head-disk interface with polar perfluoropolyether lubricant," *Journal of Applied Physics*, vol. 81, no. 8, p. 5387, 1997.

[56] X. Ma, H. Tang, and J. Gui, "Temperature effect on spreading of perfluoropolyethers on amorphous carbon films," *Tribology Letters*, vol. 10, no. 4, pp. 203–209, 2001.

[57] S. V. Canchi and D. B. Bogy, "Slider-Lubricant Interactions and Lubricant Distribution for Contact and Near Contact Recording Conditions," *IEEE Transactions on Magnetics*, vol. 47, no. 7, pp. 1842–1848, jul 2011.

[58] ——, "Thermal Fly-Height Control Slider Instability and Dynamics at Touchdown: Explanations Using Nonlinear Systems Theory," *Journal of Tribology*, vol. 133, no. 2, p. 021902, 2011.

[59] D. Pan, A. Ovcharenko, R. Tangaraj, M. Yang, and F. E. Talke, "Investigation of lubricant transfer between slider and disk using molecular dynamics simulation," *Tribology Letters*, vol. 53, no. 1, pp. 373–381, 2014.

[60] Y. Fu, R. Brunner, J.-p. Peng, J. Apte, J. Mcfadyen, and F. E. Talke, "The Effects of Parking Time, Temperature and Slider Position on Lubricant Migration in Hard Disk Drives," *IEEE Transactions on Magnetics*, vol. 9464, no. c, pp. 1–1, 2014.

[61] Y. Shimizu, K. Ono, N. Umehara, and J. Xu, "Experimental and Numerical Simulation Study on Low-Surface Energy Slider With Thermal Flying-Height Control Function," *IEEE Transactions on Magnetics*, vol. 45, no. 10, pp. 3620–3623, oct 2009.

[62] S. V. Canchi and D. B. Bogy, "Slider dynamics in the lubricant-contact regime," in *IEEE Transactions on Magnetics*, vol. 46, no. 3 PART 1, mar 2010, pp. 764–769.

[63] J. Liu, J. Li, J. Xu, and S. Yoshida, "Optimization of micro-thermal actuator for flying height control," *Microsystem Technologies*, vol. 16, no. 1-2, pp. 249–255, apr 2009.

[64] L. Ng, M. Zhang, B. Liu, and Y. Ma, "Slider-Disk Contact Characterization Using a Thermal Fly-Height Control Slider," *IEEE Transactions on Magnetics*, vol. 45, no. 11, pp. 5026–5029, nov 2009.

[65] A. I. Vakis, S.-C. Lee, and A. A. Polycarpou, "Dynamic contact with friction of an ultra-low flying head-disk interface with thermal protrusion," *2009 Asia-Pacific Magnetic Recording Conference*, pp. 1–2, jan 2009.

[66] J. Xu, J. D. Kiely, Y.-T. Hsia, and F. E. Talke, "Effect of thermal pole tip protrusion and disk roughness on slider disk contacts," *Microsystem Technologies*, vol. 15, no. 5, pp. 687–693, feb 2009.

[67] M. Zhang, B. Liu, and S. Hu, "Reader as a contact detector," *Applied Physics Letters*, vol. 94, no. 24, p. 241911, 2009.

[68] X. Zhao and B. Bhushan, "Studies on degradation mechanisms of lubricants for magnetic thin-film rigid disks," *Proceedings of the Institution of Mechanical Engineers, Part J: Journal of Engineering Tribology*, vol. 215, no. 2, pp. 173–188, 2001.

[69] C. Bhatia, D. Bogy, S. Anders, T. Stammler, and J. Stohr, "Tribo-chemistry at the head/disk interface," *IEEE Transactions on Magnetics*, vol. 35, no. 2, pp. 910–915, mar 1999.

[70] M. S. Lim and A. J. Gellman, "Kinetics of laser induced desorption and decomposition of Fomblin Zdol on carbon overcoats," *Tribology International*, vol. 38, no. 6-7, pp. 554–561, 2005.

[71] W. Zhou, Y. Zeng, B. Liu, S. Yu, W. Hua, and X. Huang, "Evaporation of polydisperse perfluoropolyether lubricants in heat-assisted magnetic recording," *Applied Physics Express*, vol. 4, no. 9, pp. 13–16, 2011.

[72] P. H. Kasai, W. T. Tang, and P. Wheeler, "Degradation of perfluoropolyethers catalyzed by aluminum oxide," *Applied Surface Science*, vol. 51, no. 3-4, pp. 201–211, sep 1991.

[73] G. Vurens, R. Zehringer, and D. Saperstein, "The Decomposition Mechanism of Perfluoropolyether Lubricants during Wear," in *Surface Science Investigations in Tribology*, mar 1992, pp. 169–180. [Online]. Available: http://pubs.acs.org/doi/abs/10.1021/bk-1992-0485.ch010

[74] S. Matsunuma, "The initial step of tribochemical reactions of perfluoropolyether on amorphous carbon," *Wear*, vol. 213, pp. 112–116, 1997.

[75] J. V. Wasem, B. L. LaMarche, S. C. Langford, and J. T. Dickinson, "Triboelectric charging of a perfluoropolyether lubricant," *Journal of Applied Physics*, vol. 93, no. 4, pp. 2202–2207, 2003.

[76] F. E. Spada and D. Basov, "Fourier transform infrared investigation of thin perfluoropolyether films exposed to electric fields," *Tribology Letters*, vol. 8, pp. 179–186, 2000.

[77] S. Tadepalli and P. Anandan, "Flow induced vibration of head suspension assemblies in hard drives," *Digest of the Asia-Pacific Magnetic Recording Conference*, pp. 14–15, 2002.

[78] Q. Zhang, S. Chen, S. H. Winoto, and E. H. Ong, "Design of high-speed magnetic fluid bearing spindle motor," *IEEE Transactions on Magnetics*, vol. 37, no. 4 I, pp. 2647–2650, 2001.

[79] W. C. Blount, "Fluid Dynamic Bearing Spindle Motors Their future in hard disk drives," HGST, a Western Digital company, Tech. Rep. November, 2007. [Online]. Available: https://goo.gl/eWXj8p

[80] R. Wood, "Future hard disk drive systems," *Journal of Magnetism and Magnetic Materials*, vol. 321, no. 6, pp. 555–561, 2009.

[81] G. Bouchard, L. Lau, and F. Talke, "Investigation of non-repeatable spindle runout 3687," *IEEE Transactions on Magnetics*, vol. M, no. 5, pp. 3687–3689, 1987.

[82] U. Boettcher, "Nano-scale Positioning, Control and Motion Planning in Hard Disk Drives," Ph.D. dissertation, University of California, San Diego, 2011.

[83] H. Matthews, "Air bearing head displacement sensor and positioner (US 4,605,977)," 1986.

[84] C. Yeack-Scranton, V. D. Khanna, K. F. Etzold, and A. P. Praino, "An active slider for practical contact recording," *IEEE Transactions on Magnetics*, vol. 26, no. 5, pp. 2478–2483, 1990.

[85] W. D. Pohl, J. K. Gimzewski, and P. R. Muralt, "Method and apparatus for controlling the flying height of the head in a magnetic storage unit (US 4,853,810)," 1989.

[86] S. H. Chang, F. Hendrik, V. D. Khanna, and E. G. Lean, "Programmable air bearing slider including magnetic read/write element (US 5,021,906)," 1991.

[87] D. W. Meyer, P. E. Kupinski, and J. C. Liu, "Slider with temperature responsive transducer positioning (US 5,991,113)," 1999.

[88] B. E. Schultz, "Thermal Fly-height Control (TFC) Technology in Hitachi Hard Disk Drives," p. 4, 2007.

[89] H. Li, H. Zheng, J. Fritzsche, K. Amemiya, and F. E. Talke, "Simulation of Flying Height and Response Time of Thermal Flying Height Control Sliders With Thermal Insulators," *IEEE Transactions on Magnetics*, vol. 46, no. 6, pp. 1292–1294, 2010.

[90] M. Kurita, T. Shiramatsu, K. Miyake, A. Kato, M. Soga, H. Tanaka, S. S. Saegusa, and M. Suk, "Active Flying-height Control of Magnetic Head Slider using MEMS Thermal Actuator," *Microsystem Technologies*, vol. 12, no. 4, pp. 267–273, feb 2006.

[91] K. Miyake, T. Shiramatsu, M. Kurita, H. Tanaka, M. Suk, and S. Saegusa, "Optimized Design of Heaters for Flying Height Adjustment to Preserve Performance and Reliability," *IEEE Transactions on Magnetics*, vol. 43, no. 6, pp. 2235–2237, jun 2007.

[92] H. Li, C.-T. Yin, and F. E. Talke, "Thermal insulator design for optimizing the efficiency of thermal flying height control sliders," *Journal of Applied Physics*, vol. 105, no. 7, p. 07C122, 2009.

[93] U. Boettcher, H. Li, R. A. de Callafon, and F. E. Talke, "Dynamic Flying Height Adjustment in Hard Disk Drives Through Feedforward Control," *IEEE Transactions on Magnetics*, vol. 47, no. 7, pp. 1823–1829, jul 2011.

[94] J. N. C. Fitch, "Interview with Luminary Professor H. Peter Jost - The Man who Gave Birth to the Word 'Tribolog'," *Machinery Lubrication*, jan 2006.

[95] "OED online." [Online]. Available: www.oxforddictionaries.com/us/definition

[96] W. E. Jamison, "Introduction to tribology," *Journal of Vacuum Science and Technology*, vol. 13, no. 1, p. 76, 1976.

[97] G. Binnig and C. F. Quate, "Atomic Force Microscope," *Physical Review Letters*, vol. 56, no. 9, pp. 930–933, 1986.

[98] E. Meyer, T. Gyalog, R. M. Overney, and K. Dransfeld, *Nanoscience: Friction and Rheology on the nanometer scale*. World Scientific Pub Co Inc, 1998.

[99] D. Tabor, "Friction-The Present State of Our," *Journal of Lubrication Technology*, vol. 103, no. April, 1981.

[100] H. Yoshizawa, Y. L. Chen, and J. Israelachvili, "Fundamental Mechanisms of Interfacial Friction .1. Relation between Adhesion and Friction," *Journal of Physical Chemistry*, vol. 97, pp. 4128–4140, 1993.

[101] A. Molinari, Y. Estrin, and S. Mercier, "Dependence of the Coefficient of Friction on the Sliding Conditions in the High Velocity Range," *Journal of Tribology*, vol. 121, no. 1, p. 35, 1999.

[102] M. H. Müser, "Velocity dependence of kinetic friction in the Prandtl-Tomlinson model," *Physical Review B - Condensed Matter and Materials Physics*, vol. 84, no. 12, 2011.

[103] O. M. Braun and M. Peyrard, "Dependence of kinetic friction on velocity: Master equation approach," *Physical review. E, Statistical, nonlinear, and soft matter physics*, vol. 83, no. 4 Pt 2, p. 046129, 2011.

[104] D. Boye, "Brief history of friction." [Online]. Available: http://www.phy.davidson.edu/fachome/dmb/PY430/Friction/history.html

[105] R. Stribeck, "Kugellager für beliebige Belastungen," *Zeitshrift des Vereins Deutscher Ingenieure*, vol. 45, 1901.

[106] ——, "Die wesentlichen Eigenschaften der Gleit- und Rollenlager," *Zeitschrift des Vereins Deutscher Ingenieure*, vol. 46, 1902.

[107] H. Hertz, "Über die Berührung fester elastischer Körper," *Journal für die reine und angewandte Mathematik*, vol. 171, pp. 156–171, 1881.

[108] J. A. Greenwood and J. J. Wu, "Surface roughness and contact: An apology," *Meccanica*, vol. 36, no. 6, pp. 617–630, 2001.

[109] J. F. Archard, "Contact and rubbing of flat surfaces," *Journal of Applied Physics*, vol. 24, no. 8, pp. 981–988, 1953.

[110] J. a. Greenwood and J. B. P. Williamson, "Contact of Nominally Flat Surfaces," *Proceedings of the Royal Society A: Mathematical, Physical and Engineering Sciences*, vol. 295, no. 1442, pp. 300–319, 1966.

[111] J. F. Archard, "Elastic Deformation and the Laws of Friction," *Proceedings of the Royal Society A: Mathematical, Physical and Engineering Sciences*, vol. 243, no. 1233, pp. 190–205, dec 1957.

[112] S. Shaffer, "Tribology 101 - Introduction to the Basics of Tribology," pp. 1–70, 2013.

[113] M. Sedlaček, B. Podgornik, and J. Vižintin, "Correlation between standard roughness parameters skewness and kurtosis and tribological behaviour of contact surfaces," *Tribology International*, vol. 48, pp. 102–112, 2012.

[114] C. Y. Lai, F. L. Lewis, V. Venkataramanan, X. Ren, S. S. Ge, and T. Liew, "Disturbance and Friction Compensations in Hard Disk Drives Using Neural Networks," *IEEE Transactions on Industrial Electronics*, vol. 57, no. 2, 2010.

[115] C. Du, L. Xie, and J. Zhang, "Compensation of VCM actuator pivot friction based on an operator modeling method," *IEEE Transactions on Control Systems Technology*, vol. 18, no. 4, pp. 918–926, 2010.

[116] F. P. Bowden and D. Tabor, *The friction and lubrication of solids*. Oxford University Press, 2001.

[117] B. Bhushan, "Contact mechanics of rough surfaces in tribology: multiple asperity contact," *Tribology Letters*, vol. 4, pp. 1–35, 1998.

[118] ——, *Introduction to Tribology*, 2nd ed. John Wiley & Sons, Inc., New York, 2013.

[119] E. Gutierrez-Miravete, "Topics in Mechanical Engineering: FRICTION, WEAR AND LUBRICATION OF MATERIALS," 2012. [Online]. Available: http://www.ewp.rpi.edu/hartford/{~}ernesto/F2012/FWM/Pics/Solids/Wear-Abrasive-2Body.jpg

[120] ——, "Topics in Mechanical Engineering: FRICTION, WEAR AND LUBRICATION OF MATERIALS," 2012.

[121] K. C. Ludema, *Friction, Wear, Lubrication*. CRC Press, 1996.

[122] Y. Kondo, T. Koyama, and S. Sasaki, "Tribological Properties of Ionic Liquids," in *Ionic Liquids - New Aspects for the Future*, Jun-ichi Kadokawa, Ed. INTECH, 2013.

[123] B. Jacobson, "The Stribeck memorial lecture," *Tribology International*, vol. 36, no. 11, pp. 781–789, 2003.

[124] M. H. Wahl, P. R. Lee, and F. E. Talke, "An Efficient Finite Element-Based Air Bearing Simulator for Pivoted Slider Bearings using Bi-Conjugate Gradient Algorithms," *Tribology Transactions*, vol. 39, pp. 130–138, 1996.

[125] W. Zhou, S. Yu, W. Hua, and K. S. Myo, "A modified slip model for gas lubrication at nanoscale head-disk interface," *Proceedings of the Institution of Mechanical Engineers, Part J: Journal of Engineering Tribology*, vol. 227, no. 12, pp. 1367–1375, jul 2013.

[126] M. Wahl, "Numerical and experimental investigation of the head-disk interface," Ph.D. dissertation, University of California, San Diego, 1994.

[127] M. Duwensee, F. E. Talke, S. Suzuki, J. Lin, and D. Wachenschwanz, "Direct Simulation Monte Carlo Method for the Simulation of Rarefied Gas Flow in Discrete Track Recording Head/Disk Interfaces," *Journal of Tribology*, vol. 131, no. 1, p. 012001, 2009.

[128] W. D. Zhou, B. Liu, S. K. Yu, and W. Hua, "Rarefied-gas heat transfer in micro- and nanoscale Couette flows," *Physical Review E*, vol. 81, no. 1, p. 011204, jan 2010.

[129] S. Fukui and R. Kaneko, "Analysis of Ultra-Thin Gas Film Lubrication Based on Linearized Boltzmann Equation: First Report - Derivation of a Generalized Lubrication Equation Including Thermal Creep Flow," *Journal of Tribology*, vol. 110, no. 2, p. 262, 1988.

[130] M. H. Wahl and F. E. Talke, "Numerical Simulation of the steady state flying characteristics of a 50 % slider with surface texture," *IEEE Transactions on Magnetics*, vol. 57, no. 5, pp. 749–751, 1992.

[131] B. Liu, M. Zhang, S. Yu, L. Gonzaga, Y. S. Hor, and J. Xu, "Femto slider: Fabrication and evaluation," *IEEE Transactions on Magnetics*, vol. 39, no. 2, pp. 909–914, mar 2003.

[132] H. Li, M. Kurita, J. Xu, and S. Yoshida, "Iteration method for analysis of write-current-induced thermal protrusion," *Microsystem Technologies*, vol. 16, no. 1-2, pp. 161–167, 2009.

[133] H. Zheng, H. Li, and F. E. Talke, "Numerical simulation of a thermal flying height control slider with dual heater and insulator elements," *IEEE Transactions on Magnetics*, vol. 45, no. 10, pp. 3628–3631, 2009.

[134] K. L. Johnson, *Contact mechanics*. Cambridge University Press, 1985.

[135] D. Tabor, *The Hardness of Metals (Oxford Classic Texts in the Physical Sciences)*, 1st ed. Oxford University Press, 1951.

[136] W. R. Chang, I. Etsion, and D. B. Bogy, "Static Friction Coefficient Model for Metallic Rough Surfaces," *Journal of Tribology*, vol. 110, no. 1, p. 57, 1988.

[137] L. Kogut and I. Etsion, "Elastic-Plastic Contact Analysis of a Sphere and a Rigid Flat," *Journal of Applied Mechanics*, vol. 69, no. 5, p. 657, 2002.

[138] R. Lu, H. Zhang, Y. Mitsuya, K. Fukuzawa, and S. Itoh, "Influence of surface roughness and coating on the friction properties of nanometer-thick liquid lubricant films," *Wear*, vol. 319, no. 1-2, pp. 56–61, 2014.

[139] R. J. Yeo, N. Dwivedi, E. Rismani, N. Satyanarayana, S. Kundu, P. S. Goohpattader, H. R. Tan, N. Srinivasan, B. Druz, S. Tripathy, and C. S. Bhatia, "Enhanced Tribological, Corrosion, and Microstructural Properties of an Ultrathin (<2 nm) Silicon Nitride/Carbon Bilayer Overcoat for High Density Magnetic Storage," *ACS Applied Materials & Interfaces*, vol. 6, no. 12, pp. 9376–9385, 2014.

[140] W. Zhang, K. Wazumi, A. Tanaka, and Y. Koga, "Tribological properties of nitrogen-containing amorphous carbon film produced by dc plasma chemical vapor deposition," *Journal of Vacuum Science & Technology A: Vacuum, Surfaces, and Films*, vol. 21, no. 1, p. 6, 2003.

[141] L. Ilberg, H. Manis-Levy, a. Raveh, Y. Lifshitz, and M. Varenberg, "Effect of structure of carbon films on their tribological properties," *Diamond and Related Materials*, vol. 38, pp. 79–86, 2013.

[142] D. C. Sutton, G. Limbert, D. Stewart, and R. J. K. Wood, "The friction of diamond-like carbon coatings in a water environment," *Friction*, vol. 1, no. 3, pp. 210–221, 2013.

[143] A. Erdemir and C. Donnet, "Tribology of diamond-like carbon films: recent progress and future prospects," *Journal of Physics D: Applied Physics*, vol. 39, no. 18, pp. R311–R327, 2006.

[144] Y. Liu, a. Erdemir, and E. Meletis, "An investigation of the relationship between graphitization and frictional behavior of DLC coatings," *Surface and Coatings Technology*, vol. 86-87, pp. 564–568, dec 1996.

[145] Y. Liu, A. Erdemir, and E. I. Meletis, "A study of the wear mechanism of diamond-like carbon films," *Surface and Coatings Technology*, vol. 82, no. 1-2, pp. 48–56, 1996.

[146] M. Suk, P. Dennig, and D. Gillis, "Magnetic Erasures Due to Impact Induced Interfacial Heating and Magnetostriction," p. 264, 2000.

[147] D. J. Li and Y. W. Chung, "Ultrasmooth CNx overcoats for next-generation hard disks," *IEEE Transactions on Magnetics*, vol. 39, no. 2 I, pp. 765–768, 2003.

[148] Y. Mabuchi, T. Higuchi, and V. Weihnacht, "Effect of sp2/sp3 bonding ratio and nitrogen content on friction properties of hydrogen-free DLC coatings," *Tribology International*, vol. 62, pp. 130–140, 2013.

[149] R. Goltsberg, I. Etsion, and G. Davidi, "The onset of plastic yielding in a coated sphere compressed by a rigid flat," *Wear*, vol. 271, no. 11-12, pp. 2968–2977, 2011.

[150] W.-R. Chang, "An elastic-plastic contact model for a rough surface with an ion-plated soft metallic coating," *Wear*, vol. 212, no. 2, pp. 229–237, 1997.

[151] J. I. McCool, "Greenwood Williamson Microcontact Model," *Transactions of the ASME*, vol. 122, no. July 2000, 2015.

[152] W. Song, L. Li, A. Ovcharenko, D. Jia, I. Etsion, and F. E. Talke, "Plastic yield inception of an indented coated flat and comparison with a flattened coated sphere," *Tribology International*, vol. 53, pp. 61–67, 2012.

[153] G. Guo, Q. Hao, and T.-s. Low, "A dual-stage control design for high track per inch hard disk drives," *IEEE Transactions on Magnetics*, vol. 37, no. 2, pp. 860–865, mar 2001.

[154] Q. Zeng, B. Thornton, D. Bogy, and C. Bhatia, "Flyability and flying height modulation measurement of sliders with sub-10 nm flying heights," *IEEE Transactions on Magnetics*, vol. 37, no. 2, pp. 894–899, mar 2001.

[155] N. K. V. Nilsen, "Control Design for a Piezo-Electric Dual-Stage Instrumented Suspension," in *Proceedings of International Conference on Control and Applications*, 2004, pp. 99–104.

[156] K. Sundaravadivelu, Q. D. Zhang, N. Y. Liu, E. H. Ong, T. H. Yip, G. L. Chin, and J. Q. Mou, "Flow-Induced Slider Vibration in a Functional Hard Disk Drive: Influence of Air Shroud," *IEEE Transactions on Magnetics*, vol. 45, no. 11, pp. 4923–4928, nov 2009.

[157] S. Felix and R. Horowitz, "Integration of thin film strain sensors into hard drives for active feedback vibration suppression," *IEEE Sensors Journal*, vol. 13, no. 5, pp. 1708–1715, 2013.

[158] U. Boettcher, C. A. Lacey, H. Li, K. Amemiya, R. A. de Callafon, and F. E. Talke, "Servo signal processing for flying height control in hard disk drives," *Microsystem Technologies*, vol. 17, no. 5-7, pp. 937–944, 2011.

[159] D. Guarisco, B. Higgins, and a. LeFebvre, "Perpendicular drive integration," *IEEE Transactions on Magnetics*, vol. 42, no. 2, pp. 171–175, feb 2006.

[160] B. Chen, T. Lee, and V. Peng, K., Venkataramanan, *Hard Disk Drive Servo Systems*. Springer US, 2006, vol. 28, no. 3.

[161] M. L. Workman, R. L. Kosut, and G. F. Franklin, "Adaptive Proximate Time-Optimal Servomechanisms: Continuous Time Case," *1987 American Control Conference*, 1987.

[162] T. Yamaguchi, K. Shishida, S. Tohyama, and H. Hirai, "Mode switching control design with initial value compensation and its application to head positioning control on magnetic disk drives," *IEEE Transactions on Industrial Electronics*, vol. 43, no. 1, 1996.

[163] T. Yamaguchi, H. Numasato, and H. Hirai, "A mode-switching control for motion control and its application to disk drives: Design of optimal mode-switching conditions," *IEEE/ASME Transactions on Mechatronics*, vol. 3, no. 3, pp. 202–209, 1998.

[164] B. M. Chen, T. H. Lee, K. Peng, and V. Venkataramanan, "Composite nonlinear feedback control for linear systems with input saturation: Theory and an application," *IEEE Transactions on Automatic Control*, vol. 48, no. 3, pp. 427–439, 2003.

[165] L. Y. Pao and C. La-orpacharapan, "Shaped Time-Optimal Feedback Controllers for Flexible Structures," p. 173, 2004.

[166] U. Boettcher, D. Fetzer, H. Li, R. A. de Callafon, and F. E. Talke, "Reference signal shaping for closed-loop systems with application to seeking in hard disk drives," *IEEE Transactions on Control Systems Technology*, vol. 20, no. 2, pp. 335–345, 2012.

[167] U. Boettcher, L. Matthes, B. Knigge, R. A. de Callafon, and F. E. Talke, "Suppression of cross-track vibrations using a self-sensing micro-actuator in hard disk drives," *Microsystem Technologies*, vol. 18, no. 9-10, pp. 1309–1317, jun 2012.

[168] D. Lengert, E. B. Fanslau, and F. E. Talke, "Design of suspension-based and collocated dual stage actuated suspensions," in *Microsystem Technologies*, vol. 18, no. 9-10, 2012, pp. 1615–1622.

[169] B. Liu, S. K. Yu, W. D. Zhou, C. H. Wong, and W. Hua, "Low Flying-Height Slider With High Thermal Actuation Efficiency and Small Flying-Height Modulation Caused by Disk Waviness," *IEEE Transactions on Magnetics*, vol. 44, no. 1, pp. 145–150, jan 2008.

[170] N. Liu, J. Zheng, and D. B. Bogy, "Thermo-mechanical aspects of thermal flying-height control sliders for hard disk drives," *Mathematics and Mechanics of Solids*, vol. 16, no. 7, pp. 694–705, feb 2011.

[171] S.-C. Lee, G. W. Tyndall, and M. Suk, "Flying Clearance Distribution With Thermal Flying Height Control in Hard Disk Drives," *Journal of Tribology*, vol. 132, no. 2, p. 024502, 2010.

[172] B. D. Strom, S. Zhang, S. C. Lee, A. Khurshudov, and G. W. Tyndall, "Effects of humid air on air-bearing flying height," *IEEE Transactions on Magnetics*, vol. 43, pp. 3301–3304, 2007.

[173] T. Shiramatsu, T. Atsumi, M. Kurita, Y. Shimizu, and H. Tanaka, "Dynamically Controlled Thermal Flying-Height Control Slider," *IEEE Transactions on Magnetics*, vol. 44, no. 11, pp. 3695–3697, nov 2008.

[174] J. P. R. McFadyen and B. E. Knigge, "Disk drive employing comb filter for repeatable fly height compensation," 2011.

[175] S. E. Christdhas, "Disk drive generating fly height measurement from servo burst and adjusting by position error signal," 2014.

[176] R. A. de Callafon, B. Moaveni, J. P. Conte, X. He, and E. Udd, "General Realization Algorithm for Modal Identification of Linear Dynamic Systems," *Journal of Engineering Mechanics*, vol. 134, no. 9, pp. 712–722, 2009.

[177] R. Wood, "The feasibility of magnetic recording at 1 Terabit per square inch," *IEEE Transactions on Magnetics*, vol. 36, no. 1, pp. 36–42, 2000.

[178] S. Greaves, Y. Kanai, and H. Muraoka, "Shingled recording for 2-3 Tbit/in2," *IEEE Transactions on Magnetics*, vol. 45, no. 10, pp. 3823–3829, 2009.

[179] S. Charap, P.-L. L. P.-L. Lu, and Y. H. Y. He, "Thermal stability of recorded information at high densities," *IEEE Transactions on Magnetics*, vol. 33, no. 1, pp. 978–983, 1997.

[180] D. Weller and A. Moser, "Thermal effect limits in ultrahigh-density magnetic recording," *IEEE Transactions on Magnetics*, vol. 35, no. 6, pp. 4423–4439, 1999.

[181] A. Moser, K. Takano, D. T. Margulies, M. Albrecht, Y. Sonobe, Y. Ikeda, S. Sun, and E. E. Fullerton, "Magnetic recording: advancing into the future," *Journal of Physics D: Applied Physics*, vol. 35, no. 19, pp. R157–R167, 2002.

[182] R. Wood, "Shingled Magnetic Recording and Two-Dimensional Magnetic Recording Acknowledgements," in *IEEE Magnetics Society Santa Clara Valley Chapter*, 2010, pp. 1–59.

[183] T. W. McDaniel, "Ultimate limits to thermally assisted magnetic recording," *Journal of Physics: Condensed Matter*, vol. 17, pp. R315–R332, 2005.

[184] M. H. Kryder, E. C. Gage, T. W. Mcdaniel, W. a. Challener, R. E. Rottmayer, G. Ju, Y. T. Hsia, and M. F. Erden, "Heat assisted magnetic recording," *Proceedings of the IEEE*, vol. 96, no. 11, pp. 1810–1835, 2008.

[185] G. Gibson and G. Ganger, "Principles of Operation for Shingled Disk Devices," Parallel data laboratory, Carnegie Mellon University, Tech. Rep. 54515, 2011.

[186] B. Marchon, T. Pitchford, Y. T. Hsia, and S. Gangopadhyay, "The head-disk interface roadmap to an areal density of 4 Tbit/in 2," *Advances in Tribology*, vol. 2013, 2013.

[187] R. Wood, "The feasibility of magnetic recording at 10 Terabit per square inch," *IEEE Transactions on Magnetics*, vol. 36, no. 2, pp. 917–923, 2009.

[188] K.-S. Park, Y.-P. Park, and N.-C. Park, "Prospect of Recording Technologies for Higher Storage Performance," *IEEE Transactions on Magnetics*, vol. 47, no. 3, pp. 539–545, mar 2011.

[189] Seagate, "Breaking areal density barriers with Seagate," 2014. [Online]. Available: http://www.seagate.com/tech-insights/breaking-areal-density-barriers-with-seagate-smr-master-ti/

[190] R. M. H. New, R. F. W. Pease, and R. L. White, "Submicron patterning of thin cobalt films for magnetic storage," *Journal of Vacuum Science & Technology B: Microelectronics and Nanometer Structures*, vol. 12, no. 6, p. 3196, 1994.

[191] B. D. Terris, T. Thomson, and G. Hu, "Patterned media for future magnetic data storage," *Microsystem Technologies*, vol. 13, pp. 189–196, 2006.

[192] J.-G. Zhu, Z. Lin, L. Guan, and W. Messner, "Recording, noise, and servo characteristics of patterned thin film media," *IEEE Transactions on Magnetics*, vol. 36, no. 1, pp. 23–29, 2000.

[193] J. K. W. Yang, Y. Chen, T. Huang, H. Duan, N. Thiyagarajah, H. K. Hui, S. H. Leong, and V. Ng, "Fabrication and characterization of bit-patterned media beyond 1.5 Tbit/inˆ2," *Nanotechnology*, vol. 22, p. 385301, 2011.

[194] J.-G. Zhu, X. Zhu, and Y. Tang, "Microwave Assisted Magnetic Recording," *IEEE Transactions on Magnetics*, vol. 44, no. 1, pp. 125–131, 2008.

[195] L. Wu, "Modelling and simulation of the lubricant depletion process induced by laser heating in heat-assisted magnetic recording system," *Nanotechnology*, vol. 18, no. 21, p. 215702, 2007.

[196] W. Peng, Y. T. Hsia, K. Sendur, and T. McDaniel, "Thermo-magneto-mechanical analysis of head-disk interface in heat assisted magnetic recording," *Tribology International*, vol. 38, no. 6-7, pp. 588–593, 2005.

[197] P. M. Jones, J. Ahner, C. L. Platt, H. Tang, and J. Hohlfeld, "Understanding disk carbon loss kinetics for heat assisted magnetic recording," *IEEE Transactions on Magnetics*, vol. 50, no. 3, pp. 144–147, 2014.

[198] B. Marchon, X. C. Guo, B. K. Pathem, F. Rose, Q. Dai, N. Feliss, E. Schreck, J. Reiner, O. Mosendz, K. Takano, H. Do, J. Burns, and Y. Saito, "Head-disk interface materials issues in heat-assisted magnetic recording," *IEEE Transactions on Magnetics*, vol. 50, no. 3, pp. 137–143, 2014.

[199] A. Q. Wu, Y. Kubota, T. Klemmer, T. Rausch, C. Peng, Y. Peng, D. Karns, X. Zhu, Y. Ding, E. K. C. Chang, Y. Zhao, H. Zhou, K. Gao, J. U. Thiele, M. Seigler, G. Ju, and E. Gage, "HAMR areal density demonstration of 1+ tbpsi on spinstand," *IEEE Transactions on Magnetics*, vol. 49, pp. 779–782, 2013.

[200] M. Mallary, "Microwave Assisted Magnetic Recording for 2Tb / Sqin," Western Digital Coporation, Santa Clara, Tech. Rep., 2012.

[201] K. Rivkin, M. Benakli, N. Tabat, and H. Yin, "Physical principles of microwave assisted magnetic recording," *Journal of Applied Physics*, vol. 115, no. 2014, 2014.

[202] M. Zhang, T. Zhou, and Z. Yuan, "Analysis of Switchable Spin Torque Oscillator for Microwave Assisted Magnetic Recording," *Advances in Condensed Matter Physics*, vol. 2015, pp. 1–6, 2015.

[203] M. Matsubara, M. Shiimoto, K. Nagasaka, Y. Sato, Y. Udo, K. Sugiura, M. Hattori, M. Igarashi, Y. Nishida, H. Hoshiya, K. Nakamoto, and I. Tagawa, "Experimental feasibility of spin-torque oscillator with synthetic field generation layer for microwave assisted magnetic recording," *Journal of Applied Physics*, vol. 109, no. 2011, pp. 2013–2016, 2011.

[204] S. K. Ganapathi, M. Donovan, and Y.-t. Hsia, "Contact force measurements at the head/disk interface for contact recording heads in magnetic recording," in *SPIE Proceddings*, T. A. Schwarz and M. Francis, Eds., vol. 2604, jan 1996, pp. 236–243.

[205] H. H. Gatzen, "Observations regarding the tribological properties of sic and altic sliders," *IEEE Transactions on Magnetics*, vol. 32, no. 5, pp. 3783–3785, 1996.

[206] S. S. Varanasi, J. L. Lauer, F. E. Talke, G. Wang, and J. H. Judy, "Friction and Wear Studies of Carbon Overcoated Thin Films Magnetic Sliders : Application of Raman Microspectroscopy," *Journal of Tribology*, vol. 1, no. July, pp. 7–11, 1997.

[207] M. Kawaguchi, T. Kato, and K. Tanaka, "A study of friction properties of Zdol on magnetic disk surface," *IEEE Transactions on Magnetics*, vol. 39, no. 5, pp. 2483–2485, sep 2003.

[208] A. J. Wallash, "A Dynamic Scratch Test to Study Read/Write Head Degradation Due to Head-Disk Interactions," *IEEE Transactions on Magnetics*, vol. 44, no. 11, pp. 3629–3632, nov 2008.

[209] N. Li, L. Zheng, D. B. Bogy, and Y. Meng, "Flyability and Durability Test of Dynamic Fly-Height Sliders at 1-nm Clearance," *Tribology Transactions*, vol. 53, no. 2, pp. 212–218, feb 2010.

[210] S. H. Kim, X.-C. Guo, R. J. Waltman, H.-B. Tu, T. Shatz, and D. J. Pocker, "Durability Against Contact Wear of Nonlubricated Disks in the Head-Disk Interface of Disk Drives," *IEEE Transactions on Magnetics*, vol. 47, no. 1, pp. 239–243, jan 2011.

[211] B. Knigge and B. Marchon, "Negative biasing a slider with respect to a disk to reduce slider wear and provide burnish rate control (US 8,139,309 B2)," 2012. [Online]. Available: http://www.google.com/patents/US8139309

[212] H. Tani, T. Mitsutome, and N. Tagawa, "Adhesion and Friction Behavior of Magnetic Disks With Ultrathin Perfluoropolyether Lubricant Films Having Different End-Groups Measured Using Pin-on-Disk Test," *IEEE Transactions on Magnetics*, vol. 49, no. 6, pp. 2638–2644, 2013.

[213] S. Lee and C.-D. Yeo, "Thermo-mechanical contact and micro-wear in head disk interface," in *Prooceedings of the ASME/STLE 2011 International Joint Tribology Conference*, 2014, pp. 9–11.

[214] Y. Wang, X. Wei, K.-l. Tsui, and T. W. S. Chow, "Tribological Degradation of Head-Disk Interface in Hard Disk Drives Under Accelerated Wear Condition," *IEEE Transactions on Magnetics*, vol. 50, no. 3, pp. 27–33, mar 2014.

[215] T. Yan and B. E. Jones, "Traceability of acoustic emission measurements using energy calibration methods," *Measurement Science and Technology*, vol. 11, no. 11, pp. L9–L12, 2000.

[216] M. Matsumoto, A. Iida, and T. Hamaguchi, "Measurement of Slider/Disk Collision Forces Using Acoustic Emission Source Wave Analysis," *Tribology Transactions*, vol. 36, no. 4, pp. 736–740, jan 1993.

[217] T. C. McMillan, J. C. Harrison, and F. E. Talke, "Identification of slider/disk contacts using the energy ofthe acoustic emission seignal," *IEEE Transactions on Magnetics*, vol. 34, no. 4, pp. 1819–1821, 1998.

[218] H. Jiao, C. L. Jiaa, J. Adam, and E. F. Cromwell, "Laser Texture and Tribological Study of Alternative Substrates," *Tribology Transactions*, vol. 42, no. 2, pp. 369–376, jan 1999.

[219] J. Li, J. Xu, J. Liu, and H. Kohira, "Thermal mechanics of a contact sensor used in hard disk drives," *Microsystem Technologies*, vol. 19, no. 9-10, pp. 1607–1614, jun 2013.

[220] Y. Shimizu, J. Xu, H. Kohira, M. Kurita, T. Shiramatsu, and M. Furukawa, "Nano-Scale Defect Mapping on a Magnetic Disk Surface Using a Contact Sensor," *IEEE Transactions on Magnetics*, vol. 47, no. 10, pp. 3426–3432, oct 2011.

[221] Polytec, "Basic Principles of Vibrometry," pp. 1–3, 2007. [Online]. Available: http://www.polytec.com/us/solutions/vibration-measurement/basic-principles-of-vibrometry/

[222] M. Johansmann, G. Siegmund, and M. Pineda, "Targeting the Limits of Laser Doppler Vibrometry," Polytec, Tech. Rep., 2005.

[223] D. K. Miu, G. Bouchard, D. B. Bogy, and F. E. Talke, "Dynamic response of a Winchester-type slider measured by laser Doppler interferometry," *IEEE Transactions on Magnetics*, vol. MAG-20, no. 5, pp. 2183–2185, 1984.

[224] D. B. Bogy and F. E. Talke, "Laser Doppler interferometry on magnetic recording systems," *IEEE Trans*, vol. MAG-21, no. 5, pp. 1332–1337, 1985.

[225] B. Knigge and F. Talke, "Nonlinear dynamic effects at the head-disk interface," *IEEE Transactions on Magnetics*, vol. 37, no. 2, pp. 900–905, 2001.

[226] R. Pit and B. Marchon, "Experimental study of lubricant-slider interactions," *IEEE Transactions on Magnetics*, vol. 39, no. 2, pp. 740–742, mar 2003.

[227] B. Knigge, C. Mate, O. Ruiz, and P. Baumgart, "Influence of Contact Potential on Slider-Disk Spacing: Simulation and Experiment," *IEEE Transactions on Magnetics*, vol. 40, no. 4, pp. 3165–3167, jul 2004.

[228] P. Russell and D. Batchelor, "SEM and AFM : Complementary Techniques for Surface Investigations," *Microscopy and Analysis*, pp. 9–12, 2001.

[229] E. Meyer, "Atomic force microscopy," *Progress in Surface Science*, vol. 41, no. 1, pp. 3–49, sep 1992.

[230] H.-S. Ahn, S. Chizhik, A. Dubravin, V. Kazachenko, and V. Popov, "Application of phase contrast imaging atomic force microscopy to tribofilms on DLC coatings," *Wear*, vol. 249, no. 7, pp. 617–625, 2001.

[231] W. W. Scott and B. Bhushan, "Use of phase imaging in atomic force microscopy for measurement of viscoelastic contrast in polymer nanocomposites and molecularly thick lubricant films," *Ultramicroscopy*, vol. 97, no. 1-4, pp. 151–169, 2003.

[232] R. Garcia, C. J. Gómez, N. F. Martinez, S. Patil, C. Dietz, and R. Magerle, "Identification of nanoscale dissipation processes by dynamic atomic force microscopy," *Physical Review Letters*, vol. 97, no. 1, pp. 1–4, 2006.

[233] A. J. Wallash and L. Levit, "Electrical breakdown and ESD phenomena for devices with nanometer-to-micron gaps," *Proceedings of SPIE - The International Society for Optical Engineering*, vol. 4980, pp. 87–96, 2003.

[234] G. Singh, B. Knigge, R. Payne, R.-H. Wang, C. Mate, P. Arnett, C. Davis, V. Nayak, X. Wu, K. Schouterden, and P. Baumgart, "A Novel Wear-In-Pad Approach to Minimizing Spacing at the Head/Disk Interface," *IEEE Transactions on Magnetics*, vol. 40, no. 4, pp. 3148–3152, jul 2004.

[235] L. Su, Y. Hu, E. L. Lam, P. Li, R. W. Ng, D. Liang, O. Zheng, H. Liu, Z. Deng, and J. Zhang, "Tribological and Dynamic Study of Head Disk Interface at Sub-1-nm Clearance," *IEEE Transactions on Magnetics*, vol. 47, no. 1, pp. 111–116, jan 2011.

[236] J. Y. Juang, J. Forrest, and F. Y. Huang, "Magnetic head protrusion profiles and wear pattern of thermal flying-height control sliders with different heater designs," *IEEE Transactions on Magnetics*, vol. 47, no. 10, pp. 3437–3440, 2011.

[237] W. Song, A. Ovcharenko, B. Knigge, M. Yang, and F. E. Talke, "Effect of contact conditions during thermo-mechanical contact between a thermal flying height control slider and a disk asperity," *Tribology International*, vol. 55, pp. 100–107, nov 2012.

[238] T. Melin, M. Zdrojek, and D. Brunel, "Electrostatic Force Microscopy and Kelvin Force Microscopy as a Probe of the Electrostatic and Electronic Properties of Carbon Nanotubes," *Scanning Probe microscopy in Nanoscience and Nanotechnology*, no. 2, pp. 89–128, 2010.

[239] O. C. Wells and D. C. Joy, "The early history and future of the SEM," *Surface and Interface Analysis*, vol. 38, no. 12-13, pp. 1738–1742, dec 2006.

[240] N. Li, Y. Meng, and D. B. Bogy, "Experimental Study of the Slider-Lube/Disk Contact State and Its Effect on Head-Disk Interface Stability," *IEEE Transactions on Magnetics*, vol. 48, no. 8, pp. 2385–2391, aug 2012.

[241] H. Zheng, S. Zhang, W. Yan, L. Pust, D. Fowler, and F. E. Talke, "The Effect of Thermal Radiation on Thermal Flying Height Control Sliders," *IEEE Transactions on Magnetics*, vol. 46, no. 6, pp. 2376–2378, jun 2010.

[242] G. Stachowiak and A. W. Batchelow, *Engineering Tribology*, 3rd ed. Butterworth-Heinemann, Amsterdam, 2005.

[243] A. Ovcharenko, M. Yang, K. Chun, and F. E. Talke, "Effect of impact conditions and slider corner radius on the thermal-mechanical response during slider-disk contacts," *IEEE Transactions on Magnetics*, vol. 46, no. 10, pp. 3760–3766, 2010.

[244] N. Yu, A. A. Polycarpou, and J. V. Hanchi, "Elastic contact mechanics-based contact and flash temperature analysis of impact-induced head disk interface damage," *Microsystem Technologies*, vol. 14, no. 2, pp. 215–227, may 2007.

[245] B. Liu, M. Zhang, S. Yu, W. Hua, Y. Ma, W. Zhou, L. Gonzaga, and Y. Man, "Lube-Surfing Recording and Its Feasibility Exploration," *IEEE Transactions on Magnetics*, vol. 45, no. 2, pp. 899–904, feb 2009.

[246] S. Ray and S. K. Roy Chowdhury, "Prediction of Flash Temperature at the Contact Between Sliding Bodies With Nanoscale Surface Roughness," *Journal of Tribology*, vol. 129, no. 3, p. 467, 2007.

[247] C. M. Mate, R. N. Payne, P. Baumgart, and K. Kuboi, "Meniscus Adhesion at Ultra-Low Flying Slider-Disk Interfaces," in *World Tribology Congress III, Volume 1*, 2005.

[248] W. Song, A. Ovcharenko, M. Yang, H. Zheng, and F. E. Talke, "Contact between a thermal flying height control slider and a disk asperity," *Microsystem Technologies*, vol. 18, no. 9-10, pp. 1549–1557, jun 2012.

[249] C. Zhang, A. Ovcharenko, M. Yang, N. Knudson, and F. E. Talke, "An investigation of thermal asperity sensors during contact with disk asperities," *Microsystem Technologies*, vol. 20, no. 8-9, pp. 1529–1534, apr 2014.

[250] N. Kobayashi, H. Tani, T. Shimizu, S. Koganezawa, and N. Tagawa, "Slider Wear on Disks Lubricated by Ultra-Thin Perfluoropolyether Lubricants with Different Molecular Weights," *Tribology Letters*, vol. 53, no. 1, pp. 43–49, oct 2013.

[251] Y. Aoki, K. Takahashi, J. Li, J. Xu, and Y. Ooeda, "Humidity effect on head-disk clearance," *Microsystem Technologies*, vol. 17, no. 5-7, pp. 1051–1056, apr 2011.

[252] M. Stirniman, "Environmental Effects on the Interaction of Perfluoropolyethers with Thin-Film Carbon Surfaces," *Tribology Letters*, vol. 58, no. 1, p. 14, apr 2015.

[253] T. E. Karis and M. A. Tawakkul, "Water Adsorption and Friction on Thin Film Magnetic Recording Disks," *Tribology Transactions*, vol. 46, no. 3, pp. 469–478, jan 2003.

[254] J. F. Archard and W. Hirst, "The Wear of Metals under Unlubricated Conditions," *Proceedings of the Royal Society A: Mathematical, Physical and Engineering Sciences*, vol. 236, no. 1206, pp. 397–410, aug 1956.

[255] J. Zheng and D. B. Bogy, "Investigation of Flying-Height Stability of Thermal Fly-Height Control Sliders in Lubricant or Solid Contact with Roughness," *Tribology Letters*, vol. 38, no. 3, pp. 283–289, apr 2010.

[256] J. Zheng, D. B. Bogy, S. Zhang, and W. Yan, "Effects of altitude on thermal flying-height control actuation," *Tribology Letters*, vol. 40, no. 3, pp. 295–299, 2010.

[257] P. Machtle, R. Berger, A. Dietzel, M. Despont, W. Haberle, R. Stutz, G. Binnig, and P. Vettiger, "Integrated microheaters for in-situ flying-height control of sliders used in hard-disk drives," in *Technical Digest. MEMS 2001. 14th IEEE International Conference on Micro Electro Mechanical Systems (Cat. No.01CH37090)*. IEEE, 2001, pp. 196–199.

[258] J. Contreras, L. Franca-Neto, and B. Knigge, "Integrated slider bias control."

[259] S. Rajauria, E. Schreck, and B. Marchon, "Voltage assisted asymmetric nanoscale wear on ultra-smooth diamond like carbon thin films at high sliding speeds," *Scientific Reports*, vol. 6, no. April, p. 25439, 2016.

[260] M. Suk, R. Kroeker, and D. Gills, "Investigation of slider dynamics under electrostatic force," *Microsystem Technologies*, vol. 9, pp. 256–265, 2003.

[261] Z. Feng, E. Cha, and X. Zhang, "A study of electrical charge at head-disk interface," *Tribology Letters*, vol. 18, no. 1, pp. 53–57, jan 2005.

[262] M. Zhang and B. Liu, "Measurement of contact potential difference in head disk interface by readback signal spectrum," *Microsystem Technologies*, vol. 18, pp. 599–602, 2012.

[263] KeithleyInstrumentsInc., "Model 2400 Series SourceMeter User's Manual," Cleveland, Ohio, p. 593, 2002. [Online]. Available: http://research.physics.illinois.edu/bezryadin/labprotocol/Keithley2400Manual.pdf

[264] L. M. Matthes, R. Brunner, B. Knigge, and F. E. Talke, "Head Wear of Thermal Flying Height Control Sliders as a Function of Bonded Lubricant Ratio, Temperature, and Relative Humidity," *Tribology Letters*, vol. 60, no. 3, p. 39, dec 2015.

[265] H. Tani, S. Koganezawa, and N. Tagawa, "Reduction in lubricant pickup by bias voltage between slider and disk surfaces," *Microsystem Technologies*, vol. 22, no. 6, pp. 1221–1225, 2016.

[266] M. Smallen, J. Lee, A. Chao, and J. Enguero, "The role of disk carbon and slider in water adsorption," *IEEE Transactions on Magnetics*, vol. 30, no. 6, pp. 4137–4139, 1994.

[267] K. Nakayama and J. M. Martin, "Tribochemical reactions at and in the vicinity of a sliding contact," *Wear*, vol. 261, pp. 235–240, 2006.

[268] F. Spada, D. Paul, and J. Hammond, "Application Of Surface Analytical Techniques For Understanding Deposit Formation On Magnetic Tape Recording Head Surfaces," *Microscopy and Microanalysis*, vol. 18, no. S2, pp. 874–875, nov 2012.

[269] S. Zhang and D. Bogy, "A heat transfer model for thermal fluctuations in a thin slider/disk air bearing," *International Journal of Heat and Mass Transfer*, no. 42, pp. 1791–1800, 1999.

[270] W. D. Zhou, B. Liu, S. K. Yu, W. Hua, and C. H. Wong, "A generalized heat transfer model for thin film bearings at head-disk interface," *Applied Physics Letters*, vol. 92, no. 4, p. 043109, 2008.

[271] J.-Y. Juang and D. B. Bogy, "Air-Bearing Effects on Actuated Thermal Pole-Tip Protrusion for Hard Disk Drives," *Journal of Tribology*, vol. 129, no. 3, p. 570, 2007.

[272] D. Chen, N. Liu, and D. B. Bogy, "A phenomenological heat transfer model for the molecular gas lubrication system in hard disk drives," *Journal of Applied Physics*, vol. 105, no. 8, p. 084303, 2009.

[273] S. Shen and G. Chen, "A kinetic theory analysis on the heat transfer in hard drive air bearing," *Journal of Applied Physics*, vol. 103, no. 5, p. 054304, 2008.

[274] T. Luo and G. Chen, "Nanoscale heat transfer–from computation to experiment." *Physical chemistry chemical physics : PCCP*, vol. 15, no. 10, pp. 3389–412, mar 2013.

[275] B. V. Budaev and D. B. Bogy, "Computation of radiative heat transport across a nanoscale vacuum gap," *Applied Physics Letters*, vol. 104, no. 6, p. 061109, feb 2014.

[276] R. L. Wallace, "The Reproduction of Magnetically Recorded Signals," *Bell System Technical Journal*, vol. 30, no. 4, pp. 1145–1173, 1951.

[277] M. Grant and S. Boyd, "CVX: Matlab Software for Disciplined Convex Programming," 2014. [Online]. Available: http://cvxr.com/cvx

[278] M. C. Grant and S. P. Boyd, "Graph implementations for nonsmooth convex programs," *Lecture Notes in Control and Information Sciences*, vol. 371, pp. 95–110, 2008.

[279] D. N. Miller and R. A. de Callafon, "Identification of linear time-invariant systems via constrained step-based realization," *IFAC Proceedings Volumes (IFAC-PapersOnline)*, vol. 16, no. PART 1, pp. 1155–1160, 2012.